

Tourmaline as a petrogenetic indicator mineral

The crystal chemistry of tourmaline's X site

vorgelegt von
MSc.-Earth and Planetary Sciences
Eleanor Jane Berryman
geb. in Alnwick, England

von der Fakultät VI – Planen Bauen Umwelt
der Technischen Universität Berlin
zur Erlangung des akademischen Grades

Doktor der Naturwissenschaften
– Dr. rer. Nat. –

genehmigte Dissertation

Promotionsausschluss:

Vorsitzender: Prof. Dr. Dietmar Stephan
Gutachter: Prof. Dr. Gerhard Franz
Gutachter: Prof. Dr. Wilhelm Heinrich
Gutachter: Prof. Dr. Horst Marschall

Tag der wissenschaftlichen Aussprache: 9. May 2016

Berlin 2016

Alice started to her feet, for it flashed across her mind that she had never before seen a rabbit with either a waistcoat-pocket, or a watch to take out of it, and burning with curiosity, she ran across the field after it, and fortunately was just in time to see it pop down a large rabbit-hole under the hedge.

– Lewis Carroll, *Alice's Adventures in Wonderland*

Tourmaline will always be my “white-rabbit mineral”, for having lead me down the rabbit-hole that is crystal chemistry.

Eidesstattliche Erklärung

Hiermit erkläre ich, Eleanor Jane Berryman, geboren am 27. Juni 1987 in Alnwick, England, an Eides statt, dass ich die vorliegende Dissertation selbst verfasst und mich dabei keiner anderen als der von mir ausdrücklich bezeichneten Quellen und Hilfen bedient habe.

Ich, Eleanor Jane Berryman, geboren am 27. Juni 1987 in Alnwick, England, erkläre zudem an Eides statt, dass ich an keiner anderen Stelle ein Prüfungsverfahren beantragt habe, dass ich die Dissertation nicht in dieser oder anderer Form bereits anderweitig als Prüfungsarbeit verwendet habe und dass ich sie an keiner anderen Fakultät als Dissertation vorgelegt habe.

Potsdam, den 29. Februar 2016

Abstract

The crystal chemistry of tourmaline's X site is explored using a combination of synthesis experiments, structural characterization, and an investigation of natural tourmalines. The synthesis experiments were done in the range 0.2–4.0 GPa and 500–700 °C in the system $\text{MgO-Al}_2\text{O}_3\text{-B}_2\text{O}_3\text{-SiO}_2\text{-H}_2\text{O}\pm\text{KCl}\pm\text{NaCl}\pm\text{CaCl}_2$ using an oxide mixture and excess fluid. The experimental findings show that K, Na, and Ca incorporation are all positively correlated with their respective concentrations in the fluid. The proportion of vacancies (\square) at the X site is dependent on the net concentration of X-site-occupying ions in solution. Incorporation of K at the X site increases with P and T leading to the formation of K-dominant “K-dravite” at 4.0 GPa, 700 °C from a 4.78 *m* KCl, Na-free, Ca-free fluid. Conversely, Ca incorporation at the X site increases with decreasing P, and to a lesser extent, increasing T. In contrast to both K and Ca, Na incorporation depends predominantly on fluid composition, rather than P or T, whereby the most Na-rich tourmalines were synthesized from Na-rich solutions at all investigated P and T. The experimental results support the formation of maruyamaite, K-dominant tourmaline, from the Kokchetav Massif, Kazakhstan, in a K-rich, Na-poor environment at ultrahigh-P conditions near the diamond-stability field. Additionally, tourmaline is expected to have Ca-rich compositions when it forms in low P, high T Ca-rich rocks, consistent with the current record of tourmaline occurrence.

The varying size and charge of the major X-site-occupying ions, or the presence of \square at the X site, affects both the short- and long-range crystal structure of tourmaline as determined by a combination of single and powder X-ray diffraction and Raman spectroscopy. The unit-cell volume of tourmaline increases with increasing size of the X-site occupant, ranging from 1558.4(3) Å³ for magnesio-foitite to 1588.1(2) Å³ for K-dravite, accommodated largely by the *c*-axis. In terms of the short-range structure, variation in the composition of the X site affects the neighbouring O1–H1 bond, whereby the increased size of K relative to Na results in the shortening of the O1–H1 bond, and the increased charge of Ca results in its deprotonation. In addition, the Mg–Al ratio of the Y and Z sites of the investigated synthetic endmembers is determined from the relative integrated peak intensities of the Raman bands in the O–H stretching vibrational range (3250–3850 cm^{−1}), producing values in good agreement with the single crystal structure refinement.

The experimental results are used to interpret the metamorphic fluid history recorded by tourmalines from the Pfitsch Formation in the SW Tauern Window. The tourmalines are dravitic in composition, whereby their Fe content corresponds with the relative Fe content of the host rock. Tourmalines hosted near quartz-feldspar segregations record up to three stages of growth during pro- and retrograde Alpine metamorphism. Prograde tourmaline crystallized up to peak metamorphic conditions (~300–500 °C, up to 1.0 GPa) from a fluid with a consistent or increasing Ca/(Ca+Na) ratio up to ~0.18. Retrograde tourmaline crystallized at ~0.4 GPa, 400 °C from a fluid with a Ca/(Ca+Na) ratio lower than or similar to that of the prograde fluid.

Zusammenfassung

Translated from English by Dr. Bernd Wunder

Die Kristallchemie der X-Position von Turmalin wurde studiert mit Hilfe von Syntheseexperimenten, Strukturuntersuchungen und chemischer Charakterisierung natürlicher Turmaline. Die Syntheseexperimente wurden im Druck, Temperatur-Bereich von 0.2–4.0 GPa und 500–700 °C im System $\text{MgO-Al}_2\text{O}_3\text{-B}_2\text{O}_3\text{-SiO}_2\text{-H}_2\text{O}\pm\text{KCl}\pm\text{NaCl}\pm\text{CaCl}_2$ unter Verwendung von Oxidmischungen mit Fluidüberschuß durchgeführt. Die experimentellen Ergebnisse zeigen, dass der Einbau von K, Na und Ca positiv mit der jeweiligen Fluidkonzentration korreliert. Der Gehalt an Leerstellen (\square) auf der X-Position hängt von der Konzentration der die X-Position besetzenden Ionen in der Lösung ab. Der Einbau von K auf der X-Position nimmt mit Druck und Temperatur zu, was zur Bildung von K-dominanten K-Dravit bei 4.0 GPa, 700 °C aus einem 4.78 *m* KCl, Na- und Ca-freien Fluid führt. Im Gegensatz dazu, steigt der Ca-Einbau auf der X-Position mit abnehmendem Druck und im geringeren Maß mit ansteigender Temperatur. Abweichend zu K und Ca, hängt der Na-Einbau wesentlich von der Fluidkonzentration ab und weniger von Druck und Temperatur, sodass sich die Na-reichsten Turmaline aus Na-reichen Lösungen bei allen Druck- und Temperatur-Bedingungen bildeten. Die experimentellen Ergebnisse belegen, dass die Bildung von Maruyamait, ein K-dominanter Turmalin aus dem Kokchetav Massiv, Kasachstan, bei K-reichen, Na-armen Bedingungen und bei hohem Druck nahe der Diamantstabilität erfolgte. In Übereinstimmung mit natürlichem Vorkommen, haben Turmaline eine Ca-reiche Zusammensetzung wenn sie bei niedrigen Drücken und hohen Temperaturen in Ca-reichen Gesteinen gebildet werden.

Die variierende Größe und Ladung der die X-Position besetzenden Ionen, oder die Anwesenheit von \square , beeinflussen sowohl den Nah- als auch den Fernbereich der Turmalinstruktur, was mit Hilfe einer Kombination von Einkristall-, Pulver-Röntgen-Diffraktometrie und Raman Spektroskopie untersucht wurde. Das Zellvolumen von Turmalin steigt, wesentlich bestimmt durch die Verlängerung der *c*-Achse, mit zunehmender Größe des die X-Position besetzenden Ions von 1558.4(4) Å³ für Magnesiofoitit auf 1588.1(2) Å³ für K-Dravit. Bezüglich struktureller Nahordnung beeinflusst die Variation der X-Position die benachbarte O1–H1 Bindung, indem der vergrößerte Ionenradius von K relativ zu Na zu einer Verkürzung der O1–H1 Bindung und die zunehmende Ladung von Ca zur Deprotonierung führt. Darüber hinaus konnten die Mg-Al Verhältnisse der Y und Z Positionen für die untersuchten synthetischen Endglieder, mit guter Übereinstimmung zu Daten aus den Einkristallstrukturanalysen, aus den relativen integrierten Intensitäten der Ramanbanden des OH-Streckschwingungsbereiches (3250–3850 cm^{−1}) bestimmt werden.

Die experimentellen Ergebnisse wurden verwendet, um die in Turmalinen gespeicherte metamorphe Fluidgeschichte der Pfitscher Formation im SW Tauern Fenster zu rekonstruieren. Turmaline sind Dravit, wobei ihre Fe-Gehalte mit den Fe-Gehalten der Wirtsgesteine korrespondieren. Turmaline nahe von Quarz-Feldspat Segregationen spiegeln bis zu drei Wachstumsstadien während pro- und retrograder alpiner Metamorphose wider. Prograde Turmaline bildeten sich bis hin zu peakmetamorphen Bedingungen (~300–500 °C, bis zu 1.0 GPa) aus Fluiden mit gleichen oder ansteigenden Ca/(Ca+Na)-Verhältnis von bis zu ~0.18. Retrograde Turmaline bildeten sich bei ~0.4 GPa, 400 °C aus einem Fluid mit einem Ca/(Ca+Na)-Verhältnis kleiner oder ähnlich dem des prograden Fluids.

Acknowledgements

This thesis is part of the project “Compositional variations of tourmaline from low to ultrahigh pressure”, a collaboration between the Technical University (TU) of Berlin and the GFZ German Research Centre for Geosciences in Potsdam. The project was financially supported by funding from the Deutsche Forschungsgemeinschaft (project numbers FR 557/31-1 and HE 2015/16-1) granted to Prof. Gerhard Franz and Prof. Wilhelm Heinrich. The work done in collaboration with Dr. Andreas Ertl at the Institut für Mineralogie und Kristallographie, Geozentrum, Universität Wien in Vienna, Austria, benefitted from funding from the Austrian Science Fund (FWF) (project number P-26903-N19) awarded to Dr. Andreas Ertl. In addition, I gratefully acknowledge the Natural Sciences and Engineering Research Council of Canada (NSERC) for their financial support in the form of a 3-year postgraduate scholarship.

I would like to express my sincere gratitude for the hospitality provided by my colleagues at the TU Berlin and the GFZ Potsdam throughout my time in Germany. I am indebted to Prof. Gerhard Franz and Prof. Wilhelm Heinrich for providing me with the opportunity to pursue my doctoral studies and for supporting me throughout its duration in the form of stimulating discussion and scientific guidance. Additionally, I am thankful for their support and encouragement towards the continuation of my career in academic research. I am also deeply grateful for the support of Dr. Bernd Wunder in providing daily discussion, inspiration, and friendship, as well as in sharing with me his experimental expertise and scientific methods.

Many members of the staff at both the TU Berlin and the GFZ Potsdam contributed to the work presented in this thesis. I thank Hans-Peter Nabein for teaching me how to prepare samples for powder X-ray diffraction and how to run experiments using the hydrothermal pressure apparatuses. I am also grateful for his help in generating X-ray diffraction patterns; in running the hydrothermal pressure apparatus experiments; and in solving day-to-day challenges presented by my computer, its software, and the printers. I am also thankful for the help of Uva Dittmann and Anja Schreiber in sample preparation; Dr. Dieter Rhede and Ona Appelt for their help with electron microprobe analyses; Petra Marsiske for whole rock analyses; Dr. Richard Wirth for TEM analyses; Prof. Koch-Müller for instruction in Raman Spectroscopy; and Dr. Georg Schettler for his help with ICP-AES analyses. In addition, some of the EMP analyses were done at the Museum für Naturkunde in Berlin with the help of Dr. Lutz Hecht and Peter Czaja.

Last, but most certainly not least, this thesis would not have been as enjoyable, or arguably possible, without the ongoing encouragement of my mentors, my friends, and my family. In particular, I would like to thank Prof. Willy Williams-Jones for his continued mentorship and support in multiple facets of my life: past, present, and future. I would also like to thank Prof. Vincent van Hinsberg for introducing me to the wonderful mineral called tourmaline; pointing me in the direction of this project; and providing advice and encouragement, especially at the start of my time in Germany. Finally, I would like to thank Andrew Fleet for being my husband and best friend; for cheerfully making me endless tea and sandwiches during the writing of this thesis; and for responding with enthusiasm when I first considered travelling to the other side of the Atlantic Ocean in

pursuit of this adventure.

To everyone who had a positive impact on my doctoral experience, including those I have not directly mentioned: *Thank you.*

Publications

The contents of the chapters of this doctoral thesis listed below have been published, accepted, or are being prepared for publication in peer-reviewed journals:

Chapter 3 E. Berryman^{1,2}, B. Wunder², D. Rhede² (2014) Synthesis of K-dominant tourmaline. *American Mineralogist* 99: 539–542.

Chapter 4 E.J. Berryman^{1,2}, B. Wunder², R. Wirth², D. Rhede², G. Schettler², G. Franz¹, W. Heinrich² (2015) An experimental study on K and Na incorporation in dravitic tourmaline and insight into the origin of diamondiferous tourmaline from the Kokchetav Massif, Kazakhstan. *Contributions to Mineralogy and Petrology* 169: 28

Chapter 5 E.J. Berryman^{1,2}, B. Wunder², A. Ertl^{3,4}, M. Koch-Müller², D. Rhede², K. Scheidl⁴, G. Giester⁴, W. Heinrich² (2016) Influence of the X-site composition on tourmaline's crystal structure: Investigation of synthetic K-dravite, dravite, oxy-uvite, and magnesio-foitite using SREF and Raman spectroscopy. *Physics and Chemistry of Minerals* 43: 83–102

Chapter 6 E.J. Berryman^{1,2}, B. Wunder², D. Rhede², G. Schettler², G. Franz¹, W. Heinrich² (2016) P-T-X controls on Ca and Na distribution between Mg-Al tourmaline and fluid. *Contributions to Mineralogy and Petrology* 171:31

Chapter 7 E.J. Berryman^{1,2}, M. Kutzschbach^{1,2}, A. Meixner⁵, R. Trumbull², G. Franz¹ (*in preparation*) Tourmaline as a petrogenetic indicator mineral in the Pfitsch Formation of the Pfitscher Joch, Western Tauern Window.

In addition, the following additional publications were prepared during the progress of the doctoral work:

B. Wunder², E. Berryman^{1,2}, D. Rhede², M. Koch-Müller², B. Plessen², W. Heinrich² (2015) Natural and synthetic ammonium-bearing tourmaline. *American Mineralogist* 100: 250–256.

¹ Fachgebiet Mineralogie-Petrologie, Technische Universität Berlin, 13355 Berlin, Germany

² GeoForschungsZentrum Potsdam, Telegrafenberg, 14473 Potsdam, Germany

³ Mineralogisch-Petrographische Abt., Naturhistorisches Museum, 1010 Wien, Austria

⁴ Institut für Mineralogie und Kristallographie, Geozentrum, Universität Wien, 1090 Vienna, Austria

⁵ Faculty of Geosciences and MARUM-Center for Marine Environmental Sciences, University of Bremen, Bremen, Germany

E. Berryman^{1,2}, A.E. Williams-Jones⁶ A.A. Migdisov⁶ (2015) Steel slag carbonation in a flow-through system: the role of fluid-flux. *Journal of Environmental Sciences* 27: 266–275.

⁶ Department of Earth and Planetary Sciences, McGill University, Montreal, Canada

Presentations

The contents of this thesis have been presented at scientific conferences in the following abstracts:

E. Berryman, B. Wunder, G. Franz (2013) Experimental investigation of K incorporation into tourmaline at high temperature and pressure. *Mineralogical Magazine*. 77: 695

E. Berryman, B. Wunder, R. Wirth, W. Heinrich, G. Franz (2014) Pressure's control on K incorporation in tourmaline. IMA General Meeting, Johannesburg, South Africa.

B. Wunder, E. Berryman, D. Rhede, M. Koch-Müller, B. Plessen, W. Heinrich (2014) NH₄-bearing tourmaline: experiments and natural occurrences. IMA General Meeting, Johannesburg, South Africa.

E. Berryman, B. Wunder, D. Rhede, R. Wirth, W. Heinrich, G. Franz (2014) P-T-X controls on K and Na incorporation in dravitic tourmaline. DMG Annual Meeting, Jena, Germany. (*Received the Paul-Ramdohr Prize for best student presentation*)

A. Ertl, E.J. Berryman, B. Wunder, K. Scheidl, G. Giester, G. Franz (2014) Al-Mg disorder and tetrahedrally coordinated B in synthetic K- and Mg-rich tourmaline. DMG Annual Meeting, Jena, Germany.

G. Franz, A. Loges, D. Schultze, E. Berryman, M. Kutzschbach (2014) Protolith determination of a metasedimentary series in the western Tauern Window. DMG Annual Meeting, Jena, Germany.

E.J. Berryman, M. Kutzschbach, A. Loges, D. Schultze, A. Meixner, G. Franz (2015) Tourmaline's record of fluid history in the Pfitscher Joch, Western Tauern Window. AGU-GAC-MAC Joint Assembly, Montreal, Canada.

E.J. Berryman, B. Wunder, A. Ertl, M. Koch-Müller, W. Heinrich, G. Franz (2015) Structural accommodation of K at dravitic tourmaline's X site: insight from Raman spectroscopy and single crystal X-ray diffraction. AGU-GAC-MAC Joint Assembly, Montreal, Canada.

E.J. Berryman, M. Kutzschbach, R.B. Trumbull, A. Meixner, G. Franz (2015) Tourmaline as a petrogenetic indicator in the W Tauern Window. *Goldschmidt Abstracts*. 2015: 281

B. Wunder, E. Berryman, M. Kutzschbach, M. Koch-Müller, A. Ertl (2015) Multi-method characterization of synthetic tourmaline: rossmanite, magnesio-foitite, dravite, and maruyamaite. *Goldschmidt Abstracts*. 2015: 3466

E. Berryman, B. Wunder, A. Ertl, M. Koch-Müller, W. Heinrich, G. Franz (2015) Linking crystal structure to composition in tourmaline: A multi-method investigation of synthetic dravite, maruyamaite, magnesio-foitite, and oxy-uvite. DGGV-DMG Joint Annual Meeting GeoBerlin, Berlin, Germany.

In addition, the contents of this thesis have been presented at the following invited talks:

April 4, 2014

Institut für Mineralogie und Kristallographie, Universität Wien, Austria

Title: “The first synthetic K-rich tourmaline: Synthesis experiments and the influence of pressure on K incorporation”

Invited by: Dr. Andreas Ertl

November 14, 2014

Institut für Erd- und Umweltwissenschaften, Universität Potsdam, Germany

Title: “P-T-X controls on K and Na incorporation in dravitic tourmaline: Insight into the formation environment of diamondiferous tourmaline from the Kokchetav Massif”

Invited by: Dr. Silvio Ferrero

November 18, 2015

Department of Earth and Planetary Sciences, McGill University, Canada

Title: “The crystal chemistry of tourmaline’s X site”

Invited by: Prof. Anthony Williams-Jones

Prizes and public recognition

The following prizes and public recognition were received in association with this doctoral thesis:

Postgraduate scholarship awarded by the Natural Sciences and Engineering Research Council of Canada (NSERC) to Canadian graduates who show outstanding research potential (2012–2015).

Paul-Ramdohr Prize awarded by the Deutsche Mineralogische Gesellschaft for best student presentation at the 2014 DMG Annual Meeting.

Bernd Rendel Prize awarded by the Deutsche Forschungsgemeinschaft to two promising early career geoscientists in Germany who do not yet hold a doctorate (2015).

Interview by Frankfurter Societäts-Medien for the website “Research in Germany” of the German Federal Ministry of Education and Research, published in the December 2015 Newsletter.

Student travel grant to attend the International School of Crystallography 2016 in Erice, Italy.

Contents

Eidesstattliche Erklärung	iii
Abstract	v
Zusammenfassung	vii
Acknowledgements	ix
Publications	xi
Presentations	xiii
Prizes and public recognition	xv
1 Introduction	1
1.1 Tourmaline occurrence	1
1.2 Tourmaline stability	2
1.3 Tourmaline crystal chemistry	2
1.3.1 K in tourmaline	7
1.4 Tourmaline's crystal structure	7
1.4.1 Investigation of tourmaline's crystal structure using X-ray diffraction and Raman spectroscopy	8
1.5 Tourmaline as a petrogenetic indicator mineral	9
1.5.1 Geothermometry	9
1.5.2 Record of fluid composition	10
2 Experimental and analytical methods	13
2.1 Tourmaline synthesis	13
2.1.1 One-chamber synthesis method	13
2.1.2 Two-chamber synthesis method	13
2.1.3 Piston-cylinder experiments	14
2.1.4 Experiments in the hydrothermal pressure apparatus	14
2.2 Fluid recovery and analysis	14
2.3 Electron microprobe (EMP) analysis	15
2.3.1 Synthetic samples	15
2.3.2 Natural samples	16
2.4 Transmission electron microscopy (TEM)	16
2.5 Tourmaline normalization procedures	16
2.6 Whole rock analysis	17
2.7 Powder X-ray diffraction (XRD)	18
2.8 Single-crystal X-ray diffraction (XRD)	18
2.9 Polarized Raman spectroscopy	20

3	Synthesis of K-dominant tourmaline	21
3.1	Introduction and approach	21
3.2	Results and discussion	21
3.3	Implications	26
4	An experimental study on K and Na incorporation in dravitic tourmaline and insight into the origin of diamondiferous tourmaline from the Kokchetav Massif, Kazakhstan	27
4.1	Introduction and approach	27
4.2	Results	30
4.3	Discussion	39
4.3.1	Application to the diamondiferous tourmaline from the Kokchetav Massif, Kazakhstan	44
4.4	Conclusions	45
5	Influence of the X-site composition on tourmaline's crystal structure: Investigation of synthetic K-dravite, oxy-uvite, and magnesio-foitite using SREF and Raman spectroscopy	47
5.1	Introduction and approach	47
5.2	Results	49
5.3	Discussion	59
5.3.1	Single-crystal XRD refinement (SREF)	59
5.3.2	Polarized Raman spectroscopy	60
5.3.3	Influence of X-site composition on crystal structure	65
5.4	Conclusions	66
6	P-T-X controls on Ca and Na distribution between Mg-Al tourmaline and fluid	69
6.1	Introduction and approach	69
6.2	Results	71
6.3	Discussion	75
6.3.1	Ca-Na solid solution exchange vectors	75
6.3.2	Ca-Na tourmaline-fluid partitioning behaviour	82
6.3.3	Implications for Ca-Na trends in natural tourmalines	82
6.3.4	Other possible controls on Ca-Na partitioning	83
6.4	Conclusions	84
7	Tourmaline as a petrogenetic indicator in the Pfitsch Formation of the Western Tauern Window	85
7.1	Introduction	85
7.2	Regional Geology and study area	85
7.3	Tourmaline occurrence and sampling location	87
7.3.1	Tourmaline occurrence	87
7.3.2	Sampling location	88
7.4	Results	88
7.4.1	Whole rock chemistry	88
7.4.2	Tourmaline textures	91
7.4.3	Major element chemistry of associated phases	91
7.4.4	Tourmaline major element chemistry	94
7.4.5	Tourmaline sector zoning thermometry	98
7.5	Discussion	101
7.5.1	Tourmaline solid solution	101

7.5.2	Deciphering the P-T path of the Pfitsch Formation	103
7.5.3	Metamorphic fluid movement in the Tur-gneiss	104
7.5.4	Evolving fluid composition	106
7.6	Conclusions	107
8	Conclusions and outlook	109
8.1	Outstanding questions	110
A	Improved single crystal structure refinement data of magnesio-foitite (MF2)	121
B	Supplementary material to Chapter 7	125
B.1	Abstract	125
B.2	Analytical methods	125
B.3	Results	125

Chapter 1

Introduction

Tourmaline is a mineral supergroup with the general formula $^{[9]}X^{[6]}Y_3^{[6]}Z_6^{[4]}T_6O_{18}(^{[3]}BO_3)_3V_3W$ (Hawthorne and Henry, 1999; Hamburger and Buerger, 1948). As the most abundant borosilicates in the Earth's crust (Henry and Dutrow, 1996), the members of the tourmaline supergroup play an important role in the global cycling of B. Their hardness (7–7.5 on the Mohr scale), wide range in crystal colour, with some specimens having two or more colour zones in a single crystal, and piezo- and pyroelectric properties have resulted in tourmaline's long history as an interesting mineral to scientists. Tourmaline possibly corresponds to the mineral "Lyngurium", described by Theophrastus (ca. 315 B.C.) to be green at one end and light coloured at the other in the first known book on minerals, *On Stones* (Dietrich, 1985). Since then, tourmaline's complex crystal chemistry has led it to be coveted by mineral collectors and to be seen as a powerful indicator mineral to geologists.

1.1 Tourmaline occurrence

Tourmaline can form both magmatically and hydrothermally in a variety of compositional (X), pressure (P), and temperature (T) environments. These include, but are not limited to, sedimentary basins undergoing diagenesis, ore deposits, subduction zones, orogenies, and pegmatites, as summarized in the special tourmaline volumes of *The Canadian Mineralogist* (van Hinsberg *et al.*, 2011a) and *Elements* (Dutrow and Henry, 2011a). As a result, tourmaline occurs as a common accessory mineral in both igneous and metamorphic rocks. Additionally, due to its resilience against chemical and mechanical weathering, tourmaline is often found preserved in detrital sediments. The major element limiting its formation is B. The silicate Earth comprises <0.0001 wt.% B (McDonough and Sun, 1995), whereas tourmaline has ~3 wt.% B (~10 wt.% B_2O_3). Therefore, the occurrence of tourmaline indicates that B has been concentrated by geochemical processes. Due to its incompatible behaviour in most silicate minerals (London *et al.*, 1996), B partitions preferentially into the liquid phase during melting, leading to the enrichment of silicic melts in B. Consequently, the Earth's continental crust is highly enriched in B (~15–17 ppm) relative to the the mantle (<0.1 ppm) (Anovitz and Grew, 1996; Dutrow and Henry, 2011b). In the case of metamorphic tourmaline, B can be sourced either from pre-existing B-bearing minerals and/or from fluids. In pelitic and psammitic sedimentary and metasedimentary rocks, the volumetric dominance of clay minerals make them the major host of B (Henry and Dutrow, 1996). For example, modern pelagic sediments contain 13–300 ppm B hosted either in the clay mineral structure or adsorbed to their surfaces (see summary by Henry and Dutrow, 1996). Moreover, B is highly fluid mobile, occurring principally as the 3-coordinated $B(OH)_3^0$ and the 4-coordinated $B(OH)_4^{-1}$ species in solution (Lee-man and Sisson, 1996). Consequently, fluids serve as an effective means of mobilizing and

concentrating B in rocks undergoing metamorphism and/or metasomatism, and can lead to the crystallization of metamorphic tourmaline. Thus, the occurrence of metamorphic tourmaline provides a direct record of the fluids that led to its formation.

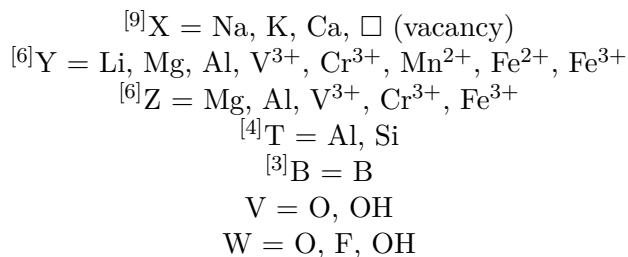
1.2 Tourmaline stability

Tourmaline is stable over a large range of P–T conditions, including most of the Earth’s crust and potentially the upper mantle (*e.g.*, van Hinsberg *et al.*, 2011b). Its widespread stability is evidenced by a combination of experiments and natural occurrences. Its lower P–T stability has not been constrained experimentally, but tourmaline has been synthesized at temperatures as low as 250 °C (Werding and Schreyer, 1996), and is known to form under diagenetic conditions as either overgrowths on detrital tourmaline grains or as fine crystals (Henry and Dutrow, 1996, 2012). Based on experimental data, tourmaline is stable up to 700–950 °C and 4–6 GPa depending on composition (Krosse, 1995; Ota *et al.*, 2008a). In nature, tourmaline with coesite inclusions has been found in ultrahigh-P metamorphic rocks from the Erzgebirge in Germany, and the Dora Maira Massif in the Western Alps (Marschall *et al.*, 2009a). Tourmaline from the Kumdy-Kol in the Kokchetav Massif, Kazakhstan, with microdiamond inclusions potentially records the highest P–T conditions of tourmaline crystallization (Shimizu and Ogasawara, 2005, 2013).

Tourmaline’s stability is also dependent on fluid composition, particularly in terms of pH. The predominance of the two B aqueous species is dependent on pH, with the 3-coordinated $\text{B}(\text{OH})_3^0$ species dominating under neutral to acidic conditions and the 4-coordinated $\text{B}(\text{OH})_4^{-1}$ species dominating under alkaline conditions (Palmer and Swihart, 1996). Tourmaline is only stable in the presence of neutral to highly acidic solutions, in which the coordination of B in the aqueous phase is consistent with its coordination in tourmaline (see Tourmaline’s crystal structure below). With increasing pH, higher concentrations of B are needed to stabilize tourmaline, and it has not been synthesized in the presence of an alkaline fluid (Dutrow and Henry, 2011b).

1.3 Tourmaline crystal chemistry

The flexible crystal structure of tourmaline supergroup minerals allows them to incorporate a large variety of elements, resulting in the growing list of 31 different endmembers currently accepted by the International Mineralogical Association’s Commission on New Minerals, Nomenclature and Classification (IMA-CNMNC) (Table 1.1). The different endmembers represent combinations of the following possible site occupants:



However, tourmaline is able to incorporate far more elements than those that make up the IMA-CNMNC-accepted endmembers, including about half the periodic table (Fig. 1.1).

Tourmaline Chemistry

$\text{X}_3\text{Y}_6\text{Z}_6\text{T}_6\text{O}_{18}(\text{BO}_3)_3\text{V}_3\text{W}$

1 H																			2 He
3 Li	4 Be										5 B	6 C	7 N	8 O	9 F	10 Ne			
11 Na	12 Mg										13 Al	14 Si	15 P	16 S	17 Cl	18 Ar			
19 K	20 Ca	21 Sc	22 Ti	23 V	24 Cr	25 Mn	26 Fe	27 Co	28 Ni	29 Cu	30 Zn	31 Ga	32 Ge	33 As	34 Se	35 Br	36 Kr		
37 Rb	38 Sr											47 Ag	48 Cd	49 In	50 Sn	51 Sb	52 Te	53 I	54 Xe
55 Cs	56 Ba	57-70	71 Lu	72 Hf	73 Ta	74 W	75 Re	76 Os	77 Ir	78 Pt	79 Au	80 Hg	81 Tl	82 Pb	83 Bi	84 Po	85 At	86 Rn	
87 Fr	88 Ra	89-94																	

57 La	58 Ce	59 Pr	60 Nd	61 Pm	62 Sm	63 Eu	64 Gd	65 Tb	66 Dy	67 Ho	68 Er	69 Tm	70 Yb
89 Ac	90 Th	91 Pa	92 U	93 Np	94 Pu								

Figure 1.1: Compilation of elements reported to occur in tourmaline (*coloured*). Elements in *green* have been reported to occur at the X site; those in *purple* at the Y site; those in *light blue* at the Z site; those in *orange* at the T site; those in *dark blue* at the V site; those in *red* at the W site. Only B has been reported to occur at the B site. Elements coloured by more than one colour have been reported to occur at multiple sites. Elements coloured in *grey* have only been reported in trace (<0.1 wt.%) amounts and have not been assigned to any particular site.

Although almost all the alkali and alkaline earth metals have been detected in tourmaline (Fig. 1.1), the X site is principally occupied by Na and Ca, or left vacant (\square), listed in order of their relative abundance (Henry *et al.*, 2011; Table 1.1). K is the third most common X-site-occupying ion and is typically considered a minor or trace element (Henry and Dutrow, 1996). Consequently, the tourmaline supergroup has been subdivided into three primary types based on the dominant occupancy of the X-site: the alkali-, calcic-, and X-vacant (\square) tourmaline groups (Henry *et al.*, 2011). The alkali-tourmaline group includes tourmalines that have $(\text{Na} + \text{K}) > \text{Ca}$ and $(\text{Na} + \text{K}) > \square$ at their X site (Henry *et al.*, 2011), whereas members of the calcic group have an X site dominated by Ca, and those of the X-vacant group, \square .

The octahedral Y and Z sites have the most variable composition of all the sites in tourmaline's structure (Table 1.1). Despite this variability, the Y site is preferentially occupied by ions with a 2+ charge, most commonly Mg and Fe^{2+} , followed by Mn^{2+} . In contrast, the Z site is preferentially occupied by ions with a 3+ charge, most commonly Al, followed by minor amounts of Fe^{3+} (Henry *et al.*, 2011). The stability of possible endmember site compositions are limited by bond-valence arguments, whereby the bond-valence incident to an anion site must closely match the valence of the anion occupying that site (Hawthorne, 2002). However, order-disorder reactions, whereby significant amounts of Mg (or Fe^{2+} ; Bosi, 2008) occupies the Z site and Al, the Y site (*e.g.*, Hawthorne *et al.*, 1993), are ubiquitous in natural dravite (Bosi and Lucchesi, 2007). It has been suggested that Mg-Al disorder between the Y and Z sites may be dependent on temperature (Ertl *et al.*, 2010) or on the occupancy of the W site (Bosi, 2013). As a result, although the endmember compositions of Table 1.1 provide idealized site occupancies and can serve as recommendations for the assignment of elements to either of the two octahedral sites, their true occupancies are largely disordered and can only be constrained through a detailed characterization of the crystal structure.

The tetrahedrally coordinated T site is predominantly occupied by Si, as in all endmember compositions (Table 1.1), but can incorporate significant amounts of Al, or in some cases B. Al is incorporated at the T site via the Tschermak substitution $[\text{YAl}^{\text{T}}\text{Al}(\text{YR}^{2+}\text{T}^{\text{Si}})_{-1}]$, where $\text{R}^{2+} = \text{Fe}^{2+}$, Mg, or Mn^{2+} . Based on observations in natural tourmaline, the amount of tetrahedral Al corresponds with increasing metamorphic grade (Henry and Dutrow, 1996). A similar substitution accounts for the incorporation of B at the tetrahedral site: $\text{YAl}^{\text{T}}\text{B}(\text{YR}^{2+}\text{T}^{\text{Si}})_{-1}$ (Schreyer *et al.*, 2000). An investigation of natural and synthetic Al-rich tourmalines by Ertl *et al.* (2008) demonstrated that T^{B} correlates with YAl , up to a maximum of $\text{T}^{\text{B}} = \text{T}^{\text{Si}} = 3$ and $\text{YAl} = 3$. This is consistent with the aforementioned incorporation mechanism. Moreover, the most B-rich tourmaline on record is an olenite $[\text{XNa}^{\text{Y}}\text{Al}_3^{\text{Z}}\text{Al}_6^{\text{T}}\text{Si}_6\text{O}_{18}(\text{BO}_3)_3\text{O}_3(\text{OH})]$ from the Koralpe, Austria, with ~ 0.83 apfu T^{B} (Ertl *et al.*, 2007). As in the case of T^{Al} , a compilation of tourmaline synthesis data by Ertl *et al.* (2008) shows that the incorporation of tetrahedral B correlates with increasing metamorphic grade.

Table 1.1: IMA-accepted tourmaline species and their end-member compositions (as of December 1, 2015)

Species	X	Y ₃	Z ₆	T ₆ O ₁₈	(BO ₃) ₃	V ₃	W	Year defined
Alkali group								
Dravite	Na	Mg ₃	Al ₆	Si ₆ O ₁₈	(BO ₃) ₃	(OH) ₃	OH	1884
Oxy-dravite	Na	Al ₂ Mg	Al ₅ Mg	Si ₆ O ₁₈	(BO ₃) ₃	(OH) ₃	O	2012
Fluor-dravite	Na	Mg ₃	Al ₆	Si ₆ O ₁₈	(BO ₃) ₃	(OH) ₃	F	2009
Chromium-dravite	Na	Mg ₃	Cr ₆ ³⁺	Si ₆ O ₁₈	(BO ₃) ₃	(OH) ₃	OH	1982
Oxy-chromium-dravite	Na	Cr ₃ ³⁺	Cr ₄ ³⁺ Mg ₂	Si ₆ O ₁₈	(BO ₃) ₃	(OH) ₃	O	2011
Vanadio-oxy-dravite	Na	V ₃ ³⁺	Al ₄ Mg ₂	Si ₆ O ₁₈	(BO ₃) ₃	(OH) ₃	O	2012
Vanadio-oxy-chromium-dravite	Na	V ₃ ³⁺	Cr ₄ ³⁺ Mg ₂	Si ₆ O ₁₈	(BO ₃) ₃	(OH) ₃	O	2012
Oxy-vanadium-dravite	Na	V ₃ ³⁺	V ₄ ³⁺ Mg ₂	Si ₆ O ₁₈	(BO ₃) ₃	(OH) ₃	O	2012
Schorl	Na	Fe ₃ ²⁺	Al ₆	Si ₆ O ₁₈	(BO ₃) ₃	(OH) ₃	OH	2007
Oxy-schorl	Na	Fe ₂ ²⁺ Al	Al ₆	Si ₆ O ₁₈	(BO ₃) ₃	(OH) ₃	O	2011
Fluor-schorl	Na	Fe ₃ ²⁺	Al ₆	Si ₆ O ₁₈	(BO ₃) ₃	(OH) ₃	F	2010
Fluor-buergerite	Na	Fe ₃ ³⁺	Al ₆	Si ₆ O ₁₈	(BO ₃) ₃	O ₃	F	1965
Bosiite	Na	Fe ₃ ³⁺	Al ₄ Mg ₂	Si ₆ O ₁₈	(BO ₃) ₃	(OH) ₃	O	2014
Povondraite	Na	Fe ₃ ³⁺	Fe ₄ ³⁺ Mg ₂	Si ₆ O ₁₈	(BO ₃) ₃	(OH) ₃	O	1990
Chromo-alumino-povondraite	Na	Cr ₃ ³⁺	Al ₄ Mg ₂	Si ₆ O ₁₈	(BO ₃) ₃	(OH) ₃	O	2014
Olenite	Na	Al ₃	Al ₆	Si ₆ O ₁₈	(BO ₃) ₃	O ₃	OH	1985
Darrellhenryite	Na	Al ₂ Li	Al ₆	Si ₆ O ₁₈	(BO ₃) ₃	(OH) ₃	O	2012
Elbaite	Na	Al _{1.5} Li _{1.5}	Al ₆	Si ₆ O ₁₈	(BO ₃) ₃	(OH) ₃	OH	1913
Fluor-elbaite	Na	Al _{1.5} Li _{1.5}	Al ₆	Si ₆ O ₁₈	(BO ₃) ₃	(OH) ₃	F	2011
Tsilaisite	Na	Mn ₃ ²⁺	Al ₆	Si ₆ O ₁₈	(BO ₃) ₃	(OH) ₃	OH	2011
Fluor-tsilaisite	Na	Mn ₃ ²⁺	Al ₆	Si ₆ O ₁₈	(BO ₃) ₃	(OH) ₃	F	2012
Luinaite-(OH)	Na, □	(Fe ²⁺ , Mg) ₃	Al ₆	Si ₆ O ₁₈	(BO ₃) ₃	(OH) ₃	OH	2009
Maruyamaite	K	Mg ₃	Al ₆	Si ₆ O ₁₈	(BO ₃) ₃	(OH) ₃	OH	2013

Continues on next page

Table 1.1: *Continued from previous page*

Species	X	Y ₃	Z ₆	T ₆ O ₁₈	(BO ₃) ₃	V ₃	W	Year defined
Calcic group								
Uvite	Ca	Mg ₃	Al ₅ Mg	Si ₆ O ₁₈	(BO ₃) ₃	(OH) ₃	OH	2000
Fluor-uvite	Ca	Mg ₃	Al ₅ Mg	Si ₆ O ₁₈	(BO ₃) ₃	(OH) ₃	F	2011
Feruvite	Ca	Fe ₃ ²⁺	Al ₅ Mg	Si ₆ O ₁₈	(BO ₃) ₃	(OH) ₃	OH	1987
Adachiite	Ca	Fe ₃ ²⁺	Al ₆	(Si ₅ Al)O ₁₈	(BO ₃) ₃	(OH) ₃	OH	2012
Fluor-liddicoatite	Ca	Li ₂ Al	Al ₆	Si ₆ O ₁₈	(BO ₃) ₃	(OH) ₃	OH	1913
X-vacant group								
Foitite	□	Fe ₂ ²⁺ Al	Al ₆	Si ₆ O ₁₈	(BO ₃) ₃	(OH) ₃	OH	1992
Magnesio-foitite	□	Mg ₂ Al	Al ₆	Si ₆ O ₁₈	(BO ₃) ₃	(OH) ₃	OH	1998
Rossmannite	□	Al ₂ Li	Al ₆	Si ₆ O ₁₈	(BO ₃) ₃	(OH) ₃	OH	1996

1.3.1 K in tourmaline

K is commonly viewed as incompatible in tourmaline, with concentrations typically not exceeding trace amounts (0.1 wt.%) in most crustal environments, most likely because of its large ionic radius (1.55 Å in ninefold coordination, *c.f.* 1.24 Å for Na in ninefold coordination; Shannon, 1976). However, there are two recorded occurrences of K-dominant tourmaline in nature. The most well-known record is K-dominant Mg-Al tourmaline, namely maruyamaite $[\text{K}(\text{Mg}_2\text{Al})\text{Al}_6\text{Si}_6\text{O}_{18}(\text{BO}_3)_3(\text{OH})_3\text{O}]$; Lussier *et al.* 2014], with 2.75 wt.% K_2O or 0.576 K pfu. Shimizu and Ogasawara (2005, 2013) discovered maruyamaite in the Kumdy-Kol in the Kokchetav Massif, Kazakhstan, a fossil subduction zone (see review by Schertl and Sobolev 2013, and references therein). The second record of K-dominant tourmaline is from the type locality of povondraite, Alto Chapare in Bolivia. Here, povondraite $[\text{NaFe}_3^{3+}(\text{Mg}_2\text{Fe}_4^{3+})\text{Si}_6\text{O}_{18}(\text{BO}_3)_3(\text{OH})_3\text{O}]$ with 0.56 K pfu (Grice *et al.*, 1993) to 0.60 K pfu (Žáček *et al.*, 2000) occurs as crystal overgrowths replacing K-rich silicate clasts in the Locotal Breccia, a brecciated and metamorphosed evaporite cap rock (Žáček *et al.*, 2000).

Thermodynamic modelling using fractional properties of cation polyhedra by van Hinsberg and Schumacher (2007b) has predicted that tourmaline will incorporate increasing amounts of K at its X site with increasing P. Moreover, the presence of microdiamond inclusions in maruyamaite from the Kokchetav Massif suggests an ultrahigh pressure origin for this K-dominant tourmaline. However, the occurrence of pristine intergranular diamonds (Korsakov *et al.*, 2004) along with quartz inclusions in other areas of the K-rich tourmaline (0.32 K pfu; Marschall *et al.*, 2009a) prevents exclusion of later, lower-pressure overgrowth of the microdiamonds by K-dominant tourmaline (Ota *et al.*, 2008b). As a result of these conflicting lines of argumentation, no consensus exists on the origin of this unique tourmaline based on petrographic, compositional, and isotopic investigations, or Ar–Ar-dating arguments (summarized in Marschall *et al.*, 2009a) alone. Nonetheless, the scarcity of maruyamaite suggests a formation environment uncommonly preserved in the exposed crust. In Chapter 3, the first synthesis of K-dominant Mg-Al tourmaline at high pressure and temperature (4.0 GPa, 700 °C) from a K-rich (4.78 *m* KCl) fluid is reported. The P-T-X controls on K incorporation were subsequently investigated, and in Chapter 4, it is demonstrated that both high pressure, temperature, and K-dominated fluids are necessary for maruyamaite’s crystallization.

1.4 Tourmaline’s crystal structure

Tourmaline crystallizes in the trigonal space group $R\bar{3}m$ (Buerger and Parrish, 1937). The cyclosilicate crystal structure (Fig. 1.2) consists of rings of six corner-sharing TO_4 tetrahedra, occupied primarily by Si and more rarely by Al and/or B. The bases of the tetrahedra face the c^+ -crystallographic axis direction, making tourmaline a polar crystal. The polar nature of tourmaline is responsible for its long-known piezo- and pyroelectric properties, whereby the c^+ and c^- poles of a crystal develop a positive and negative charge, respectively, when compressed or heated (*e.g.*, Dietrich, 1985). The ninefold-coordinated X site lies directly above the T_6O_{18} ring, coordinated with the inner corners of the tetrahedra. Below the ring, the apex of each tetrahedron shares a corner with one of three edge-sharing Y-site octahedra and one of six Z-site octahedra, which surround the Y-site trimer. The three trigonally-coordinated B atoms share corners with both the Y and Z octahedra. The W and V sites, defined as O1 and O3, respectively, can contain OH^- , O^{2-} , or, in the case of the W site, F^- . The single W (O1) site is found at the center of the T_6O_{18} ring, coordinated with the three Y sites. The O1–H1 bond is aligned with the c -axis, with H1

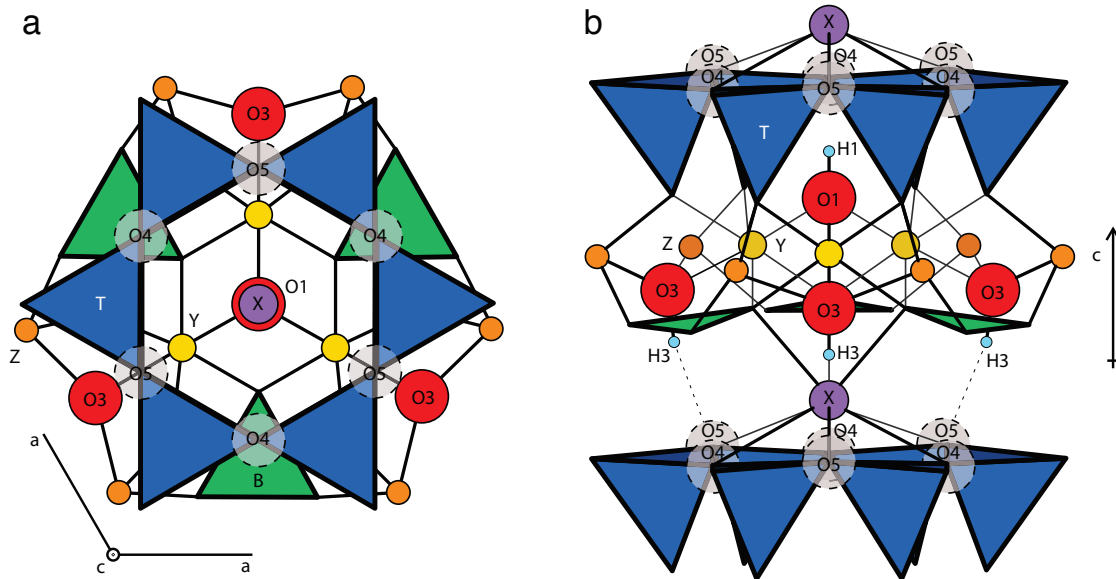


Figure 1.2: Schematic representation of tourmaline's crystal structure viewed normal (A) and parallel (B) to the c -axis. The X site (in *purple*, occupied by Na, Ca, K, or left vacant) is located just above the tetrahedral ring (in *dark blue*) and is bonded to the inner corners of each tetrahedra (T) and trigonally-coordinated B group (in *green*). The O1 (W) site (in *red*) is coordinated to three Y sites (in *yellow*). The O1–H1 bond is orientated with the hydrogen (in *light blue*) pointing toward the X site. The O3 (V) sites (in *red*) are each coordinated to one Y site (in *yellow*) and two Z sites (in *orange*). The O3–H3 bond is orientated in the c^- direction with H3 sharing a H bond with the O5 site (*dashed circle*) in the tetrahedral ring

orientated toward the X site. Asymmetry in the occupation of the coordinated Y sites can cause the O1–H1 bond to diverge from complete parallelism with the c -axis (Gatta *et al.*, 2014). Very weak hydrogen bonds exist between H1 and O4 and O5 (0.026 and 0.047 vu, respectively; Gatta *et al.*, 2014), oxygen sites in the T_6O_{18} ring. The three V (O3) sites are found around the Y-site trimer, between two Z-site octahedra. Each V (O3) site is coordinated with one Y and two Z sites. The O3–H3 bond is orientated with H3 pointing in the c^- -crystallographic axis direction. There is weak, but significant (0.114 vu; Gatta *et al.*, 2012, 2014) hydrogen bonding between H3 and O5, an oxygen atom coordinated with both the T site and the X site. As a result, these hydroxyl groups may be expected to point slightly toward the O5 site and not be completely parallel to the c -axis (Gatta *et al.*, 2014).

The K ion is significantly larger (1.55 Å) than the more common X-site-occupying cations, Na (1.24 Å) and Ca (1.18 Å) (all in ninefold coordination; Shannon, 1976). With increasing size of its occupant, the X-site coordination polyhedron is expected to expand (Ertl and Tillmanns, 2012). In addition, the major X-site occupying ions vary in terms of their ionic charge. This raises the question of how the varying size and charge of the X site is accommodated in tourmaline. The relationship between the X-site-occupying ion and the rest of the crystal structure is explored in the Chapter 5.

1.4.1 Investigation of tourmaline's crystal structure using X-ray diffraction and Raman spectroscopy

X-ray diffraction and Raman spectroscopy are powerful tools for investigating long- and short-range features of crystal structures. Single-crystal structure refinement from X-ray diffraction data of a compositionally well-characterized tourmaline provides information about average site occupancies and bond lengths. Raman spectroscopy provides further information about the bonding environment around different crystallographic sites, including qualitative information about the O–H bond lengths. Recent Raman spectroscopy studies have largely focussed on the assignment of the high wavenumber bands ($3250\text{--}3850\text{ cm}^{-1}$) of tourmalines of various compositions (*e.g.*, Gonzalez-Carreño *et al.*, 1988; Skogby *et al.*, 2012; Fantini *et al.*, 2014). The low wavenumber lattice vibration Raman bands ($100\text{--}1200\text{ cm}^{-1}$) in tourmaline are associated with cation-oxygen bonds (mainly B–O, T–O, Y–O, Z–O, *e.g.*, Mihailova *et al.*, 1996; Gasharova *et al.*, 1997; McKeown, 2008; Zhao *et al.*, 2012; Fantini *et al.*, 2014). The high wavenumber bands ($3250\text{--}3850\text{ cm}^{-1}$) are associated with O–H stretching and are influenced by substitution at the X, Y, and Z sites, as well as by deformation of the T_6O_{18} ring. For example, the presence of significant $^{\text{IV}}\text{B}$ ($>0.33(6)$ pfu; Kutzschbach *et al.*, 2016) can be detected in the Raman spectra of B-rich olenites from the O–H stretching vibrations. Similarly, shifts in the position and intensity of these bands provide insight into the structural effect of the X-site-occupying cation on its local crystal environment as explored in Chapter 5.

To date, almost all Raman spectroscopy studies have been conducted on natural tourmaline crystals, which are solid solutions of various endmember species. The presence of multiple site substitutions in these tourmalines leads to complicated Raman spectra, making it difficult to unambiguously assign bands to particular bonding environments. The investigation of compositionally restricted, synthetic tourmalines as described in Chapter 5 facilitates band assignment.

1.5 Tourmaline as a petrogenetic indicator mineral

Members of the tourmaline supergroup commonly occur as accessory minerals in rocks with diverse chemistries and formation environments due to tourmaline's complex crystal chemistry and widespread stability in pressure and temperature space (see van Hinsberg *et al.*, 2011b; Dutrow and Henry, 2011b; Henry and Dutrow, 2012). Moreover, its refractory nature and the low intravolume diffusion of elements through its structure (*e.g.*, Henry and Dutrow, 1996; Büttner, 2005; Büttner and Kasemann, 2007) result in the preservation of the tourmaline crystals, as well as their compositional zoning, even during ultrahigh grade metamorphism (*e.g.*, Marschall *et al.*, 2009a).

The characteristic growth zoning of individual tourmaline crystals found in detrital sediments serves as a fingerprint of their origin and has resulted in tourmaline's traditional application as a provenance indicator (Krynine, 1946; Henry and Dutrow, 1992). More recently, the increasing understanding of the connection between tourmaline's composition and its formation conditions has allowed tourmaline to be applied as a geochemical recorder of the temperature (*e.g.*, Henry and Dutrow, 1996; van Hinsberg and Schumacher, 2007a, 2011), fluid composition (*e.g.*, von Goerne *et al.*, 2001, 2011), and isotopic composition (*e.g.*, Marschall and Jiang, 2011; Marschall *et al.*, 2009a,b; Meyer *et al.*, 2008) of its formation environment.

However, although significant progress has been made in understanding tourmaline's

crystal chemistry as a function of temperature and bulk composition, the effect of pressure remains poorly constrained.

1.5.1 Geothermometry

As a result of the polar nature of its crystal structure, tourmaline commonly exhibits polar asymmetry in its composition, as well as sector zoning. The polar asymmetry occurs when coeval tourmaline growth at the c^+ and c^- poles of a given crystal vary in composition, despite growing at the same P-T-X conditions. For example, authigenic tourmaline growth in low-grade metasediments from Maine, USA, is characterized by a c^- pole enriched in Ca and Ti relative to the c^+ pole (Henry and Dutrow, 1992).

This phenomenon is understood to be a direct manifestation of the polarity of tourmaline's crystal structure (Fig.1.2), which leads to the c^+ and c^- poles have differing surface energies and site morphologies at the crystal surface. It is also possible that the polar composition results from tourmaline's long-known piezo- and pyroelectric properties. When exposed to pressure or heat, a tourmaline crystal develops a positive and a negative charge at the c^+ and c^- poles, respectively (*e.g.*, Dietrich, 1985). The negative charge of the c^- pole under metamorphic conditions could therefore explain the increased incorporation of high charge elements like Ca and Ti^{4+} at this pole (Henry and Dutrow, 1996). Moreover, a comparison of the extent of polar partitioning and temperature of tourmaline growth by Henry and Dutrow (1996) demonstrated that the partitioning of elements between the poles diminishes with increasing grade, and can thereby potentially serve as a valuable single crystal thermometer. However, just as the pyroelectric behaviour of tourmaline depends on the Fe^{2+} content of the Y site (Hawkins *et al.*, 1995), it is possible that tourmaline's composition also exerts a control on polar partitioning.

van Hinsberg *et al.* (2006) identified that tourmaline growth perpendicular to the c -axis can also deviate in composition from that in the c^+ and c^- direction, resulting in the development of sector zoned crystals when viewed parallel to the c -axis. Sector zoning in tourmaline is directly related to polar crystal growth in the sense that they both result from the polar nature of tourmaline's crystal structure. As a result, van Hinsberg *et al.* (2006) define three growth sectors in tourmaline: the a, c^+ and c^- sectors, where the c^+ and c^- sectors correspond to the polar growth described by Henry and Dutrow (1996). The a sector comprises crystal growth perpendicular to the c -axis. Its composition is thus considered unaffected by the polarity of tourmaline's crystal structure. As a tourmaline crystal grows, the surfaces of the different growth sectors are in local equilibrium with the growth environment. As growth progresses, the different growth sectors result in significant chemical gradients within the bulk crystal. Such chemical potential gradients represent an intracrystalline disequilibrium feature and would normally drive intravolume diffusion, homogenizing the crystal's composition. However, tourmaline's low intravolume diffusion results in their preservation. van Hinsberg and Schumacher (2007a) calibrated Ca and Ti fractionation between the c and a sectors as a function of temperature using the calibration of polar partitioning of Henry and Dutrow (1996). They show that like element fractionation between the poles, partitioning between the c and a sectors principally differentiates high charge elements like Ca and Ti, and decreases with temperature. Above 700 °C, elements no longer fractionate between the different growth sectors. Consequently, sector zoning thermometry can serve as a powerful single crystal thermometer that does not depend on the saturation of other mineral phases. However, it should be noted that the calibration of van Hinsberg and Schumacher (2007a) is purely empirical and provides estimates of crystallization temperatures within ~50 °C of error.

Sector zoning thermometry is applied in Chapter 7 in order to obtain temperature estimates for tourmaline growth in metamorphic tourmalines from the Pfitsch Formation in the Tauern Window, Eastern Alps.

1.5.2 Record of fluid composition

Fluids play a critical role in the transfer of mass and energy in the crust, particularly in dynamic geological environments, such as orogenies, subduction zones, and magmatic intrusions. In these environments, fluids are released through dehydration reactions and compositional and/or temperature gradients drive metasomatic reactions. With the exception of when they are preserved as inclusions in minerals, our knowledge of the composition of these metamorphic fluids is principally based on mineral-fluid equilibria and element partitioning (*e.g.*, Yardley and Bodnar, 2014; van Hinsberg *et al.*, 2010). This motivates the extension of our understanding of mineral-fluid element partitioning, as well as the search for key minerals that can provide us with insight into these inaccessible environments.

Experiments by von Goerne and Franz (2000), von Goerne *et al.* (2001), and von Goerne *et al.* (2011) have investigated the partitioning of the two major X-site-occupying ions, Ca and Na, between tourmaline and its formation fluid. These experimental investigations involved growing Mg-Al (Fe-free) tourmaline in a hydrothermal apparatus at 0.2 GPa and 300–700 °C, and measuring the equilibrium distribution of Ca and Na between the tourmaline rim and the product fluid. von Goerne *et al.* (2011) demonstrated that the number of vacancies at tourmaline’s X site is directly related to the ionic strength of the solution. Moreover, their results show that at 0.2 GPa, the Ca/(Ca+Na) ratio in the fluid correlates to that of tourmaline’s X site, with varying temperature having a secondary effect. These findings demonstrate that tourmaline can provide a record of the composition of the fluid from which it grew. Moreover, compositional zoning in tourmaline can provide insight into the evolution of its formation fluid. However, all the current experimental data corresponds to 0.2 GPa, whereas tourmaline is stable up to at least 4.5 GPa, 800 °C (Ota *et al.*, 2008a) and potentially as high as 6–8 GPa, 900 °C (Krosse, 1995; Schreyer and Werdning, 1997), depending on the bulk composition of the system. Consequently, experiments like those of von Goerne *et al.* (2011) need to be extended to higher pressures before the fluid composition recorded in tourmalines from medium- to high-grade rocks can be interpreted. The fluid-tourmaline partitioning experiments described in Chapter 6 expand on the findings of von Goerne *et al.* (2011) by investigating Ca-Na tourmaline-fluid partitioning at 500–700 °C and 0.2–4.0 GPa.

Chapter 2

Experimental and analytical methods

The studies presented in Chapters 3–7 apply a combination of the experimental and analytical methods detailed below.

2.1 Tourmaline synthesis

Tourmaline was synthesized at 0.2–4.0 GPa and 500–700 °C using either a hydrothermal pressure apparatus (pressure ≤ 0.4 GPa) or an end-loaded piston-cylinder press (pressure > 0.4 GPa). All experiments used solid MgO, γ -Al₂O₃, H₃BO₃ and SiO₂ (as quartz) in the atomic proportions of endmember dravite [NaMg₃Al₆Si₆O₁₈(BO₃)₃(OH)₃(OH)] with 100 mol% excess H₃BO₃ and 20 mol% excess SiO₂ to facilitate tourmaline crystallization (Werding and Schreyer, 1984). Prior to being weighed, MgO and γ -Al₂O₃ were dried at 400 °C for 1 day. A solution comprising dissolved KCl, NaCl, CaCl₂, or a combination of two of the aforementioned chlorides was used in all synthesis experiments. A list of the synthesis materials and run conditions used in all synthesis experiments described in each experimental investigation is given in its respective chapter.

2.1.1 One-chamber synthesis method

All experiments done with the piston-cylinder press, as well as some experiments done in the hydrothermal pressure apparatus, applied the one-chamber synthesis method. In this method, the oxide starting materials were ground and homogenized. The fluid and oxide mixture were then placed in clean, gold capsules. The gold capsules used for experiments done in the end-loaded piston-cylinder press were 10–13 mm in length and had a 3-mm outer diameter and a 0.25-mm wall thickness, whereas those used for experiments in the hydrothermal pressure apparatus were 30 mm in length and had a 4-mm outer diameter and a 0.25-mm wall thickness. After being loaded, the capsules were welded shut and weighed after being stored at 100 °C overnight, ensuring a complete seal.

2.1.2 Two-chamber synthesis method

To produce large (≥ 100 μ m) tourmaline crystals at a pressure attainable by the hydrothermal pressure apparatus (≤ 0.4 GPa), some experiments applied the two-chamber method of von Goerne *et al.* (1999). In this method, SiO₂ is mechanically separated from the rest of the solid starting material, thereby inhibiting tourmaline nucleation and encouraging crystal growth. One end of a clean gold capsule (30-mm length, 4-mm outer diameter, and 0.25-mm wall thickness) was loaded with the fluid and a homogenized oxide mixture of

MgO, γ -Al₂O₃, and H₃BO₃. The center of the capsule was pinched closed, thereby forming two separate chambers. SiO₂ (as quartz) was added to the second chamber and the capsule welded shut. The loaded capsule was stored at 100 °C overnight and subsequently reweighed to ensure a complete seal.

2.1.3 Piston-cylinder experiments

The one-chamber, loaded and sealed capsules were placed in pairs in a graphite/steel-furnace assembly with NaCl as a pressure medium and loaded into the piston-cylinder press. Steel furnaces were used in all experiments run at pressures >2.0 GPa. Pressure was calibrated according to the quartz-coesite transition (Mirwald and Massonne, 1980), which is accurate within 50 MPa. Temperature was measured with a Ni-CrNi thermocouple (accurate within 10 °C) placed into the assembly close to the centers of the capsules. Following pressurization, the system was heated to the target temperature and monitored throughout the experiment; pressure was maintained within 50 MPa. At the end of the experiment, the sample was quenched isobarically to a temperature below 200 °C in less than 15 s and pressure slowly released. The capsule was removed from the assembly, cleaned and reweighed to ensure no material was lost during the experiment.

2.1.4 Experiments in the hydrothermal pressure apparatus

The loaded capsules were placed in sets of three (one-chamber method) or individually (two-chamber method) in standard cold-seal pressure vessel autoclaves and loaded into the hydrothermal pressure apparatus. Pressure was raised to the target pressure and, once stable, temperature was raised to its target value. Pressure was maintained within 10 MPa of the target pressure throughout each experiment. Temperature was measured with a Ni-CrNi thermocouple placed within the wall of each autoclave, with an estimated error of ± 10 °C. The samples were quenched by cooling the autoclave with compressed air to less than 100 °C in 5 min. Once removed from their respective assemblies, the capsules were cleaned and reweighed to check for leakage.

2.2 Fluid recovery and analysis

In Chapters 4 and 6, the composition of the product fluid recovered at the end of the experiments is assumed to be that of the final fluid at run conditions. Product fluids were recovered at the end of selected experiments by completely opening individual capsules under Millipore water, rinsing out the reaction products, and diluting the released fluid to 50 mL. The concentrations of Na, Ca, K, Mg, and B were measured under the direction of Dr. G. Schettler by atomic emission spectroscopy with an iCAP 6000 Series ICP-AES from the Thermo Electron Corporation equipped with a sea-spray nebulizer. The concentrations of Na and K in solution were determined with the plasma power set to 1150 W by averaging three measurements of their emission lines at 5895 and 7664 Å, respectively. The concentrations of Mg and Ca were determined under the same conditions by averaging three measurements of two emission lines at 2025 and 3838 Å, and 1840 and 3158 Å, respectively. The concentration of B was determined with the plasma power set to 1350 W. In order to counteract adhesion of B to the wall of the uptake tube, samples were changed manually for its analysis, allowing the use of a shorter uptake tube. In addition, the system was flushed for 8–11 min with Millipore water between each sample. The concentration of B was then determined by averaging three measurements of two emission lines (2088.93 and 2089.59 Å). The concentration of Cl was determined by Dr. G. Schettler

using isocratic ion-exchange chromatography with conductivity detection after micromembrane suppression (AG18[4 × 50 mm] and AS18[4 × 250 mm] Dionex columns; 25 mM NaOH eluent; 1 mL/min flow rate; 25 μ L injection volume). Finally, the concentration of each element in solution at the end of the experiment was calculated from the concentration measured in the diluted solution. Considering error introduced by dilution and weighing of the samples, the estimated analytical error is within 5 % of the measured value.

2.3 Electron microprobe (EMP) analysis

2.3.1 Synthetic samples

Following their recovery, the solid products of each experiment were dried at 100 °C. A portion of each sample was mounted in epoxy, polished, carbon-coated and the tourmaline composition determined by EMP analysis. All EMP analyses were done on the epoxy-mounted, polished, and carbon-coated samples using a JEOL Hyperprobe JXA-8500F equipped with a thermal field-emission cathode and five wavelength-dispersive spectrometers at the GFZ German Research Centre for Geosciences, except for some analyses presented in Chapter 6, which were done with the same equipment at the Museum für Naturkunde (MfN) in Berlin, Germany. At the GFZ, analyses were done with the help of Dr. D. Rhede and at the MfN they were done under the direction of Dr. L. Hecht.

Cores of tourmaline crystals synthesized using the two-chamber method were generally inclusion-rich. To avoid contamination of the WDS analyses, spots were chosen far from the inclusion-containing cores. In Chapter 6, to obtain the composition of tourmaline in equilibrium with the product fluid, EMP analysis spots were chosen within 2 μ m of the crystal rim in the c^+ sector of the large tourmaline grains. Due to the small size of the radiating crystal aggregates produced using the one-chamber method, the EMP data of tourmaline synthesized at higher pressure represent averages of the entire crystal aggregates.

The operating conditions at both the GFZ and the MfN were as follows: 8.0–10.0 kV accelerating voltage, a 4–10 nA beam current, and a 1–5 μ m beam diameter. Signals for all elements were counted for 20 s, except for Na (10 s) and B (80 s). The standards used were orthoclase (K, Si, and Al, for K-bearing tourmalines), pyrope (Al, for K-free tourmalines), jadeite (Na), wollastonite (Ca), periclase (Mg), schorl (B), and tugtupite (Cl). At the MfN, the standards used were the same, except for sanidine (Si) and plagioclase (Ca). Data reduction was done using a $\phi(\rho Z)$ correction scheme (CITZAF; Armstrong, 1995). Under these conditions, analytical errors (1σ) and detection limits based on counting statistics are at most 13.19 % and 380 ppm for K, 0.98 % and 390 ppm for Si, 0.63 % and 235 ppm for Al, 5 % and 251 ppm for Na, 1.5 % and 350 ppm for Ca, 1.18 % and 190 ppm for Mg, 2.5 % and 1800 ppm for B, and 10 % and 70 ppm for Cl, respectively.

In the cases where boron was not measured, 3.0 B pfu was assumed in the normalization procedure of the analyses. However, the presence of tetrahedral B, particularly in tourmaline synthesized at high pressure, cannot be excluded (Ertl *et al.*, 2008).

The wavelength-dispersive element X-ray maps presented in Chapter 3 were obtained using a moving-stage program with an 8.0-kV accelerating voltage, a 10-nA beam current, and a 0.10-mm step interval. The counting time per step was 250 ms for element X-ray maps of tourmaline synthesized in the presence of a KCl fluid (EB1, Fig. 3.1a) and 300 ms for those synthesized in the presence of a KCl-NaCl fluid (EB2, Fig. 3.1b). The X-ray

intensities were measured for K, Mg, Al, and Si in both samples and, in the case of EB2, additionally for Na and plotted on separate element maps based on a colour scale.

2.3.2 Natural samples

The major-element mineral compositions of the samples presented in Chapter 7 were determined by EMP analysis of thin sections using a JEOL Hyperprobe JXA 8230 using a 20-nA beam current, a 15-kV accelerating voltage, and a beam size of 20 (tourmaline) or 10 (feldspar) μm . Signals for all elements were counted for 20 s, except for K and Na, which had a 10-s counting time. Mineral standards were used for calibration. Data reduction was done using a $\phi(\rho Z)$ correction scheme (CITZAF; Armstrong, 1995). Under these conditions, relative analytical errors (1σ) and detection limits are 0.37 % and 115 ppm for Si, 0.42 % and 112 ppm for Al, 19.15 % and 161 ppm for K, 6.71 % and 226 ppm for Ti, 68.56 % and 240 ppm for Cr, 2.15 % and 88 ppm for Ca, 93.56 % and 55 ppm for Cl, 64.31 % and 452 ppm for Ba, 3.27 % and 213 ppm for Na, 0.96 % and 171 ppm for Mg, 0.98 % and 191 ppm for Fe, 84.55 % and 188 ppm for Mn, and 59.32 % and 395 ppm for Zn, respectively. Wavelength-dispersive element X-ray maps for Ca, Na, Mg, Fe, and Ti were obtained using a moving-stage program with a 15.0-kV accelerating voltage, a 40-nA beam current, a 3- μm step interval, and a 200-ms dwell time per step.

2.4 Transmission electron microscopy (TEM)

In Chapter 4, with the exception of samples synthesized via the two-chamber method, TEM, rather than EMP, was used to measure the composition of tourmaline crystals synthesized at ≤ 1.8 GPa because of their small grain size (typically <10 μm in length and <2 μm in diameter). The TEM work was performed by Dr. R. Wirth. Material from each experiment was dispersed in an ultrasonic bath of isopropanol. A drop of this dispersion was applied to a perforated carbon film on a standard TEM copper grid and air-dried. No further carbon coating of the TEM grids was necessary. Analytical electron microscopic (AEM) analyses were performed with a FEI TECNAI G2 F20 X-Twin microscope equipped with a field-emission gun electron source and an energy-dispersive EDAX X-ray analyzer separated from the TEM column by an ultra-thin window. Spectra were acquired in the scanning transmission mode (STEM), allowing the electron beam to scan a preselected area, thereby avoiding significant mass loss during data acquisition. The following parameters were used for all AEM analyses: 200-kV acceleration voltage, spot size 7 (~ 2 nm); 60-s acquisition time; 15° goniometer tilt toward the detector; 6-keV spectrum range. An average count rate of approximately 1500 cps was obtained for each analyzed tourmaline crystal, ensuring consistent crystal thickness. kAB factors from the TIATM software were used for quantification. The errors for Mg, Al, Si, Na, and K are approximately 5, 3, 3, 10, and 50–100 %, respectively.

2.5 Tourmaline normalization procedures

As described in Henry and Dutrow (1996), tourmaline has multiple normalization procedures due to its complex chemistry, which is difficult to fully determine. Specifically, the concentrations of the light elements, B, O, H, and Li, as well as the oxidation state of transition elements are difficult to constrain. The recommended normalization procedure for tourmaline with little or no Li is to normalize the sum of the cations occupying the Y, Z, and T sites to 15 (15 YZT). This normalization procedure allows the occupancy of the

X site to be calculated, including the number of X-site vacancies. Moreover, the relative occupancy of the V and W sites by O and OH can subsequently be calculated based on charge balance of the structural formula. An innate assumption of this normalization procedure is that the valence states of all cations are known and that B is restricted to 3.0 pfu.

In Al-rich tourmalines crystallized at high temperature, B can exceed 3.0 pfu (Ertl *et al.*, 2008). In these cases, B is expected to partially occupy the T site. If B is accurately measured, the number of cations occupying the Y, Z, T, and B sites can thus be normalized to 18 (18 YZTB). Alternatively, tourmaline's structural formula can be normalized to the number of O, assuming the valence states of all cations are known. Considering the possible presence of F at the W site, this normalization procedure assumes the V and W sites are otherwise occupied by OH, up to 4 OH pfu. Tourmaline with no F has 31 O pfu. By assuming 4 OH pfu, tourmaline's structural formula can be calculated by normalization of all other oxygens to 29 (if B is measured) or 24.5 (if 3.0 B pfu are assumed).

If a transition element with multiple oxidation states is present in high concentration, commonly Fe, its valence or the concentration of H needs to be measured to determine tourmaline's structural formula. Alternatively, the predominant valence state can often be constrained from stoichiometric arguments. Depending on the relative amounts of OH, O, and F at the VW sites, tourmaline has 58–61 negative charge in its structural formula that must be charge balanced by the cations. Following normalization to 15 YZT or 18 YZTB, this range in negative charge restricts the minimum and maximum proportion of multi-valence cations (*e.g.*, Fe^{2+} versus Fe^{3+}). An example is provided in Table 7.4, where the minimum amount of Fe^{3+} and the maximum amount of Fe^{2+} is calculated by charge balancing VW sites occupied by 4 OH, after accounting for F (giving a net 58 negative charge). Conversely, the maximum amount of Fe^{3+} and the minimum amount of Fe^{2+} can be calculated by charge balancing VW sites occupied by 3 O and 1 OH, after accounting for F (giving a net 61 negative charge). In the example of Table 7.4, treating all Fe as Fe^{3+} does not necessitate 3 O at the VW sites, thereby setting its upper limit.

Each of the aforementioned normalization procedures has its respective benefits and drawbacks. As such, there is no standard normalization procedure. In the subsequent chapters, different combinations of the normalization procedures are presented, allowing the influence of the normalization procedure on the resultant structural formula to be assessed.

2.6 Whole rock analysis

Whole rock analysis of the samples presented in Chapter 7 were done by P. Marsiske in the geochemical laboratories of the Technical University of Berlin. Representative portions of the investigated hand samples were pulverized in a tungsten carbide ball mill for bulk-rock analysis by X-ray fluorescence on a Philips WD-RFA PW 2400. Major-element concentrations were measured on glass beads formed by fusing 0.6 g of rock powder with 3.6 mg of a lithium borate flux. Loss on ignition values were determined by firing a known mass of each rock powder at 1000 °C in porcelain crucibles.

2.7 Powder X-ray diffraction (XRD)

Powder XRD combined with Rietveld refinement was used to identify the solid product phases in all synthesis experiments, their relative proportions, and the unit-cell parameters of the synthesized tourmaline. A portion of the solid product from each experiment was ground, glued between two boPET foils, and placed in a transmission XRD sample holder. The powder-XRD patterns were recorded by H.P. Nabein in the $5\text{--}125^\circ 2\theta$ range on a STOE Stadi P diffractometer equipped with a position-sensitive detector (PSD) using $\text{CuK}\alpha_1$ radiation, a 40-kV accelerating voltage, a 40-mA beam current, and a germanium (111) primary monochromator. Rietveld refinement was done using the GSAS software package (Larson and Von Dreele, 1987). The initial structure parameters for tourmaline were taken from Donnay and Buerger (1950) and applied the average site-occupancy values determined by normalization of the EMP-data (Table 6.2). The initial structure parameters for the other identified phases were taken from the Inorganic Structure Database (ICSD, FIZ Karlsruhe).

2.8 Single-crystal X-ray diffraction (XRD)

The single-crystal XRD analyses presented in Chapter 5 were done by Dr. A. Ertl at the Institut für Mineralogie und Kristallographie at the University of Vienna, Austria. The quality of different crystals was determined with a Bruker APEXII diffractometer equipped with a CCD area detector and an Incoatec Microfocus Source $I\mu\text{S}$ (30 W, multi-layer mirror, $\text{Mo-K}\alpha$ radiation). The XRD pattern of a high-quality oxy-uvite crystal was recorded on the same Bruker APEXII diffractometer, whereas those of K-dravite (EB13) and magnesio-foitite (MF2) were recorded on a STOE StadiVari four-circle goniometer with a Dectris PILATUS 300-K pixel detector. Single-crystal XRD data were collected at room temperature, integrated, and corrected for Lorentz and polarization factors with an absorption correction by evaluation of partial multiscans. The structure was refined with SHELXL97 (Sheldrick, 1997) using scattering factors for neutral atoms and a tourmaline starting model taken from Ertl *et al.* (2012). The H3 atom bonded to the O3 atom was located from a difference Fourier map and subsequently refined. Refinement was performed with anisotropic displacement parameters for all non-hydrogen atoms. Table 2.1 provides crystal data and details of the structure refinement. Site occupancies were refined according to expected variations in the tourmaline structure.

Table 2.1: Single-crystal XRD refinement details for synthesized K-dravite (EB13), magnesio-foitite (MF2), and oxy-uvite (CN11)

	K-dravite (EB13)	Magnesio-foitite (MF2)	Oxy-uvite (CN11)
Crystal size (mm)	$0.02 \times 0.015 \times 0.015$	$0.10 \times 0.04 \times 0.04$	$0.15 \times 0.10 \times 0.08$
Collection mode, $2\theta_{max}$	Full sphere, 50.00°	Full sphere, 68.37°	Full sphere, 79.97°
Frame width	3°	0.5°	2°
Frame scan time (s)	240	60	100
Detector distance (mm)	35	60	35
h, k, l ranges	$-18/18, -17/18, -8/8$	$-24/23, -24/24, -6/11$	$-28/28, -28/28, -28/28, -12/12$
Total reflections measured	2083	5578	32,578
Unique reflections	650	1182	2312
$R1^a(F)$, $wR2^b(F^2)$, $R^c_{int}(\%)$	4.88, 8.02, 15.12	1.19, 2.76, 1.07	1.33, 3.41, 3.27
Flack x parameter	$-0.17(31)$	$0.04(7)$	$0.04(3)$
‘Observed’ reffs. $[F_o > 4\sigma(F_o)]$	393	1158	2287
Refined parameters	93	96	95
Goodness of Fit ^d	0.67	1.08	1.16
$\Delta\sigma_{min}, \Delta\sigma_{max}$ (e/Å ³)	$-0.47, 0.51$	$-0.32, 0.46$	$-0.26, 0.33$

X-ray radiation: $\text{MoK}\alpha$ ($\lambda = 0.71073 \text{ \AA}$); Z: 3; space group: $R3m$ (no. 160); multiscan absorption correction; refinement on F^2

Scan mode: sets of ϖ and θ scans

$$^a R1 = \Sigma ||F_o| - |F_c|| / \Sigma |F_o|$$

$$^b wR2 = \{\Sigma[w(F_o^2 - F_c^2)^2] / \Sigma[w(F_o^2)^2]\}^{1/2}$$

$$w = 1/[\sigma^2(F_o^2) + (aP)^2 + bP], P = [2F_c^2 + \text{Max}(F_o^2, 0)]/3$$

$$^c R_{int} = \Sigma |F_o^2 - F_o^2(\text{mean})| / \Sigma [F_o^2]$$

$$^d \text{GooF} = S = \{\Sigma[w(F_o^2 - F_c^2)^2] / (n - p)\}^{1/2}$$

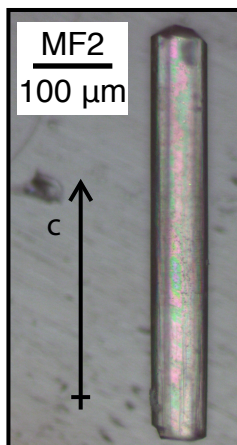


Figure 2.1: Photograph of magnesio-foitite (MF2; see Chapter 5) synthesized using the two-chamber method of von Goerne *et al.* (2001). The crystal is 516 μm long. The arrow is aligned to the crystallographic c -axis.

2.9 Polarized Raman spectroscopy

The polarized micro-Raman spectra presented in Chapter 5 were collected under the guidance of Prof. M. Koch-Müller at room temperature using either a HORIBA Jobin LabRAM HR800 UV-Vis (MF2) or HR800 Vis (EB13, EB28, EB29, CN11) spectrometer with a 1800 grooves/mm grating, a 100- μm pinhole in backscattering configuration, and a CCD detector (spectral resolution $\sim 1\text{ cm}^{-1}$). The polarization analyzer had no observable effect on the collected spectra and was therefore not used. Tourmaline crystals were mounted on a glass slide and focused on using an optical microscope with a 50 \times (MF2, CN11) or 100 \times (EB13, EB28, EB29) objective and excited with a linearly polarized blue laser (488 or 473 nm wavelength and 30- or 12-mW laser power at sample surface for spectra collected using the HR800 UV-Vis or HR800 Vis, respectively). No damage to the crystal surfaces from the laser was observed. Raman spectra in the lattice ($100\text{--}1200\text{ cm}^{-1}$) and O–H stretching ($3250\text{--}3850\text{ cm}^{-1}$) vibrational ranges were generated from three (EB13, EB28, CN11) or five (EB29) 40-s accumulations, or four 50-s accumulations (MF2). Although multiple spectra were collected from different spots on each crystal to verify consistency, only representative spectra are reported here. As O–H bonds in tourmaline’s structure are largely parallel to the crystallographic c -axis, spectra were collected with the electric field vector of the polarized laser light (E) oriented parallel to the c -axis (*e.g.*, Fig. 2.1), with the exception of one spectrum collected with E perpendicular to the c -axis of EB13. The Raman spectra in the O–H stretching range were deconvoluted using PeakFit (Jandel Scientific) to identify hidden bands, their centers, and their integrated peak intensities. The coefficient of determination (R^2) for all fitted spectra was >0.999 .

Chapter 3

Synthesis of K-dominant tourmaline

The contents of this chapter have been published in *American Mineralogist*, Volume 99, pages 539–542.

3.1 Introduction and approach

This chapter describes the first synthesis of “K-dravite”, the hydroxy form of maruyamaite, which forms a solid solution with the Na-bearing endmember dravite $[\text{NaMg}_3\text{Al}_6\text{Si}_6\text{O}_{18}(\text{BO}_3)_3(\text{OH})_3\text{OH}]$ via $^{\text{X}}\text{K}(^{\text{X}}\text{Na})_{-1}$ exchange.

K-bearing tourmaline was synthesized in the presence of either a 4.78 *m* KCl or a 2.59 *m* KCl, 2.29 *m* NaCl fluid at 4.0 GPa and 700 °C after 4 days using the one-chamber method and an end-loaded piston-cylinder press. At the end of the experiment, the solid material was carefully removed from the cleaned and dried capsules and prepared for analysis by optical microscopy, electron microprobe (EMP), and X-ray diffraction (XRD). For details on the experimental and analytical methods, see Chapter 2.

3.2 Results and discussion

The solid run products are tourmaline, coesite, and, in the Na-free system, santite ($\text{KB}_5\text{O}_8\cdot 4\text{H}_2\text{O}$) and sylvite. The synthesized tourmaline crystals were on average 10 μm long and 1–2 μm wide, but ones up to 50 μm long were observed. Tourmaline synthesized in the presence of a KCl fluid (EB1) had the highest K content, with up to 3.44 wt.% K_2O . Crystals were compositionally zoned (Fig. 3.1), the cores being less potassic (1.46 wt.% K_2O , 0.30 K pfu) than the rims (3.44 wt.% K_2O , 0.71 K pfu; Table 3.1), thereby forming K-dominant tourmaline, namely “K-dravite”. This zoning correlates with increasing Mg and decreasing Al incorporation with crystal growth. As a result, we interpret the increased K incorporation toward the rims to reflect the coupled substitution $^{\text{X}}\text{K}^+ + ^{\text{Y}}\text{Mg}^{2+} = ^{\text{X}}\square + ^{\text{Y}}\text{Al}^{3+}$, discussed in greater detail below. Although the solution was saturated with respect to KCl at atmospheric conditions, it was undersaturated at the experimental conditions. It is thus possible that even greater K incorporation could occur with a more KCl-concentrated solution. The addition of aqueous NaCl to the fluid (EB2) reduced the concentration of KCl by 45 %, from 4.78 to 2.59 *m*. However, the proportion of K incorporated at the X site decreased by far more than 45 %, down to 0.10 K pfu (Table 3.1). Even though this is still relatively K-rich compared to tourmaline typically

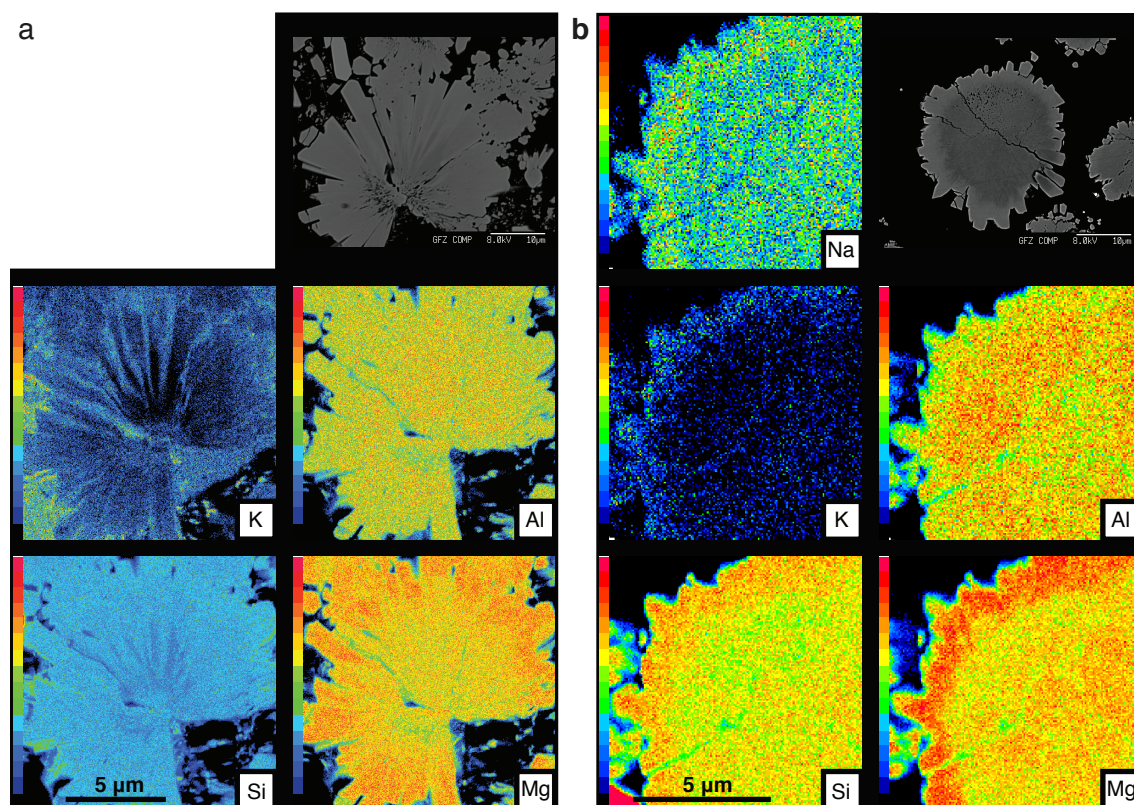


Figure 3.1: Backscattered-electron image (*top right*) and element X-ray maps of tourmaline synthesized at 700 °C and 4.0 GPa in the presence of (a) a KCl fluid (EB1) and (b) a KCl-NaCl fluid. The colour scale to the left of each element X-ray map ranged from black to red, representing low to high number of counts, respectively.

found in nature, the dominant occupancy of the X site by Na indicates that K-rich dravite, but not “K-dravite”, was synthesized. Bulk composition has a significant control on the crystallization of “K-dravite” and a K-dominant and Na-poor fluid is required for its crystallization.

The EMP data were normalized to 15 cations at the Y, Z, and T sites (15 YZT) and alternatively to 24.5 O (the number of oxygen atoms not associated with B or H, assuming 4 OH, Table 3.1). Both normalizations assume 3 B pfu and, therefore, the absence of B at the T site, which cannot be excluded. The two normalization schemes are in good agreement, with discrepancies only in terms of the W site. Although normalization to 15 YZT is normally favoured because it permits the relative occupancy of the W site by O and OH to be calculated, in the case of the “K-dravite” cores (EB1), an insufficient amount of positive charge among the cations results in the W site being underfilled (Table 3.1; Fig. 3.2b). This is best explained by the initial crystallization of tourmaline being non-stoichiometric, as observed in earlier tourmaline-synthesis experiments (*e.g.*, von Goerne *et al.*, 1999), or by inaccuracy in the EMP measurements arising from porosity between abundant crystal nuclei in the cores.

The “K-dravite” endmember formula is $\text{KMg}_3\text{Al}_6\text{Si}_6\text{O}_{18}(\text{BO}_3)_3(\text{OH})_3(\text{OH})$ and is related to endmember dravite by the exchange vector $^{\text{X}}\text{K}(^{\text{X}}\text{Na})_{-1}$. Shimizu and Ogasawara (2005) noted this exchange in their K-rich tourmaline from the Kokchetav Massif in Kazakhstan as ranging from 0.11 to 0.55 $X_{\text{K-oxy-dravite}}$ and again in showing that their most K-rich tourmaline was a continuous solid solution with Ca-, Na-, and □-tourmaline (Shimizu

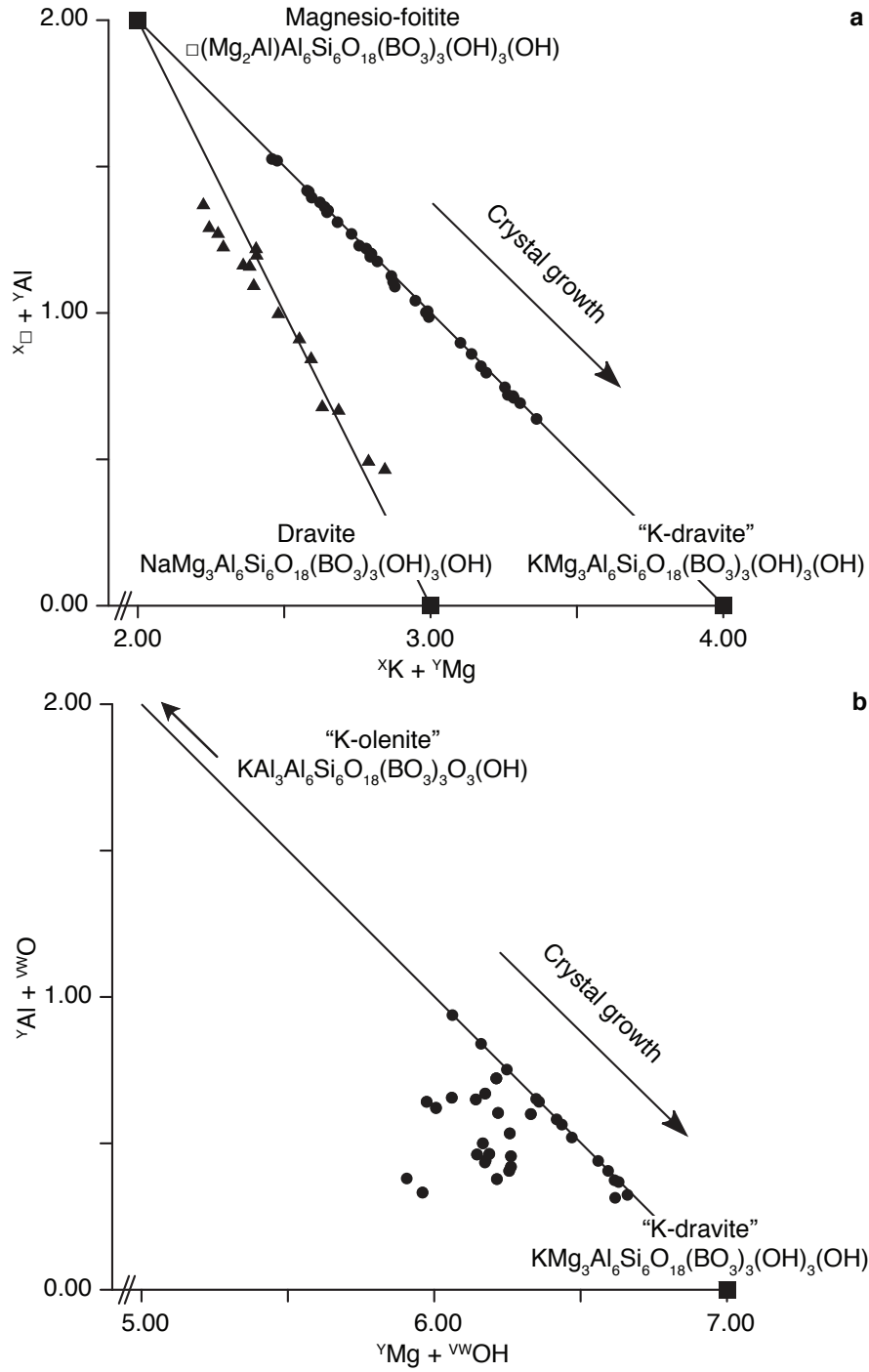


Figure 3.2: EMP analyses of compositional zoning in tourmaline, with growth direction indicated by arrows; (a) from EB1 (circles) and EB2 (triangles) representing solid solution between endmember magnesio-foitite and endmember "K-dravite" via the exchange vector $x_K y_{Mg} (x_{\square} y_{Al})_{-1}$, or endmember dravite via the analogous exchange vector $x_{Na} y_{Mg} (x_{\square} y_{Al})_{-1}$; (b) from EB1 representing a solid solution between endmember "K-dravite" and endmember "K-olenite" via the exchange vector $y_{Mg} OH (y_{Al} OH)_{-1}$.

Table 3.1: Composition (EMP analyses) and stoichiometry of synthesized tourmaline normalized to 15 YZT and 24.5 O pfu

		100 mol% KCl				49 mol% KCl, 51 mol% NaCl	
		rims		cores			
Oxide (wt.%)		$n = 10$		$n = 24$		$n = 16$	
K ₂ O		3.13(14)		1.46(53)		0.47(15)	
Na ₂ O		0.02(2)		0.03(3)		1.66(35)	
MgO		10.89(31)		10.24(57)		9.88(89)	
Al ₂ O ₃		33.85(41)		35.40(94)		36.32(158)	
SiO ₂		37.64(40)		36.49(100)		35.47(93)	
Total		85.52(57)		83.61(99)		83.80(81)	
Normalization		15 YZT	24.5 O	15 YZT	24.5 O	15 YZT	24.5 O
X	K	0.64(3)	0.64(3)	0.30(11)	0.30(11)	0.10(3)	0.10(3)
	Na	0.00(1)	0.00(1)	0.01(1)	0.01(1)	0.52(11)	0.52(11)
	□	0.36(3)	0.36(3)	0.69(11)	0.69(11)	0.38(9)	0.38(9)
Y ₃	Mg	2.60(7)	2.59(8)	2.45(13)	2.46(14)	2.38(21)	2.38(21)
	Al	0.40(7)	0.41(6)	0.55(13)	0.54(20)	0.62(21)	0.62(21)
Z ₆	Al	5.98(3)	5.97(6)	6.00(2)	6.00(20)	6.00(0)	6.00(0)
	Si	0.02(3)	0.01(3)	0.00(2)	0.00(12)	0.00(0)	0.01(4)
T ₆	Si	6.00	6.00	5.86(14)	5.89(12)	5.72(13)	5.71(14)
	Al	0.00	0.00	0.14(14)	0.20(20)	0.28(13)	0.29(14)
(BO ₃) ₃	B	3.00 ^a	3.00 ^a	3.00 ^a	3.00 ^a	3.00 ^a	3.00 ^a
V ₃	OH	3.00(0)	3.00 ^a	3.00(0)	3.00 ^a	3.00(0)	3.00 ^a
W	OH	0.92(7)	1.00 ^a	0.69(23)	1.00 ^a	0.90(9)	1.00 ^a
	O	0.08(8)	0 ^a	0.01(4)	0 ^a	0.03(5)	0 ^a

^aValues fixed during normalization. n is the number of analyses.

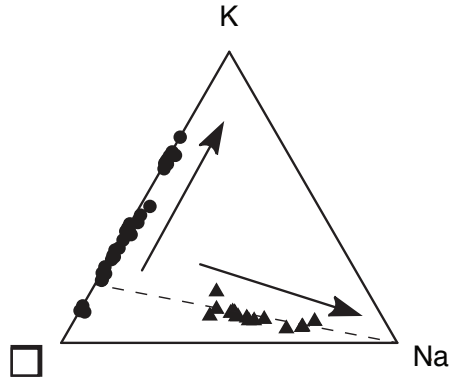


Figure 3.3: Ternary diagram of the occupancy of the X site for tourmaline formed in the presence of a KCl fluid (circles, EB1) and a KCl-NaCl fluid (triangles, EB2). The dashed line represents values of variable Na content with a ratio of 1K:4□ (X-site vacancies). Arrows indicate the direction of crystal growth.

and Ogasawara, 2013). However, whereas they propose an endmember analogous to oxydravite $[\text{Na}(\text{Mg}_2\text{Al})\text{Al}_6\text{Si}_6\text{O}_{18}(\text{BO}_3)_3(\text{OH})_3\text{O}]$, our synthetic K-tourmaline with $^{\text{Y}}\text{Al} < 1$ (Table 3.1) is analogous to dravite, as predicted by Henry *et al.* (2011). Furthermore, the compositional zoning of the synthesized “K-dravite” indicates solid solution between the endmember compositions of “K-dravite” and X-site-vacant tourmaline, magnesio-foitite $[\square(\text{Mg}_2\text{Al})\text{Al}_6\text{Si}_6\text{O}_{18}(\text{BO}_3)_3(\text{OH})_3(\text{OH})]$, via the coupled substitution $^{\text{X}}\text{K}^+ + ^{\text{Y}}\text{Mg}^{2+} = ^{\text{X}}\square + ^{\text{Y}}\text{Al}^{3+}$ [exchange vector $^{\text{X}}\text{K}^{\text{Y}}\text{Mg}(^{\text{X}}\square^{\text{Y}}\text{Al})_{-1}$; Fig. 3.2a], and, to a lesser extent, between the endmember compositions of “K-dravite” and the K analog of the Al-tourmaline, olenite $[\text{KAl}_3\text{Al}_6\text{Si}_6\text{O}_{18}(\text{BO}_3)_3\text{O}_3(\text{OH})]$, via the coupled substitution $^{\text{Y}}\text{Mg}^{2+} + (\text{OH})^- = ^{\text{Y}}\text{Al}^{3+} + \text{O}^{2-}$ [exchange vector $^{\text{Y}}\text{MgOH}(^{\text{Y}}\text{AlO})_{-1}$; Fig. 3.2b]. Element distribution in radiating crystal clusters (Fig. 3.1) shows these solid solutions, particularly that with magnesio-foitite; concurrent with the increase in K (or Na in the sodium-bearing system), the Mg content is increased and Al content decreased in the crystal rims. In the case of the K-rich dravitic tourmaline crystals (EB2), Mg and, to a lesser extent, K are also enriched in the crystal rim (Fig. 3.1b). Concurrently, Na and Si also show increasing concentration with crystal growth. The incorporation of Na in K-rich dravite (EB2) is similar in behaviour to the incorporation of K in “K-dravite” from EB1. However, whereas Na steadily increases in concentration, the ratio of K to vacancies at the X-site remains relatively constant at 1:4 (dashed line in Fig. 3.3). The increased incorporation of Si is complementary to the decreasing Al content, based on the coupled substitution $^{\text{Y}}\text{Al}^{3+} + ^{\text{T}}\text{Al}^{3+} = ^{\text{Y}}\text{Mg}^{2+} + ^{\text{T}}\text{Si}^{4+}$ [exchange vector $^{\text{Y}}\text{Mg}^{\text{T}}\text{Si}(^{\text{Y}}\text{Al}^{\text{T}}\text{Al})_{-1}$]. The favouring of the early crystallization of Al-rich tourmaline in the crystal cores is attributed to the lower mobility of Al in the fluid and, along with increasing Mg content, is consistent with earlier tourmaline-synthesis experiments (*e.g.*, von Goerne *et al.*, 1999). Increasing Si content with crystal growth is also observed in the “K-dravite”, but is overshadowed by solid solution with magnesio-foitite described above (Fig. 3.1a).

Details and results of the Rietveld refinements of powder-XRD spectra from both experiments are given in Table 3.2. Taken qualitatively, the unit-cell volumes of tourmaline synthesized in both experiments are smaller than that of endmember dravite (1595.1 \AA^3 ; Buerger *et al.*, 1962). This is likely caused by significant vacancies at the X site (Table 3.1). Furthermore, the larger unit-cell volume of the synthetic “K-dravite” (EB1) likely reflects the increased incorporation of the relatively large K ion at the X site compared to synthetic K-bearing dravite (EB2). Ertl *et al.* (2008) showed that $^{\text{T}}\text{B}$ content in Al-rich tourmaline is related to the unit-cell volume and a unit-cell volume less than 1539.3 \AA^3 is necessary to indicate significant incorporation of $^{\text{T}}\text{B}$. The unit-cell volume of tourmaline synthesized in both experiments is significantly larger than this value (Table 3.2), supporting the assumption of no $^{\text{T}}\text{B}$.

Table 3.2: Unit-cell parameters of synthesized tourmaline

Refinement details	Experiment	EB1	EB2
χ^2		2.01	1.63
DWd		1.03	1.27
Phase proportions	Tourmaline	78 wt.%	86 wt.%
	Coesite	10 wt.%	14 wt.%
	Santite	11 wt.%	n/a
	Sylvite	<1 wt.%	n/a
Unit-cell parameters	$a = b$	15.927(2) Å	15.913(1) Å
	c	7.193(1) Å	7.181(1) Å
	V	1580.1(5) Å ³	1574.9(4) Å ³

Note: DWd indicates the Durbin-Watson statistic for the refinement.
Phase proportions are approximate values (± 2 wt.%).

Two multi-anvil experiments with bulk compositions of EB1 done at 700 °C and 6 and 8 GPa, respectively, yielded a combination of mainly boromuscovite and phengite, but no tourmaline. These results suggest that the upper stability of “K-dravite” is between 4.0 and 6.0 GPa, consistent with the stability of dravite in a silica-saturated system (4.5–5.0 GPa at 700 °C; Ota *et al.*, 2008a).

3.3 Implications

Although K is ~25 % larger than Na (Shannon, 1976), the tourmaline structure is able to incorporate K at the X site given the appropriate environment. Based on our synthesis experiments, high pressure and a fluid with at least 4.78 *m* K are required to incorporate significant amounts of K. Additional experiments are needed to determine the minimum pressure required for the synthesis of K-dominant tourmaline. Although tourmaline still incorporates K in the presence of Na, the tourmaline structure preferentially incorporates the smaller Na ion. As a result, K incorporation is expected to be more prominent in Na-poor and probably Ca-poor environments.

Moreover, the alkali-tourmaline group can be subdivided to include both Na and K endmember tourmaline. Although the K-dominant tourmaline synthesized here is analogous to dravite, its solid solution with the Al-endmember olenite (Fig. 3.2b) suggests that a K-dominant olenite $[\text{KAl}_3\text{Al}_6\text{Si}_6\text{O}_{18}(\text{BO}_3)_3\text{O}_3(\text{OH})]$, namely “K-olenite”, may also exist. However, additional experiments are required to confirm its stability.

Chapter 4

An experimental study on K and Na incorporation in dravitic tourmaline and insight into the origin of diamondiferous tourmaline from the Kokchetav Massif, Kazakhstan

The contents of this chapter have been published in *Contributions to Mineralogy and Petrology*, Volume 169, Article no. 28.

4.1 Introduction and approach

This chapter includes the experimental results on the influence of pressure (0.2–4.0 GPa), temperature (500–700 °C), and fluid composition (0–3.70 *m* NaCl, 1.08–4.78 *m* KCl) on the incorporation of the relatively large and typically incompatible K ion in dravitic tourmaline, providing constraints on the formation conditions of maruyamaite in the Kokchetav Massif.

K-bearing dravitic tourmaline was synthesized in 26 experiments with 4- to 25-day runtimes at temperatures ranging from 500 to 700 °C and pressures from 0.2 to 4.0 GPa (Table 4.1), using either hydrothermal pressure equipment or an end-loaded piston-cylinder press. After each synthesis experiment, the solid material was removed and prepared for analysis by optical microscopy, scanning electron microscopy (SEM), electron microprobe analysis (EMP), transmission electron microscopy (TEM) combined with analytical electron microscopy (AEM), and X-ray diffraction (XRD). The product fluid was recovered at the end of selected experiments and analyzed by inductively coupled plasma atomic emission spectroscopy (ICP-AES). For details on the experimental and analytical methods, see Chapter 2.

Table 4.1: Experimental conditions and reaction products

No.	P (GPa)	T (°C)	Oxide (mg)	Fluid volume (μ L)	m KCl	m NaCl	Ionic strength (m)	Duration (days)	Reaction products* (values in parentheses refer to relative phase proportions)
EB3	0.2	700	40.38	13.6	4.78	–	4.78	14	Tur (81) + Qz (10) + B-Ms (9) + (Syl)
EB4	0.2	700	40.31	13.6	2.16	2.74	4.90	14	Tur (93) + Qz (7) + Aksaite? (<1) + Pyrophyllite? (<1) + (Syl <1) + ? ^a
EB5	0.2	700	41.64	13.6	1.24	3.70	4.94	14	Tur (76) + Qz (14) + Aksaite (8) + Tlc (2) + ? ^a
EB25	0.4	500	40.96	13.6	2.02	–	2.02	23	Tur (93) + Qz (6) + Tlc (< 1)
EB23	0.4	500	40.67	13.6	4.78	–	4.78	23	Tur (91) + Qz (9) + Tlc (<1)
EB24	0.4	500	41.10	13.6	2.34	2.55	4.89	23	Tur (89) + Qz (10) + Tlc (<1)
EB15 ¹	0.4	600	50.22	30.0	2.75	1.10	3.85	14	Tur (79) + Crn (15) + sinhalite (3) + AlBO ₃ (2) + Tlc (<1)
EB16 ¹	0.4	600	50.22	30.0	2.68	1.17	3.85	14	Tur (62) + Qz (3) + Crn (27) + Tlc (8)
EB6	0.4	700	40.66	13.6	4.78	–	4.78	14	Tur (97) + Qz (<1) + B-Ms (3)
EB7	0.4	700	41.15	13.6	2.29	2.61	4.90	14	Tur (62) + Qz (9) + (Syl 2) + Hl (19) + ? ^a
EB8	0.4	700	41.38	13.6	1.08	3.87	4.95	14	Tur (84) + Qz (10) + Tlc (1) + Aksaite (5) + ? ^a
EB11	1.0	700	11.22	3.4	4.78	–	4.78	11	Tur (96) + Qz (2) + Tlc (<1) + (Syl 2) + ? ^b
EB12	1.0	700	11.04	3.4	2.35	2.54	4.89	11	Tur (98) + Qz (1) + (Syl 1) + ? ^b
EB9	1.8	700	10.23	3.4	4.78	–	4.78	11	Tur (98) + Qz (1) + Tlc (1)
EB10	1.8	700	10.53	3.4	1.89	3.03	4.92	11	Tur(85) + Qz (10) + Tlc (5)
EB21	3.0	500	10.39	3.4	4.78	–	4.78	20	Tur (61) + B-Ms (12) + Boracite (6) + Coe (4) + Crn (17)

Continues on next page

Table 4.1: *Continued from previous page*

No.	P (GPa)	T (°C)	Oxide (mg)	Fluid volume (μL)	m KCl	m NaCl	Ionic strength (m)	Duration (days)	Reaction products* (values in parentheses refer to relative phase proportions)
EB22	3.0	500	10.34	4.5	2.61	2.27	4.88	20	Tur (62) + B-Ms (6) + Coe (26) + (Crn 4)
EB19 ²	3.0	600	10.62	3.4	4.78	–	4.78	10	Tur + Coe + Boracite + Tlc
EB20 ²	3.0	600	10.60	4.5	2.61	2.27	4.88	10	Tur + Coe
EB17 ²	3.0	700	10.73	3.4	4.78	–	4.78	6	Tur + Coe
EB32	3.0	700	13.46	4.5	3.64	1.19	4.83	25	Tur (92) + Coe (8)
EB18-1	3.0	700	10.30	4.5	2.77	2.11	4.88	25	Tur (96) + Coe (4)
EB1 ³	4.0	700	10.81	3.4	4.78	–	4.78	4	Tur (79) + Coe (10) + santite (10) + (Syl 1)
EB2 ³	4.0	700	10.87	4.5	2.59	2.29	4.88	4	Tur (92) + Coe (8)
EB13 ⁴	4.0	700	9.55	5.9	4.78	–	4.78	6	Tur (83) + Coe (10) + (Syl 7)
EB14 ⁵	4.0	700	10.99	5.2	4.78	–	4.78	6	Tur (56) + Coe (7) + Mc (19) + Crn (11) + santite (5) + (Syl 2)

Phases given in brackets are interpreted to be quench products

* Mineral abbreviations based on Whitney and Evans (2010)

? Unknown phases ^a(d spacings of major peaks: 2.82, 6.06, 5.91 Å), ^b(d spacings of major peaks: 5.57, 3.51, 2.76 Å)

¹Applied the two-chamber method of von Goerne *et al.* (1999)

²Powder XRD data unavailable. Phases identified by EMP

³As described in Chapter 3

⁴An additional 0.95 mg of solid KCl was added to the capsule

⁵An additional 1.10 mg of K-feldspar (sanidine) was added to the capsule

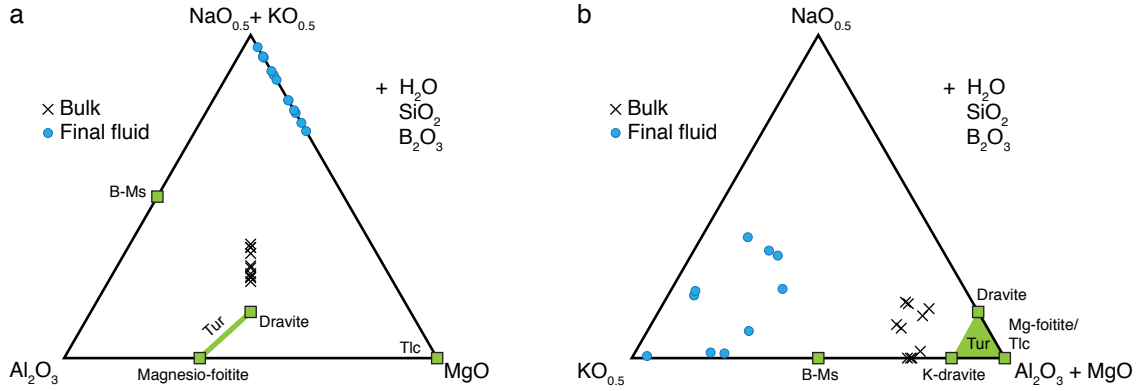


Figure 4.1: (a) (NaO_{0.5}+KO_{0.5})-Al₂O₃-MgO and (b) NaO_{0.5}-KO_{0.5}-(Al₂O₃+MgO) ternary diagrams both projected from H₂O, SiO₂, and B₂O₃ depicting bulk compositions of starting material and final fluids. The major solid products are plotted for reference.

4.2 Results

Tourmaline was synthesized in all experiments along with quartz (coesite in experiments run at ≥ 3.0 GPa) and other secondary phases observed under the electron microprobe and supported by the interpretation of the XRD spectra (Table 4.1). In general, the secondary phases make up less than 10 wt.% of the reaction products.

Tourmalines synthesized at 4.0 GPa are up to 50 μm long and 8 μm wide and display significant zoning with more aluminous, X-vacant cores and more magnesian, X-occupied rims (Fig. 4.2; see Fig. 3.1 for element maps). Decreasing pressure produced progressively smaller radiating aggregates of tourmaline with crystals down to 10 μm in length and 2 μm in width (Fig. 4.2). Backscattered electron imaging shows that the small crystals are also zoned, albeit less so than the larger tourmalines produced at higher pressure. Application of the two-chamber method of von Goerne *et al.* (1999) yielded the largest crystals, on average 100 μm in length (Fig. 4.2). The latter tourmalines are also zoned and additionally have inclusions of corundum, sinhalite [MgAl(BO₄)], and AlBO₃ in their cores. To accurately represent the compositional variation within and between different experiments, data are presented either as individual analyses, average compositions, statistical variation, or approximate rim compositions, as appropriate.

The WDS and AEM compositional analyses of all tourmaline were normalized to 15 cations at the Y, Z, and T sites assuming 3 B pfu and the relative occupancy of OH and O at the W and V sites calculated by charge balance (Table 4.2). This ignores any incorporation of tetrahedral boron at UHP conditions (Ertl *et al.*, 2008).

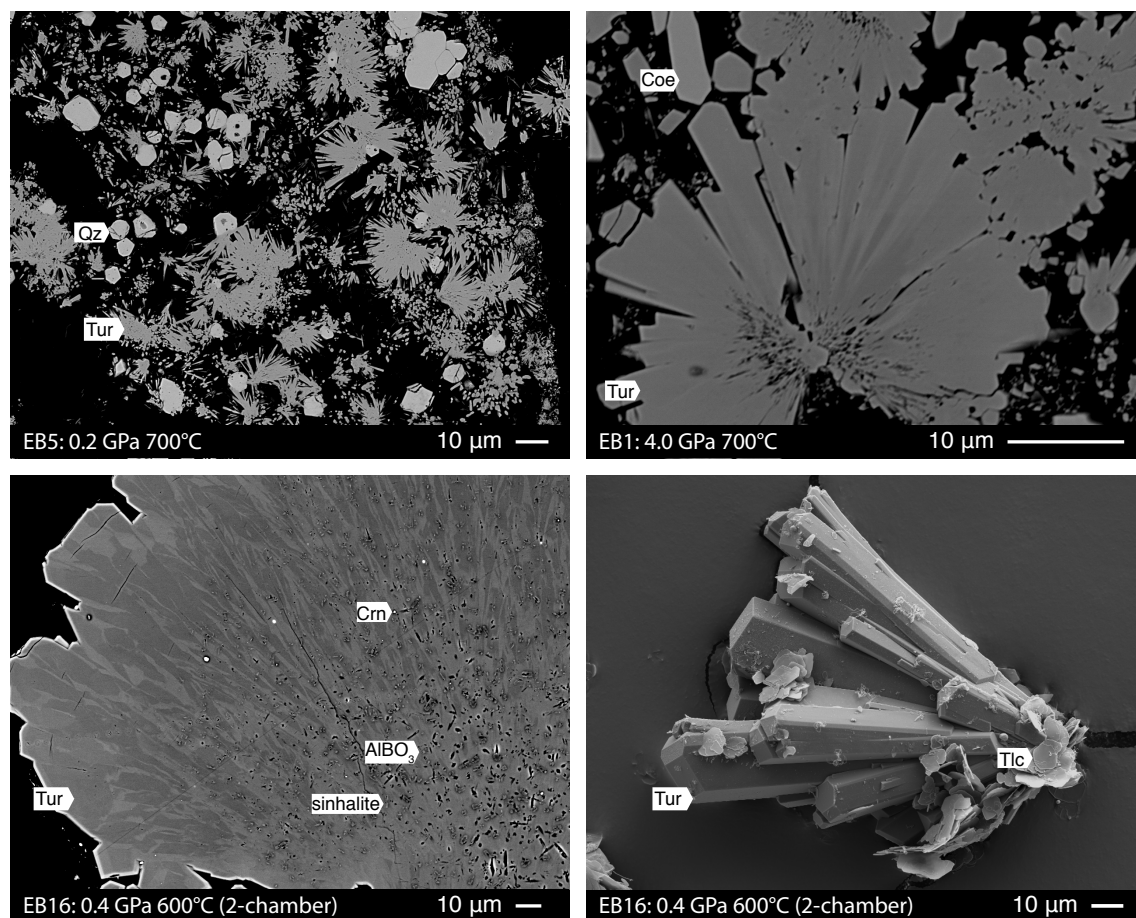


Figure 4.2: Backscattered electron (BSE) and scanning electron microscope (SEM: *bottom right*) images of tourmaline and its secondary phases synthesized at various pressures and temperatures. That of EB1 is modified after Fig. 3.1.

Table 4.2: Average compositions of synthesized tourmaline normalized assuming 3 B pfu

		EB1		EB2		EB3	EB4
Atom %/wt. %		EMP	TEM	EMP	TEM	TEM	TEM
		$n = 34$	$n = 10$	$n = 16$	$n = 10$	$n = 11$	$n = 10$
	K/K ₂ O ^b	1.95(89)	2.31(14)	0.47(15)	0.60(31)	0.66(23)	0.18(13)
	Na/Na ₂ O ^b	0.02(3)	0.00(0)	1.66(35)	3.65(92)	0.00(0)	4.4(11)
	Mg/MgO ^b	10.43(59)	14.7(17)	9.88(89)	14.9(22)	13.6(13)	15.55(87)
	Al/Al ₂ O ₃ ^b	34.9(11)	35.0(32)	36.3(16)	36.6(30)	45.1(21)	43.8(20)
	Si/SiO ₂ ^b	36.83(101)	47.2(48)	35.47(93)	44.2(51)	40.6(30)	36.2(22)
X	K	0.40(18)	0.36(22)	0.10(3)	0.09(5)	0.10(4)	0.03(2)
	Na	0.01(1)	0.00(0)	0.52(11)	0.57(15)	0.00(0)	0.70(17)
	□	0.59(18)	0.64(22)	0.38(9)	0.33(16)	0.90(4)	0.27(17)
Y ₃	Mg	2.49(13)	2.27(27)	2.38(21)	2.33(37)	2.05(20)	2.44(13)
	Al	0.51(22)	0.73(27)	0.62(31)	0.67(37)	0.95(20)	0.56(13)
Z ₆	Al	6.00(0)	4.70(70)	6.00(0)	5.08(74)	5.87(47)	6.00(0)
	Si	0.00(0)	1.30(70)	0.00(0)	0.92(76)	0.13(31)	0.00(0)
T ₆ O ₁₈	Si	5.90(14)	6.00(0)	5.72(13)	6.00(0)	6.00(23)	5.68(31)
	Al	0.11(13)	0.00(0)	0.28(13)	0.00(0)	0.00(0)	0.32(31)
(BO ₃) ₃	B	3.00 ^a	3.00 ^a	3.00 ^a	3.00 ^a	3.00 ^a	3.00 ^a
V ₃	OH	3.00(0)	2.61(82)	3.00(0)	2.72(98)	3.00(0)	3.00(0)
	O	0.00(0)	0.39(82)	0.00(0)	0.28(98)	0.00(0)	0.00(0)
W	OH	0.76(22)	0.00(0)	0.90(9)	0.00(0)	0.61(54)	0.76(14)
	O	0.03(6)	1.39(82)	0.03(5)	0.99(99)	0.28(55)	0.10(13)

		EB5	EB6	EB7	EB8	EB9	EB10
Atom %		TEM	TEM	TEM	TEM	TEM	TEM
		$n = 7$	$n = 11$	$n = 10$	$n = 9$	$n = 12$	$n = 5$
	K	0.14(11)	0.77(40)	0.20(15)	0.01(2)	1.49(64)	0.19(12)
	Na	5.58(38)	0.00(0)	4.64(53)	4.9(11)	0.00(0)	3.9(10)
	Mg	16.6(11)	13.3(13)	16.24(58)	15.4(12)	13.40(96)	15.86(64)
	Al	42.2(14)	46.2(41)	43.6(15)	40.6(20)	42.5(29)	43.1(24)
	Si	35.5(17)	39.0(39)	35.2(12)	39.0(32)	42.3(32)	36.9(14)
X	K	0.02(2)	0.10(3)	0.03(2)	0.00(0)	0.23(10)	0.03(2)
	Na	0.89(6)	0.00(0)	0.73(9)	0.82(11)	0.00(0)	0.62(17)
	□	0.09(6)	0.90(3)	0.24(9)	0.18(11)	0.77(10)	0.35(16)
Y ₃	Mg	2.64(18)	2.08(13)	2.56(10)	2.47(19)	2.05(15)	2.48(11)
	Al	0.36(18)	0.92(13)	0.44(10)	0.53(19)	0.95(15)	0.52(11)
Z ₆	Al	6.00(0)	6.00(0)	6.00(0)	5.90(34)	5.54(41)	6.00(0)
	Si	0.00(0)	0.00(0)	0.00(0)	0.10(45)	0.46(50)	0.00(0)
T ₆ O ₁₈	Si	5.65(24)	5.79(26)	5.56(19)	6.00(0)	6.00(0)	5.78(25)
	Al	0.35(24)	0.21(26)	0.44(19)	0.00(0)	0.00(0)	0.22(25)
(BO ₃) ₃	B	3.00 ^a	3.00 ^a	3.00 ^a	3.00 ^a	3.00 ^a	3.00 ^a
V ₃	OH	3.00(0)	3.00(0)	3.00(0)	3.00(0)	3.00(51)	3.00(0)
	O	0.00(0)	0.00(0)	0.00(0)	0.00(0)	0.00(0)	0.00(0)
W	OH	0.72(10)	0.60(19)	0.73(17)	0.49(49)	0.26(51)	0.74(15)
	O	0.10(17)	0.11(23)	0.02(3)	0.48(52)	0.69(56)	0.10(13)

Continues on next page

Table 4.2: *Continued from previous page*

Atom %/wt. %		EB11 TEM $n = 10$	EB12 TEM $n = 10$	EB13 EMP $n = 25$	EB14 EMP $n = 5$	EB15 EMP $n = 88$	EB16 EMP $n = 94$
	K/K ₂ O ^b	1.75(34)	0.30(28)	3.07(48)	2.54(69)	0.16(8)	0.15(10)
	Na/Na ₂ O ^b	0.00(0)	4.3(10)	0.08(6)	0.28(12)	1.37(28)	1.60(26)
	Mg/MgO ^b	15.5(12)	16.9(11)	10.34(65)	10.57(44)	10.2(13)	10.09(95)
	Al/Al ₂ O ₃ ^b	44.8(30)	41.9(21)	35.2(10)	33.77(99)	40.0(17)	39.6(20)
	Si/SiO ₂ ^b	38.0(27)	36.6(11)	36.2(10)	36.2(10)	33.3(32)	34.4(32)
X	K	0.27(5)	0.05(4)	0.63(10)	0.56(16)	0.03(1)	0.03(2)
	Na	0.00(0)	0.67(17)	0.02(2)	0.09(4)	0.49(8)	0.50(8)
	□	0.73(5)	0.28(16)	0.35(10)	0.35(12)	0.48(7)	0.47(9)
Y ₃	Mg	2.37(19)	2.65(17)	2.48(16)	2.55(3)	2.33(15)	2.33(13)
	Al	0.63(19)	0.35(17)	0.52(16)	0.45(3)	0.67(15)	0.67(13)
Z ₆	Al	6.00(0)	6.00(0)	6.00(0)	6.00(0)	6.00(0)	6.00(0)
	Si	0.00(0)	0.00(0)	0.00(0)	0.00(0)	0.00(0)	0.00(0)
T ₆ O ₁₈	Si	5.80(43)	5.76(16)	5.82(14)	5.91(14)	5.52(16)	5.60(22)
	Al	0.20(44)	0.24(16)	0.18(14)	0.09(14)	0.48(16)	0.40(22)
(BO ₃) ₃	B	3.00 ^a	3.00 ^a	3.00 ^a	3.00 ^a	3.00 ^a	3.00 ^a
V ₃	OH	3.00(0)	3.00(0)	3.00(0)	3.00(0)	3.00(0)	3.00(0)
	O	0.00(0)	0.00(0)	0.00(0)	0.00(0)	0.00(0)	0.00(0)
W	OH	0.53(28)	0.76(16)	0.87(18)	0.83(11)	0.70(14)	0.79(18)
	O	0.09(17)	0.03(10)	0.06(9)	0.08(13)	0.01(2)	0.00(1)

wt. %		EB17 EMP $n = 10$	EB18-1 EMP $n = 11$	EB19 EMP $n = 16$	EB20 EMP $n = 12$	EB21 EMP $n = 14$	EB22 EMP $n = 12$
	K ₂ O	1.98(46)	0.57(19)	1.33(33)	0.30(9)	0.97(19)	0.19(8)
	Na ₂ O	0.04(2)	1.75(29)	0.04(2)	1.37(37)	0.08(3)	1.97(11)
	MgO	9.37(53)	10.70(43)	9.01(42)	9.74(27)	8.73(31)	9.12(45)
	Al ₂ O ₃	36.8(11)	33.34(53)	36.44(76)	35.45(80)	37.98(85)	36.80(74)
	SiO ₂	34.4(13)	35.2(15)	32.3(10)	31.74(81)	31.74(81)	30.5(11)
X	K	0.41(9)	0.12(4)	0.29(7)	0.06(2)	0.22(2)	0.04(2)
	Na	0.01(1)	0.56(9)	0.01(1)	0.45(12)	0.03(1)	0.65(4)
	□	0.58(9)	0.32(8)	0.70(7)	0.48(13)	0.75(3)	0.30(4)
Y ₃	Mg	2.28(9)	2.65(11)	2.27(8)	2.47(7)	2.17(7)	2.32(9)
	Al	0.72(7)	0.35(11)	0.73(5)	0.53(3)	0.83(5)	0.68(2)
Z ₆	Al	6.00(0)	6.00(0)	6.00(0)	6.00(0)	6.00(0)	6.00(0)
	Si	0.00(0)	0.00(0)	0.00(0)	0.00(0)	0.00(0)	0.00(0)
T ₆ O ₁₈	Si	5.63(13)	5.84(18)	5.46(11)	5.41(13)	5.34(10)	5.25(15)
	Al	0.37(13)	0.16(18)	0.54(11)	0.59(13)	0.66(10)	0.75(15)
(BO ₃) ₃	B	3.00 ^a	3.00 ^a	3.00 ^a	3.00 ^a	3.00 ^a	3.00 ^a
V ₃	OH	3.00(0)	3.00(0)	3.00(0)	3.00(0)	3.00(0)	3.00(0)
	O	0.00(0)	0.00(0)	0.00(0)	0.00(0)	0.00(0)	0.00(0)
W	OH	0.77(14)	0.71(10)	0.49(15)	0.45(11)	0.42(9)	0.63(16)
	O	0.00(0)	0.08(12)	0.00(0)	0.00(0)	0.00(0)	0.00(0)

Continues on next page

Table 4.2: *Continued from previous page*

wt. %		EB23 EMP $n = 9$	EB24 EMP $n = 11$	EB25 EMP $n = 11$	EB32 EMP $n = 22$
	K ₂ O	0.48(9)	0.11(9)	0.28(7)	1.21(65)
	Na ₂ O	0.07(2)	1.49(9)	0.05(1)	1.11(28)
	MgO	8.58(19)	9.14(44)	8.58(11)	10.45(40)
	Al ₂ O ₃	36.13(45)	33.3(17)	36.99(21)	33.50(56)
	SiO ₂	31.73(62)	31.9(15)	32.79(96)	35.3(21)
X	K	0.11(2)	0.02(2)	0.06(2)	0.25(12)
	Na	0.02(1)	0.51(2)	0.02(0)	0.34(8)
	□	0.87(2)	0.46(3)	0.92(1)	0.41(9)
Y ₃	Mg	2.20(4)	2.41(4)	2.15(3)	2.45(11)
	Al	0.80(1)	0.59(4)	0.85(3)	0.55(11)
Z ₆	Al	6.00(0)	6.00(0)	6.00(0)	6.00(0)
	Si	0.00(0)	0.00(0)	0.00(0)	0.00(0)
T ₆ O ₁₈	Si	5.46(6)	5.64(6)	5.51(10)	5.61(33)
	Al	0.54(6)	0.36(6)	0.49(10)	0.65(42)
(BO ₃) ₃	B	3.00 ^a	3.00 ^a	3.00 ^a	3.00 ^a
V ₃	OH	3.00(0)	3.00(0)	3.00(0)	3.00(0)
	O	0.00(0)	0.00(0)	0.00(0)	0.00(0)
W	OH	0.39(8)	0.76(11)	0.44(12)	0.66(31)
	O	0.00(0)	0.00(0)	0.00(0)	0.05(10)

^aValues fixed during normalization^bAnalyses by TEM given in atom % and those by EMP given in wt.% oxides

A major solid solution is observed in all tourmalines between the magnesian endmembers of tourmaline's alkali group, namely dravite/K-dravite, [(Na,K)Mg₃Al₆Si₆O₁₈(BO₃)₃(OH)₃(OH)] and X-site-vacant tourmaline, magnesio-foitite [□(Mg₂Al)Al₆Si₆O₁₈(BO₃)₃(OH)₃(OH)], via the coupled substitution $^X\text{R}^+ + ^Y\text{Mg}^{2+} = ^X\text{□} + ^Y\text{Al}^{3+}$ (Fig. 4.3). Minor solid solution occurs from these endmember compositions toward the aluminous endmember compositions of alkali tourmaline, namely K-olenite or olenite, [(Na,K)Al₃Al₆Si₆O₁₈(BO₃)₃O₃(OH)], and X-vacant tourmaline, namely “□-Mg-O root name”, [□(MgAl₂)Al₆Si₆O₁₈(BO₃)₃(OH)₃O] via the coupled substitution $^Y\text{Al}^{3+} + \text{O}^{2-} = ^Y\text{Mg}^{2+} + \text{OH}^-$. Within this compositional space, the average composition of tourmalines (Table 4.2) synthesized from a KCl (NaCl-free) fluid forms a population distinct from those synthesized from a KCl-NaCl fluid (Fig. 4.3). All K-bearing, Na-free tourmaline had more vacancies at their X site (*i.e.*, a greater magnesio-foitite component) than the Na- and K-bearing tourmalines, regardless of pressure or temperature.

The calculated occupancy of the X site (Fig. 4.4) in terms of K, Na, and vacancies reflects the relative K-dravite, dravite, and magnesio-foitite components, respectively, in each analysis of the synthesized tourmalines. Since tourmalines crystallized at lower pressures were generally smaller, compositional zoning was more difficult to resolve with the EMP beam, those synthesized using the two-chamber method outstanding. Tourmalines crystallized from a KCl-bearing, NaCl-free fluid achieved the highest K contents, reaching K-dominant compositions at 4.0 GPa and 700 °C (Figs. 4.4, 4.6, 4.7). In contrast, tourmalines that crystallized from a Na- and K-bearing fluid are predominantly dravitic in

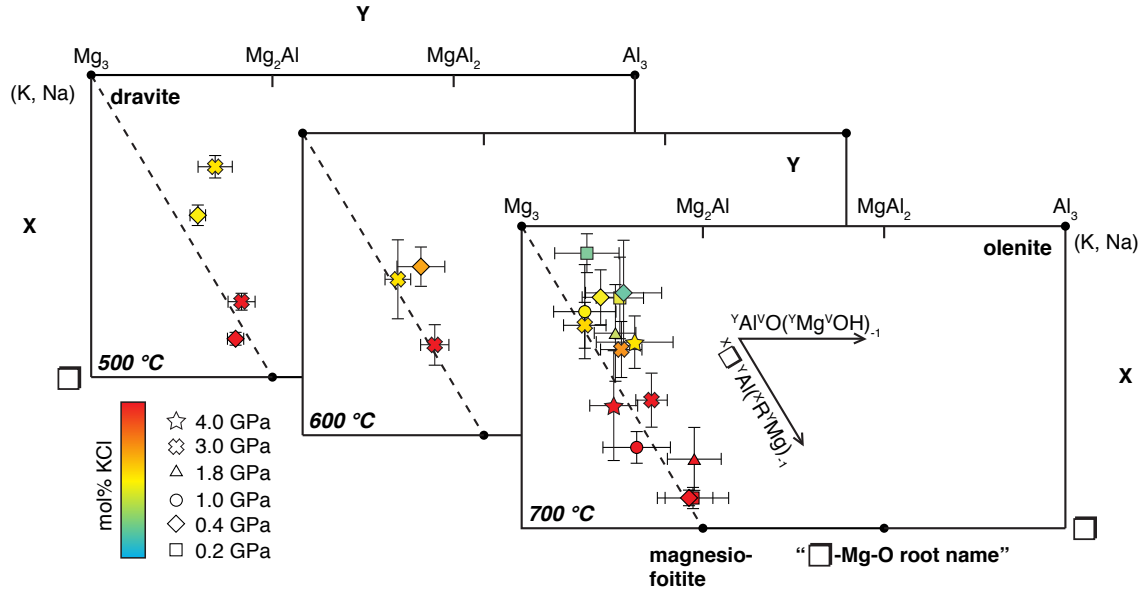


Figure 4.3: Average composition of synthesized tourmaline (Table 4.2) plotted relative to the composition of the Y site and occupancy of the X site at various temperatures. *Symbol shape* correlates to the pressure of the experiment and *colour* to the mol% of KCl relative to NaCl in the starting solution, whereby *blue* indicates a 0 mol% KCl, 100 mol% NaCl solution, and *red* indicates a 100 mol% KCl, 0 mol% NaCl solution. *Ranges* indicate one standard deviation from the average. Endmember compositions are plotted for reference. The *arrows* indicate the direction of the magnesio-foitite–(K, Na)–dravite exchange vector, shown by the *dotted line*, and the direction of the (K, Na)–dravite–olenite exchange vector.

composition, with Na dominantly occupying the X site (Fig. 4.4).

Figure 4.5 shows the occupancy of the X site by K for tourmaline synthesized in the presence of a 4.87 *m* KCl, Na-free solution with increasing pressure and temperature and provides statistical data, including the range, first and third quartiles, and the median of analyses, for each experiment. The range of data reflects the extent of zoning within tourmalines grown in a single experiment. Variation in the X-site composition is similarly plotted as a function of varying K/Na ratio (plotted as mol% KCl or NaCl) in the initial fluid at different pressures and a fixed temperature of 700 °C (Fig. 4.6), and at different temperatures and a fixed pressure of 3.0 GPa (Fig. 4.7). The maximum K content was 0.71 K pfu measured by WDS and 0.81 K pfu by AEM in K-dravite synthesized at 4.0 GPa, 700 °C from a 4.87 *m* KCl fluid. Conversely, the maximum measured Na content was 1.00 Na pfu analyzed by AEM in dravite synthesized at 0.4 GPa from a 3.87 *m* NaCl and 1.08 *m* KCl fluid.

The unit-cell parameters obtained by Rietveld refinement of the X-ray diffraction spectra (Fig. 4.8) range from $a = 15.869(1)–15.927(1)$ Å, $c = 7.116(1)–7.234(1)$ Å, $V = 1555.1(3)–1588.1(2)$ Å³. There is a positive correlation between the K content of the X site and the value of a , c , and V . In contrast, there is no clear trend with Na content. Whereas tourmaline synthesized in all experiments was inhomogeneous, as reflected in the variability in the X-site composition, the refinement provides average unit-cell parameters and should therefore only be interpreted qualitatively.

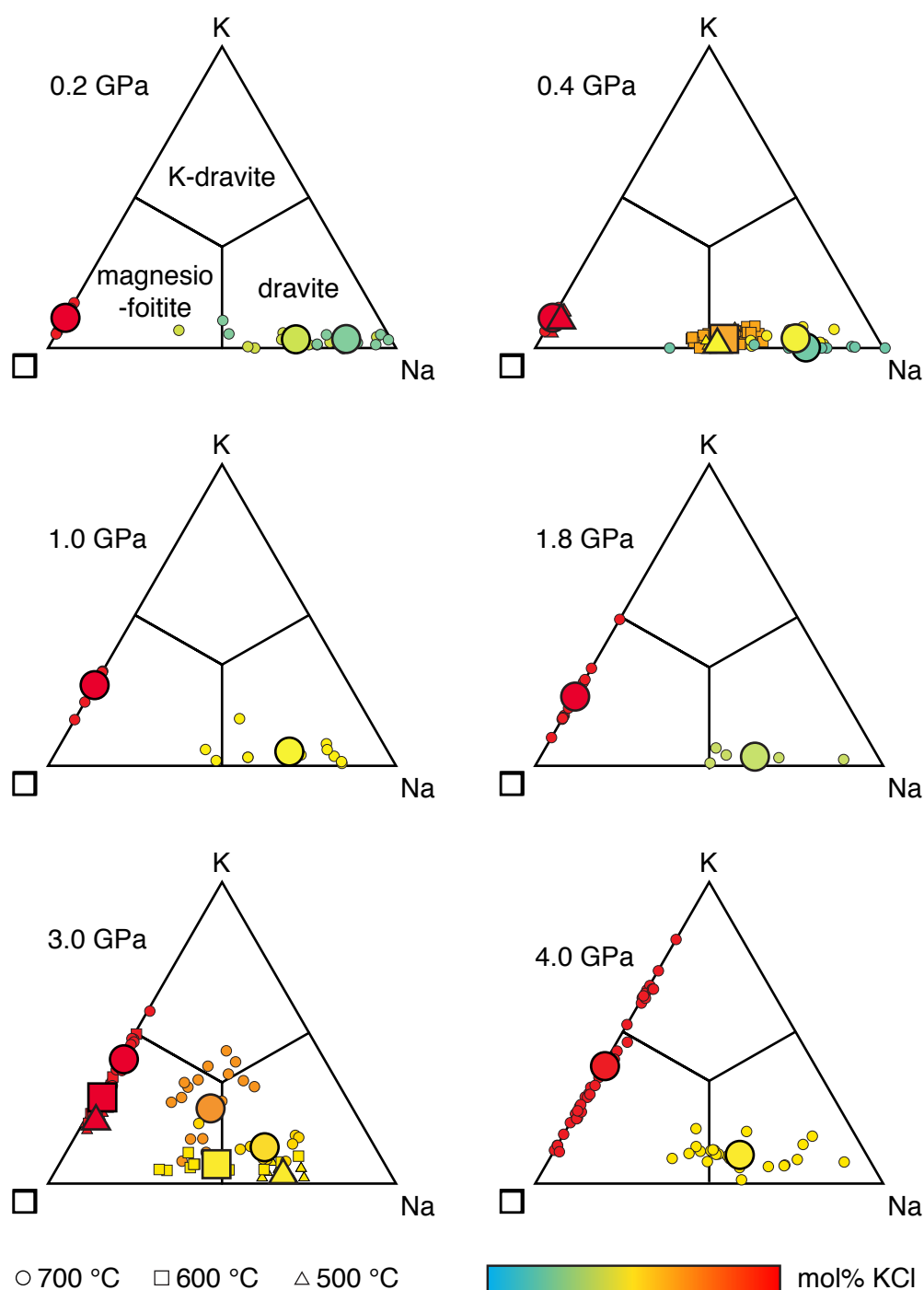


Figure 4.4: Ternary diagrams of tourmaline's X-site composition of each analysis spot (*small symbols*) and their average (*large symbols*; Table 4.2) following normalization to 15 cations at the Y, Z and T sites at various pressures. □ indicates vacancy. The *symbol shape* reflects the synthesis temperature, and the *colour* indicates the mol% of KCl in the starting solution, whereby *blue* indicates a 0 mol% KCl, 100 mol% NaCl solution, and *red* indicates a 100 mol% KCl, 0 mol% NaCl solution. Analysis points for 0.4 GPa, 600 °C include points from two experiments, EB15 and EB16. Points for 4.0 GPa include both data collected by TEM and EMP and the averages are of the combined data.

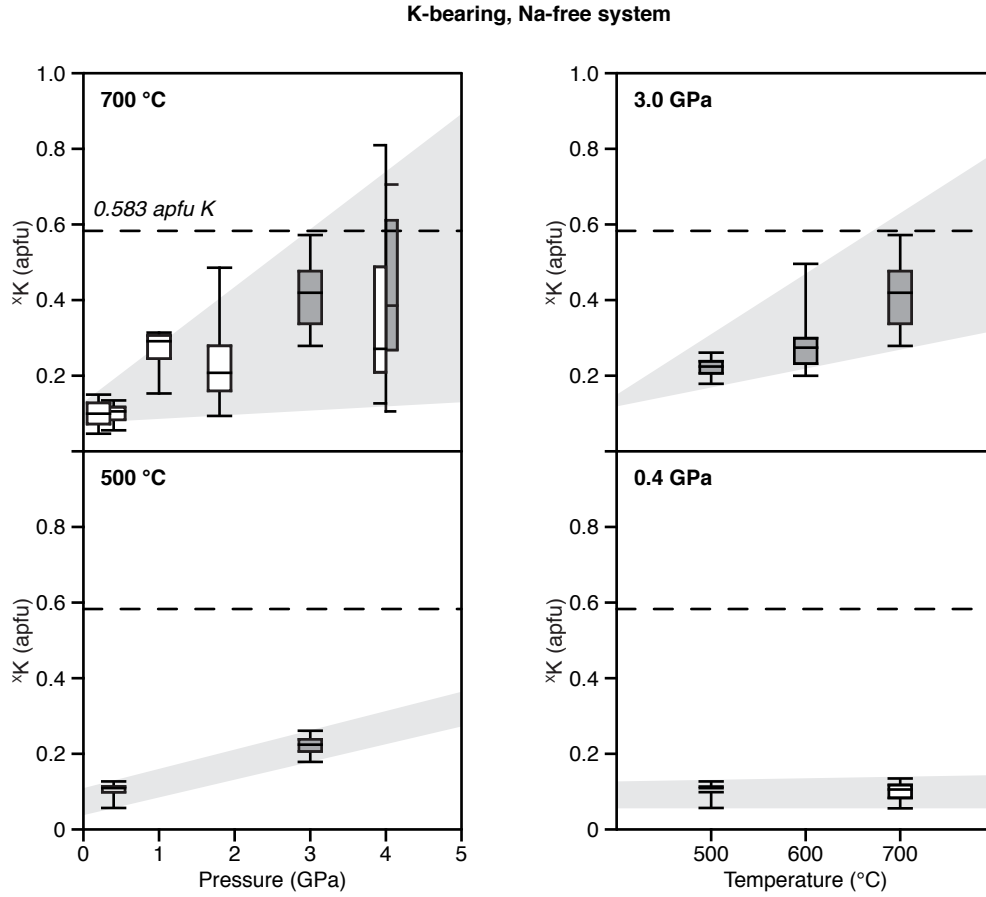


Figure 4.5: Box-and-whisker plots showing the range, first, and third quartiles, and the median of X_K for tourmaline synthesized at various pressures (*left*) and temperatures (*right*) in the presence of a 4.87 m KCl solution. *White* plots correspond to compositional analysis by TEM, whereas the *grey* plots correspond to compositional analysis by EMP, both normalized to 15 YZT. For each plot, the range of data has been interpolated and highlighted with a *grey background*. The *dashed line* gives the maximum K content of the most K-rich maruyamaite from the Kokchetav Massif, Kazakhstan, taken from Shimizu and Ogasawara (2013).

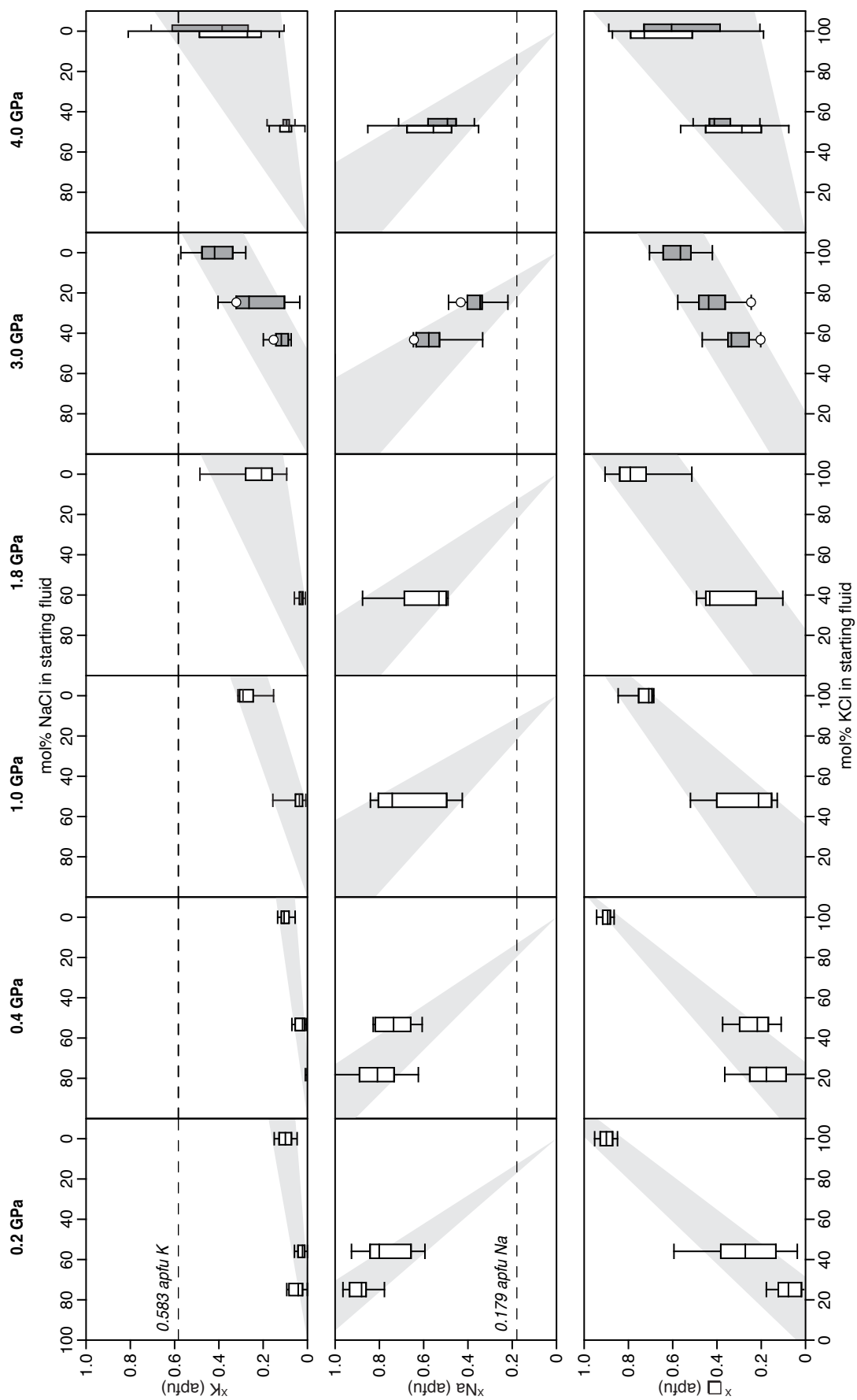


Figure 4.6: (Caption on next page.)

Figure 4.6: (*Figure on previous page.*) Effect of fluid composition and pressure on K and Na incorporation in dravite. Box-and-whisker plots show the range, first, and third quartiles, and the median of ^XK , ^XNa , and $^X\Box$ in tourmaline synthesized at 700 °C from a KCl-NaCl fluid of varying compositions but constant ionic strength ($4.85 \pm 0.07\ m$). Range in data reflects extent of zoning in tourmaline from a single experiment. *White* plots correspond to compositional analysis by TEM, whereas the *grey* plots correspond to compositional analysis by EMP, both normalized to 15 YZT. For each plot, the range of data has been interpolated and highlighted with a *grey background*. The *dashed lines* indicate the K and Na content of the most K-rich maruyamaite from the Kokchetav Massif, Kazakhstan, taken from Shimizu and Ogasawara (2013). The *white circles* indicate the value of the approximate rim composition used in Fig. 4.9.

4.3 Discussion

The synthesized tourmalines show compositional variation on a single grain level in the form of chemical zoning. We assume that the zoning behaviour in the smaller ($<10\ \mu\text{m}$) tourmaline crystals mimics that of the larger crystals. Based on this assumption, analysis points with the lowest number of vacancies are interpreted as approximate rim compositions (Fig. 4.9; Table 4.4). Comparison of the results obtained by AEM and WDS for a single experiment shows a small discrepancy in the range of data (*c.f.* AEM and WDS analyses of tourmaline synthesized at 4.0 GPa in Fig. 4.5 or 4.6) and the average composition (*c.f.* EMP and TEM data for EB1 and EB2 in Table 4.2) determined by each analytical method. This likely reflects differences in the analytical spot size attainable with each method. Since AEM uses a much smaller spot size than WDS, the composition of the crystal rim is more accurately measured because dilution of the analysis by the neighboring mantle is avoided. Alternatively, the differences may reflect variability in composition between the large and small crystals selected for analysis by WDS and AEM, respectively. Despite the inhomogeneity of the crystals, comparison of the average and range of compositions of tourmaline synthesized at different pressures, temperatures, and fluid compositions reveals insightful trends.

Differences in the occurrence and composition of the accompanying phases may have affected the composition of the synthesized tourmaline. They did not exert a significant influence on the K and Na budget, as reflected by the bulk $\text{K}/(\text{K}+\text{Na})$ ratio falling near the tie line connecting the $\text{K}/(\text{K}+\text{Na})$ ratio of the tourmaline's rim (or assumed rim) with that of the product fluid even when the K-bearing mineral, boromuscovite, occurred as a secondary phase (Fig. 4.9). If secondary phases significantly affected the K and Na budget available for the crystallizing tourmaline, we would expect the bulk $\text{K}/(\text{K}+\text{Na})$ ratio to plot far from this tie line. This partitioning diagram also shows that K preferentially partitioned into the fluid instead of the tourmaline (Fig. 4.9; Table 4.4). Thus, given that tourmaline and quartz/coesite were consistently the major crystallizing phases (Table 4.1), we expect the effect of the additional minor phases to be small. However, the effect of the additional crystallizing phases on the Mg and Al budget of the system remains unknown.

At a given pressure and temperature, tourmaline crystallizing from a fluid of higher KCl concentration incorporates more K at its X site; EB23 with 0.11 K pfu crystallized from a 4.78 *m* KCl, Na-free fluid; and EB25 with 0.06 K pfu crystallized from a 2.02 *m* KCl, Na-free fluid. In addition, the relative amount of K and Na incorporated into the crystallizing tourmaline reflects the ratio of K and Na in the crystallizing fluid; increasing the mol% of KCl (NaCl) in a fluid of constant ionic strength increases the amount of K(Na) incorporated by dravite (Figs. 4.4, 4.6, 4.7).

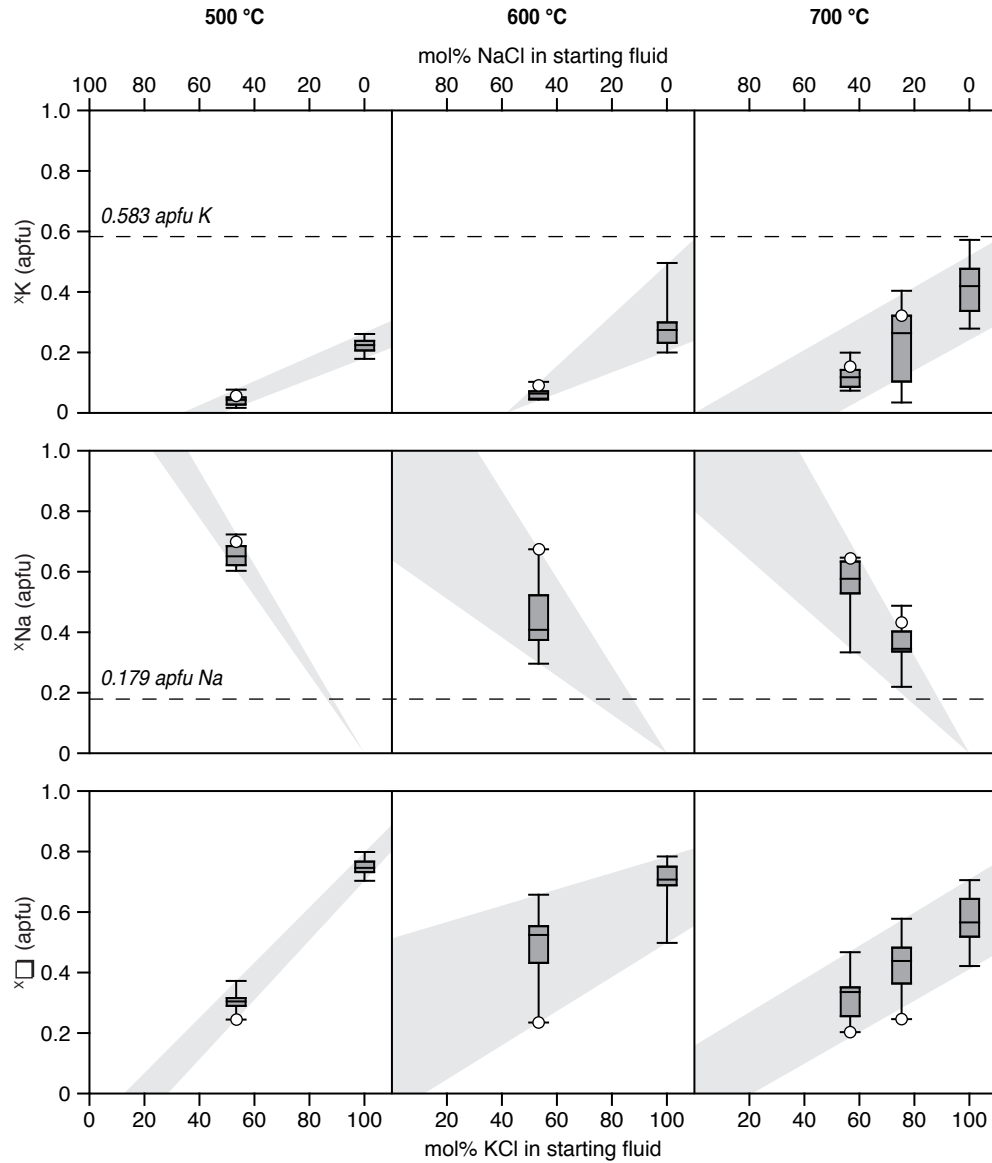


Figure 4.7: Effect of fluid composition and temperature on K and Na incorporation in dravite. Box-and-whisker plots show the range, first, and third quartiles, and the median of X_K , X_{Na} , and X_{Ca} in tourmaline synthesized at 3.0 GPa from a KCl-NaCl fluid of varying compositions but constant ionic strength ($4.84 \pm 0.05 m$). Data were collected by EMP; all data were normalized to 15 cations at the YZT sites. For each plot, the range of data has been interpolated and highlighted with a *grey background*. The *dashed lines* indicate the K and Na content of the most K-rich maruyamaite from the Kokchetav Massif, Kazakhstan, taken from Shimizu and Ogasawara (2013). The *white circles* indicate the value of the approximate rim composition used in Fig. 4.9.

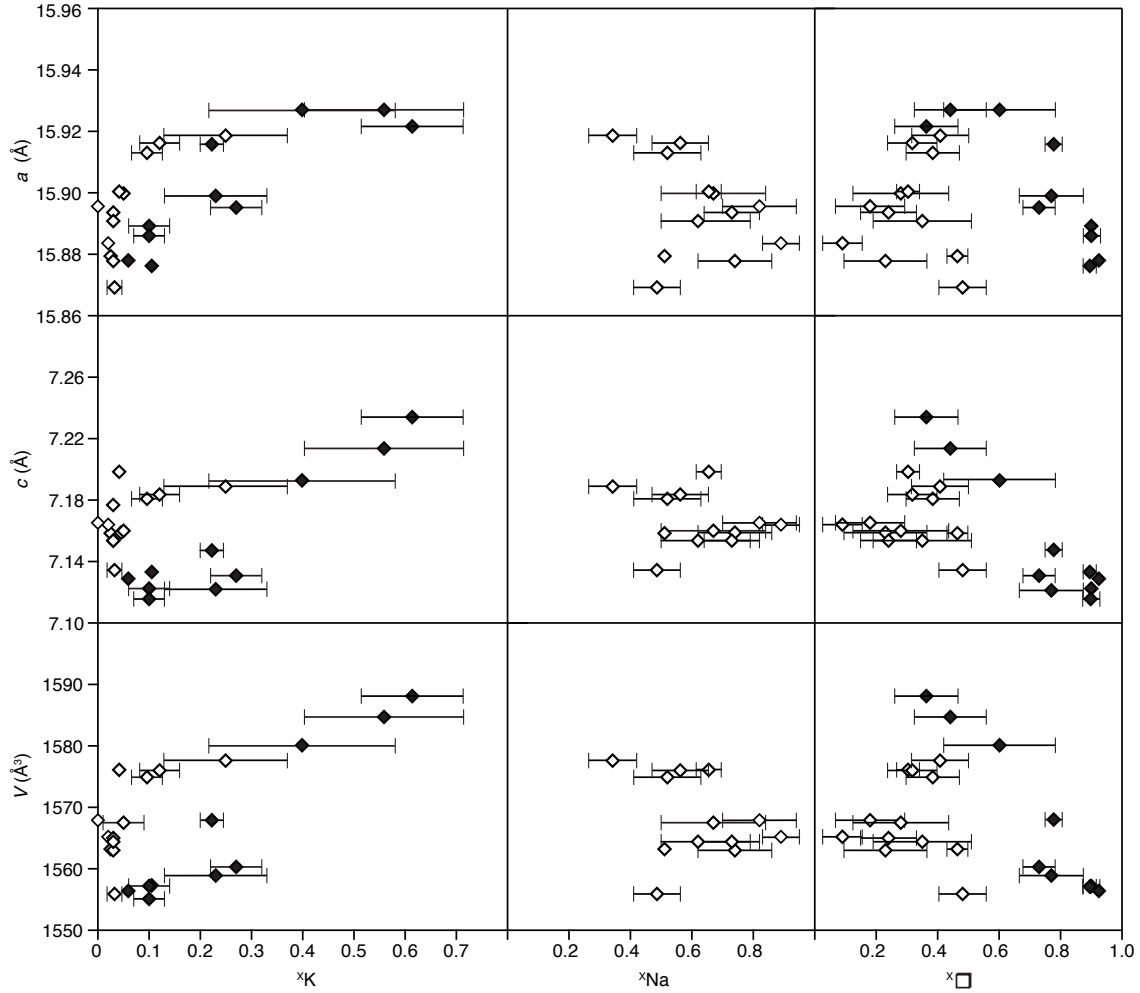


Figure 4.8: Average unit-cell parameters obtained from Rietveld refinement of powder X-ray diffraction spectra (Table 4.3) of tourmaline from all experiments as a function of their average X-site composition, shown with one standard deviation. *Black symbols* represent K-bearing, Na-free tourmaline, whereas *white symbols* represent K- and Na-bearing tourmaline. The symbols cover five times the standard deviation of the unit-cell parameter given by the refinement, which ignores zoning within the crystal and gives an average value for each unit-cell parameter.

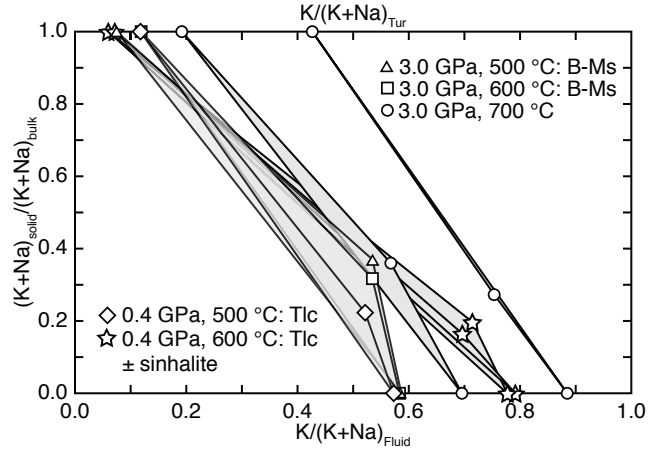


Figure 4.9: Partitioning diagram showing $K/(K+Na)$ ratios of the bulk system (*i.e.*, the initial fluid composition, shown inside the plot), the tourmaline rim (selected as the analysis with the lowest number of vacancies), and the product fluid for experiments at different pressures, temperature, and with different secondary phases (Table 4.4). Tie lines connect the composition of the product fluid with the rim of the tourmaline in each experiment. The tourmalines are zoned, but their rims are considered to be in equilibrium with the product fluid.

Table 4.3: Tourmaline unit-cell parameters

Experiment	a (Å)	c (Å)	V (Å ³)
EB1	15.927(2)	7.193(1)	1580.1(5)
EB2	15.913(1)	7.181(1)	1574.9(4)
EB3	15.889(1)	7.122(1)	1557.2(3)
EB4	15.878(1)	7.159(1)	1563.0(3)
EB5	15.884(2)	7.164(1)	1565.2(5)
EB6	15.886(1)	7.116(1)	1555.1(3)
EB7	15.894(1)	7.154(1)	1565.0(2)
EB8	15.896(1)	7.165(1)	1567.9(2)
EB9	15.899(1)	7.121(1)	1558.9(2)
EB10	15.891(2)	7.154(1)	1564.4(4)
EB11	15.895(2)	7.131(2)	1560.3(5)
EB12	15.900(1)	7.160(1)	1567.5(3)
EB13	15.922(1)	7.234(1)	1588.1(2)
EB14	15.927(1)	7.214(1)	1584.7(2)
EB15	15.869(1)	7.134(1)	1555.9(2)
EB16	15.859(2)	7.127(2)	1552.3(5)
EB18-1	15.916(1)	7.184(1)	1576.0(2)
EB21	15.916(2)	7.147(2)	1567.9(5)
EB22	15.900(2)	7.198(2)	1567.1(6)
EB23	15.876(1)	7.133(1)	1557.1(2)
EB24	15.879(1)	7.158(1)	1563.2(2)
EB25	15.878(1)	7.129(1)	1556.4(2)
EB32	15.919(1)	7.189(1)	1577.6(2)

Table 4.4: Composition of product fluids along with K/(K+Na) mol fractions of fluids and the rims of coexisting tourmalines (selected as analyses with fewest vacancies)

No.	<i>m</i> Na	<i>m</i> K	<i>m</i> Cl	<i>m</i> B	<i>m</i> Mg	K/(K+Na) _{fl}	K/(K+Na) _{tur}
EB15	0.64	2.45	3.43	3.69	0.23	0.79	0.06
EB16	0.72	2.50	3.56	3.51	0.23	0.78	0.07
EB17	<i>0.07</i>	3.32	4.45	6.37	1.08	–	
EB18-1	0.71	1.63	3.53	4.04	0.99	0.70	0.19
EB19	<i>0.08</i>	3.52	4.46	6.00	0.92	–	
EB20	1.39	1.94	4.60	2.60	0.84	0.58	0.12
EB21	<i>0.22</i>	1.85	4.02	2.95	1.40	–	
EB22	1.27	1.80	4.47	2.53	0.93	0.59	0.07
EB23	<i>0.03</i>	4.33	4.45	6.17	0.17	–	
EB24	1.62	2.18	4.57	5.96	0.54	0.57	0.12
EB25	<i>0.02</i>	1.85	1.98	5.69	0.14	–	
EB32	0.30	2.32	3.75	4.15	0.98	0.88	0.43

Italicized values are the concentrations of Na measured in nominally Na-free experiments

Tourmaline synthesized in the K-bearing, Na-free system is generally dominantly magnesio-foitite, reflecting potassium's incompatibility in tourmaline's structure (Figs. 4.3, 4.4). In contrast, tourmaline synthesized in the presence of Na has fewer vacancies and a higher dravitic component (Figs. 4.3, 4.4). Moreover, the addition of Na to the system has a significant influence on K incorporation in dravite. Even though experiment EB24 had a higher concentration of KCl in the fluid (2.34 *m* KCl, 2.55 *m* NaCl) compared to EB25 (2.02 *m* KCl, Na-free), tourmaline in the former incorporated less K on average than the latter, *c.f.* 0.02(2) K pfu in EB24 and 0.06(2) K pfu in EB25. This reflects the control of fluid composition on the X-site composition; the presence of Na suppresses K incorporation. The concentration of NaCl in addition to that of KCl influences the amount of K incorporated into tourmaline. Both a high concentration of K and a low concentration of Na are necessary to incorporate high amounts of K in dravitic tourmaline.

K incorporation in dravitic tourmaline correlates strongly with pressure and temperature (Figs. 4.5, 4.6, 4.7). In the K-bearing, Na-free system, K-dominant dravite crystallizes at pressures and temperatures above 3.0 GPa, 600 °C (Figs. 4.5, 4.7). In the presence of Na, higher pressure and temperature are necessary to attain K-dominant compositions, due to its suppression of K incorporation. Therefore, the relative concentration of KCl in the fluid becomes increasingly important at higher pressure and temperature (>1.0 GPa, 500 °C), where variations in the concentration of KCl in solution result in larger changes in the K content of the dravite crystallized (Figs. 4.6, 4.7).

Unlike for K, neither pressure (Fig. 4.6) nor temperature (Fig. 4.7) appears to significantly influence the amount of Na incorporated at dravite's X site. At a fixed pressure, increasing temperature reduces the amount of Na incorporated into dravite slightly (Fig. 4.7), as observed by von Goerne *et al.* (2001). However, the effect of temperature on Na incorporation is minor compared to K. It thus follows that the incorporation of Na depends mainly on the concentration of Na in the fluid, with temperature having a

secondary control, in agreement with results obtained by von Goerne *et al.* (2001).

As the third component at the X site, vacancies complement the amount of Na and K at the X site; as K incorporation increased with pressure and temperature, the number of vacancies decreased. However, this trend is minor compared to the effect of fluid composition, whereby vacancies at the X site increased with decreasing mol% NaCl in the fluid (Figs. 4.6, 4.7). In naturally-occurring tourmaline, increasing occupancy of the X site in dravite has been correlated with increasing metamorphic grade, *e.g.*, by Henry and Dutrow (1996) in Al-rich metapelites. However, this tendency is not reflected by the dravitic tourmaline synthesized here, where no distinct correlation of X-site occupancy with pressure (Fig. 4.6) nor temperature (Fig. 4.7) exists. Instead, vacancies reflect the incorporation of the principle X-site-occupying cation, Na, whose incorporation principally depends on Na concentration in the fluid. This is supported by experiments by Krosse (1995), who synthesized dravite with up to 0.82 Na pfu at 5.0 GPa and 952 °C and 0.90 Na pfu at 6.0 GPa and 807 °C, noting that the highest Na incorporation occurred in experiments with excess Na in the starting material, as summarized by Werding and Schreyer (1996). In addition, von Goerne *et al.* (2001) synthesized dravite with up to 0.95 Na pfu at 0.2 GPa and 500 °C in their most Na-rich experiment. Combined, experimental observations suggest a correlation between X-site occupancy and concentration of X-site-occupying cations in the fluid (ionic strength). It is thus likely that the correlation of metamorphic grade and occupancy of the X site observed in naturally- occurring dravite reflects the nature of metamorphic fluids and the increasing concentration of Na in them with increasing grade. This emphasizes the importance of understanding variations in fluid composition throughout the crust and the potential of minerals like tourmaline to provide insight into these otherwise inaccessible environments.

All unit-cell parameters show a positive correlation with K content (Fig. 4.8), as predicted by van Hinsberg and Schumacher (2007b). The greater increase in tourmaline's crystal volume from K incorporation is expected from the 25 % larger ionic radius of K than that of Na in ninefold coordination (Shannon, 1976). Tourmalines with both Na and K at the X site have unit-cell parameters generally larger than the Na-free tourmaline, due to the presence of fewer vacancies at their X site. In addition, variations in Na content do not appear to significantly influence the unit-cell size, compared to the large changes caused by varying K content. von Goerne *et al.* (2001) correlated the length of the *c*-axis with Na content, whereby dravite with 0.83 Na pfu had a *c*-axis 0.07 Å longer than Na-free magnesio-foitite. Na is thus expected to have a smaller, but still significant, influence on the lattice parameters; it is likely that in our experiments, this effect is masked by the presence of K. Indeed, the apparent negative correlation between *a* and Na content (Fig. 4.8) is likely due to decreasing K content, rather than increasing Na content. In the K-bearing, Na-free tourmalines, vacancies correlate to decreasing unit-cell parameters, essentially mirroring the latter's correlation with K. In summary, the apparent lack of correlation between vacancies and unit-cell parameters in the K- and Na-bearing tourmalines likely results from their variable K contents, which overprints any other existing trends.

4.3.1 Application to the diamondiferous tourmaline from the Kokchetav Massif, Kazakhstan

Shimizu and Ogasawara (2005) made the first recorded discovery of K-dominant tourmaline, found in a tourmaline, K-feldspar, and quartz rock from the Kumdy-Kol dump in the Kokchetav Massif, Kazakhstan. Shimizu and Ogasawara (2013) further described the oc-

currence of K-rich and K-dominant tourmalines in the diamondiferous UHP metamorphic rocks from the Kumdy-Kol. Their original discovery remains of particular interest, as these tourmalines are zoned, with their diamondiferous K-dominant “oxy-dravite” cores having the composition $^X(\text{K}_{0.583}\text{Ca}_{0.230}\text{Na}_{0.179}\square_{0.008})^Y(\text{Mg}_{2.224}\text{Fe}_{0.383}^{2+}\text{Al}_{0.250}\text{Ti}_{0.134}\text{Mn}_{0.009}\text{Cr}_{0.001})^Z(\text{Al}_6)^T(\text{Si}_{5.979}\text{Al}_{0.021})\text{O}_{18}(\text{BO}_3)_3(\text{OH})_3(\text{OH})_{0.123}\text{O}_{0.719}$, defining the 30th tourmaline end-member, maruyamaite (Lussier *et al.*, 2014). Overgrowing these cores is diamond-free dravite with lower, but still relatively high K contents, around 0.1 pfu, and 0.5–0.6 Na pfu. The K and Na contents of the K-dominant tourmaline are plotted as dashed lines in Figs. 4.5, 4.6 and 4.7. Based on our experimental results, K-rich fluids as well as high pressure and temperature account for the crystallization of this K-dominant tourmaline. Moreover, increasing concentrations of K would be necessitated with decreasing formation pressures. In addition, since pressure and temperature appear to have little effect on the incorporation of Na, the relatively low Na content of the diamondiferous maruyamaite indicates crystallization from a Na-poor fluid (probably <1 m Na) (Figs. 4.5, 4.6). Given peak metamorphic conditions for the Kokchetav UHP rocks of at least 4.3 GPa and 950–1000 °C (Schertl and Sobolev, 2013), it is reasonable that the diamondiferous tourmaline cores formed near these conditions, as argued by Ota *et al.* (2008b) and Shimizu and Ogasawara (2013), or shortly after on the retrograde path from K-rich, B-bearing fluids as suggested by Schertl and Sobolev (2013). Since dravite is not expected to be stable in silica-saturated systems above ~ 4.5 GPa, 800 °C (Ota *et al.*, 2008a), the latter might be considered more likely. Subsequent K-poor, Na-dominant tourmaline growth would have occurred on the retrograde path and/or in the presence of Na-rich fluids. Therefore, we conclude that a high-grade origin for maruyamaite from the Kokchetav Massif is likely. The requisite of K-rich, Na-poor fluids is consistent with the occurrence of other UHP K-rich phases, such as K-cymrite (Mikhno *et al.*, 2013), K-rich clinopyroxene, and K-feldspar exsolutions in clinopyroxene (Schertl and Sobolev, 2013, and references therein) as well as the presence of nanometer K-rich fluid inclusions in microdiamonds (Hwang *et al.*, 2005) in other rocks from the Kumdy-Kol.

Although the incorporation of K occurs via the isovalent substitution $^X\text{K}(^X\text{Na})_{-1}$ at the X site, it is likely that the composition of the other crystallographic sites will exert an influence. In particular, the occurrence of “K-povondraite” as clast overgrowths in brecciated meta-evaporites in Alto Chapare, Cochabamba, Bolivia, with up to 0.6 K pfu (Grice *et al.*, 1993; Žáček *et al.*, 2000) raises the possibility of high amounts of K incorporation occurring at crustal pressures in Al-poor, Fe^{3+} -rich tourmaline. Moreover, both Grice *et al.* (1993) and Žáček *et al.* (2000) correlated increasing K/(Na + K) ratios to increasing Fe content in these tourmalines, suggesting Fe at the Y and Z sites may facilitate the incorporation of K at the X site. As a result, insight into the incorporation of K in tourmaline given here is limited to magnesian tourmaline, including magnesio-foitite and dravite, the tourmaline endmember composition most common in high-grade rocks (Henry and Dutrow, 1996). It is therefore important to bear in mind the possibility that the presence of other elements in the Kokchetav Massif K-dominant tourmaline, particularly Fe and Ca, whose effect on K and Na incorporation remain to be investigated, may have influenced K incorporation. However, their concentrations are only 0.383 Fe^{2+} and 0.230 Ca pfu in the most K-rich maruyamaite (Shimizu and Ogasawara, 2013), and are therefore not expected to change the conclusion of a high-grade origin for the K-dominant tourmaline from the Kokchetav Massif.

4.4 Conclusions

Pressure and temperature exert a strong control on the incorporation of K at the X site of dravitic tourmaline, particularly in the presence of K-dominant fluids. In contrast, they have only a minor effect on the incorporation of the smaller and more commonly incorporated Na ion and on the number of vacancies at the X site. The latter's abundance depends principally on the composition and ionic strength of the crystallizing fluid. Dravite can incorporate a significant amount of K at upper-mantle conditions, and given an appropriate formation fluid, maruyamaite can crystallize, as observed in the UHP rocks from the Kundy-Kol in the Kokchetav Massif, Kazakhstan. Based on the occurrence of K-dominant povondraite in nature, the composition of tourmaline's other crystallographic sites is expected to influence K incorporation at the X site. However, this remains to be investigated experimentally.

If the controls (*e.g.*, pressure, temperature, fluid, and tourmaline composition) on K incorporation in dravite can be fully constrained, the K content of tourmaline has the potential to serve as a geobarometer and to provide insight into fluid compositions throughout the crust. As demonstrated here, the K and Na contents of tourmaline from the Kokchetav Massif provide a qualitative constraint on the metamorphic grade and composition of their formation environment, as well as the nature of their crystallizing fluid. Combined with its ability to record its formation environment's chemical and isotopic composition and its application as a geothermometer, tourmaline's potential as a geobarometer makes it an even more powerful petrogenetic indicator mineral.

Chapter 5

Influence of the X-site composition on tourmaline's crystal structure: Investigation of synthetic K-dravite, oxy-uvite, and magnesio-foitite using SREF and Raman spectroscopy

The contents of this chapter have been published in *Physics and Chemistry of Minerals*, Volume 43, pages 83–102.

5.1 Introduction and approach

To better understand how the tourmaline structure accommodates variations in the composition of the X site, synthetic K-dravite, dravite, oxy-uvite, and magnesio-foitite were characterized by electron microprobe, single-crystal (except dravite) and powder X-ray diffraction, and oriented Raman spectroscopy. Each of these synthetic tourmalines has a different X-site composition [K, Na, Ca, or vacancy (\square)], and comparison of their combined crystal structure data allows us to better understand the X-site occupancy's influence on tourmaline's crystal structure.

K-dravite crystals synthesized and described in Chapter 4 (EB13) were used in this study. In addition, four tourmaline-synthesis experiments were done to produce dravite (EB28 and EB29), oxy-uvite (CN11), and magnesio-foitite (MF2) using the one-chamber method and the piston-cylinder press, or the two-chamber method and the hydrothermal pressure apparatus. The details of each tourmaline synthesis are provided in Table 5.1. The synthesized tourmalines were characterized by EMP analysis, powder and single crystal XRD, as well as polarized Raman spectroscopy. For details on the experimental and analytical methods, see Chapter 2.

Table 5.1: Details of synthesis experiments

Experiment Tourmaline	EB13 ^a K-dravite	EB28 Dravite	EB29 Dravite	CN11 Oxy-uvite	MF2 Magnesio-foitite
Temperature (°C)	700	600	600	700	700
Pressure (GPa)	4.0	4.0	4.0	0.2	0.4
Duration (days)	6	8	8	15	7
Atomic proportions of oxide mixture	3Mg:6Al:7.2Si:6B	3Mg:6Al:11.2Si:6B		3Mg:6Al:6B	2Mg:7Al:6B
Fluid composition	4.78 <i>m</i> KCl	1.99 <i>m</i> KCl 3.99 <i>m</i> NaCl	3.00 <i>m</i> KCl 1.70 <i>m</i> NaCl	2.00 <i>m</i> CaCl ₂	Pure H ₂ O
Experimental setup	One chamber	One chamber	One chamber	Two chamber	Two chamber
Oxide mixture added (mg)	10.50	13.74	14.68	40.96	45.69
SiO ₂ added (mg)	–	–	–	21.57	12.35
Fluid added (mg)	5.90	12.25	12.14	39.55	30.43
Additional synthe- sis products wt. %	Coesite 9.9(1) Sylvite 6.7(5)	Coesite 36.2(3)	Coesite 8.7(1) Boromuscovite 7.8(3)	Quartz 25.9(1) Boralsilite ^b 17(1) Talc < 1	Boralsilite ^b 37.3(5) Pinnoite ^c < 1

^aExperiment EB13 is taken from Chapter 4. An additional 0.95 mg of solid KCl was added to the starting material.

^bBoralsilite: Al₁₆B₆Si₂O₂₇

^cPinnoite: MgB₂O₄–3H₂O

5.2 Results

Table 5.2: Composition of synthesized tourmaline determined by EMPA

wt. %	K-dravite EB13 $n = 15$	Dravite EB28 $n = 14$	Dravite EB29 $n = 14$	Magnesio-foitite MF2 $n = 16$	Oxy-uvite CN11 $n = 13$
K ₂ O	3.28(27)	0.10(2)	0.16(7)	0.02(3)	0.02(2)
Na ₂ O	0.10(6)	2.57(9)	2.02(15)	0.04(6)	0.02(1)
CaO	0.01(1)	0.01(2)	0.02(1)	0.03(3)	4.15(55)
MgO	10.65(50)	9.98(56)	10.44(77)	8.20(64)	10.87(87)
Al ₂ O ₃	32.94(72)	33.68(84)	33.5(11)	38.1(15)	33.7(17)
SiO ₂	35.89(58)	33.8(11)	34.2(11)	36.2(15)	36.1(12)
B ₂ O ₃	11.50(49)	13.26(89)	13.23(79)	11.77(85)	10.79(84)
Cl	0.01(1)	0.07(3)	0.04(2)	Not analyzed	Not analyzed
Total	94.48(57)	93.57(66)	93.69(50)	94.6(10)	95.9(12)
Cation units					
Normalized to 18 YZTB. ^{VW} OH and ^{VW} O determined by charge balance.					
K	0.68(6)	0.02(0)	0.03(1)	0.00(1)	0.00(0)
Na	0.03(2)	0.81(3)	0.63(5)	0.01(2)	0.01(0)
Ca	0.00(0)	0.00(0)	0.00(0)	0.00(0)	0.72(10)
□	0.28(7)	0.17(3)	0.33(5)	0.98(2)	0.27(10)
Mg	2.59(13)	2.41(14)	2.50(20)	1.94(15)	2.64(21)
Al	6.33(13)	6.42(15)	6.33(18)	7.11 (29)	6.46(37)
Si	5.85(8)	5.47(21)	5.50(20)	5.73(25)	5.88(17)
B	3.24(12)	3.70(22)	3.67(19)	3.22(20)	3.02(18)
Si + B	9.09(14)	9.17(30)	9.17(28)	8.95(32)	8.90(25)
^{VW} OH	3.92(6)	3.83(16)	3.66(22)	3.78(23)	3.30(16)
^{VW} O	0.03(6)	0.03(6)	0.00(1)	0.02(4)	0.70(16)
Normalized to 15 YZT with B fixed at 3 pfu. ^{VW} OH and ^{VW} O determined by charge balance.					
K	0.69(6)	0.02(0)	0.03(1)	0.00(1)	0.00(0)
Na	0.03(2)	0.85(3)	0.66(5)	0.01(2)	0.01(0)
Ca	0.00(0)	0.00(0)	0.00(0)	0.00(0)	0.72(10)
□	0.27(7)	0.13(3)	0.30(4)	0.98(2)	0.27(10)
Mg	2.62(12)	2.53(13)	2.62(19)	1.97(14)	2.64(22)
Al	6.43(14)	6.74(21)	6.63(25)	7.22(29)	6.47(33)
Si	5.94(6)	5.73(14)	5.75(14)	5.82(24)	5.89(18)
B	3.00	3.00	3.00	3.00	3.00
Si + B	8.94(6)	8.73(14)	8.75(14)	8.82(24)	8.89(18)
^{VW} OH	3.92(7)	3.85(11)	3.78(15)	3.81(21)	3.30(12)
^{VW} O	0.06(8)	0.11(11)	0.03(8)	0.04(5)	0.70(12)
Normalized to 31 O with B fixed at 3 pfu.					
K	0.69(6)	0.02(0)	0.03(1)	0.00(1)	0.00(0)
Na	0.03(2)	0.84(3)	0.66(5)	0.01(2)	0.01(0)
Ca	0.00(0)	0.00(0)	0.00(0)	0.00(0)	0.73(10)
□	0.27(7)	0.13(3)	0.30(5)	0.98(2)	0.26(10)
Mg	2.63(12)	2.52(14)	2.63(20)	1.97(15)	2.66(23)

Continues on next page

Table 5.2: *Continued from previous page*

Al	6.42(14)	6.73(21)	6.65(25)	7.24(32)	6.51(32)
Si	5.94(6)	5.72(13)	5.77(13)	5.83(22)	5.92(18)
B	3.00	3.00	3.00	3.00	3.00
Si + B	8.94(6)	8.72(13)	8.77(13)	8.83(22)	8.92(18)
^{VW} OH	4.00	4.00	4.00	4.00	3.00
^{VW} O	0.00	0.00	0.00	0.00	1.00

n indicates the number of EMP analyses.

All synthesis experiments produced tourmaline along with the additional phases listed in Table 5.1. Tourmaline crystals synthesized at 4.0 GPa (EB13, EB28, EB29) were up to 10 μm in length, whereas those synthesized using the two-chamber method (CN11, MF2) were up to $\sim 600 \mu\text{m}$ in length (Fig. 2.1). All synthesized tourmalines were relatively homogeneous in composition (Fig. 5.1; Table 5.2), with those from EB28 showing the highest amount of inhomogeneity in the backscattered electron image (Fig. 5.1). In general, the total oxides measured by EMPA (Table 5.2) are lower than expected for tourmaline (~ 96 – $97 \text{ wt.}\%$, depending on composition) by $\sim 2 \text{ wt.}\%$. This likely reflects the larger excitation volume of the electron beam relative to the crystal size. The minor reduction in total measured oxides is expected to be shared proportionally among the different oxides and therefore should mostly not affect the ratio of the elements determined by their normalization. The tourmaline compositions determined by EMPA were normalized both to 18 cations at the Y, Z, and T and B sites (18 YZTB) and alternatively to 15 cations at the Y, Z, and T sites (15 YZT) allowing the effect of the measured B concentrations on the normalized values to be evaluated. The quantities of O and OH at the V and W sites were determined by charge balance (Table 5.2). In the case of EB13, EB28, and EB29, the 18 YZTB normalized values give $\text{Si} + \text{B} > 9$, which cannot be accommodated in tourmaline's structure. This likely reflects an analytical problem, particularly in the measurement of B resulting from the small crystal size of these samples. The larger crystal sizes of MF2 and CN11 correlate with 15 YZT and 18 YZTB normalized cation values with $\text{Si} + \text{B} < 9$, supporting this conclusion (Table 5.2). Normalization of the data to 15 YZT, assuming 3 B pfu, avoids this problem. The proportion of OH and O at the VW sites calculated using either the 15 YZT or 18 YZTB normalizations indicates that only oxy-uvite (CN11) has a largely deprotonated W site. However, in the case of EB13, EB28, EB29, and MF2, these normalization schemes result in significant vacancies at the VW sites (*i.e.*, $^{\text{VW}}(\text{OH}) + ^{\text{VW}}\text{O} < 4$). To overcome this problem, the values are additionally normalized to 31 oxygens pfu, assuming 3 B pfu and fully protonated VW sites (*i.e.*, 4 OH pfu) for EB13, EB28, EB29, and MF2 (Table 5.2). The same normalization scheme was applied to CN11, but assuming a deprotonated W site (*i.e.*, $^{\text{V}}(\text{OH})_3$ and $^{\text{W}}\text{O}$). Comparison of the different normalization schemes (Table 5.2) shows that only the proportion of tetrahedral B and the occupancy of the VW sites are significantly influenced by the different normalization schemes. The synthesized K-dravite (EB13) has an average of 0.68(6) [0.69(6)] K pfu based on the 18 YZTB [15 YZT or 31 O] normalization. Tourmaline synthesized in the alkali-free system (MF2) is endmember magnesio-foitite in composition. In the Na-bearing system (EB28, EB29), dravite with variable Na content was synthesized. Dravite crystallized from a 3.99 *m* NaCl fluid (EB28) has an average of 0.81(3) [0.85(3) or 0.84(3)] Na pfu and that crystallized from a 3.00 *m* fluid (EB29) has 0.63(5) [0.66(5)] Na pfu based on the 18 YZTB [15 YZT or 31 O] normalization (Table 5.2). The correlation of Na content in the dravitic tourmaline with Na concentration in the fluid is consistent with the findings of von Goerne *et al.* (2001) and (Chapter 4). In the Ca system (CN11), oxy-uvite with

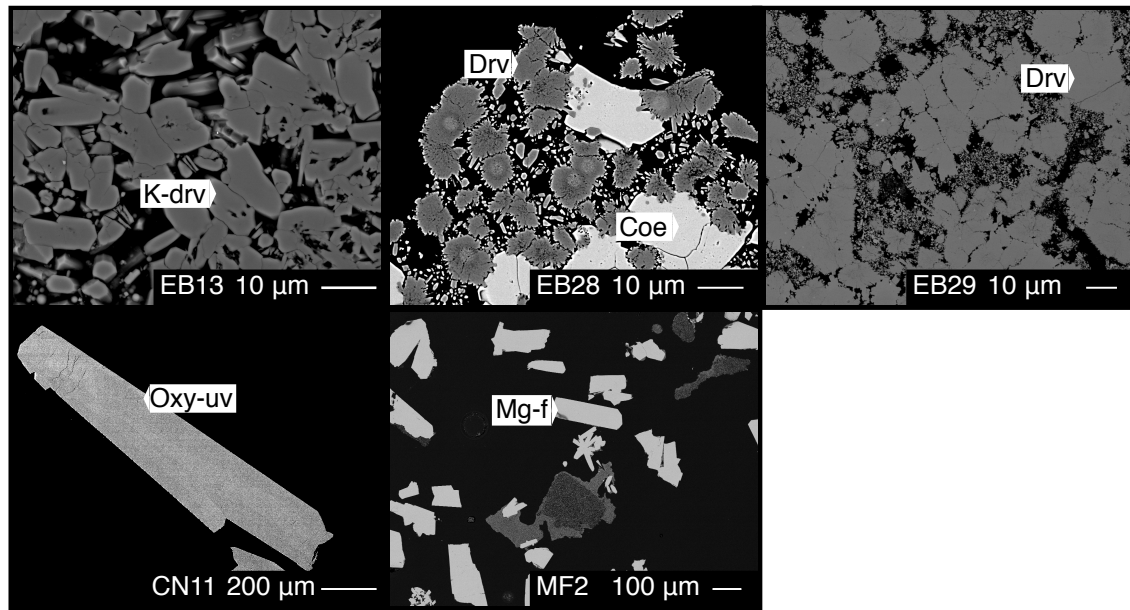


Figure 5.1: Backscattered electron images of polished grain mounts of synthetic tourmaline (K-drav: K-dravite; Drv: dravite; Mg-f: magnesio-foitite; Oxy-uv: oxy-uvite). The lighter grey round spots in the center of the tourmaline aggregates in EB28 are caused by the electron beam during EMPA. The non-tourmaline phases in the dravite synthesis (EB29: coesite and boromuscovite) and magnesio-foitite synthesis (MF2: boralsilite and pinnoite) were identified by powder XRD.

0.72(10) [0.73(10)] Ca pfu was synthesized based on the 18 YZTB and 15 YZT [31 O] normalization schemes (Table 5.2). The EMPA for all tourmalines except oxy-uvite (CN11) show 0.22(20)–0.70(22) B in excess of 3 B pfu when normalized to 18 YZTB, with the two synthetic dravites (EB28 and EB29) having the highest amounts (Table 5.2; 0.70(22) and 0.67(19) excess B pfu, respectively).

The average unit-cell parameters obtained by powder XRD are in good agreement with those obtained by single-crystal XRD (Table 5.3). K-dravite (EB13) has the largest unit-cell parameters, which are comparable to those reported for the K-dominant tourmaline maruyamaite ($a = 15.955(10)$ Å, $c = 7.227(4)$ Å, $V = 1593.2(17)$ Å³; Lussier *et al.*, 2014). The synthetic magnesio-foitite (MF2) has the smallest unit-cell parameters of the investigated tourmalines, consistent with values obtained for synthetic ($a = 15.902(1)$ Å, $c = 7.1263(3)$ Å, $V = 1560.52(12)$ Å³; von Goerne *et al.*, 2001; Rosenberg and Foit, 1979) and natural ($a = 15.884(4)$ Å, $c = 7.178(3)$ Å, $V = 1568.0(6)$ Å³; Hawthorne *et al.*, 1999) magnesio-foitite. The unit-cell parameters of the two synthesized dravites (EB28 and EB29) are very similar despite their variable Na content, and are comparable to those of the synthesized oxy-uvite (CN11) (Table 5.3). The values are consistent with previously synthesized dravite and oxy-uvite [*cf.* $a = 15.875(1)$ Å, $c = 7.1790(2)$ Å, $V = 1566.78(2)$ Å³ for dravite (von Goerne *et al.*, 2001); $a = 15.919(2)$ Å, $c = 7.167(2)$ Å, $V = 1572.97(4)$ Å³ for oxy-uvite (von Goerne and Franz, 2000)]. The unit-cell parameters of dravite and oxy-uvite are intermediate in value between those of K-dravite and magnesio-foitite (Table 5.3). The atom parameters and a selection of interatomic distances for synthetic K-dravite, oxy-uvite, and magnesio-foitite as determined by refinement of the single-crystal X-ray diffraction data (SREF) are given in Tables 5.4 and 5.5, respectively. The values obtained for magnesio-foitite are similar to values for synthetic foitite (Kahlenberg and Veličkov, 2000), with the average <Y–O> distance being slightly smaller in magnesio-

Table 5.3: Unit-cell parameters determined by powder XRD and single-crystal XRD

Sample	Method	Endmember and abbreviated formula	$a = b$ (Å)	c (Å)	V (Å ³)
EB13	Powder	K-dravite	15.922(1)	7.234(1)	1588.1(2)
	Single crystal	^X K ^Y Mg ₃ ^Z Al ₆ ^T Si ₆	15.947(4)	7.231(2)	1592.5(7)
EB28	Powder	dravite	15.891(2)	7.177(1)	1569.5(4)
		^X Na ^Y Mg ₃ ^Z Al ₆ ^T Si ₆			
EB29	Powder	dravite	15.901(1)	7.178(1)	1571.7(3)
MF2	Powder	magnesio-foitite	15.894(1)	7.124(1)	1558.4(3)
	Single crystal	^X □ ^Y (Mg ₂ Al) ^Z Al ₆ ^T Si ₆	15.910(1)	7.131(1)	1563.2(3)
CN11	Powder	oxy-uvite	15.906(1)	7.176(1)	1572.4(2)
	Single crystal	^X Ca ^Y Mg ₃ ^Z Al ₆ ^T Si ₆	15.907(1)	7.179(1)	1573.2(3)

foitite (*cf.* $\langle Y-O \rangle = 1.992$ and 2.020 Å for magnesio-foitite and foitite, respectively). The quality of the SREF of synthetic oxy-uvite (CN11) and magnesio-foitite (MF2) is significantly higher than that of K-dravite (EB13) (Table 2.1), likely due to the different size and quality of the investigated crystals. As a result, in the former two tourmalines, it was feasible to refine the occupancies of the Y and Z sites by Mg and Al from the electron densities at each respective site (Table 5.4). The presence of tetrahedral B was identified in the SREF of K-dravite (EB13) and, to a lesser extent, magnesio-foitite (MF2). No tetrahedral B was identified in the SREF of oxy-uvite, consistent with the 18 YZTB normalized EMPA (Table 5.2).

Table 5.4: Atom parameters and site symmetry of K-dravite (EB13), oxy-uvite (CN11), and magnesio-foitite (MF2) determined by single-crystal XRD refinement

Site	x	y	z	U_{eq}	Site symmetry	Occupancy
K-dravite (EB13)						
X	0	0	0.2195(12)	0.011(3)	3m	K _{0.76} □ _{0.24(3)} ^a
Y	0.1261(3)	$1/2x$	0.6344(8)	0.0060(12)	m	Mg _{3.00}
Z	0.2984(2)	0.2619(2)	0.6119(6)	0.0093(8)	1	Al _{6.00}
B	0.1096(7)	$2x$	0.457(3)	0.008(3)	m	B _{3.00}
T	0.1925(2)	0.1905(2)	-0.0024(4)	0.0060(9)	1	Si _{5.4} B _{0.6(1)} ^a
H3	0.246(9)	$1/2x$	0.36(2)	0.00(4)	m	H _{1.00}
W (O1)	0	0	0.775(3)	0.022(5)	3m	O _{1.00}
O2	0.0614(4)	$2x$	0.4970(18)	0.017(3)	m	O _{1.00}
V (O3)	0.2628(9)	$1/2x$	0.5118(18)	0.018(3)	m	O _{1.00}
O4	0.0939(4)	$2x$	0.0645(19)	0.014(3)	m	O _{1.00}
O5	0.1873(7)	$1/2x$	0.0890(16)	0.011(3)	m	O _{1.00}
O6	0.1972(5)	0.1859(5)	0.7776(9)	0.0093(16)	1	O _{1.00}
O7	0.2835(5)	0.2861(5)	0.0759(11)	0.0092(18)	1	O _{1.00}
O8	0.2090(5)	0.2703(5)	0.4409(12)	0.0149(19)	1	O _{1.00}

Continues on next page

Table 5.4: *Continued from previous page*

Site	x	y	z	U_{eq}	Site symmetry	Occupancy
Oxy-uvite (CN11)						
X	0	0	0.22020(8)	0.0122(1)	3m	$\text{Ca}_{0.64}\square_{0.36(1)}^a$
Y	0.12338(2)	$1/2x$	0.63638(4)	0.0070(1)	m	$\text{Mg}_{1.52}\text{Al}_{1.48(10)}^a$
Z	0.29747(1)	0.26115(1)	0.61043(3)	0.0049(1)	1	$\text{Al}_{4.90}\text{Mg}_{1.10(15)}^a$
B	0.10955(3)	$2x$	0.45300(13)	0.0061(1)	m	$\text{B}_{3.00}$
T	0.19164(1)	0.18975(1)	0.00028(3)	0.0046(1)	1	$\text{Si}_{6.00}$
H3	0.257(2)	$1/2x$	0.402(4)	0.041(7)	m	$\text{H}_{1.00}$
W (O1)	0	0	0.7737(2)	0.0122(2)	3m	$\text{O}_{1.00}$
O2	0.06013(2)	$2x$	0.48516(11)	0.0125(1)	m	$\text{O}_{1.00}$
V (O3)	0.26024(6)	$1/2x$	0.51000(10)	0.0133(1)	m	$\text{O}_{1.00}$
O4	0.09289(3)	$2x$	0.07334(10)	0.0105(1)	m	$\text{O}_{1.00}$
O5	0.18299(6)	$1/2x$	0.09452(10)	0.0104(1)	m	$\text{O}_{1.00}$
O6	0.19399(3)	0.18380(3)	0.77755(7)	0.0082(1)	1	$\text{O}_{1.00}$
O7	0.28527(3)	0.28459(3)	0.07800(7)	0.0083(1)	1	$\text{O}_{1.00}$
O8	0.20892(3)	0.26945(3)	0.43911(7)	0.0094(1)	1	$\text{O}_{1.00}$
Magnesio-foitite (MF2)						
X	0	0	-0.02(3)	0.73(19)	3m	$\square_{0.91}\text{Na}_{0.09(6)}^a$
Y	0.12599(3)	$1/2x$	0.62831(6)	0.0075(3)	m	$\text{Al}_{1.62}\text{Mg}_{1.38(18)}^a$
Z	0.29775(2)	0.26151(2)	0.61077(3)	0.0075(3)	1	$\text{Al}_{4.92}\text{Mg}_{1.08(24)}^a$
B	0.10963(5)	$2x$	0.4567(2)	0.0079(2)	m	$\text{B}_{3.00}$
T	0.19169(2)	0.18947(2)	0.00177(4)	0.0050(1)	1	$\text{Si}_{5.66}\text{B}_{0.34(4)}^a$
H3	0.262(2)	$1/2x$	0.395(4)	0.040(8)	m	$\text{H}_{1.00}$
W (O1)	0	0	0.7757(3)	0.0143(3)	3m	$\text{O}_{1.00}$
O2	0.06112(3)	$2x$	0.49681(15)	0.0125(2)	m	$\text{O}_{1.00}$
V (O3)	0.26152(8)	$1/2x$	0.50774(13)	0.0120(2)	m	$\text{O}_{1.00}$
O4	0.09443(4)	$2x$	0.06926(14)	0.0117(2)	m	$\text{O}_{1.00}$
O5	0.18852(7)	$1/2x$	0.09509(14)	0.0115(2)	m	$\text{O}_{1.00}$
O6	0.19580(5)	1.8422(5)	0.77670(10)	0.0087(1)	1	$\text{O}_{1.00}$
O7	0.28551(4)	0.28572(4)	0.07766(9)	0.0083(1)	1	$\text{O}_{1.00}$
O8	0.20941(5)	0.27004(5)	0.43969(9)	0.0094(1)	1	$\text{O}_{1.00}$

Tourmaline has space group $R3m$, and its unit cell with hexagonal axes is centred on 3m. For definition of U_{eq} see Fischer and Tillmanns (1988).

^aDetermined by refinement

The polarized lattice-vibration Raman spectra of synthetic K-dravite, dravite, and oxy-uvite share the same major bands (Fig. 5.2). The relative intensities of the bands are similar, with the exception of the band at 661 cm^{-1} having a higher relative intensity in the spectrum of oxy-uvite and that at 676 cm^{-1} having a higher relative intensity in the spectra of K-dravite and dravite. The lattice-vibration Raman spectrum of magnesio-foitite is generally similar to those of the other tourmalines, but is distinguished by the bands at 228, 267, 311, and 688 cm^{-1} having higher and that at 676 cm^{-1} reduced relative intensities. The polarized Raman spectra in the O–H stretching region are more characteristic of each investigated tourmaline (Fig. 5.3). In particular, bands at 3769 and 3817

Table 5.5: Selected interatomic distances in K-dravite (EB13), oxy-uvite (CN11), and magnesio-foitite (MF2) determined by SREF

Cation site	Anion site	Bond length (Å)		
		K-dravite (EB13)	Oxy-uvite (CN11)	Magnesio-foitite (MF2)
X	O2 \times 3	2.628(13)	2.5224(9)	Vacant
	O5 \times 3	2.752(10)	2.6774(8)	
	O4 \times 3	2.830(12)	2.7679(8)	
	Mean	2.737(12)	2.656(1)	—
Y	O2 \times 2	1.983(9)	1.9991(6)	1.9509(7)
	O6 \times 2	1.993(8)	1.9698(5)	1.9827(7)
	W (O1)	2.018(13)	1.9647(7)	2.0293(10)
	V (O3)	2.085(14)	2.0923(9)	2.0559(12)
	Mean	2.009(11)	1.999(1)	1.992(1)
Z	O6	1.884(8)	1.9072(5)	1.8838(7)
	O8	1.897(8)	1.9001(5)	1.8881(7)
	O7	1.907(8)	1.9072(5)	1.8898(7)
	O8'	1.942(9)	1.9236(5)	1.9165(7)
	O7'	1.957(8)	1.9570(5)	1.9418(7)
	V (O3)	1.997(7)	1.9951(4)	2.0001(5)
	Mean	1.931(8)	1.932(1)	1.920(1)
T	O7	1.594(7)	1.5995(5)	1.6063(6)
	O6	1.597(7)	1.6033(6)	1.6102(8)
	O4	1.625(5)	1.6271(3)	1.6159(4)
	O5	1.643(6)	1.6445(3)	1.6320(5)
	Mean	1.615(6)	1.619(1)	1.616(1)
B	O2	1.36(2)	1.3810(11)	1.3668(17)
	O8 \times 2	1.38(1)	1.3726(6)	1.3804(10)
	Mean	1.37(2)	1.375(1)	1.376(1)

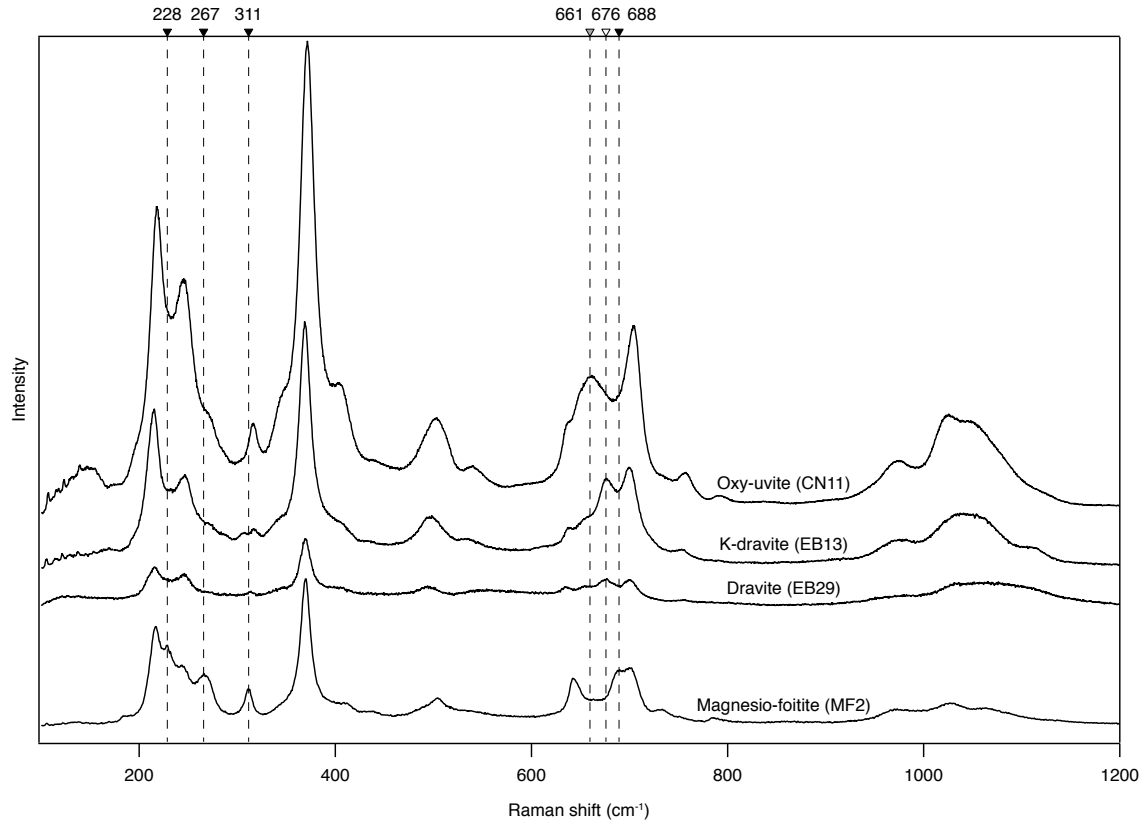


Figure 5.2: Polarized lattice-vibration Raman spectra for synthetic oxy-uvite (CN11), K-dravite (EB13), dravite (EB29), and magnesio-foitite (MF2). All spectra were collected with the electrical field vector of the linearly polarized laser light parallel to the crystallographic c -axis. The *inverted triangles* indicate the wavenumber of deviations between the spectra, whereby *black symbols* indicate a band more pronounced in magnesio-foitite; the *white symbol* indicates a band more pronounced in dravite and K-dravite; and the *grey symbol* indicates a band more pronounced in oxy-uvite.

cm^{-1} are unique to K-dravite (EB13); bands at 3723, 3739–3740, and 3776–3778 cm^{-1} are unique to dravite; and the band at 3459 cm^{-1} is unique to magnesio-foitite (MF2) (Fig. 5.3, Tables 5.6, 5.7). All bands in the polarized Raman O–H stretching spectrum of oxy-uvite can be identified in the spectra of the other tourmalines.

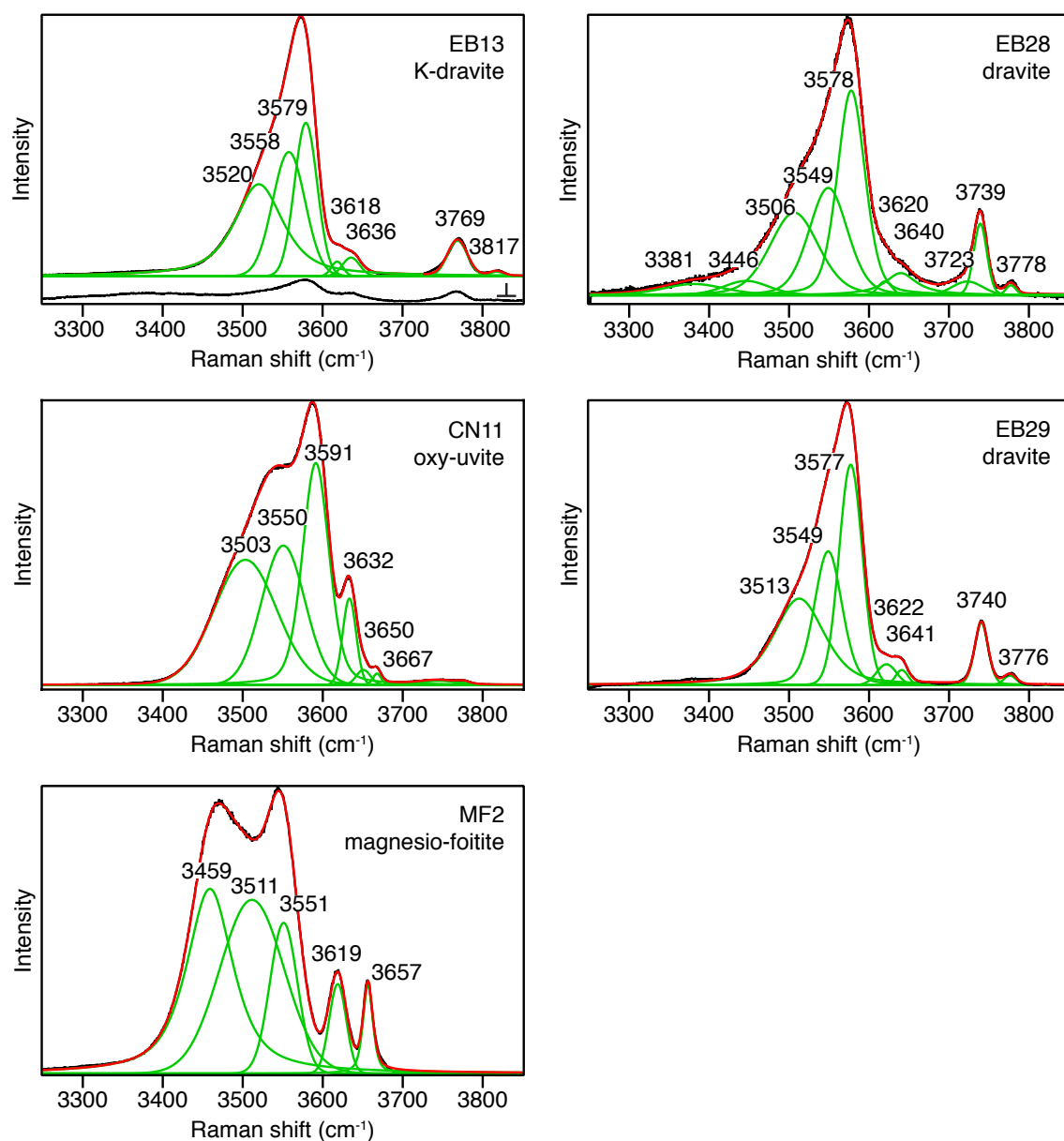


Figure 5.3: Polarized Raman spectra in the O–H stretching vibration range for synthetic K-dravite, dravite, magnesio-foitite, and oxy-uvite. The baseline-corrected spectra (*black*) were collected with the electrical field vector of the linearly polarized laser light parallel to the crystallographic *c*-axis, except for the second spectrum of K-dravite (EB13 marked with \perp), which was collected with the electrical field vector of the laser light polarized perpendicular to the crystallographic *c*-axis. The intensity scales for both EB13 spectra are identical. The spectra have been deconvoluted (*red*) with the PeakFit program to identify the underlying bands (*green*).

Table 5.6: Band assignments and Y- and Z-site compositions calculated from the relative integrated peak intensities of the bands in the O–H stretching Raman spectra of K-dravite, dravite, and oxy-uvite

OH	Band (cm ⁻¹)	Assign.	Mg/ occ.	Al/ occ.	K-dravite (EB13)			Dravite (EB28)			Dravite (EB29)			Oxy-uvite (CN11)		
					Area	Mg	Al	Area	Mg	Al	Area	Mg	Al	Area	Mg	Al
W (O1)	3817	^X K ^Y Mg ₃	3	0	5 %	0.15	0									
	3776–3778	^X Na ^Y Mg ₃	3	0				4 %	0.11	0	7 %	0.22	0			
	3769	^X K ^Y Mg ₂ Al	2	1	56 %	1.13	0.56									
	3739–3740	^X Na ^Y Mg ₂ Al	2	1				36 %	0.72	0.36	56 %	1.12	0.56			
	3723	^X Na ^Y MgAl ₂	1	2				15 %	0.15	0.30						
	3657–3667	^X □ ^Y Mg ₃	3	0										7 %	0.21	0
	3636–3650	^X □ ^Y Mg ₂ Al	2	1	25 %	0.51	0.25	38 %	0.76	0.38	12 %	0.23	0.11	14 %	0.29	0.14
	3618–3632	^X □ ^Y MgAl ₂	1	2	14 %	0.14	0.27	7 %	0.07	0.14	25 %	0.25	0.50	79 %	0.79	1.57
					ΣY	1.9	1.1	ΣY	1.8	1.2	ΣY	1.8	1.2	ΣY	1.3	1.7
														SREF	1.5	1.5
V (O3)	3577–3591	^{YZ} Mg ₂ Al	2	1	26 %	1.54	0.77	37 %	2.24	1.12	36 %	2.13	1.06	32 %	1.94	0.97
	3549–3558	^{YZ} MgAl ₂	1	2	30 %	0.89	1.79	27 %	0.81	1.62	28 %	0.84	1.69	29 %	0.87	1.75
	3503–3520	^{YZ} Al ₃	0	3	44 %	0	4.01	36 % ^a	0	3.21	36 %	0	3.28	39 %	0	3.48
					ΣYZ	2.4	6.6	ΣYZ	3.1	5.9	ΣYZ	3.0	6.0	ΣYZ	2.8	6.2
					EMPA	2.6	6.3	EMPA	2.4	6.4	EMPA	2.5	6.3	EMPA	2.6	6.5
														SREF	2.6	6.4
					Z	0.5	5.5	Z	1.6	4.4	Z	1.2	4.8	Z	1.5	4.5
														SREF	1.1	4.9

Compositions determined by EMPA and SREF (CN11) are given for comparison.

The Z-site composition is calculated by subtracting the ΣY value from the corresponding ΣYZ value.

^aThe relative area of the band assigned to ^{YZ}Al₃ in EB28 includes the integrated peak intensity of the broad bands at 3381 and 3446 cm⁻¹, which were also assigned to a coordination environment of ^{YZ}Al₃, but are unique to EB28 (Fig. 5.3).

Table 5.7: Band assignments and X-site compositions calculated from the relative integrated peak intensities of the O–H stretching bands in the Raman spectra of K-dravite and dravite

OH	Band (cm ⁻¹)	Assign.	K/ occ.	□/ occ.	Na/ occ.	K-dravite (EB13)			Dravite (EB28)			Dravite (EB29)		
						Area	K	□	Area	Na	□	Area	Na	□
W (O1)	3817	^X K ^Y Mg ₃	1	0	0	5 %	0.05	0						
	3776–3778	^X Na ^Y Mg ₃	0	0	1				4 %	0.04	0	7 %	0.07	0
	3769	^X K ^Y Mg ₂ Al	1	0	0	56 %	0.56	0						
	3739–3740	^X Na ^Y Mg ₂ Al	0	0	1				36 %	0.36	0	56 %	0.56	0
	3723	^X Na ^Y MgAl ₂	0	0	1				15 %	0.15	0			
	3657–3667	^X □ ^Y Mg ₃	0	1	0									
	3636–3650	^X □ ^Y Mg ₂ Al	0	1	0	25 %	0	0.25	38 %	0	0.38	12 %	0	0.12
	3618–3632	^X □ ^Y MgAl ₂	0	1	0	14 %	0	0.14	7 %	0	0.07	25 %	0	0.25
						ΣX	0.6	0.4	ΣX	0.6	0.4	ΣX	0.6	0.4
						EMPA	0.7	0.3	EMPA	0.8	0.2	EMPA	0.6	0.3

Compositions determined by EMPA are given for comparison.

Oxy-uvite is absent in this table due to the lack of W (O1) bands assigned to Ca at the X site.

5.3 Discussion

5.3.1 Single-crystal XRD refinement (SREF)

K-dravite (EB13)

Comparison of the interatomic distances obtained from the SREF of synthetic K-dravite (EB13; Table 5.5) to those obtained for naturally occurring Na- and Ca-bearing tourmalines reveals significant expansion of the X-site polyhedron in accommodating the relatively large K ion. For example, whereas the average $\langle X-O \rangle$ distance determined for the synthesized K-dravite (EB13) was 2.737(12) Å, the largest $\langle X-O \rangle$ distance measured by Bloodaxe *et al.* (1999) was 2.696(5) Å, corresponding to dravitic tourmaline with an average X-site occupancy of 0.540(52) Na, 0.027(2) Ca, and 0.025(31) K pfu. The average $\langle Y-O \rangle$ bond length of 2.009(11) Å obtained for synthetic K-dravite (EB13) is relatively small compared to tourmaline with a Y site dominated by Mg (*cf.* 2.044 Å; Pertlik *et al.*, 2003). This suggests that the smaller Y-site-occupying ion Al (*cf.* atomic radius of 0.535 Å for ^{VI}Al with 0.72 Å for ^{VI}Mg ; Shannon, 1976) is present, reducing the size of the Y-site coordination polyhedron. Moreover, comparison of the average $\langle Z-O \rangle$ bond length of synthetic K-dravite (1.931(8) Å) with values obtained for Mg- and Al-bearing tourmalines investigated by Bloodaxe *et al.* (1999) suggests the Z site is occupied by $\sim Al_5Mg$. Increasing amounts of Mg at the Z site would result in increasing $\langle Z-O \rangle$ bond lengths (Bloodaxe *et al.*, 1999). Based on the measured $\langle Y-O \rangle$ and $\langle Z-O \rangle$ bond lengths, we expect significant Mg–Al disorder between the Y and Z sites in the synthetic K-dravite. The average $\langle T-O \rangle$ bond length of 1.615(6) Å is slightly smaller than, albeit within error of the bond length expected for a T site fully occupied by Si (~ 1.62 Å; MacDonald and Hawthorne, 1995). Nevertheless, based on electron densities in the tourmaline structure, the single-crystal structure refinement suggests the presence of 0.6(1) tetrahedral B pfu, a value 3σ greater than that determined by EMPA. The occurrence of tetrahedral B is not uncommon for tourmalines crystallized at high temperature and pressure (Ertl *et al.*, 2008, 2010); however, the $\langle T-O \rangle$ bond length and EMPA data suggest it is minor. Comparison of the position of H3 [$x = 0.246(9)$] and O3 [$x = 0.2628(9)$] in the atom parameters (Table 5.4) shows that the H3 atom is not perfectly in line with O3. It is slightly shifted toward the tetrahedral site, as expected from the presence of its hydrogen bond with O5 (Fig. 1.2).

Oxy-uvite (CN11)

In the structure of the ideal, ordered oxy-uvite endmember $[^XCa^Y Mg_3^Z Al_6^T Si_6 O_{18} (BO_3)_3 V(OH)_3^W O]$, Mg is found at the octahedral Y site and Al at the octahedral Z site. The synthesized oxy-uvite (CN11) has a lower Mg/Al ratio than the endmember (Table 5.2), indicating that some Al must occur at the Y site. In addition, the SREF revealed that in the investigated crystal, not all the Mg is restricted to the Y site. Instead, there is Mg–Al disorder between the two octahedral sites, which results in an average of 1.52(10) Mg and 1.48(10) Al pfu occurring at the Y site and 1.10(15) Mg and 4.90(15) Al pfu at the Z site (Table 5.4). The average $\langle T-O \rangle$ bond length of 1.619(1) Å is in agreement with a T site fully occupied by Si (MacDonald and Hawthorne, 1995), as determined by EMPA. The absence of tetrahedral B is expected from the low synthesis pressure of 0.2 GPa. Compared to K-dravite (EB13; Table 5.4), the O3–H3 bond in oxy-uvite (CN11) is slightly more parallel to the *c*-axis [$x = 0.26024(6)$ for O3 and $x = 0.257(2)$ for H3]. This suggests that H bonding between H3 and O5 is less pronounced in oxy-uvite than in K-dravite.

Magnesio-foitite (MF2)

In the structure of the ideal, ordered magnesio-foitite endmember $[\text{X}\square^{\text{Y}}(\text{Mg}_2\text{Al})^{\text{Z}}\text{Al}_6^{\text{T}}\text{Si}_6\text{O}_{18}(\text{BO}_3)_3^{\text{V}}(\text{OH})_3^{\text{W}}(\text{OH})]$, Mg is found at the octahedral Y site. Although the synthetic magnesio-foitite (MF2) has approximately endmember stoichiometry with ~ 2 Mg and 7 Al as determined by EMPA (Table 5.2), the SREF revealed that in the investigated crystal, an average of 1.38(18) Mg and 1.62(18) Al pfu occurs at the Y site and 1.08(24) Mg and 4.92(24) Al pfu at the Z site (Table 5.4). The presence of minor Na refined at the X site [$\sim 0.09(6)$ apfu; Table 5.4] likely reflects Na contamination in the synthesis procedure. This emphasizes the high preference of Na for tourmaline over the coexisting fluid, as even traces of Na in the fluid are incorporated into the crystallizing tourmaline. Small amounts of Na [0.01(2) apfu] were also detected by EMPA in the nominally Na-free magnesio-foitite crystals. The low occupancy of the X site in MF2 produced an erroneous z coordinate in its structure refinement (Table 5.2). Removal of the X site from the SREF did not significantly affect the coordinates of the other refined sites (see Appendix A). The average $\langle \text{T}-\text{O} \rangle$ bond length of 1.616(1) Å is comparable to that of synthetic K-dravite (EB13, Table 5.5), but the amount of B refined at the T site based on electron densities is less [*cf.* 0.34(4) $^{\text{IV}}\text{B}$ in MF2 with 0.6(1) $^{\text{IV}}\text{B}$ in EB13], as expected from the lower synthesis pressure of 0.4 GPa (*cf.* 4.0 GPa for EB13; Table 4.1). The low amount of tetrahedral B refined for magnesio-foitite (MF2) is in agreement with the results of EMPA (Table 5.2) to a higher degree than for K-dravite (EB13), likely due to the higher quality of the former's SREF (*cf.* $R_1 = 1.19\%$ for MF2 and 4.88% for EB13).

Compared to K-dravite (EB13) and oxy-uvite (CN11; Table 5.4), the O3–H3 bond in magnesio-foitite (MF2) is the most parallel to the c -axis [$x = 0.26152(8)$ for O3 and $x = 0.262(2)$ for H3]. This suggests that H bonding between H3 and O5 is least pronounced in magnesio-foitite (MF2).

5.3.2 Polarized Raman spectroscopy

Lattice-vibration Raman spectra

In the lattice-vibration Raman spectra, bands in the 200–300 cm^{-1} wavenumber range have been previously assigned to vibrations at the Y site (*e.g.*, Gasharova *et al.*, 1997). The increased intensity of the bands around 228 and 267 cm^{-1} in magnesio-foitite (MF2) compared to dravite (EB29), K-dravite (EB13), and oxy-uvite (CN11) may reflect the higher occupancy of the Y site by Al (Fig. 5.2). This is consistent with the lattice-vibration Raman spectrum of synthetic olenite $[\text{XNa}^{\text{Y}}\text{Al}_3^{\text{Z}}\text{Al}_6^{\text{T}}(\text{Si}_6\text{O}_{18})(\text{BO}_3)_3\text{O}_3(\text{OH})]$, which also has distinct bands around 228 and 267 cm^{-1} (Martin Kutzschbach, *personal communication*). Although the sharp band at 311 cm^{-1} in the spectrum of magnesio-foitite has not been previously assigned, its increased intensity for magnesio-foitite (as well as for synthetic olenite) compared to dravite and K-dravite may also reflect its association with Al at the Y site. The bands between 600 and 800 cm^{-1} have been associated with Si–O vibrations in the Si_6O_{18} ring and are affected by substitutions at the neighbouring Y and Z sites (Mihailova *et al.*, 1996; Bosi and Lucchesi, 2007; Fantini *et al.*, 2014). Although the position and intensities of these bands are similar for K-dravite and dravite, they are distinct in the lattice-vibration Raman spectra of magnesio-foitite (MF2) and oxy-uvite (CN11) (Fig. 5.2). The different shape of these bands in the spectrum of magnesio-foitite (MF2) likely reflects the effect of the vacant X site on the Si_6O_{18} ring. In the case of oxy-uvite, the different shape likely results from the increased charge of Ca as an X-site-occupying ion, or less likely, the effect of a deprotonated W (O1) site on the Si_6O_{18} ring structure. Together, the variations in the lattice vibrations of MF2, and to a lesser extent CN11,

show distinct differences in the structure of magnesio-foitite and oxy-uvite compared to K-dravite and dravite. In contrast, the lattice-vibration Raman spectra of K-dravite and dravite are comparable, with no clear variations in major band positions or relative intensities. This observation suggests that substituting K for Na at dravite's X site does not significantly influence the bonding environment around the other sites in the structure.

O–H stretching Raman spectra

The O–H stretching vibrations in the Raman spectra (Fig. 5.3) are more sensitive than the lattice vibrations (Fig. 5.2) to compositional variations in tourmaline. With the exception of magnesio-foitite, if the synthesized tourmaline crystals had their exact endmember compositions, whereby each site is occupied by a single element, we would expect two symmetrical bands in the O–H stretching region of the Raman spectra: one for each OH-occupied site, W (O1) and V (O3). In the case of magnesio-foitite, its ordered, endmember composition with ${}^Y\text{Mg}_2\text{Al}$ would generate three bands in the O–H stretching region: one for the W (O1) site and two for the V (O3) site, corresponding to the latter's coordination with either ${}^Y\text{Mg}$ or ${}^Y\text{Al}$. Additional bands reflect variations in the local bonding environment around the different hydroxyl groups, with each band representing a different bonding environment. If either of the W (O1) or V (O3) sites is deprotonated [as is the case for W (O1) in oxy-uvite (${}^X\text{Ca}{}^Y\text{Mg}_3{}^Z\text{Al}_6{}^T\text{Si}_6\text{O}_{18}(\text{BO}_3)_3{}^V(\text{OH})_3{}^W\text{O}$)], its associated bands will be absent. The OH bond at the W (O1) site is sensitive to variations in the occupation of the three coordinated Y sites and the nearby X site (Fig. 1.2). The three OH bonds at the V (O3) sites are sensitive to variations in the occupation of the coordinated Z and Y sites. Variation in the occupancy of the T or X sites might also exert an effect on the OH bond at the V (O3) site by means of their coordination with the O5 site, which shares a weak hydrogen bond with the O3 site (Gatta *et al.*, 2012; Fig. 1.2). In general, any variation in the short-range environment around an OH bond that results in the shortening (*i.e.*, strengthening) of the OH bond is expected to result in an increase in its vibrational energy and thus in an increase in its Raman shift. Conversely, variations that result in the lengthening (*i.e.*, weakening) of the OH bond are expected to result in a decrease in its Raman shift. As a result, the position of an OH bond's Raman band is inversely proportional to the charge and electronegativity of the coordinated cations. Band assignments were thus made following the theory that OH bonds coordinated to cations of higher charge and electronegativity will produce bands of lower Raman shifts (Martínez-Alonso *et al.*, 2002).

W (O1) O–H stretching Raman bands

The five investigated tourmalines have between two and five bands assigned to the higher frequency, W (O1) site range (Fig. 5.3; Tables 5.6, 5.7, 5.8). Each of these five bands must reflect a unique bonding environment around the W (O1) site in terms of the occupancy of the X and Y sites. Given the restricted composition of the synthetic tourmalines, the Y sites can only be occupied by Al or Mg and the X site can only be vacant or occupied by K (EB13), Na (EB28 and EB29), or Ca (CN11; Table 5.2). The W (O1) bands at 3769 and 3817 cm^{-1} (Fig. 5.3) are unique to K-dravite (EB13), unambiguously associating these bands with the presence of K at the X site. Similarly, the W (O1) bands at 3723, 3739–3740, and 3776–3778 cm^{-1} are unique to dravite (EB28 and EB29; Fig. 5.3) and are therefore assigned to Na at the X site. The W (O1) bands in the range 3618–3667 cm^{-1} are common to all synthetic tourmaline and are therefore assigned to the presence of vacancies at the X site. The increased intensity of these bands in the spectrum of X-

Table 5.8: Band assignments and Y- and Z-site compositions calculated from the relative integrated peak intensities of the O–H stretching bands in the Raman spectrum of magnesio-foitite

OH	Band (cm ⁻¹)	Assign.	Mg/ occ.	Al/ occ.	Magnesio-foitite (MF2)		
					Area	Mg	Al
W (O1)	3817	^X K ^Y Mg ₃	3	0			
	3776–3778	^X Na ^Y Mg ₃	3	0			
	3769	^X K ^Y Mg ₂ Al	2	1			
	3739–3740	^X Na ^Y Mg ₂ Al	2	1			
	3723	^X Na ^Y MgAl ₂	1	2			
	3657–3667	^X □ ^Y Mg ₃	3	0	42 %	1.27	0
	3636–3650	^X □ ^Y Mg ₂ Al	2	1			
	3618–3632	^X □ ^Y MgAl ₂	1	2	58 %	0.58	1.16
					ΣY	1.8	1.2
					SREF	1.4	1.6
V (O3)	3551	^Y ZMg ₂ Al	2	1	15 %	0.93	0.46
	3511	^Y ZMgAl ₂	1	2	42 %	1.25	2.49
	3459	^Y ZAl ₃	0	3	43 %	0	3.87
					ΣYZ	2.2	6.8
					EMPA	1.9	7.1
					SREF	2.5	6.5
					Z	0.4	5.6
					SREF	1.1	4.9

The compositions determined by EMPA and SREF are given for comparison.

The V (O3) band assignments given here are unique to magnesio-foitite. In contrast, the W (O1) band assignments are shared by the other investigated tourmalines. The Z-site composition is calculated by subtracting the ΣY value from the corresponding ΣYZ value.

vacant magnesio-foitite (MF2) supports this assignment. There are no bands assigned to Ca at the X site because the W (O1) site in oxy-uvite is deprotonated and therefore does not produce a corresponding band in the O–H stretching range of the Raman spectrum. However, W (O1) bands corresponding to a vacant X site (3618–3667 cm⁻¹) are present (CN11; Fig. 5.3), indicating that the W (O1) site in oxy-uvite is locally protonated in the presence of a vacant X site.

The presence of multiple W (O1) bands associated with each X site composition reflects variations in the amount of Mg and Al at the Y sites coordinated to the W (O1) site. In the structural formulae for the ideal, ordered endmembers of dravite and K-dravite, the Y site is occupied entirely by Mg. However, based on the SREF of EB13, we expect significant Mg-Al disorder between the Y and Z sites resulting in the presence of significant Al at the Y site. We therefore assign the three bands associated with a K- or Na-occupied X site (Tables 5.6, 5.7; EB13, EB28, and EB29) to a coordination environment of ^YMg^YMg^YMg, ^YMg^YMg^YAl, and ^YMg^YAl^YAl, with decreasing wavenumbers, respectively.

Considering the Raman spectra of all investigated tourmalines (Fig. 5.3), there are a total of three W (O1) bands ($>3600\text{ cm}^{-1}$) assigned to vacancies at the X site: $3618\text{--}3632$, $3636\text{--}3650$, and $3657\text{--}3667\text{ cm}^{-1}$. As in the case of the X-occupied bands, assignments were made with the proportion of Al (and therefore charge) increasing with decreasing Raman shift (Tables 5.6, 5.7, 5.8). In the Raman spectrum of magnesio-foitite (MF2), the band assigned to ${}^X\Box{}^Y\text{Mg}^Y\text{Mg}^Y\text{Al}$ is absent ($3636\text{--}3650\text{ cm}^{-1}$; Table 5.8; Fig. 5.3), and only the two Y-site configurations ${}^X\Box{}^Y\text{Mg}^Y\text{Mg}^Y\text{Mg}$ and ${}^X\Box{}^Y\text{Mg}^Y\text{Al}^Y\text{Al}$ are present. The absence of the $3636\text{--}3650\text{ cm}^{-1}$ band in the spectrum of magnesio-foitite has been observed in previous investigations of synthetic magnesio-foitite (Veličkov, 2002) and therefore seems to be characteristic of the magnesio-foitite endmember. Our Raman band assignments suggest that the Y-site composition of the synthetic magnesio-foitite ($\sim{}^Y\text{Mg}_{1.4}\text{Al}_{1.6}$; Table 5.4) as determined by SREF reflects a combination of ${}^Y\text{Mg}_3$ and ${}^Y\text{MgAl}_2$ Y-site trimers, in an approximately 2:3 proportion (Table 5.8). This implies a long-range ordering of Mg and Al at the Y sites for magnesio-foitite. This is not the case for the X-vacant components in the synthesized K-dravite (EB13) and dravite (EB28, and EB29) samples, none of which has a band assigned to the configuration ${}^X\Box{}^Y\text{Mg}^Y\text{Mg}^Y\text{Mg}$. From bond valence arguments, vacancies at the X site in these tourmalines are expected to be associated with Al at the Y site, with additional Al possibly resulting from Mg–Al disorder between the Y and Z sites. Therefore, it is reasonable that the band assigned to ${}^X\Box{}^Y\text{Mg}^Y\text{Mg}^Y\text{Mg}$ is absent from the synthetic K-dravite and dravite. In the case of oxy-uvite (CN11), all three X-vacant bands are observed in the O–H stretching Raman spectrum, with that at $3618\text{--}3632\text{ cm}^{-1}$ having the highest intensity. This high intensity band is assigned to ${}^X\Box{}^Y\text{Mg}^Y\text{Al}^Y\text{Al}$. In the SREF of CN11, a Y-site occupancy of 1.5 Al and 1.5 Mg was refined, indicating a significant degree of Mg–Al disorder between the Y and Z sites. This disorder, which puts additional Al at the Y site, combined with the preferential occurrence of Al at the Y site in the presence of a vacant X site justifies the configuration ${}^X\Box{}^Y\text{Mg}^Y\text{Al}^Y\text{Al}$ as the highest intensity W (O1) band for oxy-uvite.

V (O3) O–H stretching Raman bands

The Raman spectrum of each tourmaline crystal has three bands fitted beneath the broad V (O3) band ($3400\text{--}3600\text{ cm}^{-1}$; Fig. 5.3). The positions of the fitted bands in the spectra of dravite, K-dravite, and oxy-uvite (EB28, EB29, EB13, and CN11) are in good agreement with each other, and also with the Raman spectra of dravite and uvite from natural rocks (*e.g.*, Fantini *et al.*, 2014). In contrast, the V (O3) bands in the spectrum of magnesio-foitite (MF2) are all shifted to lower wavenumbers. For this reason, the assignments of the V (O3) bands in the latter are performed separately and subsequently compared to the other tourmalines. The positions of the V (O3) bands are principally influenced by their respective coordinating environment: one Y-site octahedron and two Z-site octahedra (Fig. 1.2). In the ideal, ordered endmembers of K-dravite, dravite, and oxy-uvite, the Z site is fully occupied by Al and the Y site by Mg (${}^Y\text{Mg}^Z\text{Al}^Z\text{Al}$). Al–Mg disorder between the Z and Y sites results in additional Mg occurring at the Z site (${}^Y\text{Mg}^Z\text{Mg}^Z\text{Al}$) and additional Al occurring at the Y site (${}^Y\text{Al}^Z\text{Al}^Z\text{Al}$). These three coordination environments were assigned to the three fitted V (O3) bands in the O–H stretching Raman spectra of K-dravite (EB13), dravite (EB28 and EB29), and oxy-uvite (CN11) with Mg content increasing with the band’s wavenumber (Table 5.6). The assignment of the $3549\text{--}3558\text{ cm}^{-1}$ band to ${}^Y\text{Mg}^Z\text{Al}^Z\text{Al}$ is consistent with the results of Bosi *et al.* (2015). The same coordination environments were assigned in the same order to the three V (O3) bands fitted in the spectrum of magnesio-foitite (MF2).

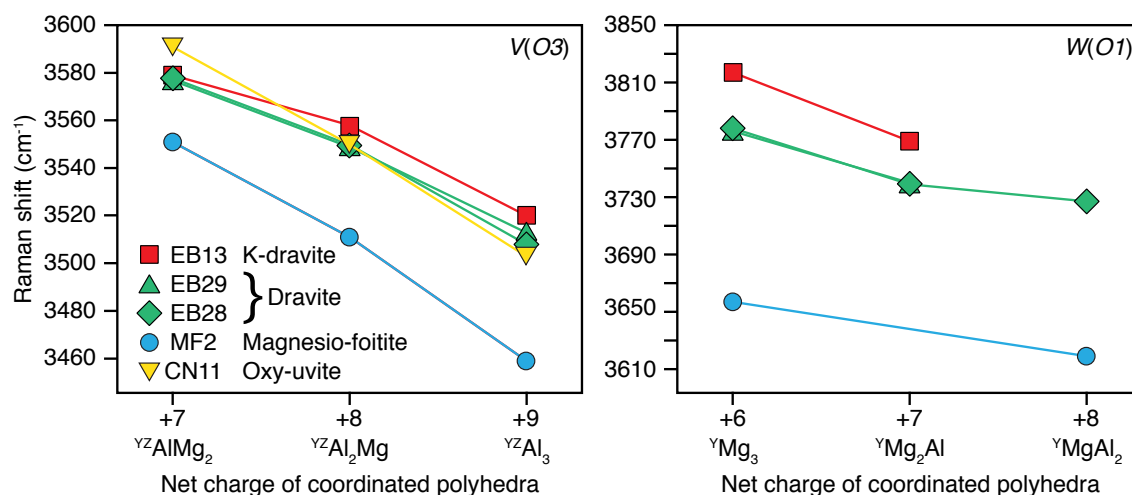


Figure 5.4: Raman shift of O–H stretching bands plotted against the net charge of the coordinated polyhedra (${}^Y{}_Z\text{AlMg}_2$, ${}^Y{}_Z\text{Al}_2\text{Mg}$, and ${}^Y{}_Z\text{Al}_3$; or ${}^Y\text{Mg}_3$, ${}^Y\text{Mg}_2\text{Al}$, and ${}^Y\text{MgAl}_2$). Only data points associated with the endmember X-site composition are shown for the W (O1) bands (*i.e.*, ${}^X\text{K}$ for K-dravite, ${}^X\text{Na}$ for dravite, ${}^X\Box$ for magnesio-foitite). As no O1 bands in the Raman spectrum of oxy-uvite were assigned to ${}^X\text{Ca}$, data points for oxy-uvite in the W (O1) plot are not available.

Controls on O–H stretching Raman band position

Band assignments for each hydroxyl site were consistently based on the principle that the Raman shift of a particular band should be inversely proportional to the net charge of the coordinated polyhedra. Comparison of the band position to the assigned coordination environment provides additional insight into this correlation. The Raman shift of the V (O3) O–H stretching vibration is more sensitive to the net charge (or electronegativity) of the coordinated polyhedra than those assigned to the W (O1) site, as reflected by the steeper slope of the V (O3) curve in Fig. 5.4. For both sites, increasing the charge/electronegativity of the coordination environment results in a consistent shift in the position of the Raman band regardless of the occupancy of the X site, as reflected in the curves of each endmember for the W (O1) and V (O3) bands in Fig. 5.4 being approximately parallel. It is therefore reasonable that substitution of elements of different charge/electronegativity at the Y and Z sites will produce bands at positions consistent with the observed trend for each endmember. This will in turn facilitate band assignments in tourmalines with complex chemistries, more typical of naturally occurring tourmalines.

The overall shift of the V (O3) bands in the spectrum of magnesio-foitite (MF2) to lower wavenumbers reflects the lengthening (weakening) of the OH bond at this site (Fig. 5.4). This is likely a further indication of the deformation of the Si_6O_{18} ring in the presence of a vacant X site. The V (O3) OH bond is affected by the Si_6O_{18} ring via the hydrogen bond between H3 and the O5 site (Fig. 1.2). The shift of the V (O3) bands to lower wavenumbers was also observed for synthetic magnesio-foitite and foitite investigated by Veličkov (2002). In contrast, the overall lengthening of the V (O3) OH bonds was not observed in the Raman spectrum of the naturally occurring magnesio-foitite investigated by Fantini *et al.* (2014), which has an average X-site composition of ${}^X\Box_{0.56}\text{Na}_{0.31}\text{Ca}_{0.13}$. The significant amount of Na at the X site of the natural magnesio-foitite is sufficient to make the Raman spectra in the lattice and O–H stretching range more comparable to those of synthetic dravite.

Calculating tourmaline compositions from their O–H stretching Raman spectra

For a group of bands assigned to a particular hydroxyl-bearing site (V or W), the integrated peak intensity under a given band is proportional to the occurrence of the local bonding environment assigned to it. For example, the integrated peak intensity under the band assigned to ${}^X\text{K}^Y\text{Mg}_2\text{Al}$ (Fig. 5.3, Tables 5.6, 5.7) is the highest of all bands assigned to the W (O1) site in EB13. We therefore expect this to be the most common coordination environment for hydroxyl-occupied W (O1) sites in EB13. Furthermore, the relative integrated peak intensity can be linked to the proportion of its assigned compositional environment within the structure. Since the Mg and Al are the only two elements present at the Y and Z sites, their relative amounts in each tourmaline can thus be calculated from the relative integrated peak intensities. In addition, dravite and K-dravite have vacancies and either Na or K at their X sites, respectively. The ratio of the two possible X-site compositions can be calculated from the ratio of the integrated peak intensities. Following this reasoning, the compositions of the X, Y, and Z sites were calculated from the O–H stretching region of the Raman spectra for each tourmaline (Tables 5.6, 5.7). Since oxy-uvite does not have W (O1) bands assigned to an X site occupied by Ca, the X-site composition cannot be calculated. However, the relative integrated peak intensities of the W (O1) bands assigned to vacancies at the X site are sufficient to calculate the Y site composition. This approach assumes that the X-site composition has no bearing on the local Y-site composition, an assumption that is unlikely true. Instead, because of local charge balance of the vacant X site, we expect the calculated Y-site composition to have increased Al relative to the true value. A comparison of the calculated values to those determined by SREF indicates this to be the case (Table 5.6). The V (O3) bands of oxy-uvite are unaffected by this bias and can be used to calculate the net Y and Z site composition following the same procedure as for the other tourmalines. The good agreement between the calculated Mg–Al ratios and those measured by EMP or refined by SREF (Tables 5.6, 5.8) supports the Raman band assignments. It should be noted that partially deprotonated V (O3) or W (O1) sites will not contribute a signal to the Raman spectrum and will therefore not contribute to the calculated compositions, introducing error into the calculation of all investigated tourmalines.

5.3.3 Influence of X-site composition on crystal structure

The composition of the X site affects tourmaline's long-range crystal structure. This is reflected in the expansion of the unit-cell volume from $1560 \pm 3 \text{ \AA}^3$ for tourmaline with a vacant X site to $1570 \pm 1 \text{ \AA}^3$ or $1573 \pm 1 \text{ \AA}^3$ with the intermediate in size Na or Ca ions, respectively, to $1590 \pm 2 \text{ \AA}^3$ with the large K ion (averages of powder and single-crystal unit-cell parameter determinations; Table 5.3). The gradual increase in unit-cell volume is mainly accounted for by changes in the length of the *c*-axis (Table 5.3) and is expected to increase with increasing K content (see Chapter 4). Tourmaline's extension, or contraction, parallel to its *c*-axis in response to the size of the X-site-occupying ion reflects tourmaline's increased elasticity in this direction (Dietrich 1985, and references therein).

Even though tourmaline's crystal structure expands with increasing size of the X-site-occupying ion, the Raman spectra show minimal changes in the lattice vibrations of oxy-uvite, dravite, and K-dravite. In particular, the lattice vibration Raman spectrum of K-dravite is very similar to that of dravite (Fig. 5.2), suggesting that the overall structure is not strongly influenced by changing the size of the X-site-occupying ion. The differences observed in the spectra of magnesio-foitite (MF2) and oxy-uvite (CN11; Fig. 5.2) likely

reflect the different charge of the X site, rather than the ion size. Nonetheless, comparison of the average bond lengths of tourmaline with the largest unit cell, K-dravite, and that with the smallest, magnesio-foitite, reveals that the Y and Z sites are only slightly expanded in the former, with the T site remaining unchanged (Table 5.5).

Changes in tourmaline's structure with changing X-site composition appear to be localized around the X-site polyhedron. This is demonstrated by the large shifts in the band positions assigned to O–H stretching at the W (O1) site in the Raman spectra of K-dravite, dravite, and magnesio-foitite. The Raman shifts of the W (O1) bands assigned to the K-occupied X site in K-dravite are overall of higher value than those assigned to the Na-occupied X site in dravite (Fig. 5.4). The OH bond at the W (O1) site is oriented toward the X site (Fig. 1.2), and the value of the Raman shift is proportional to the energy of the OH bond. The overall increase in the Raman shift of the bands from dravite to K-dravite therefore reflects an increase in the energy of the O–H vibration at the W (O1) site. This strengthening likely results from the larger K ion repelling the H1 ion away from X site toward O1, thereby decreasing the O1–H1 bond length and increasing its bond strength. In oxy-uvite, the 2+ charge of Ca at the X site locally results in the deprotonation of the neighbouring W (O1) site. In contrast, given a vacant X site, the neighbouring W (O1) site is not deprotonated. This is reflected in the O–H stretching Raman spectrum of oxy-uvite (Fig. 5.3) by the presence of W (O1) bands assigned to vacancies at the X site but not those assigned to Ca (Table 5.6). In all the investigated tourmalines, the W (O1) bands assigned to vacancies at the X site occur at wavenumbers lower than those assigned to K and Na at the X site (Table 5.6, magnesio-foitite in Fig. 5.4). In addition, they are at a wavenumber lower than expected for an isolated OH group (3735 cm^{-1} ; Branscomb (1966)). This indicates that in the presence of a vacant X site, the OH bond at the W (O1) site is lengthened relative to an isolated hydroxyl molecule, reducing its energy.

The presence of a mostly vacant X site, as in magnesio-foitite, affects more than the neighbouring W (O1) site. The Si_6O_{18} ring structure changes shape as reflected by changes in its assigned bands in the lattice-vibration Raman spectra. In turn, the hydrogen bond between H at the O3 site and O5 in the Si_6O_{18} ring (Fig. 1.2) is weakened, leading to its increased alignment with tourmaline's *c*-axis. The O3–H3 bond is lengthened and its associated O–H stretching bands shifted to lower wavenumbers. The 2+ charge of Ca also leads to changes in the Si_6O_{18} ring and, correspondingly, a reduction in the H bond between the H3 and O5 sites. However, in oxy-uvite, these changes were of lesser degree than in magnesio-foitite and did not affect the length of the OH bonds at the V (O3) site.

5.4 Conclusions

The combination of long- and short-range structural data collected by SREF and Raman spectroscopy, respectively, allows the effect of the X-site composition on tourmaline's crystal structure to be investigated. In particular, the use of synthetic tourmalines with restricted compositions largely eliminates the ambiguity in refining the occupancy of different sites from their respective scattering power in the SREF and in assigning bands in the Raman spectra to particular coordination environments. As a result, band assignments for K-dravite, dravite, oxy-uvite, and magnesio-foitite were made and used to calculate the Mg–Al ratio of the Y and Z sites of each investigated tourmaline, giving values consistent with the net Mg–Al ratio determined by EMPA and the specific site oc-

cupancies determined by SREF. Moreover, a combination of the data collected by SREF and that by Raman spectroscopy demonstrated that the composition of tourmaline's X site, which leads to the expansion or contraction of the crystal structure, is accommodated locally around the X site. With increasing size of the X-site-occupying ion, the X-site-coordination polyhedron expands, impinging on the hydroxyl at the O1 site leading to its shortening. The other sites in the crystal structure are not measurably affected. Increasing the charge of the X-site-occupying ion from a 1+ to a 2+ ion, as in the case of oxy-uivite, can result in the local deprotonation of the neighbouring W (O1) site. The absence of an X-site-occupying ion, as is the case for the magnesio-foitite endmember or for magnesio-foitite components in the other tourmalines, leads to the lengthening of the H1–O1 bond. In addition, the magnesio-foitite endmember has demonstrable variations in the bonding environment around the other crystallographic sites, leading to distinct differences in its lattice-vibration Raman spectrum. This structural difference also affects the O3–H3 bond, shifting the associated V (O3) Raman bands to lower wavenumbers. However, the band positions of vibrations assigned to the O1–H1 bond were consistent with bands assigned to vacant X sites in the other investigated tourmalines. Combined, SREF and polarized Raman spectroscopy of single crystals are powerful tools for investigating subtle changes in crystal structure and help to elucidate the feedback between structure and composition in tourmaline supergroup minerals.

Chapter 6

P-T-X controls on Ca and Na distribution between Mg-Al tourmaline and fluid

The contents of this chapter have been published in *Contributions to Mineralogy and Petrology*, Volume 171, Article no. 31.

6.1 Introduction and approach

In this chapter, Ca-Na tourmaline-fluid partitioning at 0.2–4.0 GPa, 500–700 °C is investigated using tourmaline-synthesis experiments. The results demonstrate the influence of pressure, temperature, and fluid composition on the relative incorporation of Na, Ca, and vacancies in Fe-free tourmaline. In addition, the findings reported are used to explain the distribution of Ca-rich tourmalines in nature, and allow the Ca/(Ca+Na) ratio of tourmaline's X site to be used to gain insight into the composition and evolution of the metamorphic fluid from which it grew.

Tourmaline was synthesized in the system CaO–Na₂O–B₂O₃–Al₂O₃–MgO–SiO₂–H₂O–Cl in 14 experiments in the temperature and pressure range of 500–700 °C and 0.2–4.0 GPa (Table 6.1; Fig. 6.1). The synthesis experiment CN11 is also described in Chapter 5. Runs at 0.2 GPa (CN9, CN10, and CN11; Table 6.1) were done in a standard cold-seal hydrothermal pressure apparatus and all other experiments were performed in an end-loaded piston-cylinder press. At the end of each experiment, the solid material was characterized by EMP analysis and powder XRD. The product fluid was recovered and its composition analyzed at the end of all experiments. For details on the experimental and analytical methods, see Chapter 2.

Table 6.1: Experimental conditions and reaction products

No.	P (GPa)	T (°C)	Solid (mg)		Fluid volume (μ L)	m CaCl ₂	m NaCl	Duration (days)	Reaction products* (values in parentheses refer to wt.% of phase)
			Oxide mix	SiO ₂					
CN9	0.2	700	39.61	21.19	35	1.00	1.00	15	Tur (99) + Combeite (<1) + Fo (<1)
CN10	0.2	700	40.02	21.82	35	1.50	0.50	15	Tur (97) + Grandidierite (<1) + Werdingerite (1) + Kornerupine (1)
CN11	0.2	700	40.96	21.57	35	2.00	0.00	15	Tur (56) + Qz (26) + Boralsilite (17) + Tlc (<1)
CN13	1.0	500	15.02	-	9	1.00	1.00	33	Tur (85) + Qz (13) + Tlc (2)
CN20	2.5	500	15.17	-	9	1.00	1.00	14	Tur (85) + Qz (15)
CN21	2.5	500	15.80	-	9	1.50	0.50	14	Tur (87) + Qz (13)
CN14	4.0	500	14.89	-	9	1.00	1.00	34	Tur (87) + Coe (13)
CN15	4.0	500	15.09	-	9	1.50	0.50	34	Tur (85) + Coe (15)
CN5	4.0	600	14.81	-	9	1.00	1.00	11	Tur (95) + Coe (5)
CN6	4.0	600	15.10	-	9	1.50	0.50	11	Tur (90) + Coe (10)
CN18	4.0	700	14.99	-	9	0.50	1.50	7	Tur (43) + Coe (57)
CN1	4.0	700	14.94	-	9	1.00	1.00	10	Tur (83) + Coe (17)
CN2	4.0	700	14.56	-	9	1.50	0.50	10	Tur (90) + Coe (9) + Nobleite (1)
CN19	4.0	700	14.88	-	9	2.00	0.00	7	Tur (79) + Coe (21) + Dellaite (<1)

* Mineral abbreviations based on Whitney and Evans (2010).

Other phases: grandidierite [(Mg, Fe)Al₃(BO₃)(SiO₄)O₂], werdingite [(Mg, Fe)₂Al₁₄Si₄B₄O₃₇], kornerupine [(Mg, Fe)₄(Al, Fe)₆(SiO₄, BO₄)₅(O,OH)₂], boralsilite [Al₁₆B₆Si₂O₂₇], combeite [Na₂Ca₂Si₃O₉], nobleite [CaB₆O₉(OH)₂·3H₂O], dellaite [Ca₆Si₃O₁₁(OH)₂]. SiO₂ was included in the oxide mix in experiments without a given SiO₂ (mg) value.

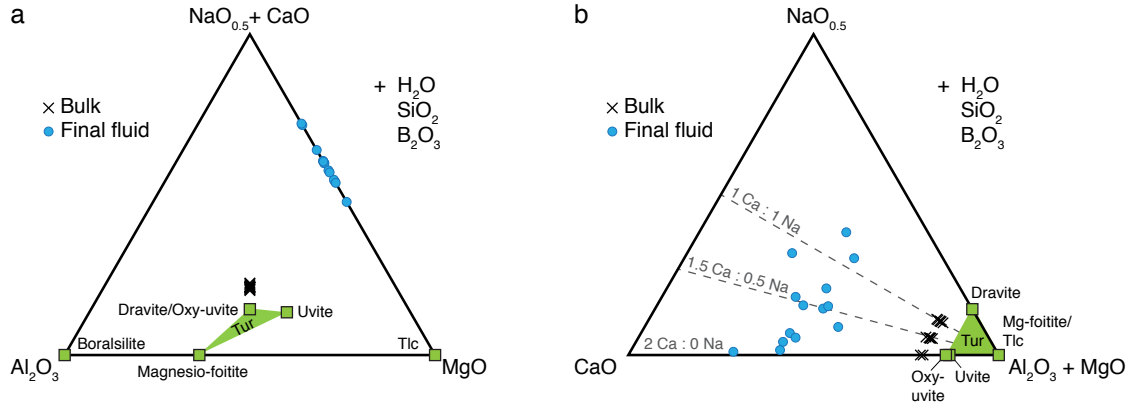


Figure 6.1: Bulk starting compositions (×) plotted in (a) MgO-(NaO_{0.5}+CaO)-Al₂O₃ and (b) (Al₂O₃+MgO)-NaO_{0.5}-CaO ternary space. The compositions of the most prevalent solid products are shown in green and the product fluid in blue.

6.2 Results

Along with tourmaline, the synthesis experiments produced a silica phase (quartz or coesite), and in some cases, additional phases comprising <1 wt.% of the total solid product (Table 6.1). The exception is CN11, the Na-free experiment run at 0.2 GPa, 700 °C, in which 17 wt.% of the solid product was boralsilite (Al₁₆B₆Si₂O₂₇). Tourmalines synthesized in the piston-cylinder press are typically ~5–10 μm in length and <1 μm in width and form radiating crystal aggregates with relatively porous cores (Fig. 6.2). Tourmalines synthesized at 0.2 GPa using the two-chamber method of von Goerne *et al.* (1999) were ~500 μm in length and ~50–100 μm in width, often had inclusions, and were less homogeneous in composition than those synthesized at higher pressure using one-chamber capsules (Fig. 6.2). A significant amount of the inhomogeneity of the crystals results from the presence of minor hourglass sector-zoning, a feature common in natural Ca-bearing tourmaline (*e.g.*, van Hinsberg *et al.*, 2006; van Hinsberg and Schumacher, 2007a). Whereas the distribution of Na in the crystals was relatively homogeneous, Ca partitioned preferentially into the a sector relative to the c⁺ sector with crystal growth in all experiments conducted at 0.2 GPa and 700 °C using the two-chamber method. To investigate the equilibrium distribution of Ca and Na between tourmaline and the product fluid, only rim compositions within the c⁺ sector are considered here. In the case of the smaller crystals synthesized in one-chamber capsules at higher pressures, compositional zoning could not be resolved using the electron microprobe with the 1 μm minimum beam diameter. As a result, in the case of the latter, the entire crystals were considered in equilibrium with the product fluid.

The EMP analyses were normalized to 15 cations at the Y, Z, and T sites (*i.e.*, Mg, Al, and Si), assuming 3 B per formula unit. Tourmaline has been shown to incorporate B in excess of 3 pfu at the tetrahedral T site (Ertl *et al.*, 2008), particularly in Al-rich compositions at high pressure and temperature, but this is ignored here. The proportion of O and OH occupying the anion V and W sites was calculated based on charge balance. The normalized compositions of the synthesized tourmalines are given in Table 6.2.

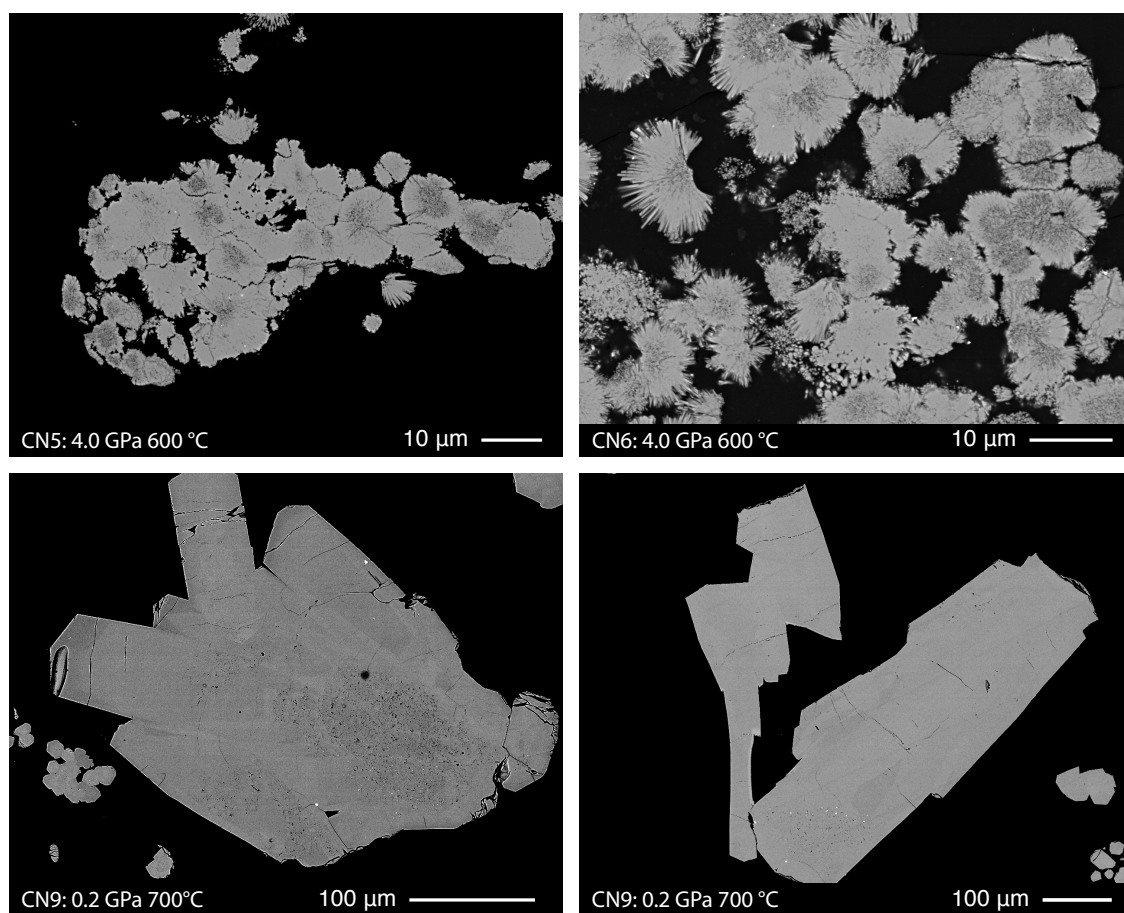


Figure 6.2: Backscattered electron images of tourmaline synthesized at 4.0 GPa, 600 °C [CN5 (*top left*) and CN6 (*top right*)] and 0.2 GPa, 700 °C [CN9 (*bottom*)].

Table 6.2: Composition of synthesized tourmaline rims normalized to 15 YZT and assuming 3 B pfu

wt. %	CN1 GFZ $n = 27$	CN1 MfN $n = 8$	CN2 GFZ $n = 15$	CN2 MfN $n = 7$	CN5 GFZ $n = 13$	CN6 GFZ $n = 18$	CN9 MfN $n = 15$	CN10 MfN $n = 14$
CaO	1.97(37)	1.54(52)	1.89(22)	1.84(13)	1.75(33)	2.10(28)	1.94(52)	2.26(22)
Na ₂ O	1.07(17)	1.07(36)	0.96(20)	0.83(20)	1.23(24)	0.68(19)	0.70(6)	0.28(4)
MgO	9.51(43)	9.22(71)	9.97(42)	9.5(11)	9.72(66)	9.40(39)	10.52(59)	10.41(23)
Al ₂ O ₃	33.4(10)	32.6(13)	33.22(48)	30.7(18)	33.7(11)	33.28(73)	32.94(89)	33.34(43)
SiO ₂	33.71(94)	33.29(82)	35.24(60)	34.77(90)	33.8(11)	34.06(55)	34.74(39)	34.91(41)
Total	79.9(15)	77.8(13)	81.45(64)	77.8(23)	80.31(58)	79.69(82)	80.96(44)	81.32(48)
Ca	0.38(5)	0.29(10)	0.34(4)	0.35(3)	0.32(6)	0.39(5)	0.35(9)	0.40(4)
Na	0.35(6)	0.37(13)	0.31(6)	0.28(6)	0.41(8)	0.23(6)	0.23(2)	0.09(1)
□	0.27(6)	0.34(6)	0.35(4)	0.37(5)	0.27(2)	0.38(6)	0.42(10)	0.50(4)
Mg	2.46(10)	2.41(19)	2.50(9)	2.49(23)	2.47(15)	2.41(10)	2.64(16)	2.60(6)
Al	6.76(19)	6.74(23)	6.58(9)	6.38(23)	6.78(27)	6.74(13)	6.53(15)	6.57(8)
Si	5.78(14)	5.85(12)	5.92(11)	6.14(33)	5.75(15)	5.85(6)	5.84(5)	5.84(5)
B ^a	3.00	3.00	3.00	3.00	3.00	3.00	3.00	3.00
^{VW} OH	3.56(10)	3.62(19)	3.58(16)	3.37(53)	3.66(13)	3.55(12)	3.86(9)	3.86(7)
^{VW} O	0.44(10)	0.38(19)	0.42(16)	0.63(53)	0.34(13)	0.45(12)	0.14(9)	0.14(7)
Ca/(Ca+Na)	0.52(9)	0.44(18)	0.52(9)	0.55(7)	0.44(10)	0.63(12)	0.60(19)	0.82(11)

Continues on next page

Table 6.2: *Continued from previous page*

wt. %	CN11 MfN $n = 15$	CN13 GFZ $n = 12$	CN14 GFZ $n = 14$	CN15 GFZ $n = 13$	CN18 GFZ $n = 13$	CN19 GFZ $n = 13$	CN20 MfN $n = 13$	CN21 MfN $n = 8$
CaO	3.28(7)	1.48(29)	1.48(29)	1.91(25)	0.95(24)	2.73(19)	1.55(22)	2.03(47)
Na ₂ O	0.02(2)	0.55(6)	1.49(27)	1.05(22)	1.81(27)	0.05(3)	1.13(14)	0.64(17)
MgO	10.73(23)	8.49(25)	9.77(67)	9.77(56)	10.22(71)	9.74(48)	9.99(55)	9.73(37)
Al ₂ O ₃	32.23(59)	36.70(54)	33.72(94)	33.49(70)	33.00(99)	33.54(60)	34.4(16)	34.6(12)
SiO ₂	34.88(48)	31.53(85)	34.0(11)	35.03(61)	35.6(14)	35.44(41)	32.8(13)	33.9(10)
Total	81.26(65)	78.94(60)	80.67(91)	81.51(56)	81.9(14)	81.69(47)	79.9(20)	81.0(12)
Ca	0.59(1)	0.27(6)	0.27(5)	0.34(5)	0.17(5)	0.49(4)	0.28(4)	0.37(9)
Na	0.01(1)	0.18(2)	0.49(9)	0.34(7)	0.59(8)	0.02(1)	0.37(4)	0.21(5)
□	0.40(1)	0.54(5)	0.23(6)	0.31(5)	0.24(5)	0.49(4)	0.34(4)	0.42(4)
Mg	2.70(6)	2.17(7)	2.47(15)	2.45(13)	2.55(14)	2.43(11)	2.53(15)	2.44(9)
Al	6.41(11)	7.42(12)	6.75(24)	6.65(16)	6.51(27)	6.63(13)	6.90(24)	6.86(20)
Si	5.89(6)	5.41(11)	5.77(12)	5.90(7)	5.95(15)	5.94(5)	5.57(14)	5.70(14)
B ^a	3.00	3.00	3.00	3.00	3.00	3.00	3.00	3.00
^{VW} OH	3.62(5)	3.91(6)	3.66(11)	3.52(13)	3.66(11)	3.49(15)	3.87(7)	3.80(12)
^{VW} O	0.38(5)	0.03(6)	0.34(11)	0.48(13)	0.34(11)	0.51(15)	0.05(8)	0.20(12)
Ca/(Ca+Na)	0.99(3)	0.60(15)	0.36(9)	0.50(9)	0.23(7)	0.97(11)	0.43(8)	0.64(19)

n indicates the number of EMP analyses.

^a Values fixed during normalization.

^{VW}OH and ^{VW}O calculated from charge balance.

In terms of their X-site composition, the synthesized tourmalines (or rims of the tourmaline synthesized at 0.2 GPa) are calcic, alkali, or X-vacant tourmaline following the nomenclature of Henry *et al.* (2011) (Fig. 6.3). The most Ca-rich tourmaline with 0.59(1) Ca pfu was synthesized in experiment CN11 at 0.2 GPa, 700 °C in the presence of a NaCl-free, 2.00 *m* CaCl₂ solution, the most Ca-rich fluid used. Similarly, the most Na-rich tourmaline with 0.59(8) Na pfu was synthesized in experiment CN18 at 4.0 GPa, 700 °C in the presence of a 0.50 *m* CaCl₂, 1.50 *m* NaCl solution, the most Na-rich fluid used. Tourmaline with the highest number of vacancies at the X-site [0.54(5) ^X□ pfu] was synthesized in experiment CN13 at 1.0 GPa, 500 °C in the presence of a 1.00 *m* CaCl₂, 1.00 *m* NaCl solution.

The composition of the product fluid in each experiment is given in Table 6.3 and shown in Figure 6.1. For each investigated pressure and temperature, the Ca/(Ca+Na) ratio of the tourmaline and the product fluid are given in Table 6.3 and shown in Figures 6.4 and 6.5. At 0.2 GPa, 700 °C, and to a lesser extent at 1.0 GPa, 500 °C, the Ca/(Ca+Na) ratio in the tourmaline exceeds that in the fluid. In contrast, at all temperatures investigated at 2.5 and 4.0 GPa, the Ca/(Ca+Na) ratio of the fluid exceeds that of the coexisting tourmaline (Figs. 6.4 and 6.5).

The unit-cell parameters of all synthesized tourmaline are given in Table 6.4 and their variation with tourmaline composition shown in Figure 6.6. In the hexagonal setting of the trigonal-rhombohedral lattice system, the unit-cell dimensions range in size from $a = 15.857(2)$ – $15.915(2)$ Å, $c = 7.131(1)$ – $7.183(0)$ Å, and $V = 1552.8(4)$ – $1575.2(1)$ Å³, depending on composition. The unit-cell dimensions of previously synthesized Na-Ca Mg-Al tourmalines fit within this range, *e.g.*, $a = 15.875(1)$ Å, $c = 7.1790(2)$ Å for dravite (von Goerne *et al.*, 2001); $a = 15.919(2)$ Å, $c = 7.167(2)$ Å for oxy-uvite (von Goerne and Franz, 2000). Naturally occurring tourmalines tend to have slightly larger unit cells than their synthetic counterparts, *e.g.*, $a = 15.965(1)$ Å, $c = 7.199$ Å, for Ca-rich dravite (Bloodaxe *et al.*, 1999); $a = 15.954(1)$ Å, $c = 7.214(1)$ Å for uvite (Clark *et al.*, 2010). In our dataset, tourmaline with the smallest unit-cell parameters (CN13; Table 6.4) has the highest number of X-site vacancies (Table 6.2). The tourmaline with the longest *a*-axis (CN20; Table 6.4) is among the more Ca-rich tourmalines (Table 6.2), and that with the longest *c*-axis and unit-cell volume (V) (CN9; Table 6.4), has a highly occupied X site, dominated by Ca (Table 6.2).

6.3 Discussion

6.3.1 Ca-Na solid solution exchange vectors

Based on the normalization scheme (see Results; Table 6.2), all the synthesized tourmalines are solid solutions of oxy-uvite (*i.e.*, “Ca-Mg-O root name” in the nomenclature of Henry *et al.*, 2011) [CaMg₃Al₆Si₆O₁₈(BO₃)₃(OH)₃O], dravite [NaMg₃Al₆Si₆O₁₈(BO₃)₃(OH)₃(OH)] and magnesio-foitite [□(Mg₂Al)Al₆Si₆O₁₈(BO₃)₃(OH)₃(OH)] (Fig. 6.7), consistent with the results of von Goerne *et al.* (2011). Ca-Na exchange at the X site occurs between these endmembers via the exchange vector ^XCa^WO[^XNa^W(OH)]_{−1}, whereby the 2+ charge of Ca is balanced by deprotonation of the W site, independent of the occupancy of the Y and Z sites. This interpretation is supported by the lack of correlation between Ca and Mg (Fig. 6.8; *left*), which would reflect the ^XCa^{YZ}Mg(^XNa^{YZ}Al)_{−1} exchange vector. Henry and Dutrow (1990) invoked this Ca-incorporation exchange mechanism to explain chemical zoning of dravitic tourmaline from the wallrock of a pegmatite in Maine, USA. Taylor *et al.* (1995) further demonstrated its plausibility from a crystal structure standpoint in a

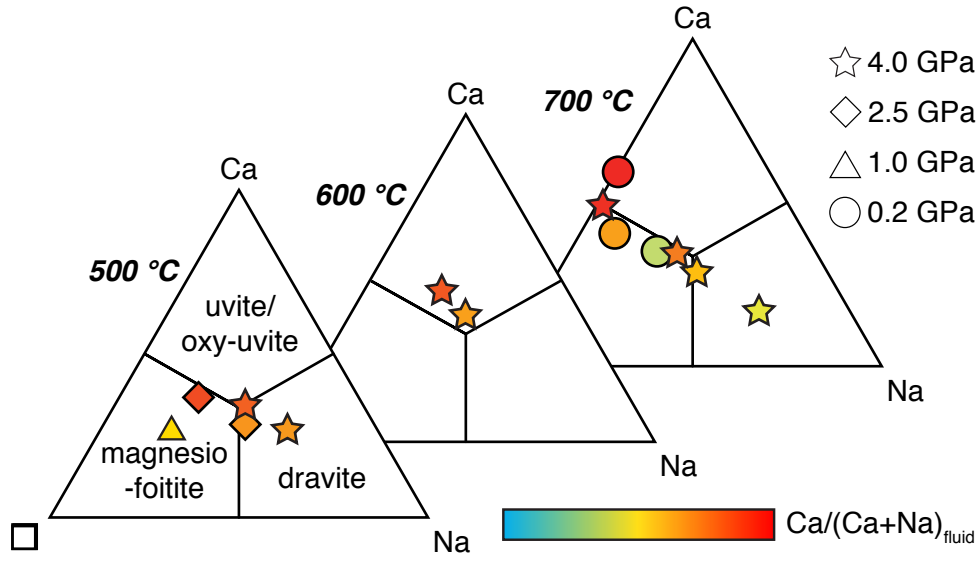


Figure 6.3: Average X-site composition of tourmaline (or, in the case of those synthesized at 0.2 GPa, their rims) plotted in ternary Na-Ca-□ (vacancy) space following normalization to 15 cations at the Y, Z, and T sites at 500, 600, and 700 °C. The data points correspond to the values in Table 6.2. *Symbol shape* correlates to the pressure of the experiment and *colour* to the $\text{Ca}/(\text{Ca}+\text{Na})_{\text{fluid}}$ ratio, whereby *blue* indicates a Ca-free fluid and *red* a Na-free fluid.

Table 6.3: Composition of product fluids along with $\text{Ca}/(\text{Ca}+\text{Na})$ mole fractions of fluids and the rims of coexisting tourmalines

No.	$m \text{ Na}$	$m \text{ Ca}$	$m \text{ Cl}$	$m \text{ B}$	$m \text{ Mg}$	$\text{Ca}/(\text{Ca}+\text{Na})_{\text{fl}}$	$\text{Ca}/(\text{Ca}+\text{Na})_{\text{tur}}$
CN1	0.51	0.89	3.84	1.53	1.05	0.64	0.44(18)
CN2	0.18	0.80	3.63	0.68	1.07	0.82	0.55(7)
CN5	0.29	0.74	2.95	1.49	0.89	0.72	0.44(10)
CN6	0.12	1.14	3.36	1.45	0.93	0.91	0.63(12)
CN9	0.61	0.35	3.25	1.68	0.64	0.37	0.57(10)
CN10	0.32	0.81	3.58	1.61	0.64	0.72	0.81(13)
CN11	0.02	1.42	3.89	0.94	0.56	0.99	0.99(7)
CN13	0.53	0.67	2.86	1.21	0.47	0.56	0.60(15)
CN14	0.30	0.82	3.13	1.37	0.93	0.73	0.36(9)
CN15	0.17	1.28	3.67	1.37	0.97	0.89	0.50(9)
CN18	0.57	0.45	3.00	1.59	0.86	0.44	0.23(7)
CN19	0.04	1.44	4.07	1.45	1.00	0.97	0.97(11)
CN20	0.28	0.80	3.13	1.39	0.70	0.74	0.43(8)
CN21	0.08	1.10	3.38	1.44	0.78	0.93	0.64(19)

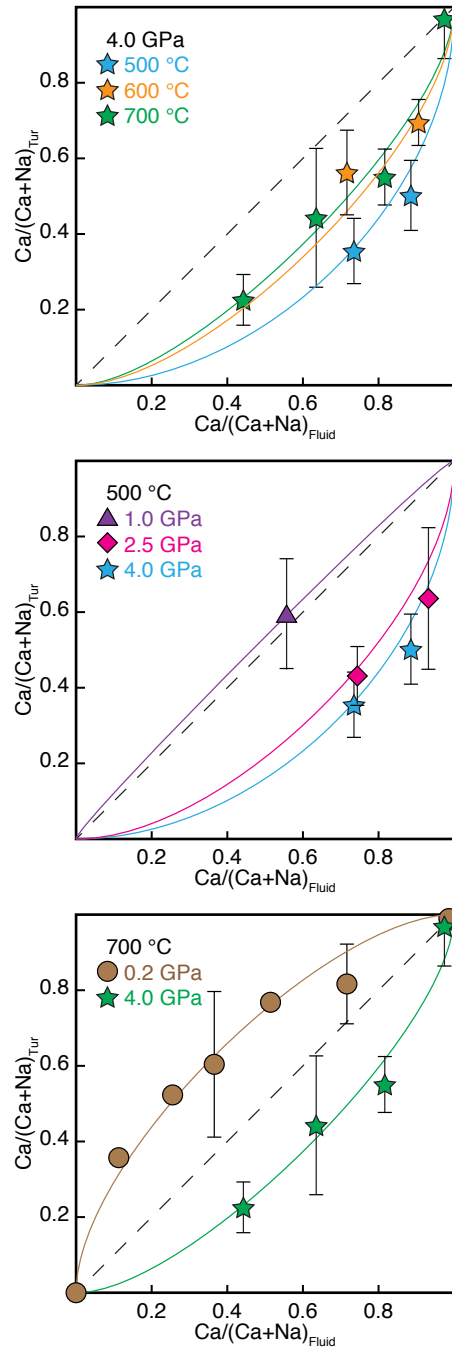


Figure 6.4: $\text{Ca}/(\text{Ca}+\text{Na})$ ratio of tourmalines (or in the case of those synthesized at 0.2 GPa, their rims) and the coexisting fluid at 4.0 GPa (*top*), 500 °C (*middle*), and 700 °C (*bottom*) (Table 6.3). *Symbol shape* corresponds to the synthesis pressure. Data points given for 0.2 GPa, 700 °C without standard deviations are taken from von Goerne *et al.* (2011). The *coloured lines* interpolate the data for a given pressure or temperature and assume ideal mixing. The 1:1 correlation is shown as a *dashed line*.

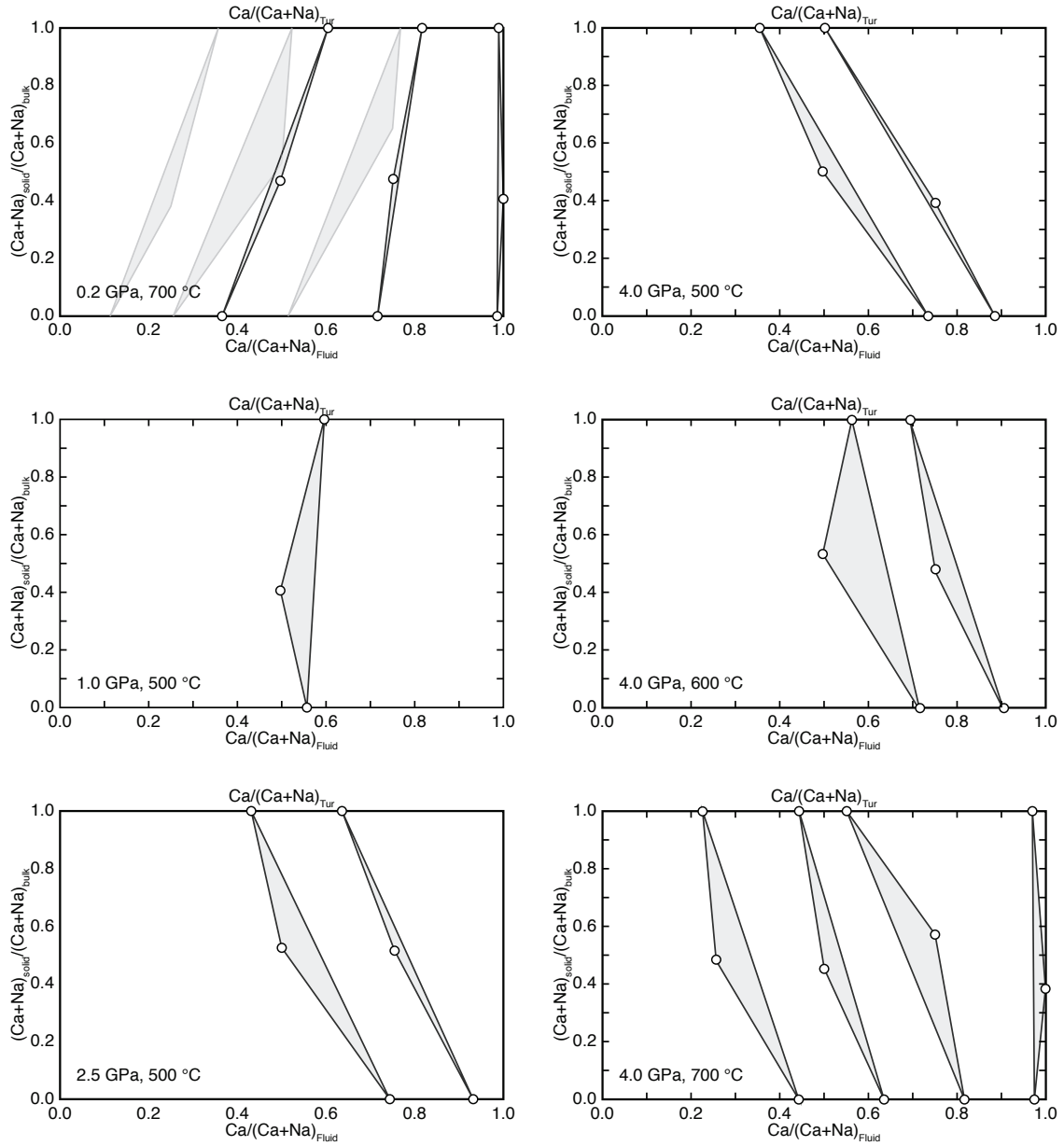


Figure 6.5: Partitioning diagrams showing $\text{Ca}/(\text{Ca}+\text{Na})$ ratios of the bulk system (*i.e.*, the initial fluid composition, shown inside the plot), the tourmaline, and the final fluid for experiments at different pressures and temperatures (Table 6.3). Tie lines connect the composition of the fluid to that of the tourmaline in each experiment. The tourmaline compositions given for the data at 0.2 GPa, 700 °C (*top left*) were taken from large tourmalines synthesized using the two-chamber method of von Goerne *et al.* (1999) and were measured within 2 μm of the crystal rim in the c^+ sector. Partitioning values collected by von Goerne *et al.* (2011) at 0.2 GPa, 700 °C (*top left*) are shown in lighter grey without circular symbols.

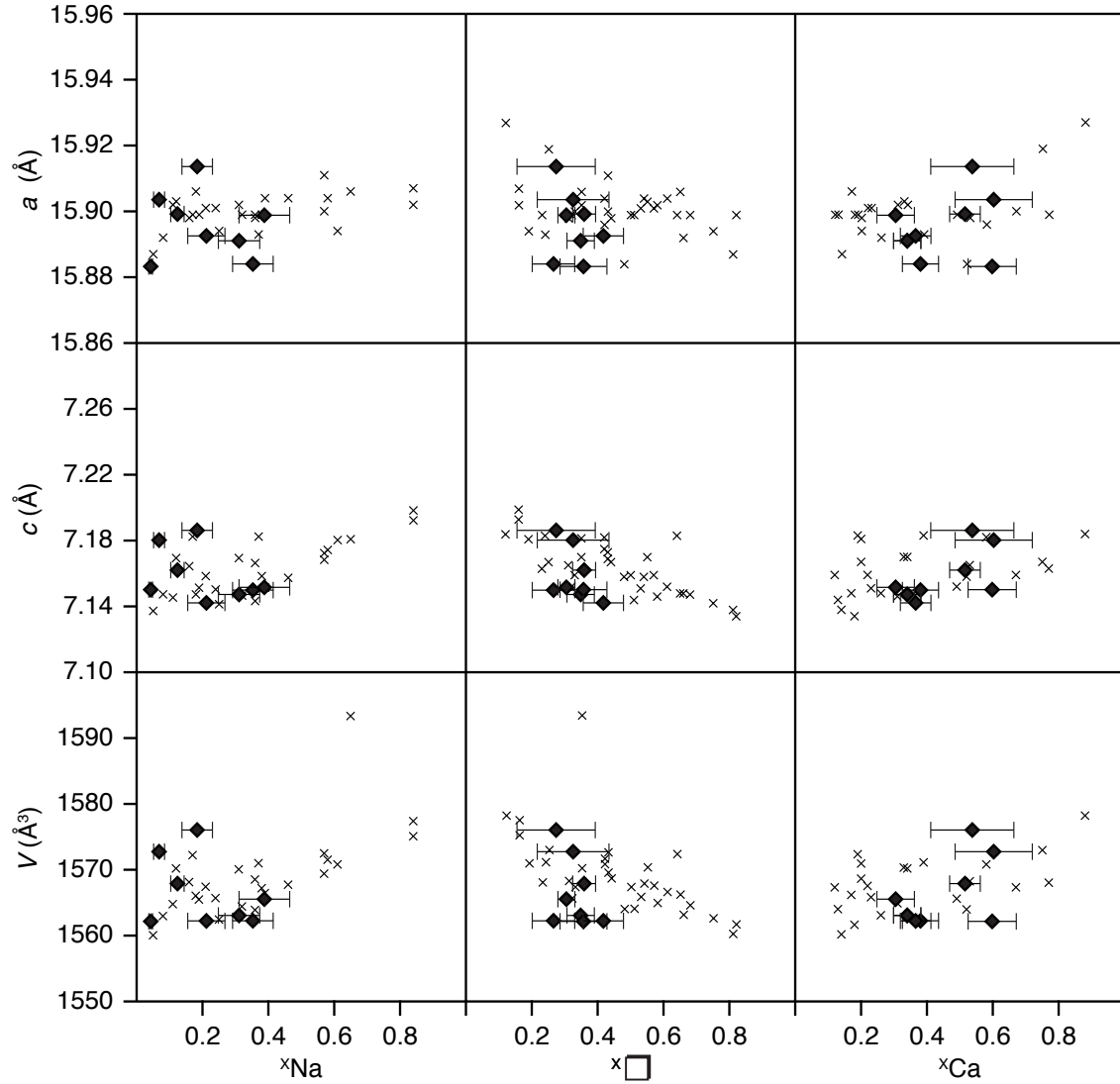


Figure 6.6: Average unit-cell parameters obtained from Rietveld refinement of powder X-ray diffraction spectra (Table 6.4) of tourmaline as a function of their average X-site composition (Table 6.2). Data points marked by *crosses* (\times) are taken from von Goerne *et al.* (2011). The symbols cover five times the standard deviation of each unit-cell parameter given by the refinement. The refinement ignores compositional zoning and gives an average value for each unit-cell parameter.

Table 6.4: Tourmaline unit-cell parameters

Experiment	a (Å)	c (Å)	V (Å ³)
CN1	15.884(1)	7.150(1)	1562.2(2)
CN2	15.891(1)	7.147(1)	1563.1(2)
CN5	15.892(2)	7.150(1)	1563.8(4)
CN6	15.886(2)	7.141(1)	1560.7(4)
CN9	15.913(1)	7.183(0)	1575.2(1)
CN10	15.903(1)	7.172(0)	1570.9(1)
CN11	15.906(1)	7.176(1)	1572.4(2)
CN13	15.857(2)	7.131(1)	1552.8(4)
CN14	15.907(1)	7.171(1)	1571.5(3)
CN15	15.896(1)	7.158(1)	1566.3(3)
CN18	15.913(2)	7.167(2)	1571.7(5)
CN19	15.894(1)	7.137(1)	1561.5(3)
CN20	15.915(2)	7.177(1)	1574.3(4)
CN21	15.897(1)	7.161(1)	1567.2(2)

detailed structural investigation of OH-deficient uvite from an unknown location in East Africa. However, as neither the B nor H contents of the tourmalines synthesized here were measured, the possible exchange vector $^X\text{Ca}^T\text{B}(^X\text{Na}^T\text{Si})_{-1}$ must also be considered. In this case, the synthesized tourmalines would be solid solutions of dravite, magnesio-foitite, and the hypothetical B-rich endmember $\text{CaMg}_3\text{Al}_6(\text{Si}_5\text{B})\text{O}_{18}(\text{BO}_3)_3(\text{OH})_3(\text{OH})$. Using a combination of single crystal structure refinement and Raman spectroscopy, in Chapter 5, we constrained the structure of the most Ca-rich synthesized tourmaline (CN11; Table 6.2) as dominantly oxy-uvite, with only 3 B pfu. Even though the $^X\text{Ca}^T\text{B}(^X\text{Na}^T\text{Si})_{-1}$ exchange vector may contribute to Ca-incorporation, particularly in the Ca-bearing tourmalines synthesized at high pressure and temperature where tetrahedral B is more likely to occur (*e.g.*, Ertl *et al.*, 2008), the $^X\text{Ca}^W\text{O}(^X\text{Na}^W(\text{OH}))_{-1}$ exchange mechanism is thus considered as dominant.

von Goerne *et al.* (2011) observed that the number of vacancies at the X site largely depends on the net ionic strength of the solution, whereby decreasing ionic strength correlates with an increasing number of vacancies. Whereas Ca-Na exchange at the X site of the synthesized tourmalines occurs largely independent of the octahedral Y and Z sites, vacancies (\square) at the X site are charge balanced by Mg-Al exchange via the exchange vector $^X\square^{YZ}\text{Al}(^X\text{Na}^{YZ}\text{Mg})_{-1}$ or $^X\square^{YZ}\text{Al}^W(\text{OH})(^X\text{Ca}^{YZ}\text{Mg}^W\text{O})_{-1}$. As a result, the number of vacancies may additionally depend on the bulk Mg-Al ratio of the system. Here, the occupancy of the X site is relatively consistent (Fig. 6.7) compared to the variability observed in other experimental studies (*c.f.* von Goerne *et al.*, 2011 and results presented in Chapter 4). This likely reflects both the constant ionic strength of the solutions used (2.00 *m*) and the consistent bulk Mg-Al ratio (3:6). In Figure 6.3, the relatively consistent number of vacancies is apparent. Additionally, there is a slight increase in the number of vacancies as the tourmalines move to more Ca-rich compositions (Fig. 6.8; *right*), occurring as a second-order trend. This was also observed in the experiments of von Goerne *et al.* (2011) and suggests $^X(\text{Ca}\square)^X(2\text{Na})_{-1}$ as a minor, but possible Ca-incorporation mechanism. The majority of the synthesized tourmalines also show minor Mg-Al exchange via the exchange vector $^{YZ}\text{Al}^{VW}\text{O}(^{YZ}\text{Mg}^{VW}\text{OH})_{-1}$, drawing their average compositions away

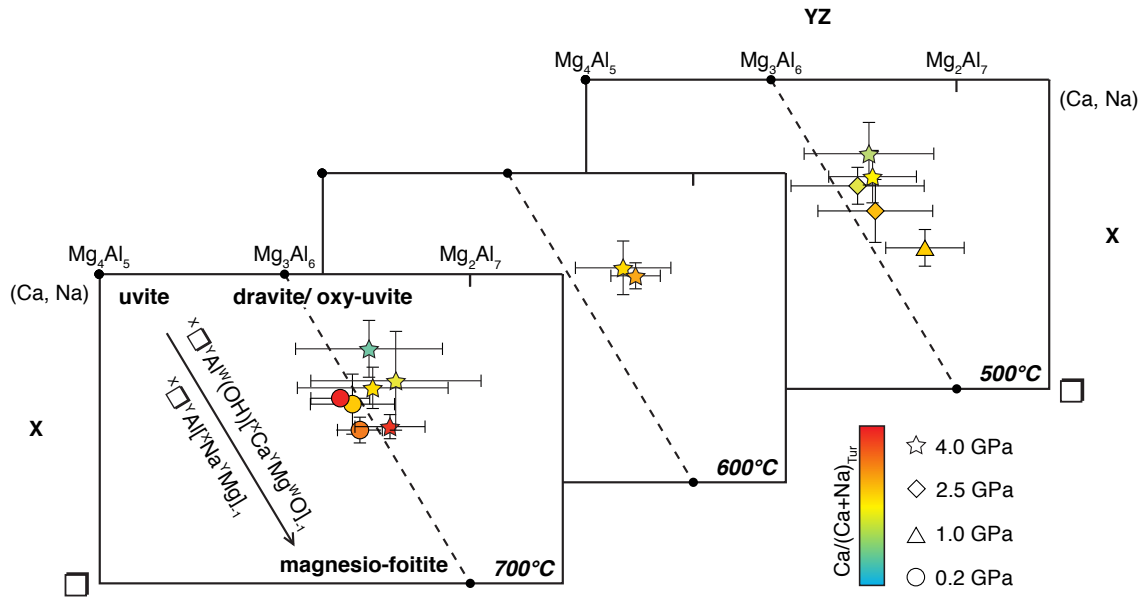


Figure 6.7: Average composition of tourmalines (or, in the case of those synthesized at 0.2 GPa, their rims) plotted relative to their combined Y- and Z-site compositions (*horizontal axis*) and the occupancy of the X site (*vertical axis*) following normalization to 15 cations at the Y, Z, and T sites at 500, 600, and 700 °C. The data points and their standard deviations correspond to the values in Table 6.2. *Symbol shape* correlates to the pressure of the experiment and *colour* to the $\text{Ca}/(\text{Ca}+\text{Na})$ ratio in the tourmaline, whereby *blue* indicates a Ca-free X site and *red* a Na-free X site. Relevant tourmaline endmember compositions are plotted for reference. The *dashed line* indicates the dravite/oxy-uvite–magnesio-foitite exchange vector.

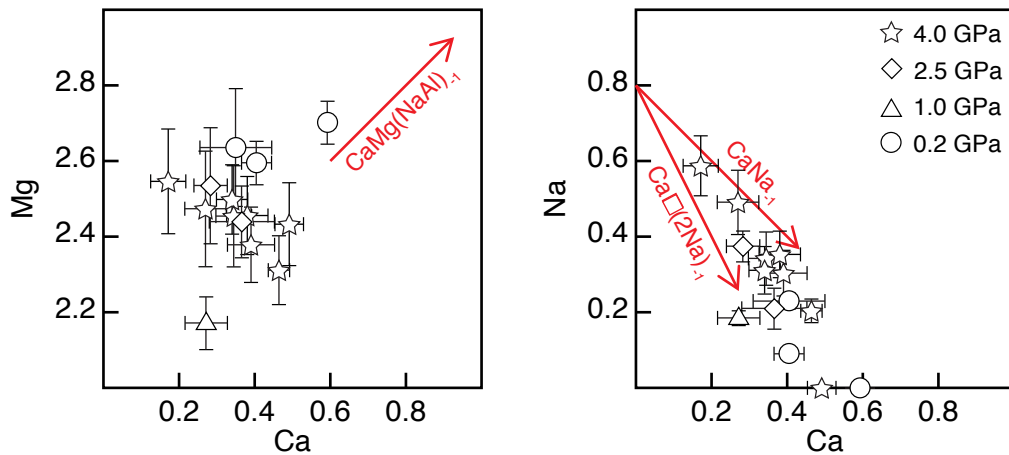


Figure 6.8: Average composition of tourmalines (or, in the case of those synthesized at 0.2 GPa, their rims) plotted in terms of Mg versus Ca pfu (*left*) and Na versus Ca pfu (*right*). The data points and their standard deviations correspond to the values in Table 6.2. *Symbol shape* correlates to the pressure of the experiment. The *arrows* indicate the direction of relevant exchange vectors.

from the oxy-uvite/dravite–magnesian-foitite join in Figure 6.7.

6.3.2 Ca-Na tourmaline-fluid partitioning behaviour

In Figure 6.5, the bulk $\text{Ca}/(\text{Ca}+\text{Na})$ ratio generally occurs near the tie-line connecting the $\text{Ca}/(\text{Ca}+\text{Na})$ of the tourmaline to that of the fluid. This indicates that Ca and Na partitioned between those two phases, and that the secondary product phases reported in Table 6.1 did not significantly affect the Ca-Na budget of the system.

The Ca-Na tourmaline-fluid partitioning behaviour at 0.2 GPa, 700 °C is consistent with the results of von Goerne *et al.* (2011) (0.2 GPa, 700 °C; Figs. 6.4, 6.5). The $\text{Ca}/(\text{Ca}+\text{Na})$ ratio in tourmaline correlates with that of the fluid, whereby the most Ca-rich tourmalines crystallize from the most Ca-rich fluids (Figs. 6.4, 6.5). As a result, the $\text{Ca}/(\text{Ca}+\text{Na})$ in tourmaline records the fluid composition, but pressure, and to a lesser extent, temperature, both influence the Ca-Na tourmaline-fluid partitioning behaviour.

As pressure increases, Ca incorporation in tourmaline decreases (*e.g.*, 500 or 700 °C in Fig. 6.3). The effect of pressure is best seen in Figures 6.4 and 6.5. At 0.2 GPa and to a lesser extent at 1.0 GPa, Ca partitions preferentially into tourmaline over the fluid, as observed by von Goerne *et al.* (2011) (Figs. 6.4, 6.5). However, at all other investigated pressures, regardless of temperature, Ca preferentially partitions into the fluid.

In the range of the investigated conditions (500–700 °C, 0.2–4.0 GPa), temperature has a less pronounced effect than pressure on Ca-Na partitioning. Increasing temperature correlated with Ca increasingly partitioning into tourmaline over the fluid (Figs. 6.4, 6.5). As a result, experiments with a similar fluid composition done at constant pressure showed increasing Ca incorporation with temperature (*e.g.*, 4.0 GPa in Fig. 6.5).

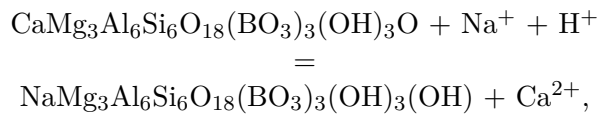
6.3.3 Implications for Ca-Na trends in natural tourmalines

Tourmaline compositions typically reflect the bulk composition of their host rock, with Ca-rich tourmalines occurring principally in calcareous rocks and metamorphosed carbonates (*e.g.*, Dunn *et al.*, 1977; Henry and Dutrow, 1996). However, there are records of Ca-poor tourmaline occurring in Ca-rich environments. For example, Dunn *et al.* (1977) report dravite hosted in limestone from DeKalb, New York; Pertlik *et al.* (2003) describe marble-hosted dravite from the Friesach, Carinthia, in Austria with only ~0.2 Ca pfu and 0.7 Na pfu; Marschall *et al.* (2008) describe metamorphic dravite with 0.10 Ca pfu overgrowing detrital tourmaline in siliceous marble from the high-pressure metasediments of Syros, Greece; and in the high pressure Eclogite Zone in the Eastern Alps, Ca-poor dravitic tourmaline is hosted in marble and calc-mica schist (Zoheidi, 1990). Based on their host rock composition alone, one would expect these tourmalines to be Ca-rich. As such, other factors beyond bulk rock composition must have an effect on Ca incorporation. Based on our experimental findings, at pressures >1.0 GPa, Na preferentially partitions into tourmaline and Ca into the fluid. It is therefore likely that the pressure at which they grew precluded the incorporation of Ca in their structure, particularly in the cases of the dravitic tourmalines from Friesach, Syros, and the Eclogite Zone. Indeed, Marschall *et al.* (2009a) summarize that almost all known tourmalines occurring in (ultra)high-pressure metamorphic rocks are dravitic, as we would expect based on our current experimental findings.

The Ca-Na partitioning behaviour observed in our experiments suggests that Ca-rich tourmalines are expected to be most common in Ca-rich, low-pressure, high-temperature rocks, such as contact aureoles around intrusive magmatic bodies or pegmatites. Indeed, the original type locality of uvitic tourmaline is Uva, Sri Lanka, where it occurs as fluor-uvite in a contact aureole metasomatized by B-bearing fluids. Clark *et al.* (2010) described true uvite (OH-dominant) from Brumado mine, Bahia, Brazil, a metasomatized sequence of calcareous sediments (Barbosa *et al.*, 2000).

6.3.4 Other possible controls on Ca-Na partitioning

The principal Ca-Na exchange vector observed in our synthetic tourmaline is expected to be sensitive to pH, via the reaction:



whereby increasing pH drives the reaction to the left, resulting in increasing Ca incorporation. Tourmaline is only stable in acidic to neutral pH solutions, in which B occurs as the trigonally-coordinated $\text{B}(\text{OH})_3^0$ species (*e.g.*, Palmer and Swihart, 1996). In our experiments, pH is controlled by the addition of B as H_3BO_3 and does not change with varying bulk Ca-Na content. However, with varying pressure and temperature, the pH of the system will change as the dissociation of H_2O depends largely on pressure and temperature. Considering a closed system, the pH in our experiments is expected to correlate with temperature and inversely correlate with pressure. As such, based on the behaviour of pH alone, Ca incorporation in magnesian tourmaline is predicted to increase with temperature and decrease with pressure, exactly as observed in our experiments. However, our system considers a restricted bulk composition with a simplified mineralogy, far from the complex chemistry of natural fluids. Moreover, the dearth of fluid speciation data at the high pressures investigated here makes it difficult to speculate on the pH of our system at the investigated conditions. Additionally, it is difficult to exclude the possibility of H-diffusion through the gold capsule wall, particularly at high temperature (Zvezdin and Belyakov, 1968). Despite the difficulties in considering the pH in our experiments, the exchange vector $^{\text{X}}\text{Ca}^{\text{W}}\text{O}[^{\text{X}}\text{Na}^{\text{W}}(\text{OH})]_{-1}$ should in theory be sensitive to the pH of the system, and thus its possible contribution to the observed Ca-Na tourmaline-fluid partitioning behaviour cannot be excluded. As a result, the possible influence of pH should be considered when comparing Ca-incorporation under different conditions in natural tourmalines.

In addition to dependence on the Ca content, pressure, temperature, and possibly the pH of the tourmaline-forming environment, it is likely that the Mg-Al content of the host rock, and thereby the tourmaline, has an influence on Ca incorporation via the exchange vector $^{\text{X}}\text{Ca}^{\text{YZ}}\text{Mg}(^{\text{X}}\text{Na}^{\text{YZ}}\text{Al})_{-1}$. Ca incorporation may be hindered in Al-rich tourmalines. For example, considering a Li-free system, the Al-dominant tourmaline olenite $[\text{NaAl}_3\text{Al}_6\text{Si}_6\text{O}_{18}(\text{BO}_3)_3\text{O}_3(\text{OH})]$ has no capacity for Ca-incorporation except via the exchange vector $^{\text{X}}(\text{Ca}\square)^{\text{X}}(2\text{Na})_{-1}$. This hypothesis is supported by the observation that in Al-rich metasediments, tourmalines tend to be solid solutions of schorl-dravite, with only moderate amounts of Ca (Henry and Dutrow, 1996). Conversely, Ca-incorporation is expected to be favoured in Mg- or Fe^{2+} -rich systems following the observation that all tourmaline endmembers with $\text{Mg}+\text{Fe}^{2+}>3$ are in the calcic group.

Finally, the current experimental results are limited to Fe- and Li-free tourmaline. Fe is a common constituent of natural tourmaline and may affect Ca and Na incorporation at the X site. In general, variation in the radii of the ions occupying the octahedral sites is expected to have a structural influence on the composition of the X site. The effect of Fe is complicated by its possible incorporation in tourmaline in both the 2+ and 3+ valence states. This can create difficulties in identifying the exchange vectors in compositionally zoned tourmalines. Heterovalent Ca-Na exchange at the X site is expected to be sensitive to the presence and oxidation state of Fe, whereby high concentrations of Fe^{3+} may hinder Ca incorporation from bond valence arguments similar to those given above for the Al-dominant, Li-free system.

6.4 Conclusions

Fluid composition, pressure, and temperature affect Ca-Na partitioning between tourmaline and a coexisting fluid. Ca incorporation in Mg-Al tourmaline increases with the Ca concentration in the fluid and temperature, but decreases with increasing pressure via the exchange mechanism $^{\text{X}}\text{Ca}^{\text{W}}\text{O}[^{\text{X}}\text{Na}^{\text{W}}(\text{OH})]_{-1}$. Based on these findings, Ca-poor tourmalines found in Ca-rich environments likely formed under high pressure, favouring the incorporation of Na over Ca. Moreover, the varying Ca/Na ratio in tourmaline can provide insight into the metamorphic fluid composition and its evolution for rocks with independently constrained pressure and temperature histories. It is likely that pH and bulk Mg-Al ratio exert additional controls on Ca-Na partitioning via the exchange vectors $^{\text{X}}\text{Ca}^{\text{W}}\text{O}[^{\text{X}}\text{Na}^{\text{W}}(\text{OH})]_{-1}$ and $^{\text{X}}\text{Ca}^{\text{YZ}}\text{Mg}[^{\text{X}}\text{Na}^{\text{YZ}}\text{Al}]_{-1}$, respectively, but this remains to be investigated experimentally. Consequently, the Ca-incorporation method must be carefully considered prior to interpreting the likely fluid composition. The progressive development of our understanding of tourmaline's crystal chemistry further establishes this diverse borosilicate as a powerful petrogenetic indicator mineral.

Chapter 7

Tourmaline as a petrogenetic indicator in the Pfitsch Formation of the Western Tauern Window

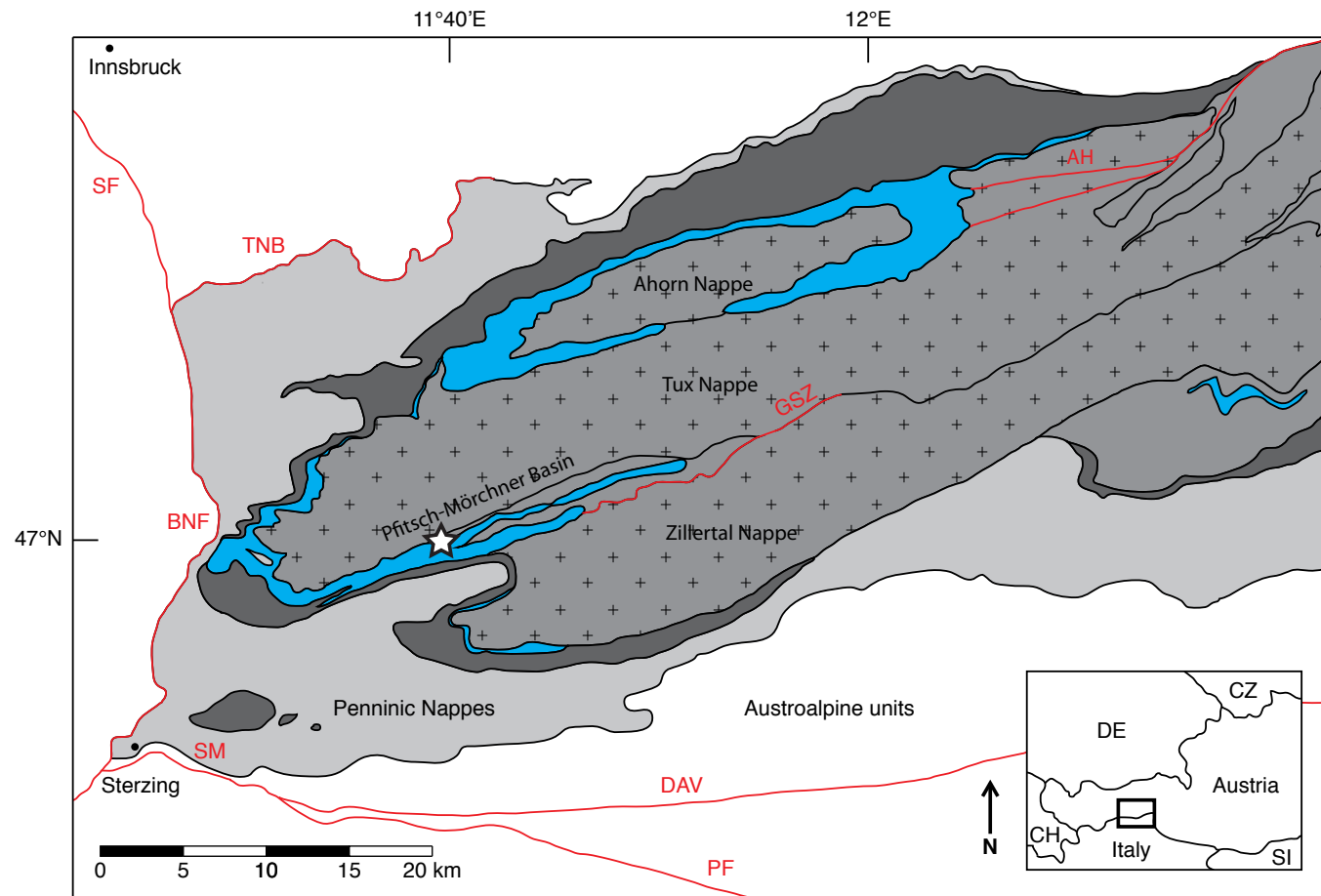
The contents of this chapter are being prepared for publication in combination with B-isotope analyses by M. Kutzschbach, R. Trumbull, and A. Meixner.

7.1 Introduction

In this chapter, tourmalines from the metasedimentary Pfitsch Formation are characterized in terms of their major element chemistry to probe their host rock's pro- and retro-grade fluid-rock interaction history. This is achieved by applying our current understanding of tourmaline-fluid element partitioning behaviour (von Goerne *et al.*, 2011; and the results of Chapter 6) and sector zoning thermometry (van Hinsberg and Schumacher, 2007a).

7.2 Regional Geology and study area

The Tauern Window is a tectonic window in the Eastern Alps exposing part of the Subpenninic and Penninic units, which are otherwise hidden by the overthrust Austroalpine superunit (Fig. 7.1). The Subpenninic and Penninic units are paleogeographically interpreted to represent the pre-Alpine distal European margin and remnants of the Tethys Ocean, respectively. Within the Subpenninic units, exposed at the core of the Tauern Window, the stratigraphically lowermost tectonic unit consists of Variscan basement rocks (*e.g.*, Schmid *et al.*, 2013, and references therein), intruded by Late- and Post-Variscan granitoids (*e.g.*, Cesare *et al.*, 2002; Schmid *et al.*, 2004). In the Western Tauern Window, these units are traditionally referred to as the Zentralgneise and comprise the Ahorn, Tux, and Zillertal Nappes, stacked to form the Venediger Duplex (*e.g.*, Frisch, 1980; Lammerer *et al.*, 2008; Schmid *et al.*, 2013). Overlying the Zentralgneise are the Post-Variscan cover units. At the contacts of the Zentralgneise Nappes, these cover units are folded into elongated basins (Veselá and Lammerer, 2008; Veselá *et al.*, 2011), defining the nappe boundaries.



Exposed Subpenninic Nappes (distal European margin):

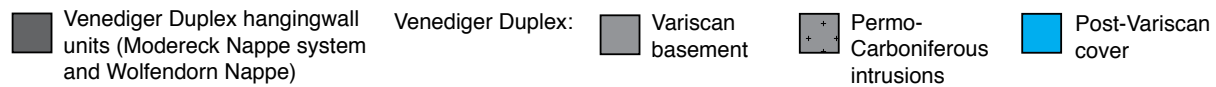


Figure 7.1: (Caption on next page.)

Figure 7.1: (*Figure on previous page.*) Geological sketch map of the Western Tauern Window emphasizing the exposed units of the Subpenninic Nappes (modified after Schmid *et al.*, 2013). The *star* indicates the position of the Pfitscher Joch Haus, the study area within the Pfitsch-Mörchner Basin. Alpine faults and shear zones are abbreviated as follows: AH Ahorn Fault; BNF Brenner Normal Fault; DAV Deferegggen-Antholz Vals Fault; GSZ Greiner Shear Zone; PF Pustertal Fault; SM Sterzing-Mauls Fault; TNB Tauern Northern Boundary Fault.

Veselá and Lammerer (2008) and Veselá *et al.* (2011) have described the stratigraphy and ages of the major basins of the Western Tauern Window. Their Carboniferous to Jurassic age (Veselá *et al.*, 2011) indicates they experienced only Alpine metamorphism (*e.g.*, Schmid *et al.*, 2013). The Venediger Duplex, including its Post-Variscan cover, experienced temperatures up to 500–550 °C (Selverstone *et al.*, 1984; Oberhänsli *et al.*, 2004; Schuster *et al.*, 2004, and references therein) and pressures up to 1.0–1.1 GPa (Selverstone *et al.*, 1984). Decompression was rapid and nearly isothermal (Selverstone *et al.*, 1984) during orogeny-parallel extrusion (*e.g.*, Ratschbacher *et al.*, 1991) and large-scale E-W extension (Frisch *et al.*, 2000).

The samples investigated here were collected from within the Pfitsch-Mörchner Basin, near the Pfitscher Joch Haus in the Passo di Vizzi on the Austrian-Italian border. The basin forms a NEE-SWW-striking isoclinally folded syncline, running parallel to the Greiner Shear Zone, which defines the contact of the Tux and the Zillertal Zentralgneis nappes (Fig. 7.1). Tourmaline has been previously described in this area in sheared tourmalinite veins from the lazulite-kyanite quartzite of the Windtal Formation (Henry *et al.*, 2002), estimated to be Early Triassic in age (Veselá and Lammerer, 2008). The tourmaline is highly heterogeneous in composition and comprises three generations of growth; the first generation is schorl-dravite and the second and third generations are schorl-foitite (Henry *et al.*, 2002). Henry *et al.* (2002) interpreted the first generation as forming the primary vein tourmaline, sourcing its B from nearby evaporites. They suggest the second generation grew from reactive fluids introduced early on in the Alpine orogeny during activation of the Greiner Shear Zone (Lammerer *et al.*, 2008) and the third generation grew post-deformation from similar fluids (Henry *et al.*, 2002).

We investigate tourmaline from the major tourmaline-bearing units in what has been called the Pfitsch Formation by Veselá and Lammerer (2008), which is stratigraphically below the Windtal Formation investigated by Henry *et al.* (2002). It is described as a sequence of meta-conglomerates, meta-rhyolites, and meta-pelites (Veselá and Lammerer, 2008). A layer of quartz-pyrite schist defines the base of the formation. Heading into the fold, the formation consists of a fining-upward meta-conglomerate grading into biotite schist, followed by ~30 m of the most tourmaline-rich unit, a foliated quartzofeldspathic rock, which we refer to as the Tur-gneiss. In sharp contact with the latter is fine-grained chlorite-biotite schist grading into biotite schist followed by ankerite-biotite-epidote schist. In some areas, thin 20-cm lenses of a white fine-grained muscovite-bearing quartzite unit appear between the Tur-gneiss and the chlorite-biotite schist. The Tur-gneiss is estimated to be Permian in age based on its position in the stratigraphy and zircons within it have been dated at 280.5 ± 2.6 Ma (Veselá *et al.*, 2011).

7.3 Tourmaline occurrence and sampling location

7.3.1 Tourmaline occurrence

Tourmaline is observed as euhedral crystals, typically 0.1–1.5 cm in length in the Chl-Bt schist, the Tur-schist, the Ms-quartzite, and the Tur-gneiss. The major tourmaline-bearing unit in terms of stratigraphic thickness and tourmaline abundance is the Tur-gneiss. Here, tourmaline is associated with quartz, albite, K-feldspar, muscovite, along with minor amounts of biotite, chlorite, apatite, and trace amounts of monazite, hematite, zircon, and rutile. A conspicuous feature of the Tur-gneiss is the presence of coarse-grained quartzofeldspathic segregations lying subparallel to the foliation. On the hand sample scale, K-feldspar-dominated lenses 2 to 70 mm in length and <1 to 6 mm in thickness (Fig. 7.2a), as well as quartzofeldspathic segregations 2–3 cm in thickness (Fig. 7.2b), are common. On the outcrop scale, coarse-grained segregations dominated by K-feldspar and quartz are up to 50 cm in thickness. The modal amount of tourmaline is variable and increases in proximity to the segregations. Tourmaline from the Tur-gneiss in contact with the segregations are up to 3 cm in length (Fig. 7.2a, b). The largest tourmaline crystals, up to 6 cm in length and 2 cm in width, are associated with the thickest segregations, particularly in the necks of segregation boudins. The best exposure of the segregations and the most concentrated occurrence of tourmaline are found 50 m S of the Pfitscher Joch Haus. The large-scale segregations and their associated tourmaline can be followed along strike to the SW. Along strike to the NE, large segregations are not visible at the surface and the modal proportion of tourmaline correspondingly decreases, occurring only in the Tur-gneiss as accessory 1–3 cm long black needles lying in the foliation of the rock. The large segregations reappear in one outcrop near the base of the Rotbachlspitze and are again associated with an increase in the size and modal proportion of tourmaline.

7.3.2 Sampling location

Samples were collected primarily from the most Tur-rich unit of the Pfitsch Formation, the Tur-gneiss, from the southern limb exposure of the Pfitsch formation, 50 m S of the Pfitscher Joch Haus. These samples were located in direct contact with the quartzofeldspathic segregations. Additional Tur-rich samples from the Tur-gneiss away from the segregations as well as from the tourmaline-bearing neighboring units were also collected from the roadcut located ~300 m SW of the Pfitscher Joch Haus. These samples include tourmaline schist (Tur-schist), chlorite-biotite schist (Chl-Bt-schist), and muscovite quartzite (Ms-quartzite), located within 1 m of the contact with the Tur-gneiss.

7.4 Results

7.4.1 Whole rock chemistry

The whole rock compositions and the B contents of the investigated tourmaline-bearing samples are given in Tables 7.1 and 7.2, respectively. The two schists (Tur-schist and Chl-Bt-schist) have the lowest SiO₂ contents (65 wt.%; Table 7.1) and the Ms-quartzite the highest (79 wt.%, Table 7.1). The aluminum and iron contents are variable, ranging from 9.61–14.99 wt.% Al₂O₃ and 0.79–4.79 wt.% Fe₂O₃. As the most feldspathic of all samples, the Tur-gneiss is distinguished from the other samples by its high alkali and Ca contents (see Table 7.1). If considered to represent their sedimentary parent rock compositions, the Tur-schist and Chl-Bt-schist have compositions corresponding to a wacke, and the Ms-quartzite and Tur-gneiss to an arkose based on the classification scheme of Herron

Table 7.1: Whole rock compositions of Tur-gneiss and neighbouring tourmaline-bearing units

Sample	28-11 Tur-schist	28-14 Ms-quartzite	28-15 Chl-Bt-schist	28-17 Tur-gneiss
wt. %				
SiO ₂	64.97	78.91	64.90	67.80
Al ₂ O ₃	14.64	9.61	14.99	11.29
TiO ₂	0.57	<0.10	0.54	0.16
Fe ₂ O ₃	4.79	0.79	4.23	1.05
MnO	0.19	0.10	0.07	0.23
MgO	3.07	0.54	2.34	1.17
CaO	0.80	1.04	1.22	5.40
Na ₂ O	0.16	1.08	0.84	3.81
K ₂ O	6.81	5.41	6.39	4.08
P ₂ O ₅	0.16	0.05	0.14	0.06
LOI	2.71	1.56	3.05	4.77

Table 7.2: Whole rock B contents of investigated samples

	28-11	28-14	28-15	22-1	28-17	TU15B
ppm	Tur-schist	Ms-quartzite	Chl-Bt-schist	Tur-poor gneiss	Tur-gneiss	Tur-gneiss/segregation
B	516	419	40	21	165	1196

Tur-gneiss/segregation refers to Tur-gneiss occurring in contact with segregations.

(1988). Veselá and Lammerer (2008) interpreted the Tur-gneiss as having a volcanoclastic protolith, in which case its composition corresponds to a trachydacite based on the classification of Le Maitre *et al.* (1989). However, the pervasive presence of tourmaline reflects widespread fluid movement, making it unlikely that the measured bulk compositions match those of the protoliths.

7.4.2 Tourmaline textures

Tourmalines in the Tur-gneiss are between 4 and 23 mm in length, with the majority being approximately 10 mm long. They are preferentially oriented parallel to the foliation and the larger crystals commonly have orthogonal extensional fractures (Fig. 7.2a). The fractures are typically filled with feldspar and quartz, and late-stage tourmaline overgrowths visible in thin section (Fig. 7.2d). Unlike in the surrounding rock, coarse tourmalines occurring in segregations do not show a systematic orientation (Fig. 7.2b).

The larger tourmaline crystals in the Tur-gneiss found near segregations often show multiple stages of crystal growth; are sector-zoned; have fractures perpendicular to the crystal's long axis; are frequently overgrown by secondary tourmaline along the fracture surfaces; and are rich in mineral inclusions (*e.g.*, Fig. 7.2c). Sector zoning in a tourma-

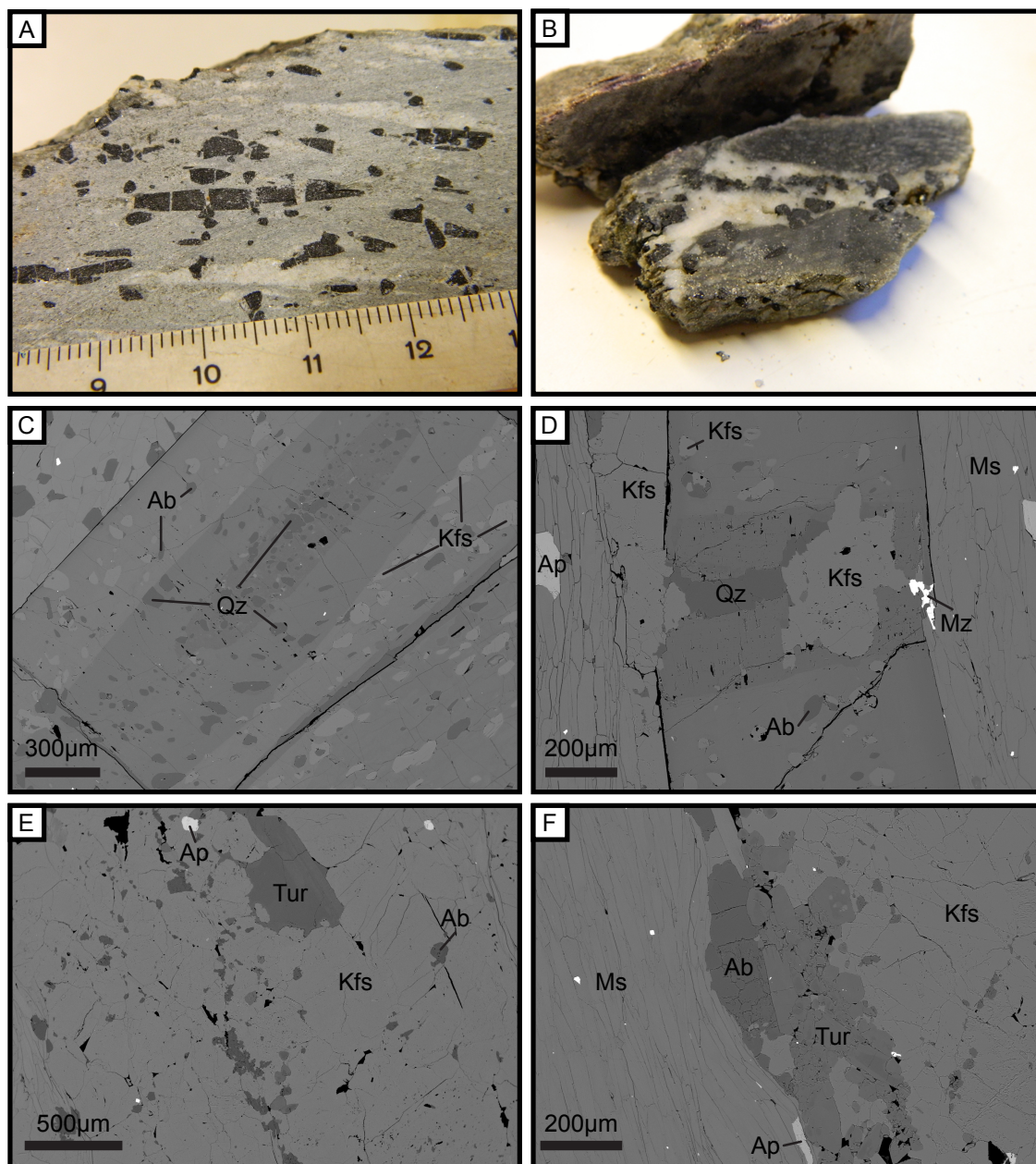


Figure 7.2: Tourmaline textures in (a, b) handsample and (c–f) BSE images of the Tur-gneiss occurring near the quartzofeldspathic segregations. The minerals labelled as inclusions in tourmaline and in the matrix are albite (Ab), quartz (Qz), K-feldspar (Kfs), apatite (Ap), muscovite (Ms), and monazite (Mz).

line crystal cut at an angle oblique to its *c*-axis can easily be mistaken for two stages of growth because the *c* sector will appear as a core of differing composition from the outer rim (*e.g.*, van Hinsberg and Schumacher, 2007a). As a result, the combined occurrence of both multi-stage growth as well as sector zoning in tourmaline from the Tur-gneiss can make it difficult to distinguish the different growth stages. To avoid misinterpretation, crystals where two-stage growth and sector zoning were clearly distinguishable were carefully selected. The first two stages of tourmaline growth have distinct mineral inclusions (Fig. 7.2c). The first stage of tourmaline growth is characterized by a dominance of quartz inclusions, whereas the second stage predominantly has K-feldspar and albite inclusions (Fig. 7.2c). Apatite is found as an inclusion in both stages of tourmaline growth. Moreover, the inclusions within the first growth zone often have their edge perfectly aligned with the crystal edge of the first stage of tourmaline growth, emphasizing their association. The final, third stage of tourmaline growth is relatively easy to identify in back-scattered-electron images. It is found along the surfaces of extensional fractures in the tourmaline and is generally free of mineral inclusions (Fig. 7.2d).

Tourmalines showing only one generation of growth are smaller crystals and occur in all tourmaline-bearing samples. Those in samples collected far from segregations are typically inclusion-free.

7.4.3 Major element chemistry of associated phases

White mica and K-feldspar are common phases in all the investigated samples. The white micas in all samples have a high phengite component and a very minor paragonite component (Table 7.3). The composition of K-feldspar is consistent throughout all samples, as well as when it occurs as inclusions in tourmalines near segregations in the Tur-gneiss (Tur-gneiss/segregation; Table 7.3). Plagioclase, biotite, and chlorite were only analysed by EMP in the Tur-gneiss occurring near the segregations. The plagioclase is near end-member albite when it occurs both as inclusions in tourmaline as well as in the matrix (Table 7.3). The biotite has significant Ti concentrations (1.57 wt.% TiO₂; Table 7.3), however the absence of graphite in the Tur-gneiss precludes application of the Ti in biotite thermometer of Henry *et al.* (2005).

Table 7.3: Composition of phases coexisting with tourmaline as inclusions and in the host rock matrix (Fe treated as Fe²⁺)

wt. %	K-feldspar					
	Tur-gneiss/segregation		Tur-gneiss	Ms-quartzite	Tur-schist	Chl-Bt-schist
	Incl. in Tur	Matrix				
<i>n</i>	49	64	20	20	19	5
SiO ₂	64.60(69)	64.65(46)	66.35(27)	66.8(24)	65.91(26)	65.52(24)
TiO ₂	0.01(1)	0.01(1)	<i>n.d.</i>	<i>n.d.</i>	<i>n.d.</i>	<i>n.d.</i>
Al ₂ O ₃	18.61(19)	18.60(11)	18.10(11)	17.7(12)	17.99(10)	17.97(5)
Fe ₂ O ₃	0.30(16)	0.09(6)	0.06(4)	0.03(3)	0.07(4)	0.03(4)
MnO	0.00(1)	<i>n.d.</i>	<i>n.d.</i>	<i>n.d.</i>	<i>n.d.</i>	<i>n.d.</i>
MgO	0.02(7)	0.01(1)	0.01(1)	0.01(1)	0.01(1)	0.00(0)

Continues on next page

Table 7.3: *Continued from previous page*

Cr ₂ O ₃	0.00(1)	<i>n.d.</i>	<i>n.d.</i>	<i>n.d.</i>	<i>n.d.</i>	<i>n.d.</i>
ZnO	0.02(2)	0.02(2)	<i>n.d.</i>	<i>n.d.</i>	<i>n.d.</i>	<i>n.d.</i>
BaO	0.21(6)	0.21(5)	0.23(4)	0.20(4)	0.21(4)	0.23(5)
CaO	0.01(2)	0.01(1)	0.01(1)	0.01(1)	0.01(1)	0.03(3)
Na ₂ O	1.15(93)	0.77(17)	0.71(11)	0.72(13)	0.72(11)	0.52(9)
K ₂ O	15.1(14)	15.68(24)	15.13(14)	15.01(99)	15.10(19)	15.33(9)
F	0.00(0)	<i>n.d.</i>	<i>n.d.</i>	<i>n.d.</i>	<i>n.d.</i>	<i>n.d.</i>
Cl	0.00(1)	<i>n.d.</i>	<i>n.d.</i>	<i>n.d.</i>	<i>n.d.</i>	<i>n.d.</i>
Total	100.01(83)	100.05(54)	100.61(30)	100.47(27)	100.01(32)	99.63(24)
apfu	Normalized to 8 O pfu					
Si	3.00(1)	3.00(1)	3.03(0)	3.05(7)	3.03(0)	3.03(0)
Al	1.00(1)	1.00(0)	0.97(0)	0.95(7)	0.97(0)	0.98(0)
Fe ³⁺	0.01(1)	0.00(0)	0.00(0)	0.00(0)	0.00(0)	0.00(0)
Mn ²⁺	0.00(0)	0.00(0)	<i>n.d.</i>	<i>n.d.</i>	<i>n.d.</i>	<i>n.d.</i>
Ti ²⁺	0.00(0)	0.00(0)	<i>n.d.</i>	<i>n.d.</i>	<i>n.d.</i>	<i>n.d.</i>
Mg	0.00(0)	0.00(0)	0.00(0)	0.00(0)	0.00(0)	0.00(0)
Cr ³⁺	0.00(0)	0.00(0)	<i>n.d.</i>	<i>n.d.</i>	<i>n.d.</i>	<i>n.d.</i>
Zn	0.00(0)	0.00(0)	<i>n.d.</i>	<i>n.d.</i>	<i>n.d.</i>	<i>n.d.</i>
Na	0.10(8)	0.07(2)	0.06(1)	0.06(1)	0.06(1)	0.05(1)
Ca	0.00(0)	0.00(0)	0.00(0)	0.00(0)	0.00(0)	0.00(0)
K	0.89(8)	0.93(2)	0.88(1)	0.87(6)	0.89(1)	0.90(1)
Ba	0.00(0)	0.00(0)	<i>n.d.</i>	0.00(0)	0.00(0)	<i>n.d.</i>
F	0.00(0)	0.00(0)	<i>n.d.</i>	<i>n.d.</i>	<i>n.d.</i>	<i>n.d.</i>
Cl	0.00(0)	0.00(0)	0.00(0)	<i>n.d.</i>	<i>n.d.</i>	<i>n.d.</i>
White mica						
wt. %	Tur-gneiss/ segregation	Tur- gneiss	Ms- quartzite	Tur- schist	Chl- Bt- schist	
<i>n</i>	52	20	17	20	5	
SiO ₂	47.91(76)	49.85(90)	50.41(53)	48.95(71)	48.8(12)	
TiO ₂	1.14(23)	1.06(13)	0.33(5)	0.88(3)	0.93(3)	
Al ₂ O ₃	25.3(10)	23.94(81)	25.19(31)	24.17(74)	23.93(83)	
Fe ₂ O ₃	6.56(43)	6.79(56)	5.05(23)	7.19(28)	7.28(56)	
MnO	0.01(1)	0.05(2)	0.03(2)	0.04(2)	0.03(2)	
MgO	3.16(37)	3.82(30)	3.80(14)	3.53(27)	3.66(31)	
Cr ₂ O ₃	0.01(2)	0.02(1)	0.01(1)	0.02(2)	0.01(2)	
ZnO	0.03(3)	<i>n.d.</i>	<i>n.d.</i>	<i>n.d.</i>	<i>n.d.</i>	
CaO	0.02(3)	0.02(3)	0.01(1)	0.00(0)	0.01(1)	
Na ₂ O	0.23(4)	0.19(4)	0.20(2)	0.20(3)	0.21(4)	
K ₂ O	10.83(13)	10.43(19)	10.48(16)	10.45(10)	10.34(14)	
BaO	0.12(5)	0.14(4)	0.15(5)	0.14(2)	0.14(4)	
F	<i>n.d.</i>	0.05(5)	0.15(5)	0.06(4)	0.08(4)	
Cl	0.01(0)	0.00(0)	0.00(0)	0.00(0)	0.00(0)	
Total	95.1(16)	96.69(56)	95.30(63)	94.91(50)	94.70(53)	
apfu	Normalized to 24 O+F+Cl pfu					

Continues on next page

Table 7.3: *Continued from previous page*

Si	6.52(9)	6.69(11)	6.75(5)	6.64(7)	6.63(13)
^{IV} Al	1.48(9)	1.31(11)	1.25(5)	1.36(7)	1.37(13)
^{VI} Al	2.58(9)	2.47(6)	2.73(2)	2.50(6)	2.46(5)
Ti ²⁺	0.12(2)	0.11(1)	0.03(0)	0.09(0)	0.10(0)
Fe ³⁺	0.67(4)	0.69(6)	0.51(2)	0.73(3)	0.74(6)
Mn ²⁺	0.00(0)	0.01(1)	0.00(0)	0.00(0)	0.00(0)
Mg	0.64(7)	0.76(6)	0.76(3)	0.71(5)	0.74(6)
Cr ³⁺	0.00(0)	0.00(0)	0.00(0)	0.00(0)	0.00(0)
Zn	0.00(0)	<i>n.d.</i>	<i>n.d.</i>	<i>n.d.</i>	<i>n.d.</i>
ΣY	4.01(2)	4.04(1)	4.04(1)	4.04(1)	4.05(2)
Ca	0.00(0)	0.00(0)	0.00(0)	0.00(0)	0.00(0)
Na	0.06(1)	0.05(1)	0.05(1)	0.05(1)	0.06(1)
K	1.88(2)	1.79(3)	1.79(2)	1.81(2)	1.79(3)
Ba	0.01(0)	0.01(0)	0.01(0)	0.01(0)	0.01(0)
ΣX	1.95(2)	1.85(3)	1.85(2)	1.87(2)	1.86(4)
OH	4.00(0)	3.98(2)	3.94(2)	3.97(2)	3.96(2)
F	<i>n.d.</i>	0.02(2)	0.06(2)	0.03(2)	0.04(2)
Cl	0.00(0)	0.00(0)	0.00(0)	0.00(0)	0.00(0)
Plagioclase		Biotite		Chlorite	
wt. %	Tur-gneiss/segregation		Tur-gneiss	Tur-gneiss	
	Incl. in Tur	Matrix			
<i>n</i>	18	35	4	2	
SiO ₂	68.48(82)	68.48(61)	39.60(45)	29.29(66)	
TiO ₂	0.02(4)	0.01(4)	1.57(12)	0.03(0)	
Al ₂ O ₃	19.63(26)	19.93(36)	15.89(23)	19.63(40)	
Fe ₂ O ₃	0.32(13)	0.11(6)	–	14.67(21)	
FeO	–	–	10.56(41)		
MnO	0.01(1)	0.00(0)	0.06(2)	0.05(0)	
MgO	0.01(1)	0.00(1)	17.34(55)	24.07(5)	
Cr ₂ O ₃	0.01(1)	0.01(1)	0.00(0)	0.02(2)	
ZnO	0.03(2)	0.01(2)	0.17(2)	0.66(8)	
CaO	0.05(5)	0.23(35)	0.01(0)	0.03(2)	
Na ₂ O	11.52(42)	11.46(38)	0.12(3)	0.05(1)	
K ₂ O	0.17(4)	0.18(15)	10.05(18)	0.04(5)	
BaO	0.08(4)	0.08(4)	0.08(5)	0.08(4)	
F	0.00(0)	0.00(0)	0.00(0)	0.00(0)	
Cl	0.00(0)	0.00(0)	0.00(0)	0.02(1)	
Total	100.36(92)	100.51(54)	95.45(54)	88.62(52)	
apfu	Normalized to 8 O pfu		24 O	36 O	
Si	2.99(1)	2.98(2)	5.77(3)	5.77(9)	
^{IV} Al	1.01(1)	1.02(2)	2.23(3)	2.23(9)	
^{VI} Al	–	–	0.49(5)	2.33(3)	
Ti ²⁺	0.00(1)	0.00(0)	0.17(1)	0.00(0)	
Fe ³⁺	0.00(0)	0.00(0)	–		
ΣZ		0.67(6)			
Fe ²⁺	–	–	1.29(5)	2.42(2)	

Continues on next page

Table 7.3: *Continued from previous page*

Mn ²⁺	0.00(0)	0.00(0)	0.01(0)	0.01(0)
Mg	0.00(0)	0.00(0)	3.76(13)	7.07(3)
ΣY		5.05(9)	11.92(3)	
Cr ³⁺	0.00(0)	0.00(0)	0.00(0)	0.00(0)
Zn	0.00(0)	0.00(0)	0.02(0)	0.10(1)
Na	0.97(5)	0.97(3)	0.03(1)	0.02(0)
Ca	0.00(0)	0.01(2)	0.00(0)	0.01(0)
K	0.02(3)	0.01(1)	1.87(4)	0.01(1)
Ba	0.00(0)	0.00(0)	0.00(0)	0.01(0)
F	0.00(0)	0.00(0)	0.00(0)	0.00(0)
Cl	0.00(0)	0.00(0)	0.00(0)	0.01(0)

n indicates number of analyses. *n.d.* indicates value not determined.

Tur-gneiss/segregation refers to Tur-gneiss occurring in contact with segregations.

Valence of Fe in respective minerals assumed from stoichiometry.

7.4.4 Tourmaline major element chemistry

Following the nomenclature of Henry *et al.* (2011), all generations of tourmaline in the Pfitsch formation are dravite, with a significant Fe content (Figs. 7.3 and 7.4). On average, tourmaline in the Tur-gneiss has an X-site composition of 76–88% Na, 7–19% Ca, 1–2% K, and up to 6% vacancies (Table 7.4; Fig. 7.3). These values are based on electron microprobe analyses that have been normalized to 15 cations at the Y, Z, and T sites and assume 3 B per formula unit. Due to the inclusion-rich nature of tourmalines occurring near segregations in the Tur-gneiss, it is possible that the EMP analyses were contaminated by inclusions hidden beneath the polished crystal surface, leading to some analyses having an over-filled X site following normalization (*i.e.*, Na+Ca+K>1). These analyses are excluded from Fig. 7.3, but it is possible that the remaining data was still affected by contamination from the inclusions. All collected data is included in Table 7.4 to allow a comprehensive comparison of the different tourmaline generations. Whenever sector zoning was apparent, analysis points in the a sector were selected, unless the magnitude of sector zoning was the target of investigation.

Table 7.4: Average tourmaline compositions in the Pfitsch Formation

wt. %	Tur-gneiss near segregations			Tur-gneiss	Chl-Bt-schist	Tur-schist	Ms-quartzite
	Core	Mantle	Rim				
SiO ₂	36.7(4)	36.2(4)	36.7(4)	37.5(2)	37.5(3)	37.0(2)	38.0(2)
Al ₂ O ₃	27.5(4)	27.5(4)	28.9(6)	27.5(6)	26.6(5)	26.7(2)	29.8(5)
K ₂ O	0.09(1)	0.09(2)	0.08(3)	0.08(2)	0.09(4)	0.09(1)	0.07(1)
CaO	0.42(8)	0.86(14)	1.1(2)	0.6(1)	0.78(8)	0.4(2)	0.4(1)
Na ₂ O	2.77(8)	2.6(1)	2.39(8)	2.6(1)	2.4(1)	2.67(8)	2.7(1)
BaO	0.08(4)	0.07(3)	0.05(3)	0.06(3)	0.05(4)	0.08(4)	0.08(3)
MgO	8.5(2)	8.1(3)	9.1(1)	9.6(2)	9.0(4)	8.6(3)	9.8(1)
Fe ₂ O ₃	11.9(7)	12.7(8)	9.4(6)	11.1(9)	11.8(2)	13.5(7)	7.8(6)
Cr ₂ O ₃	0.01(1)	0.02(2)	0.02(2)	0.01(1)	0.01(0)	0.01(1)	0.01(1)

Continues on next page

Table 7.4: *Continued from previous page*

MnO	0.03(2)	0.02(1)	0.01(1)	0.06(2)	0.05(2)	0.05(1)	0.03(2)
ZnO	0.09(3)	0.09(3)	0.07(2)	0.07(4)	0.07(6)	0.08(4)	0.16(3)
TiO ₂	0.9(2)	0.56(7)	0.45(6)	0.6(1)	0.46(5)	0.61(7)	0.28(7)
Cl	0.00(0)	0.00(0)	0.01(1)	0.00(0)	0.00(0)	0.00(0)	0.00(0)
F	0.07(8)	0.00(0)	0.00(0)	0.10(5)	0.06(5)	0.06(4)	0.21(5)
Total	89.0(5)	88.8(4)	88.3(6)	89.9(4)	88.9(9)	89.8(3)	89.3(3)
apfu	Normalized to 15 YZT, assuming 3 B pfu.						
Na	0.88(3)	0.84(4)	0.76(2)	0.82(3)	0.76(2)	0.84(3)	0.84(3)
Ca	0.07(1)	0.15(3)	0.19(3)	0.10(2)	0.14(1)	0.07(3)	0.07(2)
K	0.02(0)	0.02(0)	0.01(0)	0.02(0)	0.2(1)	0.02(0)	0.01(0)
Ba	0.02(3)	0.00(0)	0.00(0)	0.00(0)	0.00(0)	0.00(0)	0.00(0)
□	0.01(3)	0.00(2)	0.03(1)	0.06(2)	0.08(3)	0.06(2)	0.07(2)
Mg	2.08(4)	2.00(8)	2.22(2)	2.31(3)	2.21(6)	2.09(7)	2.33(3)
Al	5.32(8)	5.35(7)	5.6(1)	5.2(1)	5.13(4)	5.13(3)	5.60(8)
Si	6.01(5)	5.98(5)	6.00(4)	6.04(2)	6.13(7)	6.03(2)	6.07(2)
B ^a	3.00	3.00	3.00	3.00	3.00	3.00	3.00
Cr	0.00(0)	0.00(0)	0.00(0)	0.00(0)	0.00(0)	0.00(0)	0.00(0)
Mn	0.00(0)	0.00(0)	0.00(0)	0.01(0)	0.01(0)	0.01(0)	0.02(0)
Zn	0.01(0)	0.01(0)	0.01(0)	0.01(0)	0.01(1)	0.01(0)	0.00(0)
Ti	0.11(2)	0.07(1)	0.06(1)	0.07(1)	0.06(1)	0.08(1)	0.03(1)
Cl	0.00(0)	0.00(0)	0.00(0)	0.00(0)	0.00(0)	0.00(0)	0.00(0)
F	0.04(4)	0.00(0)	0.00(0)	0.05(2)	0.03(3)	0.03(2)	0.11(3)
Fe treated as Fe ³⁺ and O/(OH+F) calculated by charge balance (max. Fe ³⁺ pfu)							
Fe ³⁺	1.46(9)	1.6(1)	1.15(8)	1.4(1)	1.46(3)	1.66(8)	0.94(8)
OH	3.8(1)	3.30(8)	3.42(4)	3.13(5)	3.0(1)	3.02(6)	3.15(5)
O	0.2(1)	0.70(8)	0.58(4)	0.82(5)	1.0(1)	0.98(6)	0.75(5)
Assume 4 OH+F pfu and Fe ³⁺ /Fe ²⁺ calculated by charge balance (min. Fe ³⁺ pfu)							
Fe ²⁺	0.2(1)	0.65(8)	0.54(4)	0.82(5)	1.0(1)	0.98(6)	0.75(5)
Fe ³⁺	1.3(2)	0.93(1)	0.61(9)	0.53(7)	0.46(9)	0.67(7)	0.19(6)
OH	3.96(4)	4.00(0)	4.00(0)	3.95(2)	3.97(3)	3.97(2)	3.89(3)

^aValues fixed during normalization.

The minimum and maximum Fe³⁺ and Fe²⁺ pfu in tourmaline from each investigated unit are given in Table 7.4. The minimum amount of Fe³⁺ (or maximum amount of Fe²⁺) pfu is obtained by assuming 4 OH pfu and calculating the Fe²⁺/Fe³⁺ ratio of the octahedral sites by charge balance. Additional Fe³⁺ exceeding the minimum value can be accommodated by deprotonation of the VW sites. As such, the maximum amount of Fe³⁺ is calculated by treating all Fe as ferric and calculating the O/OH ratio of the VW sites. In this case, the minimum amount of Fe²⁺ is 0. Fe likely occurs as a combination of both valence states. As such, the values given by assuming 4 OH pfu can be considered more realistic. However, their actual proportions cannot be determined without measuring H or otherwise constraining the Fe²⁺/Fe³⁺ ratio.

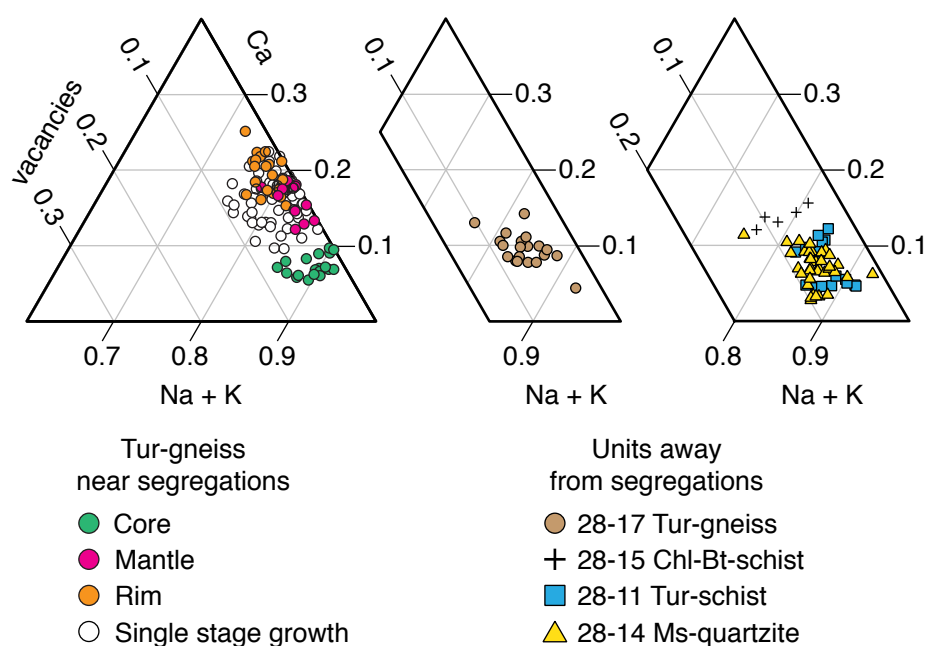


Figure 7.3: X-site compositions of tourmaline in the Tur-gneiss and neighbouring units from the Pfitsch Formation plotted in (Na+K)-Ca-vacancy ternary compositional space. Different stages of growth in tourmaline occurring near segregations in the Tur-gneiss are differentiated by *colour*. Symbols for tourmalines showing a single stage of growth are present everywhere under the symbols of the core, mantle, and rim compositions of tourmalines with multi-stage growth. Data points for analyses with overfilled (*i.e.*, $\text{Na}+\text{Ca}+\text{K}>1$) have been excluded. Contamination of the analysis points shown by feldspar inclusions is possible.

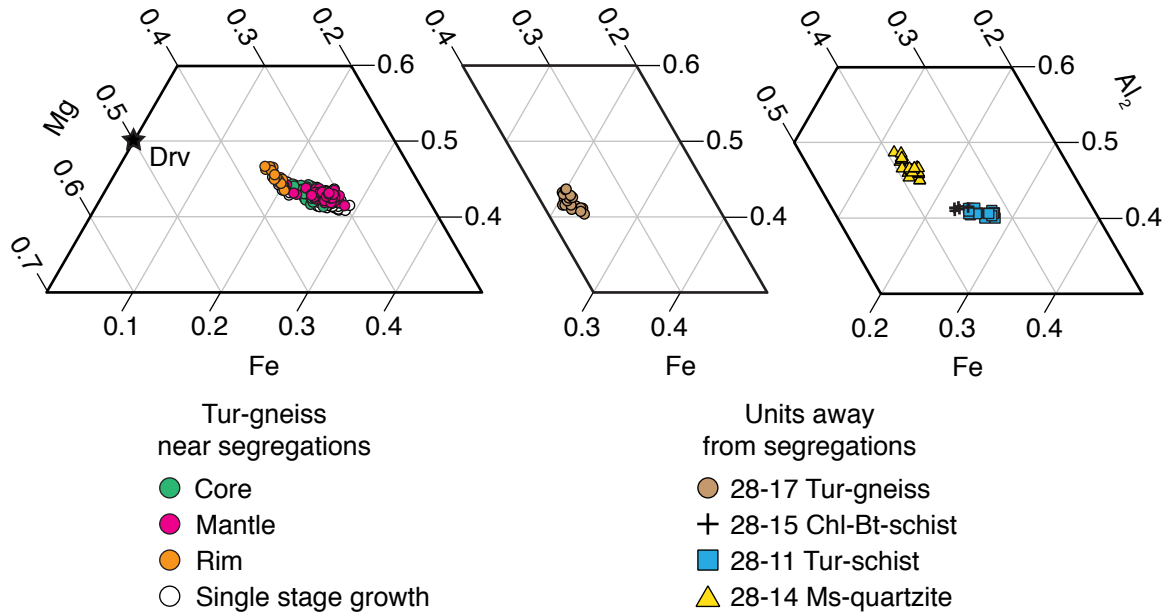


Figure 7.4: Compositions of tourmaline in the Tur-gneiss and neighbouring units from the Pfitsch Formation plotted in Mg-Fe-Al₂ ternary compositional space. Different stages of growth in tourmaline occurring near segregations in the Tur-gneiss are differentiated by *colour*. Symbols for tourmalines showing a single stage of growth are present everywhere under the symbols of the core, mantle, and rim compositions of tourmalines with multi-stage growth. The position of endmember dravite (Drv) is shown with a *star*.

Tourmaline in the major units of the Pfitsch Formation

In general, tourmalines from the different units of the Pfitsch Formation are similar in composition (Table 7.4). Excluding those occurring near the segregations, they are all equally Na-rich with <15% Ca pfu (Fig. 7.3). The different units are most easily distinguished in Mg-Fe-Al₂ ternary compositional space (Fig. 7.4), with tourmaline from each unit having a restricted composition relative to the compositional range of tourmaline occurring near segregations in the Tur-gneiss (Fig. 7.4). The variation in the Fe content of the tourmalines from the neighbouring units correlates well with the Fe content of their host rocks; the most Fe-rich host rock, the Tur-schist (4.79 wt.% Fe₂O₃; Table 7.1) contains the most Fe-rich tourmalines (Fig. 7.4; 28-11 Tur-schist) and the least Fe-rich host rock, the Ms-quartzite (0.79 wt.% Fe₂O₃; Table 7.1) contains the least Fe-rich tourmalines (Fig. 7.4; 28-14 Ms-quartzite). With the exception of the Ms-quartzite, at least 32% of Fe in tourmalines occurring away from segregations is ferric (Table 7.4). In the Ms-quartzite, the possible range in Fe³⁺ is less constrained, and could represent as little as 20% of the total Fe.

Tourmaline occurring near segregations

Within the Tur-gneiss, tourmalines show a larger range in composition in terms of both their X site (Fig. 7.3) and in Mg-Fe-Al₂ compositional space (Fig. 7.4). This is largely a result of the tourmalines near segregations having multiple stages of growth (Figs. 7.2c, d and 7.5). The different generations of tourmaline growth are distinguished based on their major element chemistry, particularly in terms of the Ca/Na ratios. The first generation

of tourmaline growth (cores: stage 1) is the most Na-rich and the subsequent generations (mantle: stage 2 and rims: stage 3) are increasingly Ca-rich, reaching a maximum value of 0.25 Ca pfu in stage 3 tourmaline (Fig. 7.3). Variation in the Fe/Mg ratio is also observed, but to a lesser extent than the X-site composition (*c.f.* Figs. 7.3 and 7.4). Compositional variation within and between different tourmaline generations is best observed in the element maps of a tourmaline crystal displaying all three generations of tourmaline growth (Fig. 7.5). In addition to clearly distinguishing the inclusion mineralogy of the different generations (stage 1: quartz; stage 2: K-feldspar and plagioclase), the Na element map shows a gradual decrease in the Na content of tourmaline with growth. There is no distinct boundary in the Na element maps between stage 1 and stage 2 growth (Fig. 7.5, Na). In contrast, the contact between the first and second generations can be distinguished in the Ca element map (Fig. 7.5, Ca) by the presence of a Ca-rich boundary layer. Although the net variation in Fe/Mg contents is small (Fig. 7.4), their distribution in element maps shows a distinct behaviour between the different growth stages. Within stage 1 tourmaline growth, the Mg (Fe) content increases (decreases) up to the boundary with stage 2 (Fig. 7.5, Mg, Fe). With the start of stage 2 growth, the Mg (Fe) content sharply decreases (increases) prior to once again gradually increasing (decreasing) with growth (Fig. 7.5, Mg and Fe). The third generation of tourmaline growth (stage 3) forms as Ca- and Mg-rich overgrowths on the fracture surfaces and well as crystal rims. Ca and Ti are strongly, and Mg and Fe moderately, sector zoned.

The tourmalines occurring near segregations have a distinctly higher minimum proportion of ferric iron than those occurring away from the segregations (Table 7.4). In all three stages of growth, the minimum amount of Fe^{3+} exceeds the maximum amount of Fe^{2+} , demonstrating that Fe is predominantly ferric. In the first stage of tourmaline growth (core; Table 7.4), >87% of Fe is Fe^{3+} . This value decreases in the second stage of growth to 59%, and in the third stage to 53%.

7.4.5 Tourmaline sector zoning thermometry

Hourglass sector zoning is a common feature in many tourmalines from the Pfisch Formation, visible in both transmitted light as well as in back-scattered electron images. It is most easily resolved in element maps (Fig. 7.5) and displays a behaviour consistent with sector-zoned tourmalines from other localities (see van Hinsberg *et al.*, 2006). Ti and Ca show the highest amount of partitioning between the a, c^+ , and c^- sectors, followed by Fe. Sector zoning can also be discerned in the Mg element map, and slightly in the Na map (Fig. 7.5). Element partitioning between the different growth sectors of a tourmaline crystal has been demonstrated to be dependent on temperature, with partitioning decreasing with increasing temperature (van Hinsberg and Schumacher, 2007a). Using the calibration of van Hinsberg and Schumacher (2007a), temperatures growth profiles for each generation of tourmaline could be determined (Fig. 7.6). The estimated uncertainty of the calibration for absolute temperatures is at least 50 °C (van Hinsberg and Schumacher, 2007a), however, the uncertainty in the relative temperatures between adjacent points and different growth zones is much less.

The first generation of tourmaline growth (stage 1) qualitatively shows decreasing partitioning of elements between the different sectors with growth (Fig. 7.5). This trend is reflected in the core-rim temperature profiles of two crystals (Fig. 7.6). The first crystal is sector zoned in its core, corresponding to stage 1 growth. Sector zoning in the second crystal (Fig. 7.6, bottom) extends from the core through the mantle, covering both stage 1 and stage 2 growth. The stage 1 temperatures of both crystals are in good agreement,

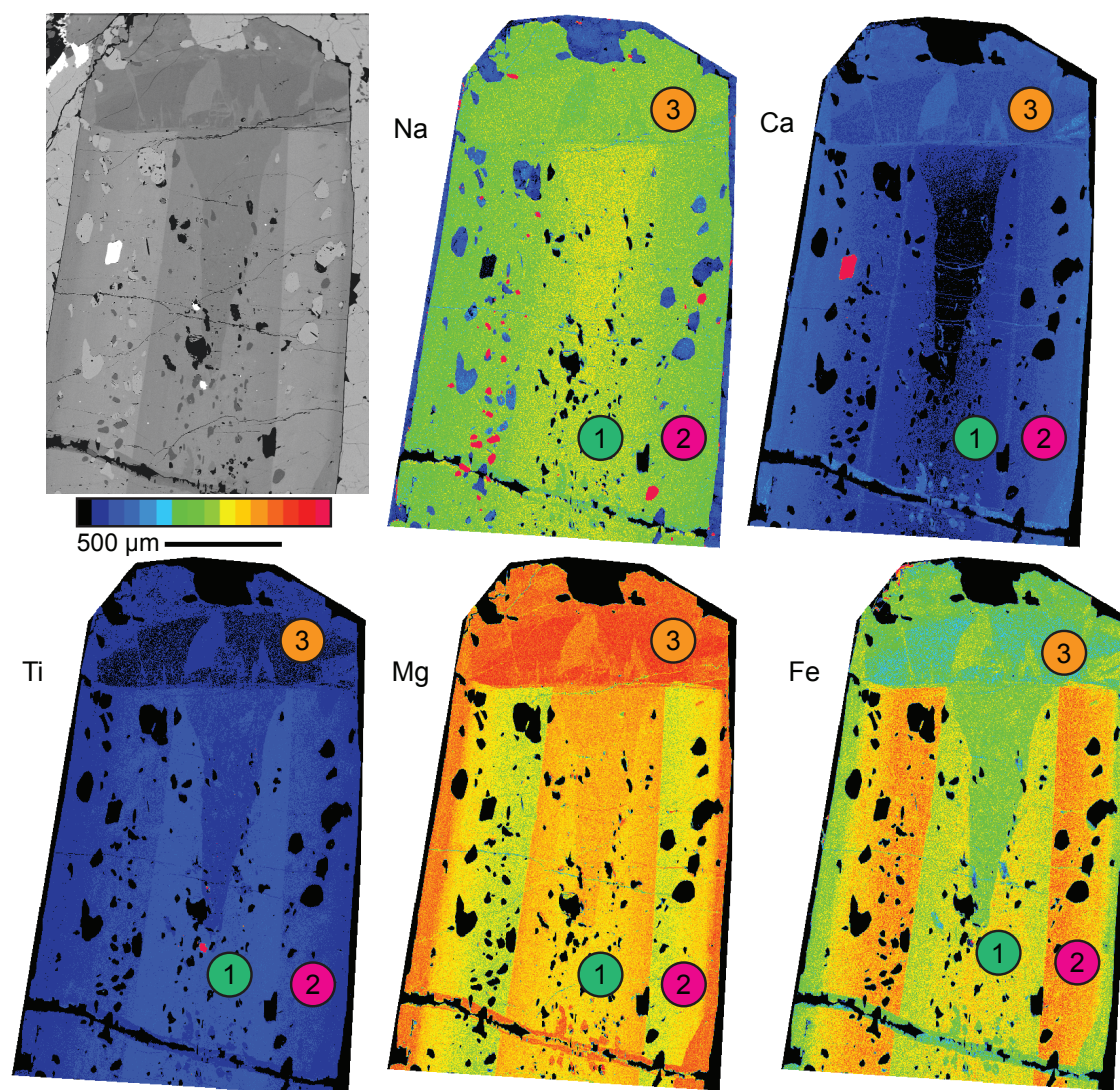


Figure 7.5: Backscattered electron image and Na, Ca, Ti, Mg, and Fe element maps of a tourmaline crystal occurring near a segregation in the Tur-gneiss. In each map, the abundance of the respective element is represented by the colour scale, whereby *dark blue* corresponds to the lowest abundance and *red*, the highest. The three stages of growth are labeled and correspond to 1-cores, 2-mantle, and 3-rims.

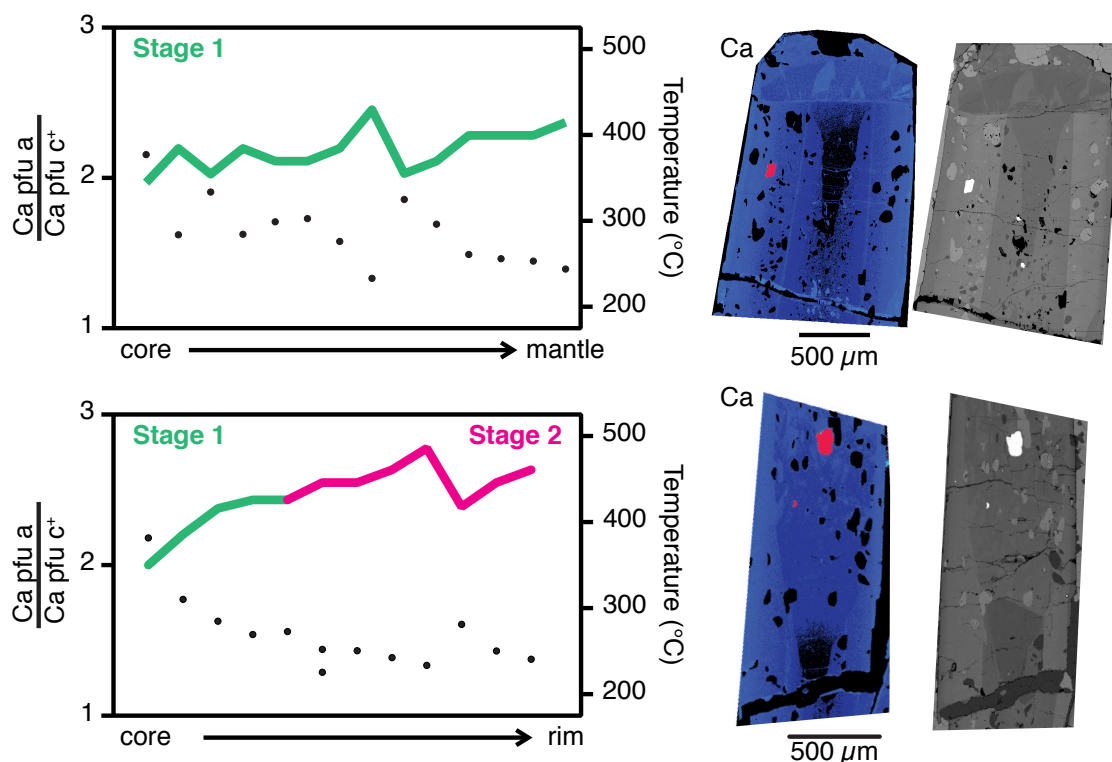


Figure 7.6: Examples of sector zoning thermometry of two tourmaline crystals (Ca element maps and BSE images at right) from near segregations in the Tur-gneiss. The *points* indicate the ratio of Ca pfu in the a and c+ sectors and the *lines* mark the associated temperature following the method of van Hinsberg and Schumacher (2007a). Temperatures determined for the first generation of tourmaline growth (stage 1; crystal cores) are shown in *green* and those for the second generation of tourmaline growth (stage 2; crystal mantles) are shown in *pink*.

showing temperatures increasing from ~300 to 400 °C with growth. The temperature profile from stage 1 to stage 2 growth increases gradually, reaching temperatures up to 500 °C (Fig. 7.6). Zoning in the third generation fracture overgrowth depicted in Fig. 7.5 is also interpreted as element partitioning between the a and c⁺ growth sectors, giving values of (Ca pfu a)/(Ca pfu c⁺) = 1.63–1.66. Based on the calibration of van Hinsberg and Schumacher (2007a), this corresponds to a formation temperature of ~400 ± 50 °C.

7.5 Discussion

7.5.1 Tourmaline solid solution

Although all tourmalines show relatively restricted compositions, especially those not occurring in proximity to segregations, the compositional variations in the different units are controlled by different exchange vectors. This is most apparent in the element variation plots given in Fig. 7.7.

Tourmalines in the major units of the Pfitsch Formation

Tourmalines in the Tur-gneiss and the Ms-quartzite show similar element variation, including Fe-Al and Na-Ca exchange, with Mg values remaining relatively constant (Fig. 7.7, *left*). Additionally, Ca is positively correlated with Fe with crystal growth (Fig. 7.9; element maps available in Appendix B). Fe-Al exchange occurs at the octahedral YZ sites and could reflect homovalent substitution via the $^{YZ}Fe^{3+}Al_{-1}$ exchange vector. However, tourmalines in these units may have predominantly ferrous Fe (Table 7.4). As such, Fe-Al exchange may reflect the following heterovalent substitutions: $^{X}Ca^{YZ}Fe^{2+}(^{X}Na^{YZ}Al)_{-1}$, $^{X}Na^{YZ}Fe^{2+}(^{X}\square^{YZ}Al)_{-1}$, and/or $^{YZ}Fe^{2+}VW^{OH}(^{YZ}Al^{VWO})_{-1}$. The first heterovalent exchange vector additionally accounts for Ca-Na exchange and positively correlates Ca and Fe.

Tourmalines in the Tur-schist and the Chl-Bt-schist show similar element variation that contrasts the behaviour of tourmalines in the Tur-gneiss and the Ms-quartzite (Fig. 7.7, *left*). The predominant element variation is Fe-Mg exchange followed by Na-Ca exchange. Additionally, Ca is positively correlated with Mg with crystal growth (Fig. 7.9; element maps available in Appendix B). As in the case of the Tur-gneiss and the Ms-quartzite, Fe may be predominantly ferrous (Table 7.4), and thus Fe-Mg exchange may reflect $Fe^{2+}Mg_{-1}$ homovalent substitution at the YZ sites. Heterovalent Ca-Na exchange at the X site stipulates heterovalent exchange at either the YZ or VW sites via $^{X}Na^{YZ}Fe^{3+}(^{X}Ca^{YZ}Mg)_{-1}$, $^{X}\square^{YZ}Fe^{3+}(^{X}Na^{YZ}Mg)_{-1}$, and/or $^{X}Ca^{VWO}(^{X}Na^{VWO}OH)_{-1}$. The first of these heterovalent exchange vectors additionally accounts for the positive correlation of Ca with Mg during crystal growth.

The relative predominance of Fe-Al or Fe-Mg exchange in tourmalines from the Tur-gneiss/Ms-quartzite or Tur-schist/Chl-Bt-schist, respectively, corresponds with the expected Fe-exchange behaviour of the major Fe-bearing mineral of each rock type. Specifically, in the Tur-schist and the Chl-Bt-schist, the major Fe-bearing minerals are biotite and chlorite. These minerals are well-known for Fe-Mg exchange, whereby their Fe/(Fe+Mg) ratios decrease with metamorphic grade. In contrast, the major Fe-bearing mineral in the Tur-gneiss and the Ms-quartzite is muscovite. With prograde metamorphism, muscovite is expected to have an increasing phengitic component via the Tschermak substitution $FeSiAl_{-2}$. Thus, Fe-exchange in the tourmalines from the Pfitsch Formation is interpreted

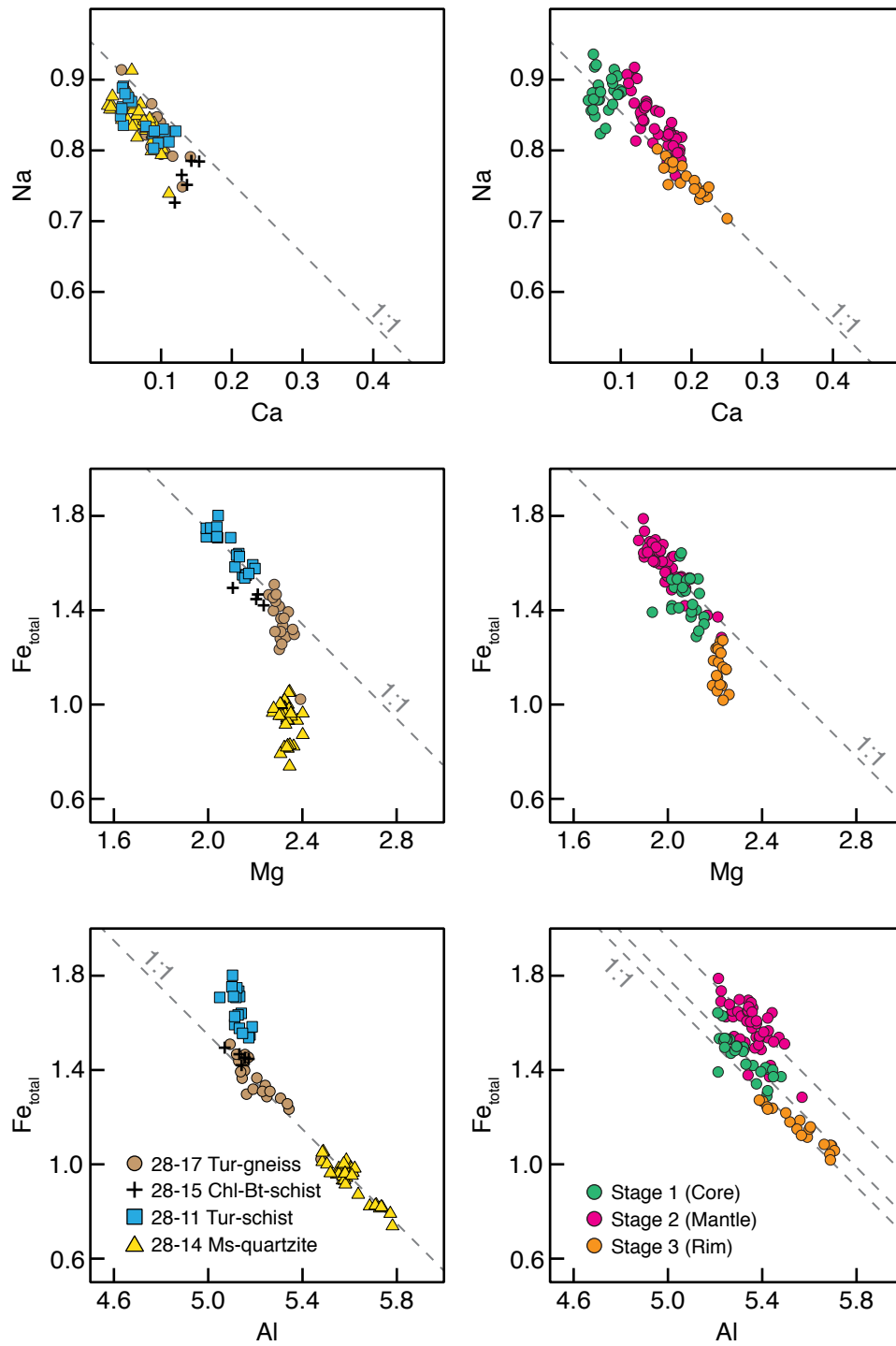


Figure 7.7: Na-Ca, Fe-Mg, and Fe-Al variation plots for tourmaline in units away from (*left*) and near (*right*) segregations. The *dashed lines* show 1:1 variation in each plot. Values are given as atoms pfu following normalization to 15 YZT.

as dependent on the major Fe-bearing mineral in its host rock. Therefore, tourmalines in these units are interpreted as prograde because their Fe-variation reflects the prograde behaviour of their coexisting Fe-bearing minerals.

Tourmalines occurring near segregations

The increased complexity of element exchange in tourmalines occurring near segregations is revealed in the increased scatter in the element variation diagrams (Fig. 7.7, *right*). The first stage of tourmaline growth is characterized by Fe-Al exchange with relatively constant Mg and Ca contents. Fe in this stage of tourmaline growth is >87% ferric (Table 7.4). Thus, the major exchange vector is $^{YZ}\text{Fe}^{3+}\text{Al}_{-1}$. Minor variation in the X-site composition (Figs. 7.3, 7.9) can be accommodated by the following minor exchange vectors: $^{\text{X}}\text{Ca}^{YZ}(\text{Mg}, \text{Fe}^{2+})[\text{Na}^{YZ}(\text{Fe}^{3+}, \text{Al})]_{-1}$ and/or $^{\text{X}}\text{Ca}^{VW}\text{O}(\text{Na}^{VW}\text{OH})_{-1}$. The correlation of Ca and Mg with crystal growth supports the occurrence of the first heterovalent exchange vector, in which the contribution of Fe^{2+} is expected to be minor.

The second stage of tourmaline growth in crystals occurring near segregations shows the most compositional variation of all investigated tourmalines. This includes Fe-Mg, Fe-Al, and Na-Ca exchange (Fig. 7.7, *right*). This stage of growth likely has more ferrous Fe than the first stage (Table 7.4). As a result, it is expected that both $^{YZ}\text{Fe}^{2+}\text{Mg}_{-1}$ and $^{YZ}\text{Fe}^{3+}\text{Al}_{-1}$ homovalent exchange are occurring at the octahedral sites. Na-Ca exchange at the X site requires heterovalent exchange, involving the exchange vectors given for the first stage of tourmaline growth.

The third and final stage of tourmaline growth in tourmalines near segregations is the most Ca-rich of all tourmalines investigated (Table 7.4 and Fig. 7.3). It is characterized by Fe-Al and Na-Ca exchange with a relatively constant Mg content (Fig. 7.7, *right*). In addition, Ca correlates with Fe during crystal growth (Figs. 7.5, 7.9). This behaviour is comparable to element exchange described in the Ms-quartzite and the Tur-gneiss. However, stage 3 is distinguished from those tourmalines by its occurrence on fracture surfaces, its significantly higher Ca content, and its higher minimum ferric Fe content. As such, homovalent $^{YZ}\text{Fe}^{3+}\text{Al}_{-1}$ exchange is expected to be more prevalent in stage 3 tourmaline growth, leaving $^{\text{X}}\text{Ca}^{VW}\text{O}(\text{Na}^{VW}\text{OH})_{-1}$ as perhaps the more important Ca-Na exchange vector.

7.5.2 Deciphering the P-T path of the Pfitsch Formation

The textural relationships between the three stages of tourmaline growth in crystals occurring near segregations in the Tur-gneiss provide a timeline of tourmaline formation: (a) stage 1 tourmaline growth coprecipitating with quartz inclusions; (b) stage 2 tourmaline growth coprecipitating with feldspar inclusions; (c) extensional fracture of the tourmaline crystals; and (d) overgrowth of fracture surfaces by secondary tourmaline (stage 3).

Sector zoning thermometry of tourmaline from the Tur-gneiss supports gradual prograde growth of stage 1 and stage 2 (Fig. 7.6), nearly reaching peak metamorphic conditions of 500–550 °C (Selverstone *et al.*, 1984). Although no geobarometer is currently calibrated for tourmaline, from the known P-T path of the underlying units (Selverstone *et al.*, 1984), we can expect corresponding pressures to have ranged from ~0.7 up to 1.0 or 1.1 GPa (Fig. 7.8). The occurrence of stage 3 tourmaline growth on fracture surfaces supports their growth following regional uplift and E-W extension. Sector zoning ther-

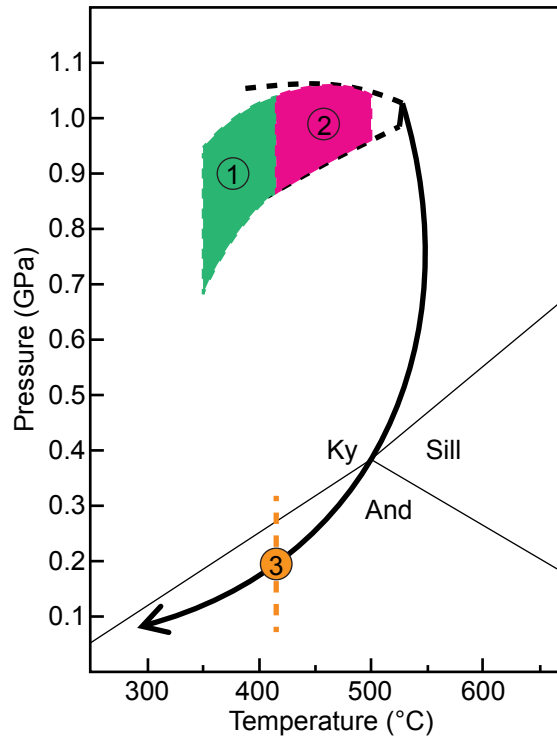


Figure 7.8: Temperatures of each generation of tourmaline growth (1, 2, and 3) determined by sector zoning thermometry superimposed on the metamorphic P-T path constrained by Selverstone *et al.* (1984). Aluminosilicate phase diagram included for reference.

metry suggests stage 3 grew at $\sim 400^\circ\text{C}$, which corresponds to 0.2 GPa on the retrograde metamorphic P-T path of Selverstone *et al.* (1984).

The major element composition of tourmalines from the Pfitsch Formation is comparable to tourmalines found in other medium-grade Ca-poor metapelites and metapsammities, which typically have 0.4–0.7 X_{Mg} and <0.4 Ca pfu as summarized by Henry and Dutrow (1996) and Henry and Guidotti (1985). In addition, the gradual increase in Ca content and X_{Mg} along core-to-rim profiles (Fig. 7.5) is common in metamorphic tourmalines (*e.g.*, Henry and Guidotti, 1985; van Hinsberg and Schumacher, 2011) and has been correlated with increasing metamorphic grade (Henry and Dutrow, 1996). This is consistent with the interpretation that both the first and second stages of tourmaline grew on the prograde path. In contrast, the third stage of tourmaline growth, forming fracture overgrowths as well as one-stage single crystals, shows increasing X_{Fe} compositions with growth (Fig. 7.9). This is consistent with the interpretation of the final stage of tourmaline forming on the retrograde path.

7.5.3 Metamorphic fluid movement in the Tur-gneiss

The distribution of B, and thus tourmaline, within metamorphic rocks depends on the initial distribution of B within the precursor rock, the remobilization of B during metamorphism, as well as the introduction of boron from metasomatic fluids. B concentrations in the Tur-gneiss range from 21–1196 ppm B, with a typical sample having 165 ppm B. The B concentration and, correspondingly, the abundance of tourmaline in the Tur-gneiss are highly variable, with the highest concentrations occurring in and near segregations and

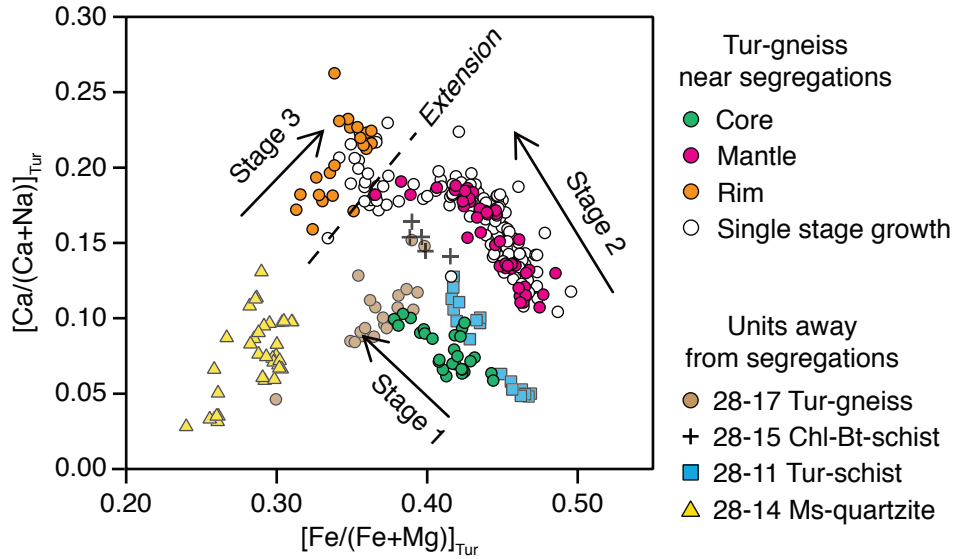
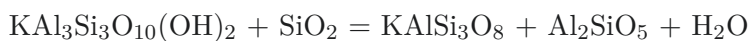


Figure 7.9: Compositions of different stages of growth (stage 1 in *green*, stage 2 in *pink*, stage 3 in *orange*) from tourmaline occurring near segregations in the Tur-gneiss plotted in $\text{Ca}/(\text{Ca}+\text{Na})$ versus $\text{Fe}/(\text{Fe}+\text{Mg})$ space. The *white* symbols indicate tourmaline that could not be classified texturally into one of the three growth stages. The *arrows* indicate the direction of growth based on the compositional zoning within each growth stage. The *dashed line* separates the second and third stages of growth, indicating the formation of extensional fractures. The composition of tourmaline from the tourmaline-bearing units sampled from the roadcut are plotted for comparison. Crystallization in the latter always moves towards increasing $\text{Ca}/(\text{Ca}+\text{Na})$ values.

the lowest occurring far from segregations (Table 7.2). The field association of tourmaline with quartzofeldspathic segregations in the Tur-gneiss combined with the corresponding increase in whole rock B contents in the unit with proximity to the segregations suggests a link between B mobilization and the segregation-forming event.

The association of the highest B concentrations with the quartzofeldspathic segregations indicates that the segregation-forming metamorphic fluids mobilized and concentrated B, leading to the crystallization of tourmaline on the prograde path. This interpretation is supported by the prevalence of quartz and feldspar inclusions in tourmalines crystallizing near the segregations, indicating that both quartz and tourmaline, followed by feldspar and tourmaline co-crystallization occurred. The first stage of tourmaline growth observed in samples in and near segregations is dominated by quartz inclusions, reflecting the saturation of segregation-forming fluids with respect to quartz. Feldspar inclusions only appear in the second stage of tourmaline growth. The composition of the feldspar inclusions in stage 2 tourmaline matches that in the segregation matrix, supporting the interpretation of their coeval precipitation. Thus, the tourmaline inclusion mineralogy suggests that feldspar crystallization occurred after quartz in the segregation, possibly resulting from the progressive breakdown of muscovite:



However, no aluminosilicate phases were identified in thin section. Thermodynamic modelling by van Hinsberg and Schumacher (2007b) predicted that the saturation of tourmaline destabilizes aluminosilicate, consistent with its absence in the Tur-gneiss. Moreover, sheet silicates like micas are important hosts of B in metapelites and their progressive breakdown is often invoked as a B source for tourmaline formation (*e.g.*, Bebout and Nakamura,

2003; Marschall *et al.*, 2009a).

Following peak metamorphic conditions, during uplift and regional E-W extension (Frisch *et al.*, 2000), the larger tourmaline crystals developed brittle extensional fractures and the segregations developed boudinage. Subsequent fluid mobilization associated with fracturing and increased porosity during this extensional event resulted in the overgrowth of tourmaline fracture surfaces, as well as the crystallization of tourmaline in the necks of the segregation boudins. This tourmaline-forming event is represented by the third stage of tourmaline growth at $\sim 400 \pm 50$ °C, which correlates to a pressure of ~ 0.2 GPa based on the P-T path of Selverstone *et al.* (1984) (Fig. 7.8). Unlike stage 1 and stage 2 tourmaline growth near the segregations, the tourmaline-fracture overgrowths are inclusion-free, suggesting this late-stage fluid did not co-crystallize other mineral phases.

7.5.4 Evolving fluid composition

The experimental investigation of von Goerne *et al.* (2011) linked the number of vacancies at the X site in tourmaline to the ionic strength of the fluid. The relatively low and constant number of vacancies (<0.1 ; Fig. 7.3) at the X site of tourmaline from the Tur-gneiss supports their crystallization from a consistently high concentration fluid. From the experimental investigation on the incorporation of Ca and Na in dravitic tourmaline (Chapter 6), the Ca/(Ca+Na) ratio in the fluid is expected to nearly correspond with that in the tourmaline at 1.0 GPa, 500 °C (Fig. 6.4). Therefore, at the peak metamorphic conditions of the Pfitsch Formation (~ 1.0 GPa, 500 °C; Selverstone *et al.*, 1984), the fluid composition likely corresponded with the peak Ca/(Ca+Na) ratio observed in the second stage of tourmaline growth (~ 0.18 ; Fig. 7.9). Moreover, the experimental results of Chapter 6 demonstrated that at pressures <1.0 GPa, Ca preferentially partitions into tourmaline over the fluid. Consequently, as tourmaline crystallization in the Pfitsch Formation did not exceed 1.0 GPa (Fig. 7.8), the Ca/(Ca+Na) of the metamorphic fluid is not expected to have exceeded that observed in the tourmalines. As such, all observed Ca/(Ca+Na) ratios in tourmaline can be considered as maxima for the Ca/(Ca+Na) ratios of the fluid.

With prograde growth (stages 1 and 2; Fig. 7.9), the Ca/(Ca+Na) ratio of tourmaline ranges from ~ 0.05 up to the peak conditions of ~ 0.18 . This trend reflects either: the evolution of the fluid composition; variation in tourmaline's relative incorporation of Ca and Na with changing P and T; or a combination of both. Based on the experimental results of Chapter 6, increasing T results corresponds with increasing Ca/(Ca+Na) ratios in tourmaline. Therefore, increasing Ca/(Ca+Na) ratios with growth across stage 1 and stage 2 may reflect the increasing temperature of crystallization, with the fluid composition remaining constant. However, the experimental results also demonstrated that increasing P has the opposite effect, reducing Ca incorporation in tourmaline. As a result, the combined effects of increasing P and T may counteract each other, leading to a constant partitioning of Ca and Na between tourmaline and the fluid. Since the relationship between P and T and Ca-Na distribution between tourmaline and the fluid have not been constrained in detail in the full range of the metamorphic conditions of the Pfitsch Formation, it is difficult to determine variations in Ca-Na partitioning with prograde growth. The relatively large increase in Ca/(Ca+Na) values with growth (Fig. 7.9) encourages the interpretation that the Ca/(Ca+Na) ratio of the fluid increased with prograde metamorphism. However, the pervasiveness of increasing Ca/(Ca+Na) ratios with growth in metamorphic tourmalines (*e.g.*, Henry and Dutrow, 1996) suggests a P-T control.

The final stage of tourmaline growth (stage 3) occurred at a pressure much lower than

the prograde tourmaline (~ 0.2 GPa), but in the same temperature range (Fig. 7.8). Decreasing pressure is expected to increase Ca incorporation (see Chapter 6), consistent with the increased $\text{Ca}/(\text{Ca}+\text{Na})$ ratio observed in stage 3 tourmaline growth (Fig. 7.9). As a result, it is possible that the $\text{Ca}/(\text{Ca}+\text{Na})$ ratio of the retrograde metamorphic fluid is comparable, or perhaps lower, than that of the prograde metamorphic fluid.

Another potentially insightful feature of tourmalines in the Pfitsch Formation is the variability in the minimum amount of ferric Fe. The first tourmaline growth associated with segregation-formation comprises distinctly ferric Fe ($>87\%$ of total Fe). The minimum amount of ferric Fe gradually decreases with subsequent tourmaline growth (Table 7.4). Moreover, tourmalines occurring away from the segregations have distinctly lower minimum ferric Fe contents ($>20\%$ of total Fe). This suggests that the first segregation-forming fluids were distinctly oxidized relative to the surrounding rocks and progressively became more reduced with segregation development, perhaps reflecting increased involvement of less-oxidized fluids from the neighbouring units.

7.6 Conclusions

Tourmaline in the Pfitsch Formation of the Tauern Window, Eastern Alps, grew on the pro- and retrograde path, recording the formation's evolution during Alpine metamorphism. The B concentration, and thus the tourmaline content, of the different units increases towards coarse-grained quartzofeldspathic segregations present in the Tur-gneiss. Tourmalines occurring near the segregations record the mobilization and concentration of B during prograde metamorphism ($\sim 300\text{--}500$ °C, up to 1.0 GPa), as well as the crystallization of quartz followed by feldspar during the formation of the segregations. In addition, the gradual increase in the minimum ferric Fe content of tourmaline occurring near segregations suggests the gradual reduction of the segregation fluid with progressive metamorphism. The evolution of tourmaline's X site composition supports crystallization from a concentrated fluid with a consistent or increasing $\text{Ca}/(\text{Ca}+\text{Na})$ ratio up to ~ 0.18 . Subsequently, the unit experienced brittle extension during regional uplift, concurrent with the mobilization of fluids along fracture surfaces, leading to the development of retrograde overgrowths on pre-existing tourmaline, as well as the nucleation of tourmaline in boudin necks. This final stage of tourmaline growth occurred at ~ 400 °C and ~ 0.2 GPa. The retrograde fluid has a $\text{Ca}/(\text{Ca}+\text{Na})$ ratio lower than or comparable to that of the prograde metamorphic fluid.

Chapter 8

Conclusions and outlook

Although tourmaline's complex crystal chemistry allows it to sample a wide selection of the elements present during its growth, their degree of incorporation is not solely based on their concentration in the formation environment. Tourmaline does not serve as a passive recorder of the composition of its growth environment, but rather pressure (P) and temperature (T), in addition to fluid composition (X), affect the partitioning of elements between tourmaline and the coexisting fluid. Development of our understanding of tourmaline's crystal chemistry will allow this common accessory mineral to provide increasing amounts of insight into the composition and evolution of its formation environment.

The studies detailed in this thesis have focussed on the crystal chemistry of the ninefold-coordinated X site. Specifically, the experiments were designed to constrain the P-T-X controls on the incorporation of the major X-site-occupying ions, K, Na, and Ca, in Mg-Al tourmaline. As one would expect, increasing the relative concentration of each element in the crystallizing fluid results in a corresponding increase in its occupancy of the X site at a given P and T. As a result, tourmaline's chemistry is largely dependent on the composition of its growth environment. However, the relative incorporation of elements is also highly dependent on the P and T conditions. Therefore, variations in the concentration of elements with growth in a given tourmaline grain do not simply parallel their variation in the coexisting fluid during growth, but must be interpreted in the context of the changing P and T of the environment.

With increasing P and T, Mg-Al tourmaline was demonstrated to incorporate increasing amounts of K at its X site, particularly given a K-rich environment. As a result, K-dominant Mg-Al tourmaline, namely "K-dravite" or its deprotonated equivalent, maruyamaite, can form at upper-mantle conditions given a suitable fluid composition. The occurrence of diamondiferous maruyamaite in the UHP rocks from the Kokchetav Massif, Kazakhstan, therefore provides a record of the presence of K-rich, Na-poor fluids near the diamond stability field in this fossil subduction zone. In contrast, Ca incorporation was demonstrated to be favoured by low P, whereby at $P < 1.0$ GPa, Ca preferentially partitions into tourmaline over the coexisting fluid. T had a secondary effect, with increasing T favouring Ca incorporation. Based on these results, one would expect to find Ca-rich tourmalines in Ca-rich environments metamorphosed at low P and high T. This is consistent with the distribution of uvite in nature and further explains the occurrence of dravite in high-P calcareous rocks.

Tourmalines in the metasedimentary Pfitsch Formation from the Pfitscher Joch in the western Tauern Window record the mobilization of B and the evolution of the metamorphic fluid during pro- and retrograde Alpine metamorphism. Tourmalines occurring near

the quartzo-feldspathic segregations often show up to three stages of growth, differentiated by their inclusion mineralogy and composition. Based on sector zoning thermometry, compositional zoning, and textural relationships, the first two stages of growth occurred on the prograde path, potentially up to peak metamorphic conditions (1.0 GPa, 500 °C; Selverstone *et al.*, 1984). In contrast, the final growth stage occurred on the retrograde path at ~0.2 GPa following brittle E-W extension. With crystal growth, as well as with development of the different growth stages, the Ca/(Ca+Na) ratio in individual tourmaline grains increases up to ~0.18. At the P and T of their metamorphic growth, the Ca/(Ca+Na) ratio of tourmaline is expected to exceed that of the coexisting fluid. As such, the recorded Ca/(Ca+Na) values in the tourmaline from the Pfitsch Formation can be taken as maximum values for the metamorphic fluid.

Variability in the incorporation of the different X-site-occupying ions results from variation in their size and ionic charge, and the corresponding effect on tourmaline's long- and short-range structure. When compared to an X site occupied by Na, the larger ionic radius of K is accommodated in tourmaline locally via shortening of the neighbouring O–H bond at the W(O1) site. In addition, the unit-cell volume of tourmaline increases with K incorporation, largely due to expansion along the more flexible *c*-axis. The ionic radius of ninefold-coordinated Ca (1.18 Å) is only slightly smaller than that of Na (1.24 Å) (Shannon, 1976). Correspondingly, its incorporation results in only a minor change in tourmaline's unit-cell volume. However, increasing the charge of the X-site-occupying ion from 1+ to 2+ has a significant effect on the local crystal structure. The presence of Ca in oxy-uvite results in the local deprotonation of the neighbouring W(O1) OH-bearing site. In contrast, W(O1) sites neighbouring a vacant X site in oxy-uvite remain protonated. The 2+ charge of Ca is therefore locally accommodated in tourmaline's structure. Bond valence arguments may lead one to expect the increased charge at the X site to correspond with a decrease in charge at the coordinated octahedral Y and Z sites [*e.g.*, ${}^{\text{X}}\text{Ca}^{\text{YZ}}\text{Mg}({}^{\text{X}}\text{Na}^{\text{YZ}}\text{Al})_{-1}$]. However, this was not observed. Instead, the Mg/Al ratio of all synthesized tourmalines behaved independently of the Ca/Na ratio of the X site, reflecting instead the consistent Mg/Al ratio of the starting material. Conversely, the presence of vacancies at the X site in nearly all synthesized tourmalines corresponded with a significant magnesio-foitite component. Solid solution between the different investigated endmembers and magnesio-foitite is the principle cause of variation in the Mg/Al ratio of the synthesized tourmalines [*e.g.*, ${}^{\text{X}}\square^{\text{YZ}}\text{Al}({}^{\text{X}}\text{Na}^{\text{YZ}}\text{Mg})_{-1}$]. The absence of an X-site-occupying ion results in a decrease in tourmaline's unit-cell volume as well as the lengthening of the O–H bond at the W(O1) site.

8.1 Outstanding questions

This thesis focussed on the major element crystal chemistry of Mg-Al tourmaline's X site. Consequently, the synthesized tourmalines are solid solutions of two or three endmembers, with compositional variation principally occurring at the X site, and Mg/Al consistently occupying the octahedral Y and Z sites. In contrast, natural tourmalines show more complex chemistry with the most extensive compositional variation occurring at the Y and Z sites (see Table 1.1). As a result, the possible effect of variation at the Y and Z sites on the crystal chemistry of the X site remains to be explored. This applies to both hetero- as well as homovalent substitutions at the X site. For instance, heterovalent substitutions at the X site, such as ${}^{\text{X}}\text{Ca}^{\text{YZ}}\text{Mg}({}^{\text{X}}\text{Na}^{\text{YZ}}\text{Al})_{-1}$ or ${}^{\text{X}}\text{Na}^{\text{YZ}}\text{Mg}({}^{\text{X}}\square^{\text{YZ}}\text{Al})_{-1}$, are clearly linked to the composition of the Y and Z sites. The Y site can incorporate cations with charges ranging from 1+ (Li) to 3+ (Al, V, Cr, Fe) in major element concentrations. Since the Y

site is coordinated to the X site, bond valence arguments dictate that the composition of the Y site will affect that of the X site.

Perhaps less intuitively, homovalent substitutions at the X site [*i.e.*, ${}^X\text{K}({}^X\text{Na})_{-1}$] may also depend on substitutions at the other sites. This can be expected from the long- and short-range structural effects of substitutions, rather than simple bond valence arguments. For example, the experiments described in Chapters 3 and 4 establish that significant K incorporation in otherwise dravitic tourmaline can only occur at relatively high P and T, even in the presence of a K-rich, Na-poor fluid. However, the occurrence of K-rich povondraite $[\text{NaFe}_3^{3+}(\text{Mg}_2\text{Fe}_4^{3+})\text{Si}_6\text{O}_{18}(\text{BO}_3)_3(\text{OH})_3\text{O}]$ as clast overgrowths in brecciated meta-evaporites in Alto Chapare, Cochabamba, Bolivia (Grice *et al.*, 1993; Žáček *et al.*, 2000), suggests high amounts of K incorporation can occur at crustal pressures. It appears that the presence of Fe^{3+} at the Y and Z sites affects tourmaline's structure, such that incorporation of the otherwise incompatible K ion is facilitated. As a result, the effects of changing the size and charge of ions at the Y and Z sites on the chemistry of the X site needs to be explored.

Moreover, other intensive properties beyond P, T, and X may affect the chemistry of tourmaline's X site. For example, in the Ca-Na partitioning experiments described in Chapter 6, the main Ca-incorporation mechanism is ${}^X\text{Ca}^{\text{VW}}\text{O}[{}^X\text{Na}^{\text{VW}}(\text{OH})]_{-1}$. This exchange mechanism is expected to be sensitive to pH, whereby increasing pH encourages Ca incorporation. Another intensive property that may be expected to affect tourmaline's crystal chemistry is the fugacity of oxygen. Some of the major elements found in the different tourmaline endmembers have multiple oxidation states, the most important being Fe. The valence state of Fe occurring at tourmaline's Y and Z sites likely affects both the local charge budget, as well as the short- and long-range structure of the X site. For example, it is likely that the variation in the oxidation state of Fe between buergerite, schorl, and povondraite affects the partitioning of the major X-site-occupying ions between tourmaline and a coexisting fluid.

Finally, although compositionally simple synthetic tourmalines have distinct Raman bands, natural tourmalines form solid solutions of multiple endmembers. As a result, their Raman spectra in the O–H stretching vibrational range are expected to include bands of the different endmembers they comprise. Some of these bands assigned to different coordination environments may overlap, making their identification as well as the integration of their respective peak intensities difficult. Moreover, the long-range effects of the solid solution may lead to small shifts in the band positions, resulting in their misassignment. Combined, these effects will complicate Raman band assignment in natural tourmalines, making the calculation of their composition potentially more difficult. As a result, it is necessary that the Raman spectra of simple endmember tourmalines continue to be investigated, as well as the spectra of their solid solutions.

References cited

- Anovitz LM, Grew ES (1996) Mineralogy, petrology and geochemistry of boron: an introduction. In ES Grew, AL M (Eds.), *Boron: mineralogy, petrology and geochemistry*, Reviews in mineralogy and geochemistry, vol. 33. Mineralogical Society of America, Chantilly, Virginia, 1–40
- Armstrong JT (1995) CITZAF: a package for correction programs for the quantitative electron microbeam X-ray-analysis of thick polished materials, thin films, and particles. *Microbeam Analysis* 4:177–200
- Barbosa CP, Falster AU, Simmons WB, Webber KL, Nizamoff J, Gaines RV (2000) Minerals of the Brumado Magnesite Deposits, Serra das Éguas, Bahia, Brazil. *Rocks and Minerals* 75:32–39
- Bebout GE, Nakamura E (2003) Record in metamorphic tourmaline of subduction-zone devolatilization and boron cycling. *Geology* 31:407–410
- Bloodaxe E, Hughes J, Dyar M, Grew E, Guidotti C (1999) Linking structure and chemistry in the Schorl–Dravite series. *American Mineralogist* 84:922–928
- Bosi F (2008) Disordering of Fe^{2+} over octahedrally coordinated sites of tourmaline. *American Mineralogist* 93:1647–1653
- Bosi F (2013) Bond-valence constraints around the O1 site of tourmaline. *Mineralogical Magazine* 77:343–351
- Bosi F, Lucchesi S (2007) Crystal chemical relationships in the tourmaline group: structural constraints on chemical variability. *American Mineralogist* 92:1054–1063
- Bosi F, Skogby H, Lazor P, Reznitskii L (2015) Atomic arrangements around the O3 site in Al- and Cr-rich oxy-tourmalines: a combined EMP, SREF, FTIR and Raman study. *Physics and Chemistry of Minerals* 42:441–453
- Branscomb L (1966) Photodetachment cross section, electron affinity, and structure of the negative hydroxyl ion. *Physical Review* 148:13–18
- Buerger M, Parrish W (1937) The unit cell and space group of tourmaline (an example of the inspective equi-inclination treatment of trigonal crystals). *American Mineralogist* 22:1139–1150
- Buerger MJ, Burnham CW, Peacor DR (1962) Assessment of the several structures proposed for tourmaline. *Acta Crystallographica* 15:583–590
- Büttner SH (2005) Deformation-controlled cation diffusion in compositionally zoned tourmaline. *Mineralogical Magazine* 69:471–489

- Büttner SH, Kasemann SA (2007) Deformation-controlled cation diffusion in tourmaline: A microanalytical study on trace elements and boron isotopes. *American Mineralogist* 92:1862–1874
- Cesare B, Rubatto D, Hermann J, Barzi L (2002) Evidence for Late Carboniferous subduction type magmatism in mafic-ultramafic cumulates of the Tauern Window (Eastern Alps). *Contributions to Mineralogy and Petrology* 142:449–464
- Clark CM, Hawthorne FC, Grice JD (2010) Uvite, IMA 2000-030a CNMNC Newsletter, April 2010, page 377. *Mineralogical Magazine* 74:375–377
- Dietrich R (1985) *The Tourmaline Group*. Van Nostrand Reinhold Company Inc., New York
- Donnay G, Buerger MJ (1950) The determination of the crystal structure of tourmaline. *Acta Crystallographica* 3:379–388
- Dunn PJ, Appleman D, Nelen JA, Norberg J (1977) Uvite, a new (old) common member of the tourmaline group and its implications to collectors. *The Mineralogical Record* 8:100–108
- Dutrow BL, Henry DJ (Eds.) (2011a) *Elements*, vol. 7
- Dutrow BL, Henry DJ (2011b) Tourmaline: a geologic DVD. *Elements* 7:301–306
- Ertl A, Tillmanns E (2012) The [9]-coordinated X site in the crystal structure of tourmaline-group minerals. *Zeitschrift für Kristallographie* 227:456–459
- Ertl A, Hughes JM, Prowatke S, Ludwig T, Brandstätter F, Körner W, Dyar MD (2007) Tetrahedrally coordinated boron in Li-bearing olenite from "mushroom" tourmaline from Momeik, Myanmar. *The Canadian Mineralogist* 45:891–899
- Ertl A, Tillmanns E, Ntaflos T, Francis C, Giester G, Körner W, Hughes JM, Lengauer C, Prem M (2008) Tetrahedrally coordinated boron in Al-rich tourmaline and its relationship to the pressure-temperature conditions of formation. *European Journal of Mineralogy* 20:881–888
- Ertl A, Marschall H, Giester G, Henry D, Schertl HP, Ntaflos T, Luvizotto G, Nasdala L, Tillmanns E (2010) Metamorphic ultrahigh-pressure tourmaline: structure, chemistry, and correlations to P-T conditions. *American Mineralogist* 95:1–10
- Ertl A, Giester G, Ludwig T, Meyer HP, Rossman G (2012) Synthetic B-rich olenite: correlations of single-crystal structural data. *American Mineralogist* 97:1591–1597
- Fantini C, Tavares M, Krambrock K (2014) Raman and infrared study of hydroxyl sites in natural unite, fluor-uvite, magnesio-foitite, dravite and elbaite tourmalines. *Physics and Chemistry of Minerals* 41:247–254
- Fischer R, Tillmanns E (1988) The equivalent isotropic displacement factor. *Acta Crystallographica A* C44:775–776
- Frisch W (1980) Tectonics of the western Tauern window. *Mitteilungen der Österreichischen Geologischen Gesellschaft* 71:65–71
- Frisch W, Dunkl I, Kuhleemann J (2000) Post-collisional orogen-parallel large-scale extension in the Eastern Alps. *Tectonophysics* 327:239–265

- Gasharova B, Mihailova B, Konstantinov L (1997) Raman spectra of various types of tourmaline. *European Journal of Mineralogy* 9:935–940
- Gatta G, Danisi R, Adamo I, Meven M, V D (2012) A single-crystal neutron and X-ray diffraction study of elbaite. *Physics and Chemistry of Minerals* 39:577–588
- Gatta G, Bosi F, McIntyre G, Skogby H (2014) First accurate location of two proton sites in tourmaline: a single-crystal neutron diffraction study of oxy-dravite. *Mineralogical Magazine* 78:681–692
- Gonzalez-Carreño T, Fernández M, Sanz J (1988) Infrared and electron microprobe analysis of tourmalines. *Physics and Chemistry of Minerals* 15:452–460
- Grice JD, Ercit TS, Hawthorne FC (1993) Povondraite, a redefinition of the tourmaline ferridravite. *American Mineralogist* 78:433–436
- Hamburger GE, Buerger MJ (1948) The structure of tourmaline. *American Mineralogist* 33:532–540
- Hawkins KD, Mackinnon IDR, Schneeberger H (1995) Influence of chemistry on the pyroelectric effect in tourmaline. *American Mineralogist* 80:491–501
- Hawthorne F, Selway J, Kato A, Matsubra S, M S, Grice J, Vajdak J (1999) Magnesiofoitite, $\square(\text{Mg}_2\text{Al})\text{Al}_6(\text{Si}_6\text{O}_{18})(\text{BO}_3)_3(\text{OH})_4$, a new alkali-deficient tourmaline. *The Canadian Mineralogist* 37:1439–1443
- Hawthorne FC (2002) Bond-valence constraints on the chemical composition of tourmaline. *The Canadian Mineralogist* 40:789–797
- Hawthorne FC, Henry DJ (1999) Classification of the minerals of the tourmaline group. *European Journal of Mineralogy* 11:201–215
- Hawthorne FC, MacDonald DJ, Burns PC (1993) Reassignment of cation site occupancies in tourmaline: Al-Mg disorder in the crystal structure of dravite. *American Mineralogist* 78:265–270
- Henry DJ, Dutrow BL (1990) Ca substitution in Li-poor aluminous tourmaline. *The Canadian Mineralogist* 28:111–124
- Henry DJ, Dutrow BL (1992) Tourmaline in a low grade clastic metasedimentary rock: an example of the petrogenetic potential of tourmaline. *Contributions to Mineralogy and Petrology* 112:203–218
- Henry DJ, Dutrow BL (1996) Metamorphic tourmaline and its petrologic applications. In ES Grew, AL M (Eds.), *Boron: mineralogy, petrology and geochemistry, Reviews in mineralogy and geochemistry*, vol. 33. Mineralogical Society of America, Chantilly, Virginia, 503–557
- Henry DJ, Dutrow BL (2012) Tourmaline at diagenetic to low-grade metamorphic conditions: its petrologic applicability. *Lithos* 154:16–32
- Henry DJ, Guidotti CV (1985) Tourmaline as a petrogenetic indicator mineral: an example from the staurolite-grade metabolites of NW Maine. *American Mineralogist* 70:1–15
- Henry DJ, Dutrow BL, Selverstone J (2002) Compositional asymmetry in replacement tourmaline – an example from the Tauern Window, Eastern Alps. *Geological Materials Research* 4:1–18

- Henry DJ, Guidotti CV, Thomson JA (2005) The Ti-saturation surface for low-to-medium pressure metapelitic biotites: implications for geothermometry and Ti-substitution mechanisms. *American Mineralogist* 90:316–328
- Henry DJ, Novák M, Hawthorne FC, Ertl A, Dutrow BL, Uher P, Pezzotta F (2011) Nomenclature of the tourmaline-supergrain minerals. *American Mineralogist* 96:895–913
- Herron MM (1988) Geochemical classification of terrigenous sands and shales from core or log data. *Journal of Sedimentary Research* 58:820–829
- Hwang SL, Shen P, Chu HT, T-F Y, Liou JG, Sobolev NV, Shatsky VS (2005) Crust-derived potassic fluid in metamorphic microdiamond. *Earth and Planetary Letters* 231:295–306
- Kahlenberg V, Veličkov B (2000) Structural investigations on a synthetic alkali-free hydrogen-deficient Fe-tourmaline (foitite). *European Journal of Mineralogy* 12:947–953
- Korsakov AV, Theunissen K, Smirnova LV (2004) Intergranular diamonds derived from partial melting of crustal rocks at ultrahigh-pressure metamorphic conditions. *Terra Nova* 16:146–151
- Krosse S (1995) Hochdrucksynthese, Stabilität und Eigenschaften der Borosilikate Dravit und Kornerupin sowie Darstellung und Stabilitätsverhalten eines neuen Mg-Al Borates. Ph.D. thesis, Ruhr Universität, Bochum, Germany
- Krynine PD (1946) The tourmaline group in sediments. *The Journal of Geology* 54:65–87
- Kutzbach M, Wunder B, Rhede D, Koch-Müller M, Ertl A, Giester G, Heinrich W, Franz G (2016) Tetrahedral boron in natural and synthetic HP/UHP tourmaline: Evidence from Raman spectroscopy, EMPA, and single-crystal XRD. *American Mineralogist* 101:93–104
- Lammerer B, Gebrande H, Lüschen E, Veselá P (2008) A crustal-scale cross-section through the Tauern Window (eastern Alps) from geophysical and geological data. *Geological Society, London Special Publications* 298:219–229
- Larson AC, Von Dreele RB (1987) Generalized structure analysis system. Tech. Rep. LAUR 86-748, Los Alamos National Laboratory
- Le Maitre RW, Streckeisen A, Zanettin B, Le Bas MJ, Bonin B, Bateman P, Bellieni G, Dudek A, Efremova S, Keller J, Lameyre J, Sabine PA, Schmid R, Sorensen H, Woolley AR (Eds.) (1989) A classification of igneous rocks and glossary of terms. Blackwell Scientific Publications
- Leeman WP, Sisson VB (1996) Geochemistry of boron and its implications for crustal and mantle processes. In ES Grew, AL M (Eds.), *Boron: mineralogy, petrology and geochemistry, Reviews in mineralogy and geochemistry*, vol. 33. Mineralogical Society of America, Chantilly, Virginia, 645–708
- London D, Morgan VI GB, Wolf MB (1996) Boron in granitic rock and their contact aureoles. In ES Grew, AL M (Eds.), *Boron: mineralogy, petrology and geochemistry, Reviews in mineralogy and geochemistry*, vol. 33. Mineralogical Society of America, Chantilly, Virginia, 299–330

- Lussier A, Ball NA, Hawthorne FC, Henry DJ, Shimizu R, Ogasawara Y, Ota T (2014) Maruyamaite, IMA 2013-123. In CNMNC Newsletter, vol. 78. Mineralogical Magazine, 550
- MacDonald D, Hawthorne F (1995) The crystal chemistry of Si–Al substitution in tourmaline. *The Canadian Mineralogist* 33:849–858
- Marschall HR, Jiang SY (2011) Tourmaline isotopes: no element left behind. *Elements* 7:313–319
- Marschall HR, Altherr R, Kalt A, Ludwig T (2008) Detrital, metamorphic and metasomatic tourmaline in high-pressure metasediments from Syros (Greece): intra-grain boron isotope patterns determined by secondary-ion mass spectrometry. *Contributions to Mineralogy and Petrology* 155:703–717
- Marschall HR, Korsakov AV, Luvizotto GL, Nasdala L, Ludwig T (2009a) On the occurrence and boron isotopic composition of tourmaline in (ultra)high-pressure metamorphic rocks. *Journal of the Geological Society, London* 166:811–823
- Marschall HR, Meyer C, Wunder B, Ludwig T, Henrich W (2009b) Experimental boron isotope fractionation between tourmaline and fluid: confirmation from in situ analyses by secondary ion mass spectrometry and from Rayleigh fractionation modelling. *Contributions to Mineralogy and Petrology* 158:675–681
- Martínez-Alonso S, Rustad J, Goetz A (2002) Ab initio quantum mechanical modelling of infrared vibrational frequencies of the OH group in dioctahedral phyllosilicates. Part II: main physical factors governing the OH vibrations. *American Mineralogist* 87:1224–1234
- McDonough WF, Sun Ss (1995) The composition of the Earth. *Chemical Geology* 120:223–253
- McKeown D (2008) Raman spectroscopy, vibrational analysis, and heating of buergerite tourmaline. *Physics and Chemistry of Minerals* 35:259–270
- Meyer C, Wunder B, Meixner A, Romer RL, Heinrich W (2008) Boron-isotope fractionation between tourmaline and fluid: an experimental re-investigation. *Contributions to Mineralogy and Petrology* 156:259–267
- Mihailova B, Gasharova B, Konstantinov L (1996) Influence of non-tetrahedral cations on Si–O vibrations in complex silicates. *Journal of Raman Spectroscopy* 27:829–833
- Mikhno AO, Schmidt U, Korsakov AV (2013) Origin of K-cymrite and kokchetavite in the polyphase mineral inclusions from Kokchetav UHP calc-silicate rocks: evidence from confocal Raman imaging. *European Journal of Mineralogy* 25:807–816
- Mirwald PW, Massonne HJ (1980) Quartz-coesite transition and the comparative friction measurements in piston-cylinder apparatus using talc-alsimag-glass (TAG) and NaCl high pressure cells: A discussion. *Neues Jahrbuch für Mineralogie* 1980:469–477
- Oberhänsli R, Bousquet R, Engi M, Goffé B, Gosso G, Handy M, Höck V, Koller F, Lardeaux JM, Polino R, Rossi P, Schuster R, Schwartz S, Spalla MI (2004) Explanatory note to the map “Metamorphic structure of the Alps”. Commission for the Geological Map of the World, Paris
- Ota T, Kobayashi K, Katsura T, Nakamura E (2008a) Tourmaline breakdown in a pelitic system: implications for boron cycling through subduction zones. *Contributions to Mineralogy and Petrology* 155:19–32

- Ota T, Kobayashi K, Kunihiro T, Nakamura E (2008b) Boron cycling by subducted lithosphere; insights from diamondiferous tourmaline from the Kokchetav ultrahigh-pressure metamorphic belt. *Geochimica et Cosmochimica Acta* 72:3531–3541
- Palmer MR, Swihart GH (1996) Boron isotope geochemistry: an overview. In ES Grew, AL M (Eds.), *Boron: mineralogy, petrology and geochemistry*, Reviews in mineralogy and geochemistry, vol. 33. Mineralogical Society of America, Chantilly, Virginia, 709–744
- Pertlik F, Ertl A, Körner W, Brandstätter F, Schuster R (2003) Na-rich dravite in the marbles from Friesach, Carinthia, Austria: chemistry and crystal structure. *Neues Jahrbuch Mineralogie Monatshefte* 2003:277–288
- Ratschbacher L, Frisch W, Linzer HG, Merle O (1991) Lateral extrusion in the Eastern Alps, part 2: structural analysis. *Tectonics* 10:257–271
- Rosenberg P, Foit FJ (1979) Synthesis and characterization of alkali-free tourmaline. *American Mineralogist* 64:180–186
- Schertl HP, Sobolev NV (2013) The Kokchetav Massif, Kazakhstan: "type locality" of diamond-bearing UHP metamorphic rocks. *Journal of Asian Earth Sciences* 63:5–38
- Schmid SM, Fügenschuh B, Kissling E, R S (2004) Tectonic map and overall architecture of the Alpine orogeny. *Eclogae Geologicae Helvetiae* 97:93–117
- Schmid SM, Scharf A, Handy MR, Rosenberg CL (2013) The Tauern Window (Eastern Alps, Austria): a new tectonic map with cross-sections and a tectonomorphic synthesis. *Swiss Journal of Geosciences* 106:1–32
- Schreyer W, Werding G (1997) High-pressure behaviour of selected boron minerals and the question of boron distribution between fluids and rocks. *Lithos* 41:251–266
- Schreyer W, Wodara U, Marler B, van Aken PA, Seifert F, Robert JL (2000) Synthetic tourmaline (olenite) with excess boron replacing silicon in the tetrahedral site: I. Synthesis conditions, chemical and spectroscopic evidence. *European Journal of Mineralogy* 12:529–541
- Schuster R, Koller F, Hoeck V, Hoinkes G, Bousquet R (2004) Explanatory notes to the map: metamorphic structure of the Alps, metamorphic evolution of the Eastern Alps. *Mitteilungen der Österreichischen Mineralogischen Gesellschaft* 149:175–199
- Selverstone J, Spear FS, Franz G, Morteau G (1984) High-pressure metamorphism in the SW Tauern Window, Austria: P-T paths from hornblende-kyanite-staurolite schists. *Journal of Petrology* 25:501–531
- Shannon RD (1976) Revised effective ionic radii and systematic studies of interatomic distances in halides and chalcogenides. *Acta Crystallographica* A32:751–767
- Sheldrick G (1997) SHELXL-97, a program for crystal structure refinement. Tech. rep., University of Göttingen, Germany
- Shimizu R, Ogasawara Y (2005) Discovery of K-tourmaline in diamond-bearing quartz-rich rock from the Kokchetav Massif, Kazakhstan. *Mitteilungen der Österreichischen Mineralogischen Gesellschaft* 150:141
- Shimizu R, Ogasawara Y (2013) Diversity of potassium-bearing tourmalines in diamondiferous Kokchetav UHP metamorphic rocks: A geochemical recorder from peak to retrograde metamorphic stages. *Journal of Asian Earth Sciences* 63:39–55

- Skogby H, Bosi F, Lazor P (2012) Short-range order in tourmaline: a vibrational spectroscopic approach to elbaite. *Physics and Chemistry of Minerals* 39:811–816
- Taylor MC, Cooper MA, Hawthorne FC (1995) Local charge-compensation in hydroxyl-deficient unite. *The Canadian Mineralogist* 33:1215–1221
- van Hinsberg VJ, Schumacher JC (2007a) Intersector element partitioning in tourmaline: a potentially powerful single crystal thermometer. *Contributions to Mineralogy and Petrology* 153:289–301
- van Hinsberg VJ, Schumacher JC (2007b) Using estimated thermodynamic properties to model accessory phases: the case of tourmaline. *Journal of Metamorphic Geology* 25:769–779
- van Hinsberg VJ, Schumacher JC (2011) Tourmaline as a petrogenetic indicator mineral in the Haut-Allier metamorphic suite, Massif Central, France. *Canadian Mineralogist* 29:177–194
- van Hinsberg VJ, Schumacher JC, Kearns S, Mason PRD, Franz G (2006) Sector zoning in metamorphic tourmaline and resultant major and trace-element fractionation. *American Mineralogist* 91:717–728
- van Hinsberg VJ, Migdisov AA, Williams-Jones AE (2010) Reading the mineral record of fluid composition from element partitioning. *Geology* 38:847–850
- van Hinsberg VJ, Henry DJ, Marschall HR (Eds.) (2011a) Tourmaline: an ideal indicator of its host environment, vol. 49. *The Canadian Mineralogist*
- van Hinsberg VJ, Henry DJ, Marschall HR (2011b) Tourmaline: an ideal indicator of its host environment. *Canadian Mineralogist* 29:177–194
- Veličkov B (2002) Kristallchemie von Fe,Mg-Turmalinen: Synthese und spektroskopische Untersuchungen. Ph.D. thesis, Technische Universität Berlin
- Veselá P, Lammerer B (2008) The Pfitsch-Mörchner Basin, an example of the post-Variscan sedimentary evolution of the Tauern Window (Eastern Alps). *Swiss Journal of Geosciences* 101, Supplement 1:S73–S88
- Veselá P, Frank S, Friedrich F, Axel G (2011) Magmato-sedimentary Carboniferous to Jurassic evolution of the western Tauern window, Eastern Alps (constraints from U-Pb zircon dating and geochemistry). *International Journal of Earth Sciences* 100:993–1027
- von Goerne G, Franz G (2000) Synthesis of Ca-tourmaline in the system $\text{CaO-MgO-Al}_2\text{O}_3\text{-SiO}_2\text{-B}_2\text{O}_3\text{-H}_2\text{O-HCl}$. *Mineralogy and Petrology* 69:161–182
- von Goerne G, Franz G, Wirth R (1999) Hydrothermal synthesis of large dravite crystals by the chamber method. *European Journal of Mineralogy* 11:1061–1077
- von Goerne G, Franz G, Heinrich W (2001) Synthesis of tourmaline solid solutions in the system $\text{Na}_2\text{O-MgO-Al}_2\text{O}_3\text{-SiO}_2\text{-B}_2\text{O}_3\text{-H}_2\text{O-HCl}$ and the distribution of Na between tourmaline and fluid at 300–700°C and 200 MPa. *Contributions to Mineralogy and Petrology* 141:160–173
- von Goerne G, Franz G, van Hinsberg VJ (2011) Experimental determination of Na-Ca distribution between tourmaline and fluid in the system $\text{CaO-Na}_2\text{O-MgO-Al}_2\text{O}_3\text{-SiO}_2\text{-B}_2\text{O}_3\text{-H}_2\text{O}$. *The Canadian Mineralogist* 49:137–152

- Werding G, Schreyer W (1984) Alkali-free tourmaline in the system $\text{MgO-Al}_2\text{O}_3\text{-B}_2\text{O}_3\text{-SiO}_2\text{-H}_2\text{O}$. *Geochimica et Cosmochimica Acta* 48:1331–1344
- Werding G, Schreyer W (1996) Experimental studies on borosilicates and selected borates. In ES Grew, AL M (Eds.), *Boron: mineralogy, petrology and geochemistry*, Reviews in mineralogy and geochemistry, vol. 33. Mineralogical Society of America, Chantilly, Virginia, 117–163
- Whitney DL, Evans BW (2010) Abbreviations for names of rock-forming minerals. *American Mineralogist* 95:185–187
- Yardley BWD, Bodnar RJ (2014) Fluids in the Continental Crust. *Geochemical Perspectives* 3:1–123
- Žáček V, Jirá F, Petrov A, Hyršl J (2000) Tourmalines of the povondraite-(oxy)dravite series from the cap rock of meta-evaporite in Alto Chapare, Cochabamba, Bolivia. *Journal of the Czech Geological Society* 45:3–12
- Zhao C, Liao L, Xia Z, Sun X (2012) Temperature-dependent Raman and infrared spectroscopy study on iron-magnesium tourmalines with different Fe content. *Vibrational Spectroscopy* 62:28–34
- Zoheidi M (1990) Chemische Zusammensetzung natürlicher Turmaline aus Hochdruckgesteinen (Eklogitzone, Tauern, Österreich). Ph.D. thesis, Technische Universität Berlin. Unpublished
- Zvezdin YI, Belyakov YI (1968) Hydrogen permeability of some transition metals and metals of group I of the periodic system. *Soviet materials science: a transl. of Fiziko-khimicheskaya mekhanika materialov*. Academy of Sciences of the Ukrainian SSR 3:255–256

Appendix A

Improved single crystal structure refinement data of magnesio-foitite (MF2)

A single crystal structure refinement of synthetic magnesio-foitite (MF2) is presented in Chapter 5. The refinement of Chapter 5 includes atom parameters for the X site of the nominally X-site-vacant magnesio-foitite with a negative z coordinate (Table 5.2). This value has a relatively large error resulting from the negligible scattering power of the predominantly vacant X site. The SREF presented below has been improved by removing the X site from the structure refinement. The improved SREF gives Y and Z site occupancy values (Table A.2) in better agreement with those determined from the integrated peak intensities of the O-H stretching Raman spectra (Table 5.8).

Table A.1: Improved single-crystal XRD refinement details for synthesized magnesio-foitite (MF2)

	Magnesio-foitite (MF2)
Crystal size (mm)	$0.10 \times 0.04 \times 0.04$
Collection mode, $2\theta_{max}$	Full sphere, 68.37°
Frame width	0.5°
Frame scan time (s)	60
Detector distance (mm)	60
h, k, l ranges	$-24/23, -24/24, -6/11$
Total reflections measured	5578
Unique reflections	1182
$R1^a(F)$, $wR2^b(F^2)$, $R^c_{int}(\%)$	1.21, 2.92, 1.07
Flack x parameter	0.04(8)
‘Observed’ reffs. [$F_o > 4\sigma_{(F_o)}$]	1158
Refined parameters	92
Goodness of Fit ^d	1.09
$\Delta\sigma_{min}, \Delta\sigma_{max}$ (e/Å ³)	-0.18, 0.46

X-ray radiation: MoK α ($\lambda = 0.71073$ Å); Z: 3; space group: R3 m (no. 160);
multiscan absorption correction; refinement on F^2

Scan mode: sets of ϖ and θ scans

$$^a R1 = \Sigma ||F_o| - |F_c|| / \Sigma |F_o|$$

$$^b wR2 = \{\Sigma[w(F_o^2 - F_c^2)^2] / \Sigma[w(F_o^2)^2]\}^{1/2}$$

$$w = 1 / [\sigma^2(F_o^2) + (aP)^2 + bP], P = [2F_c^2 + \text{Max}(F_o^2, 0)] / 3$$

$$^c R_{int} = \Sigma |F_o^2 - F_o^2(\text{mean})| / \Sigma [F_o^2]$$

$$^d \text{GooF} = S = \{\Sigma[w(F_o^2 - F_c^2)^2] / (n - p)\}^{1/2}$$

Table A.2: Improved atom parameters and site symmetry of magnesio-foitite (MF2) determined by single-crystal XRD refinement

Site	x	y	z	U_{eq}	Site symmetry	Occupancy
Magnesio-foitite (MF2)						
Y	0.12601(3)	$1/2x$	0.62831(6)	0.0076(3)	m	$Al_{1.71}Mg_{1.29(17)}^a$
Z	0.29775(2)	0.26151(2)	0.61077(3)	0.0075(3)	1	$Al_{5.01}Mg_{0.99(25)}^a$
B	0.10963(5)	$2x$	0.4568(2)	0.0079(2)	m	$B_{3.00}$
T	0.19170(2)	0.18947(2)	0.00178(4)	0.0050(1)	1	$Si_{5.65}B_{0.35(4)}^a$
H3	0.262(2)	$1/2x$	0.395(4)	0.040(8)	m	$H_{1.00}$
W (O1)	0	0	0.7758(3)	0.0143(3)	3m	$O_{1.00}$
O2	0.06112(3)	$2x$	0.49680(15)	0.0125(2)	m	$O_{1.00}$
V (O3)	0.26152(8)	$1/2x$	0.50776(14)	0.0120(2)	m	$O_{1.00}$
O4	0.09443(4)	$2x$	0.06931(15)	0.0117(2)	m	$O_{1.00}$
O5	0.18850(8)	$1/2x$	0.09507(14)	0.0115(2)	m	$O_{1.00}$
O6	0.19584(5)	1.8421(5)	0.77671(10)	0.0087(1)	1	$O_{1.00}$
O7	0.28550(4)	0.28572(4)	0.07768(9)	0.0083(1)	1	$O_{1.00}$
O8	0.20943(5)	0.27004(5)	0.43968(10)	0.0094(1)	1	$O_{1.00}$

Tourmaline has space group $R3m$, and its unit cell with hexagonal axes is centred on $3m$.
For definition of U_{eq} see Fischer and Tillmanns (1988).

^aDetermined by refinement

Table A.3: Improved selected interatomic distances in magnesio-foitite (MF2) determined by SREF

Cation site	Anion site	Bond length (Å)
		Magnesio-foitite (MF2)
Y	O2 \times 2	1.9510(7)
	O6 \times 2	1.9825(7)
	W (O1)	2.0299(10)
	V (O3)	2.0555(12)
	Mean	1.9921(4)
Z	O6	1.8835(7)
	O8	1.8880(7)
	O7	1.8897(7)
	O8'	1.9162(7)
	O7'	1.9420(7)
	V (O3)	2.0001(5)
	Mean	1.9199(3)
T	O7	1.6062(6)
	O6	1.6102(8)
	O4	1.6162(4)
	O5	1.6318(5)
	Mean	1.6161(2)
B	O2	1.3670(17)
	O8 \times 2	1.3805(10)
	Mean	1.3760(9)

Appendix B

Supplementary material to Chapter 7

B.1 Abstract

Here we present element maps of tourmalines from the major tourmaline-bearing units of the Pfitsch Formation in the SW Tauern Window, Eastern Alps, described in more detail in Chapter 7.

B.2 Analytical methods

The element maps were produced by Oona Appelt following the procedure detailed in Chapter 2.

B.3 Results

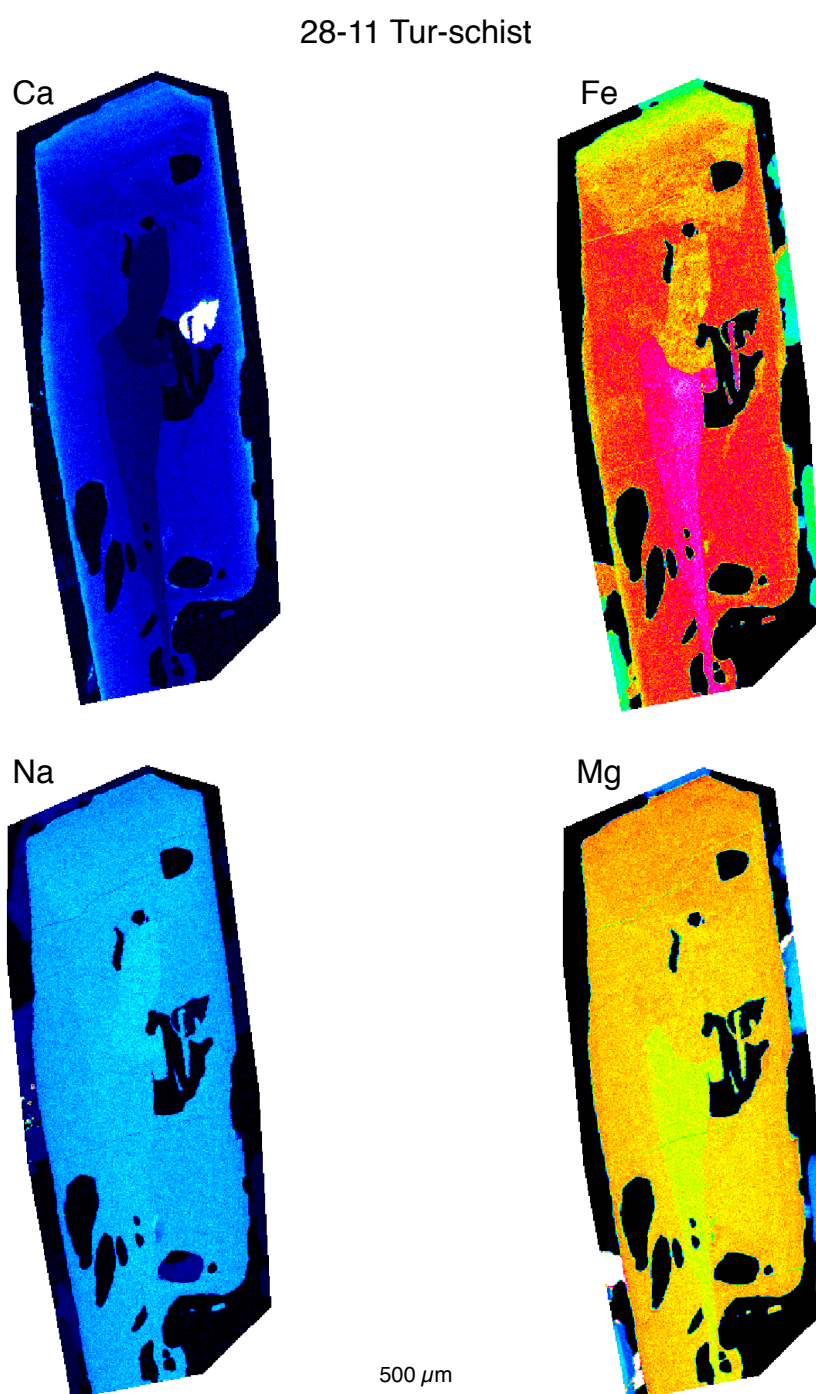


Figure B.1: Element maps of a tourmaline crystal from the Tur-schist in the Pfitsch Formation.

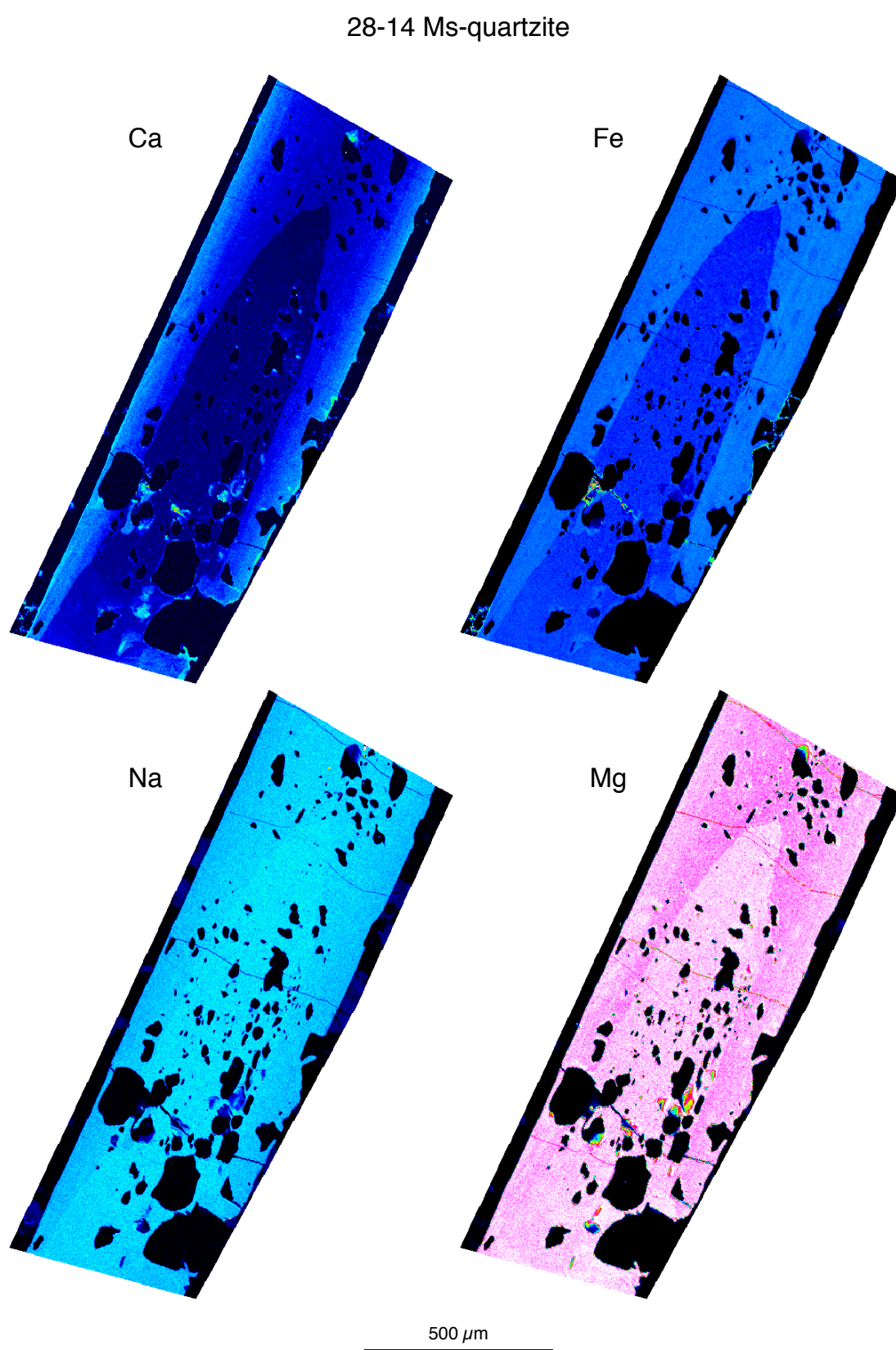


Figure B.2: Element maps of a tourmaline crystal from the Ms-quartzite in the Pfitsch Formation.

28-15 Chl-Bt-schist

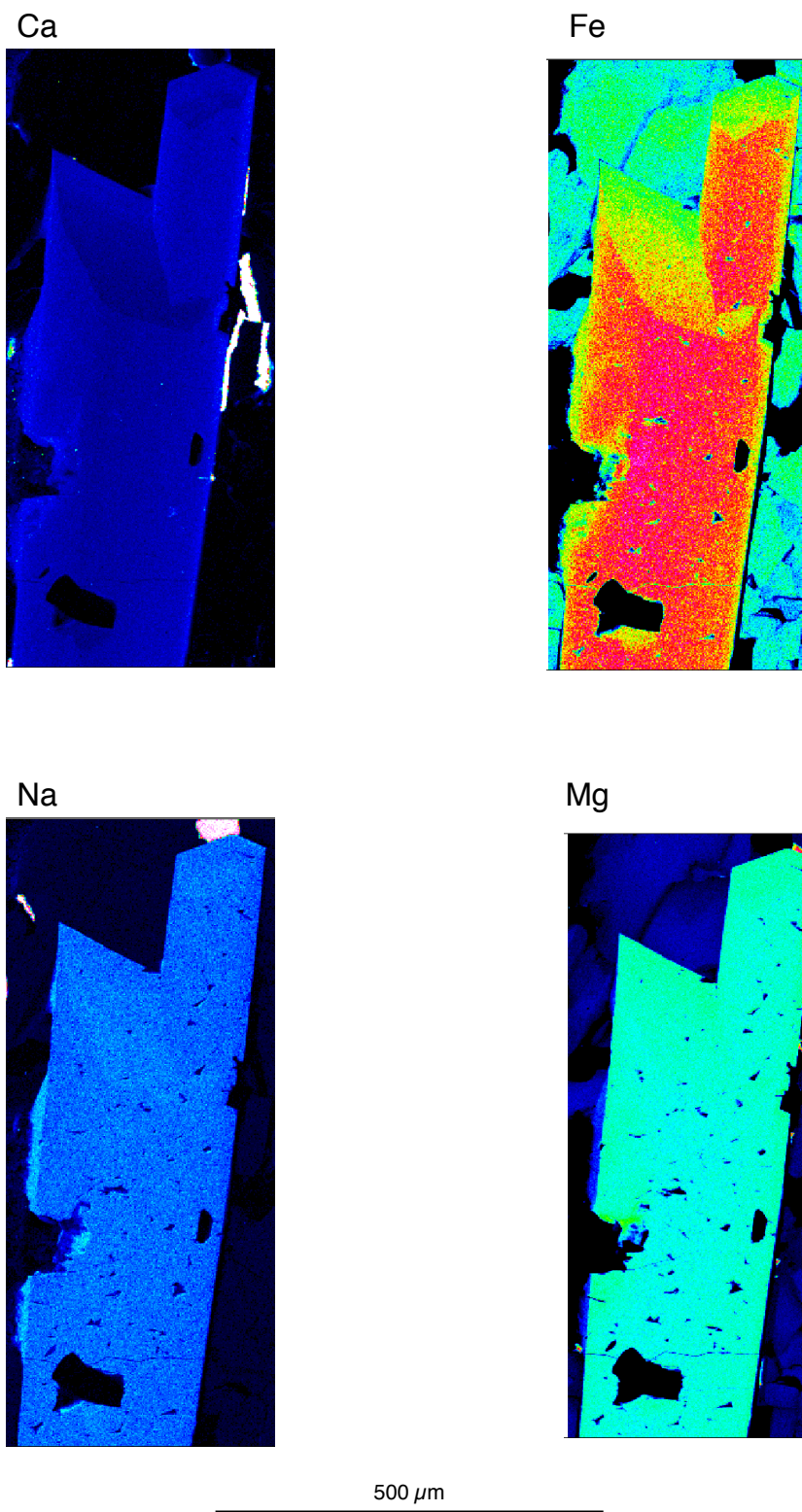


Figure B.3: Element maps of a tourmaline crystal from the Chl-Bt-schist in the Pfitsch Formation.

28-17 Tur-gneiss

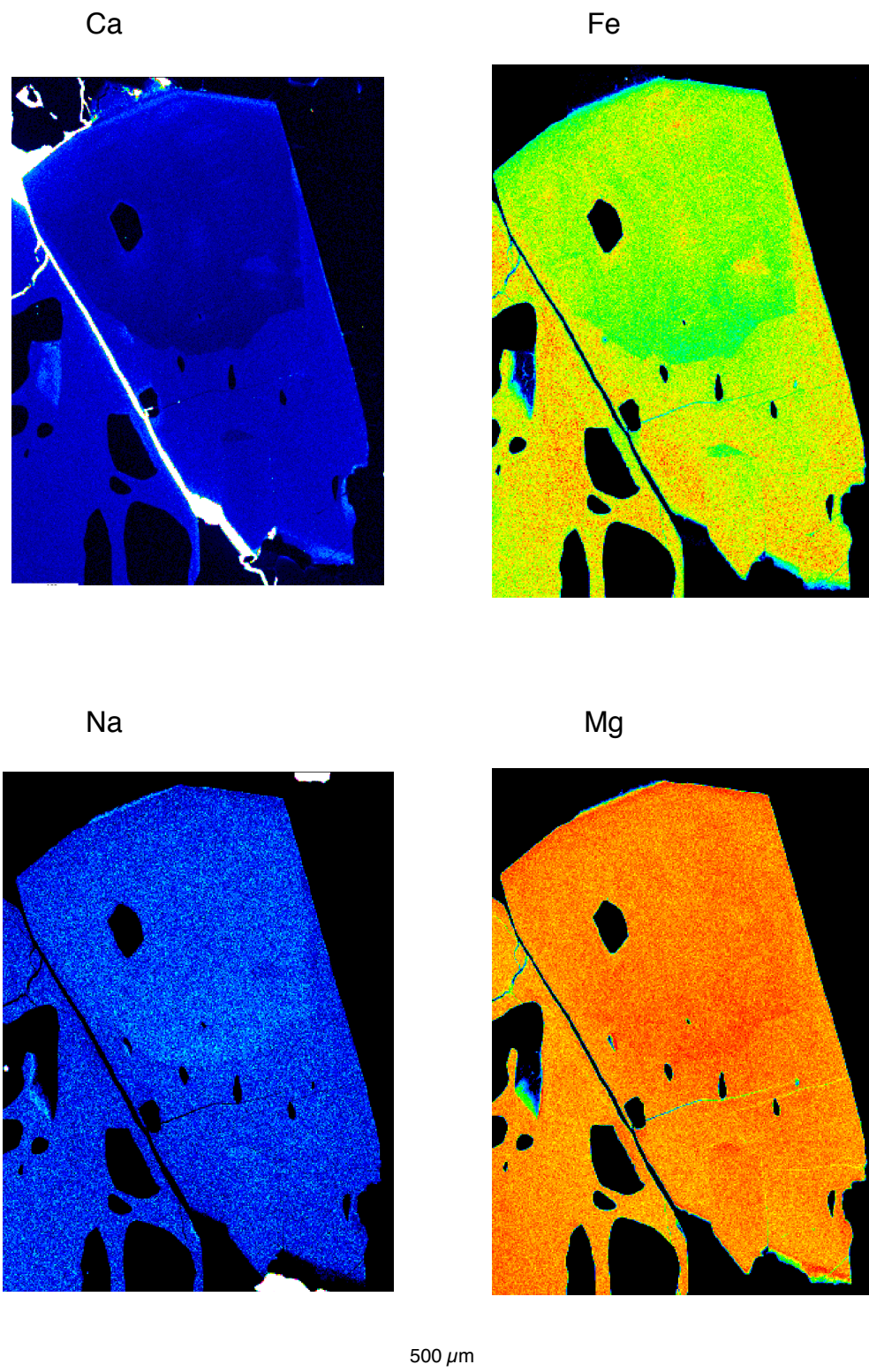


Figure B.4: Element maps of a tourmaline crystal from the Tur-gneiss in the Pfitsch Formation.

